Tampere University

JAGADISH K. SALUNKE

# Low-Cost Phenothiazine- and Pyrene-Based Hole-Transporting Materials for Halide Perovskite Solar Cells

Tampere University Dissertations 373

Tampere University Dissertations 373

JAGADISH K. SALUNKE

# Low-Cost Phenothiazine- and Pyrene-Based Hole-Transporting Materials for Halide Perovskite Solar Cells

ACADEMIC DISSERTATION
To be presented, with the permission of
the Faculty of Engineering and Natural Sciences
of Tampere University,
for public discussion at Tampere University
on 15th January 2021, at 12 o'clock.

ACADEMIC DISSERTATION
Tampere University, Faculty of Engineering and Natural Sciences
Finland

| | | |
|---|---|---|
| *Responsible supervisor and Custos* | Professor<br>Arri Priimägi<br>Tampere University<br>Finland | |
| *Supervisors* | Associate Professor (tenure track)<br>Paola Vivo<br>Tampere University<br>Finland | Postdoctoral Researcher<br>Tero-Petri Ruoko<br>Linköping University<br>Sweden |
| *Pre-examiners* | Professor Emeritus<br>Jouko Korppi-Tommola<br>University of Jyväskylä<br>Finland | Senior Research Fellow<br>Roberto Grisorio<br>Politecnico di Bari<br>Italy |
| *Opponent* | Adjunct Professor<br>Raquel Galian<br>University of Valencia<br>Spain | |

The originality of this thesis has been checked using the Turnitin Originality Check service.



Cover design: Roihu Inc.

ISBN 978-952-03-1845-1 (print)
ISBN 978-952-03-1846-8 (pdf)
ISSN 2489-9860 (print)
ISSN 2490-0028 (pdf)
http://urn.fi/URN:ISBN:978-952-03-1846-8

PunaMusta Oy – Yliopistopaino
Joensuu 2021

Dedicated to my father.

# ACKNOWLEDGEMENTS

The research reported in this Thesis was conducted at the Chemistry and Advanced Materials research group (formerly known as Laboratory of Chemistry and Bioengineering) at the Faculty of Engineering and Natural Sciences of Tampere University (previously Tampere University of Technology). The Fortum Foundation (Grant 201700234 & 201800260), Finnish Foundation for Technology promotion, Emil Aaltonen Foundation, and Academy of Finland (Decision number 31142) are duly acknowledged for funding this research work.

I would like to begin this Thesis by expressing my gratitude to my boss Prof. Arri Priimägi for giving me the opportunity to carry out doctoral research and to become an independent researcher. I am particularly grateful for his encouragement and positive support since the very early stages of my doctoral thesis when failures were frequent and expected results were not forthcoming. I would like to thank Assoc. Prof. Paola Vivo for her continuous positive support, motivation, and supervision for this work. Without her guidance and collaboration, the output of this work would not have been possible. I would like to thank Dr. Tero-Petri Ruoko for his instructions, collaboration, and help during doctoral work as well as for his supervision and Thesis-review efforts. I would particularly like to thank Prof. Nuno Candeias for his guidance and collaboration on modeling work as well as organic chemistry. I would also like to thank Dr. Kimmo Kaunisto for his guidance during the initial period of my studies. I am also thankful to Dr. Nikita Durandin for his continuous guidance especially in the topic of non-covalent interactions and physical chemistry and providing company in the office. I would also like to thank Dr. Maning Liu and Dr. Arto Hiltunen for guidance and collaboration in solar cells research. I am thankful to present and past members of the Smart Photonic Materials team and also to all the Professors and staff members of the Chemistry and Advanced Materials group for providing a friendly working atmosphere and assistance on practical matters. I would particularly like to mention Dr. Zafar Ahmed, Dr. Owies Wani, Dr. Lijo George, and Dr. Srikanth Revoju for making me feel like at home.

I would also like to thank my collaborators Dr. Nadia Camaioni and Dr. Francesca Tinti (Istituto per la Sintesi Organica e la Fotoreattività, CNR, Italy), Prof. Jingjing Chang

(Xidian University, China), Prof. Ronald Österbacka (Åbö Akademi, Turku), and Prof. Prashant Sonar (QUT, Australia) for helping with device studies, and Prof. Xavier Crispin for his constant motivation for my career. Many thanks go to my previous mentors Prof. Prakash Wadgaonkar (NCL, India) and Prof. Rahul Banerjee (IISER, India).

To my colleagues in the synthesis laboratory, Dr. Benedicta Assoah, Suvi Holmstedt, Tatu Rimpiläinen, Aleksi Paakkunainen, and Joa̋o R. Vale, thank you for all the nice moments and conversations. In particular, I thank Joa̋o. R. Vale for his friendship and for the great time especially during winter visits to Kaupinojan sauna at the weekends.

I offer my deepest gratitude to my parents, brother, sister-in-law, mother-in-law, for their faith, prayers, motivation, and support. I am also thankful to my friends Mr. Shashikant Salunke, Mr. Pradip Nandre, Mr. Vinod Salunke, Mr. Tushar Chitte, Mr.Pravin Nandre, Dr. Sachin Borse, Dr. Anil Kakuste, Dr. Kamlakar Nandre, Dr. D. B. Shinde, and Mr. Vasili Ignatev for their positive support and encouragement during difficult times.

I express my gratitude and love to my wife Lina Salunke for always being there for me through all the difficult times and for supporting me to achieve my goals. I would also like to thank and express my love for my dog Bobic for keeping me always happy positive, and calm and for helping me to get rid of all the stress and worries with his love and kindness.

Tampere September 15, 2020

Jagadish Salunke

# ABSTRACT

Organic-inorganic halide perovskite solar cells (PSCs) show great potential for energy applications due to their excellent power conversion efficiency that dramatically increased from 3.8 % to over 25% in just a decade of research. The performance of PSCs is strongly influenced by the charge-transporting (electron and hole) layers. Currently, most of the high-performing PSCs use 2,2',7,7'-tetrakis-(N,N'-di-p-methoxyphenylamine)-9,9'-spirobifluorene) (Spiro-OMeTAD) or polytriarylamine (PTAA) as hole-transporting materials (HTMs). However, Spiro-OMeTAD and PTAA suffer from several drawbacks, such as extremely high cost, difficult and multistep synthesis and purification, and low hole mobility and conductivity, thus requiring the use of additional chemical dopants. The addition of dopants not only decreases the device stability but also increases the complexity of device fabrication. Considering all the above-mentioned drawbacks it is highly desirable to design alternative HTMs to simplify the fabrication of PSCs and ensure their industrial-scale application.

This work investigates the molecular design, synthesis, and application of phenothiazine- and pyrene-core organic small molecule-based HTMs for efficient and stable PSCs. Ullman and Suzuki coupling reactions, as well as simple condensation reactions, were used to synthesize the HTMs. The optical and electrochemical properties of the HTMs were tuned by the introduction of electron donor and acceptor groups to the parent materials. The newly synthesized HTMs exhibited excellent interactions with the perovskite surface. The azomethine HTMs led to PSCs with a power conversion efficiency of up to 14% and with high stability, environmentally friendly synthesis, and very low cost (~ 10$/g). The optical and electrochemical properties of the pyrene-core HTMs, as well as the performance of corresponding PSCs, were tuned by an effective fluorination strategy.

We believe that the molecular designs presented in this work will provide useful know-how to significantly enhance the stability and the performance of PSCs, thus bringing them closer to commercialization. In particular, our focus has been on developing material with cost-efficient synthesis and minimal environmental impact.

# CONTENTS

# ABBREVIATIONS

| | |
|---|---|
| CB | Conduction band |
| DCM | Dichloromethane |
| DMSO | Dimethyl sulfoxide |
| DFT | Density functional theory |
| DPV | Differential pulse voltammetry |
| $E_g^{opt}$ | Optical bandgap |
| $E_{ox}$ | Oxidation potential |
| $E_{red}$ | Reduction potential |
| ED | Electron-donating |
| EW | Electron-withdrawing |
| ETM | Electron-transporting material |
| FF | Fill factor |
| FTO | Fluorine-doped tin oxide |
| HTM | Hole-transporting material |
| HOMO | Highest occupied molecular orbital |
| ITO | Indium tin oxide |
| $J_{sc}$ | Short-circuit current density |
| LUMO | Lowest unoccupied molecular orbital |
| LiTFSI | Lithium bis(trifluoromethanesulfonyl)imide |
| MS | Mass spectroscopy |
| NMR | Nuclear magnetic resonance |
| OLED | Organic light-emitting diode |
| OFET | Organic field effect transistor |
| OPV | Organic photovoltaic |
| PESA | Photoelectron spectroscopy in air |
| PSC | Perovskite solar cell |
| PCE | Power conversion efficiency |
| Photo-CELIV | Photo-induced charge extraction by linearly increasing voltage |
| PCBM | Phenyl $C_{61}$-butyric acid methyl ester |
| PTAA | Poly[bis(4-phenyl)(2,4,6-trimethylphenyl)amine |

| | |
|---|---|
| Spiro-OMeTAD | 2,2',7,7'-Tetrakis[N,N-di(4-methoxyphenyl)amino]-9,9'-spirobifluorene |
| T-BP | 4-tert-butylpyridine |
| PEDOT: PSS | poly(3,4-ethylenedioxythiophene) polystyrene sulfonate |
| TR-PL | Time-resolved photoluminescence |
| TOF | Time of flight |
| TMS | Tetramethyl silane |
| TCO | Transparent conductive oxide |
| THF | Tetrahydrofuran |
| $TBABF_4$ | Tetrabutylammonium tetrafluoroborate |
| VB | Valence band |
| $V_{oc}$ | Open-circuit voltage |
| XRD | X-ray diffraction |

# LIST OF PUBLICATIONS

I Durgaprasad B. Shinde, Jagadish K. Salunke, Nuno R. Candeias, Francesca Tinti, Massimo Gazzano, Prakash P. Wadgaonkar, Arri Priimagi, Nadia Camaioni, Paola Vivo. Crystallisation-enhanced bulk hole mobility in phenothiazine-based organic semiconductors. *Scientific Reports* **2017**, 7, 46268.

II Jagadish K. Salunke, Xing Guo, Zhenhua Lin, João R. Vale, Nuno R. Candeias, Mathias Nyman, Staffan Dahlström, Ronald Österbacka, Arri Priimagi, Jingjing Chang, Paola Vivo. Phenothiazine-based hole-transporting materials toward eco-friendly perovskite solar cells. *ACS Applied Energy Materials* **2019**, 2, 5, 3021-3027.

III Jagadish K. Salunke, Xing Guo, Maning Liu, Zhenhua Lin, Nuno R. Candeias, Arri Priimagi, Jingjing Chang, Paola Vivo. N-substituted phenothiazines as environmentally friendly hole-transporting materials for low-cost and highly stable halide perovskite solar cells. *ACS Omega* **2020**, 5, 36, 23334–23342.

IV Jagadish K. Salunke, Amandeep Singh, Dongxu He, Hong D. Pham, Yang Bai, Lianzhou Wang, Staffan Dahlström, Mathias Nyman, Sergei Manzhos, Krishna Feron, Ronald Österbacka, Arri Priimagi, Paola Vivo, Prashant Sonar. Fluorination of pyrene-based organic semiconductors enhances the performance of light-emitting diodes and halide perovskite solar cells. *Organic Electronics* **2019**, 77:105524.

# AUTHOR'S CONTRIBUTION

The work presented in this Thesis has been conducted with the collaborative efforts of multiple national and international research groups and with a scientific contribution from all the co-authors included in the research papers. In this Section, the personal contribution of the doctoral candidate in the published papers is described.

I This publication focuses on the design, synthesis, and investigation of the charge-transporting properties of phenothiazine-core organic semiconductors. The author designed the three novel phenothiazine derivatives, synthesized one of the final compounds and all the intermediates of the other two compounds, carried out the optical and electrochemical measurements under the supervision of Dr. Kimmo Kaunisto, analyzed the data, and wrote the manuscript draft. The hole-mobility studies were conducted by Dr. Nadia Camaioni and her team (ISOF-CNR, Italy).

II This publication demonstrates an example of novel phenothiazine-based azomethine functional hole-transporting materials with low cost and high performance in halide perovskite solar cells. The author designed and synthesized the materials, carried out the optical and electrochemical measurements under the supervision of Dr. Paola Vivo, analyzed the results, and wrote the manuscript draft. The solar cell fabrication and characterization were carried out by Prof. Jingjing Chang's group (Xidian University, China).

III This manuscript reports on the next generation of azomethine-based hole-transporting materials with phenothiazine core that are processable in green non-chlorinated solvents. The author designed and synthesized the materials, carried out the optical and electrochemical measurements under the supervision of Dr. Paola Vivo, analyzed the results, and wrote the manuscript draft. The solar cell fabrication and characterization were done by Prof. Jingjing Chang's group (Xidian University, China).

IV This manuscript involves novel pyrene-core organic hole-transporting materials for perovskite solar cells. We demonstrate that the fluorination of pyrene leads to an enhancement in the performance of dopant-free perovskite solar cells. The author designed and synthesized the materials, carried out the optical characterization, analyzed the results, and wrote the manuscript draft. The solar cell fabrication and characterization were carried out by Prof. Prashant Sonar's group (Queensland University of Technology, Australia).

All the manuscripts I–IV were finalized together with the co-authors.

# 1 INTRODUCTION

## 1.1 Motivation

The energy requirements for mankind are mostly met by non-renewable resources, e.g. crude oil, natural gas, coal, and uranium.[1] Their consumption has harmful effects on the environment and has resulted in the rapid climate change on Earth, with some countries suffering from abnormal heat while others from too harsh and snowy winters. Environmental scientists have observed that the average temperature of Earth has increased by more than 1 °C compared to 19th century.[2] Scientists agree that the main cause of the rising temperatures is the greenhouse effect, which is accelerated by the burning of non-renewable resources. If greenhouse gas emission continues growing at the current rate, by 2070 the average air temperature in the summer of Gulf countries could make the territory unsuitable to humans. [2–4] Thus, addressing the issue of climate change requires constant and significant reductions in greenhouse gas emissions.

The limited availability, as well as the above-mentioned harmful side-effects of non-renewable energy, demand sustainable and clean energy sources, such as wind, hydroelectric, and solar energy. The Sun emits around 430 quintillion Joules of energy each hour in comparison to humankind's need of 410 quintillion Joules a year.[5] This makes the Sun an excellent and clean energy source.[5] The recent renewable capacity statistical report of 2019 released by the International Renewable Energy Agency shows that the global renewable capacity reached 2351 GW by the end of 2018,[6] out of which half is accounted for hydropower. However, significant gains in 2018 came from solar energy capacity, which contributed globally to around 480 GW. This demonstrates that solar energy is a promising alternative to non-renewable energy sources and has the potential to constantly meet the ever-growing global energy demands.[6] Nevertheless, despite the increase in the global solar energy capacity, the percent of the worldwide shares of total energy consumption indicates that the modern renewables (wind, solar, biomass, geothermal and ocean energy) still acquired significantly lower (2.0%) shares compared to fossil fuels (79.7%).[7] In

order to increase this share, there is a strong demand for research and development of novel solar energy technologies.

Halide perovskite solar cells (PSCs) provide an excellent platform for solar energy conversion and promise to become among the most important and promising alternatives for solar energy technologies of the future. In the last decade, PSCs have attracted widespread attention as a rising technology and a viable alternative to silicon-based solar cells to meet the increasing global demand, due to their low cost, ease of fabrication, and outstanding power conversion efficiency with a recent record of 25.2%.[8–10] The existing PSCs suffer from several drawbacks, e.g. the poor stability, the presence of toxic lead (Pb) in the most efficient perovskite compositions, and the costly and unstable hole-transporting materials (HTMs) presently at use.[11,12] To overcome these critical points and to achieve environmentally friendly PSCs, it is paramount to design and develop novel strategies, concepts, and alternative materials to Pb as well as to the state-of-the-art HTMs to realize the next generation of stable, eco-friendly, and high-performing PSCs.

## 1.2 The aim and content of the Thesis

The work reported herein is focused on the understanding, design, synthesis, and characterization of organic small molecule-based HTMs. The key motivation is to achieve new materials from low-cost precursors and utilize the materials as hole-transporting layers in PSCs. While adopting simple and eco-friendly synthesis approaches, we aim at reducing the environmental impact as compared to conventional HTMs.

To meet the requirements of effective HTMs for PSCs we focused on two molecular design strategies: i) development of high charge-carrier mobility HTMs made/processed by environmentally friendly methods, [I,II,III] and ii) investigation of low-cost, fluorine-substituted, and stable dopant-free HTMs.[IV]

The graphical illustration of the molecular designs studied in this work is presented in **Figure 1.1**.

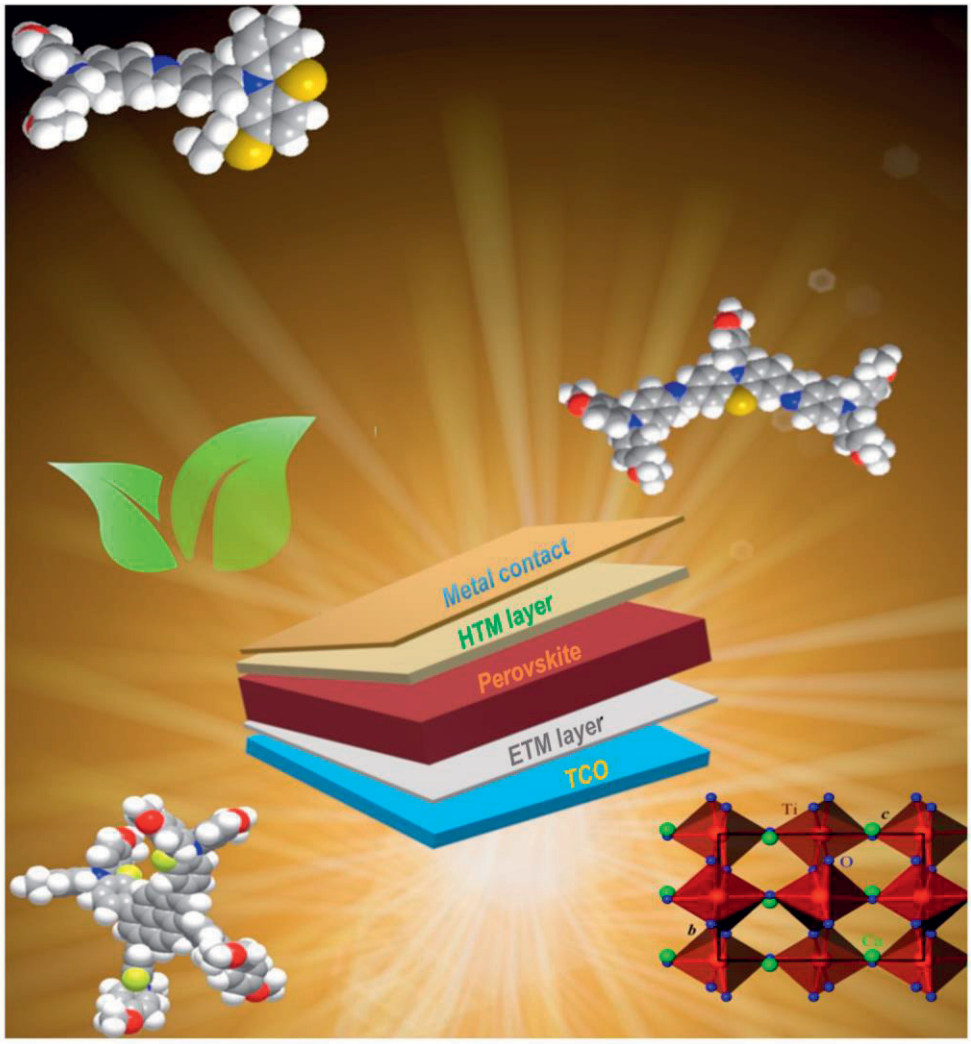


**Figure 1.1.** Graphical illustration of the various layers of a PSC with the structures of the HTMs developed in this work. Modified from an original picture drawn by Paola Vivo.

In **Publication I**, a series of new phenothiazine materials were designed to achieve high hole-mobility, thus they can be employed as charge-transport layer in PSCs. The phenothiazine molecules bearing electron-withdrawing (EW) and electron-donating (ED) groups at C(3) and C(7) positions synthesized by using Ullmann and Suzuki coupling reactions. After the optical and electrochemical characterizations, the bulk hole mobility of phenothiazine-based materials was investigated and correlated to their molecular structures with the help of impedance spectroscopy and X-ray diffraction (XRD).

Due to the promising hole mobility of the phenothiazine materials of **Publication I**, we further modified the phenothiazine core by keeping in mind their low costs, stability, energy levels, and applicability as HTM layer in PSCs in **Publication II**. The modified azomethines were synthesized via environmentally friendly simple condensation reactions. After optical, electrochemical, and time-resolved photoluminescence characterization, the compounds were utilized as HTMs in PSCs, the efficiency and stability of which was investigated and compared with reference solar cells employing the traditional Spiro-OMeTAD HTM.

To achieve a green-solvent processed route for the HTMs, in **Publication III** we further designed and modified the previously made azomethine-based HTMs and synthesized two new azomethine-functional HTMs by introducing an aryl bridge between the phenothiazine and triarylamine units. The compounds were characterized by using optical and electrochemical spectroscopies and their interactions with perovskite were studied by time-resolved photoluminescence. The PSC devices were manufactured by processing the newly made HTMs in a green-solvent and their performance, as well as device stability, were compared with those of a reference Spiro-OMeTAD-based device.

Finally, in order to obtain low-cost, dopant-free, and stable HTMs we selected the polycyclic aromatic pyrene unit as the core and designed two (non-fluorinated and fluorinated) new HTM molecules in **Publication IV**. After the optical, electrochemical, thermal, and computational characterization, the materials were employed in dopant-free perovskite-based devices as HTMs and the effect of fluorination on the performance of PSCs was investigated. Finally, the device performance was compared with that of PSCs based on the widely adopted PTAA HTM.

The subsequent chapters will provide a general overview of the publications, a summary of the main results, and a future perspective.

A literature review with the current state-of-the-art of PSCs, in particular, their basic working principle, architectures, and building blocks, HTMs, and the limitation of PSCs are discussed in Chapter 2. An introduction to all the experimental methods (synthesis, optical, electrochemical, charge-transporting, time-resolved photoluminescence, and photocurrent measurement) used for the

characterization of materials and devices is provided in Chapter 3. Molecular design, synthesis, characterizations, computational studies, solar cell fabrication, performance, and stability of PSCs are discussed in Chapter 4. Finally, Chapter 5 summarizes the conclusions based on molecular design, synthesis, solar cell performance, hole mobility, and stability results from publications I, II, III, and IV. The Chapter ends with a future outlook on the topics of this Thesis.

# 2 HALIDE PEROVSKITE SOLAR CELLS

In this Chapter, a brief introduction on halide perovskite solar cells (PSCs) is provided, starting from their discovery to the working mechanism of PSCs, the key architectures, and the different building blocks of PSCs. Furthermore, the importance of hole-transporting materials (HTMs), the most widely investigated compounds, the design strategies for efficient HTMs, and a closer look at phenothiazine- and pyrene-based materials are presented.

## 2.1 Basic working principles of PSCs

Perovskite was first discovered by the Prussian mineralogist Gustav Rose in 1839.[13] The material, made of $CaTiO_3$, was named after the Russian mineralogist Count Lev A Perovski (1792-1856). When the oxygen atoms of the $CaTiO_3$ structure were replaced by halogen atoms or a mixture of different halogen atoms, the structure became semiconducting, rendering the utilization of halides in PSC structures of key importance. More generally, perovskites are crystalline materials with $ABX_3$ structure (Figure 2.1), comprising three different organic or inorganic species: A is a monovalent organic (e.g. methylammonium, MA or $CH_3NH_3^+$) or inorganic (e.g. $Cs^+$) cation, B is a divalent cation (e.g. Pb(II) or Sn(II)), and X is a halogen or a mixture of halogens ($Cl^-$, $Br^-$, $I^-$). Methylammonium lead iodide ($CH_3NH_3PbI_3$) and methylammonium lead bromide ($CH_3NH_3PbBr_3$) were the materials first used by Kojima et al. in 2009[14] in dye-sensitized solar cells (DSSCs) as light-absorbing dyes, which led to a power conversion efficiency (PCE) of 3.81 and 3.13%, respectively. Unfortunately, both degraded rapidly due to their interactions with the iodide/triiodide liquid electrolyte present in DSSCs, which ultimately hampered the performance and resulted in the dissolution of the perovskite into the liquid electrolyte. This issue was first overcome by designing the solid-state HTM, spiro-OMeTAD, which completely replaced the liquid iodide/triiodide-based electrolyte in the cells.[15] This new generation of solar cells based on halide perovskite materials is named organic-inorganic hybrid PSCs and has captured significant attention in recent years from researchers in the field of photovoltaic technologies.

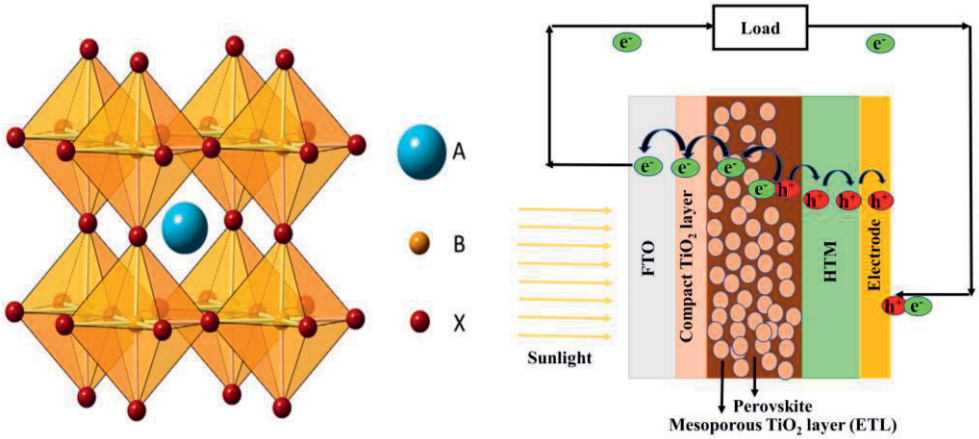


**Figure 2.1.** a) Perovskite structure where A is a monovalent cation, B typically stands for Pb(II) or Sn(II) cation, and X is $Cl^-$, $Br^-$, $I^-$ or a mixture of halides. b) Schematic diagram of the working mechanism of PSCs.[16] Reproduced with permission from [*Adv. Energy Mater.*, 2019, **9**, 1803017] published by John Wiley & Sons, Inc.

The development of PSCs has experienced rapid progress in terms of PCE, from 3.8% (2009)[14] to the recent certified record of 25.2% in just a decade of research.[8] The significant performance enhancement of PSCs has been associated to the excellent optoelectronic properties of perovskites, such as *i)* remarkably high optical absorption with direct bandgap between 1.5 – 2.3 eV depending on the halide content;[17] *ii)* widely tunable bandgap by composition engineering;[18,19,20] *iii)* lower exciton binding energy (tens of meV) as compared to organic semiconductors (from few hundreds meV to more than 1 eV), resulting in the separation of electrons and holes at room temperature; *iv)* long charge carrier diffusion lengths (e.g. electron and hole diffusion lengths of $MAPbI_3$ perovskite are 130 and 100 nm, respectively).[21] A typical PSC structure (Figure 2.1b) consists of transparent fluorine-doped tin oxide (FTO) electrode, a compact electron-transporting material (ETM, commonly $TiO_2$ with a thickness ranging from 30 to 70 nm ), a perovskite light-harvesting layer (thickness from 300 to 800 nm), an HTM layer (usually Spiro-OMeTAD (thickness from 100 to 200 nm), and a high-work-function metallic electrode (e.g. Au or Ag with a thickness between 50 and 100 nm). Sometimes, a mesoporous scaffold for the perovskite layer (typically $TiO_2$ with thickness from 150 to 300 nm) is deposited atop the compact layer. The scaffold plays a dual role, as it on one hand facilitates the electron transporting process, and on the other hand forms a homogeneous, large-area film, thus reducing contact resistance.[22] The

general working mechanism of PSCs is presented in Figure 2.1b. It includes the absorption of incident light by the perovskite layer, the generation of electrons and holes, the extraction and transporting of electrons and holes by the ETM and HTM layers, respectively, and the final charge collection at the respective electrodes of the PSCs. To achieve an efficient charge transport and extraction, the highest occupied molecular orbital (HOMO) level of the HTM should be higher than the valence band (VB) of the perovskite. Similarly, the lowest unoccupied molecular orbital (LUMO) level of the ETM should be lower than the conduction band (CB) of the perovskite.[16]

## 2.2 Perovskite solar cell architectures and building blocks

There are mainly two types of PSC architectures (Figure 2.2), the regular (*n-i-p*/ negative-intrinsic-positive) and inverted (*p-i-n*/positive-intrinsic-negative). Either can be planar or mesoporous. In the case of the *n-i-p* structure, $TiO_2$ or $SnO_2$ acts as the n-type ETM lying at the bottom of the structure, followed by the perovskite layer and finally the p-type HTM, e.g Spiro-OMeTAD, on the top. For the inverted *p-i-n* structure, the intrinsic perovskite material is sandwiched between the p-type layer (e.g. Spiro-OMeTAD) at the bottom and the n-type material (e.g. phenyl $C_{61}$-butyric acid methyl ester (PCBM) ) on the top.[23] These different architectures have their individual advantages. The normal mesoporous (also known as mesoscopic) structure is derived from DSSCs and it is still the most frequently employed in research laboratories due to its easy and reproducible fabrication.[24] Jeng *et al.*[25] have developed the first *p-i-n* inverted architecture by using poly(3,4-ethylenedioxythiophene) polystyrene sulfonate) (PEDOT:PSS) as HTM and fullerene ($C_{60}$) as ETM, respectively.

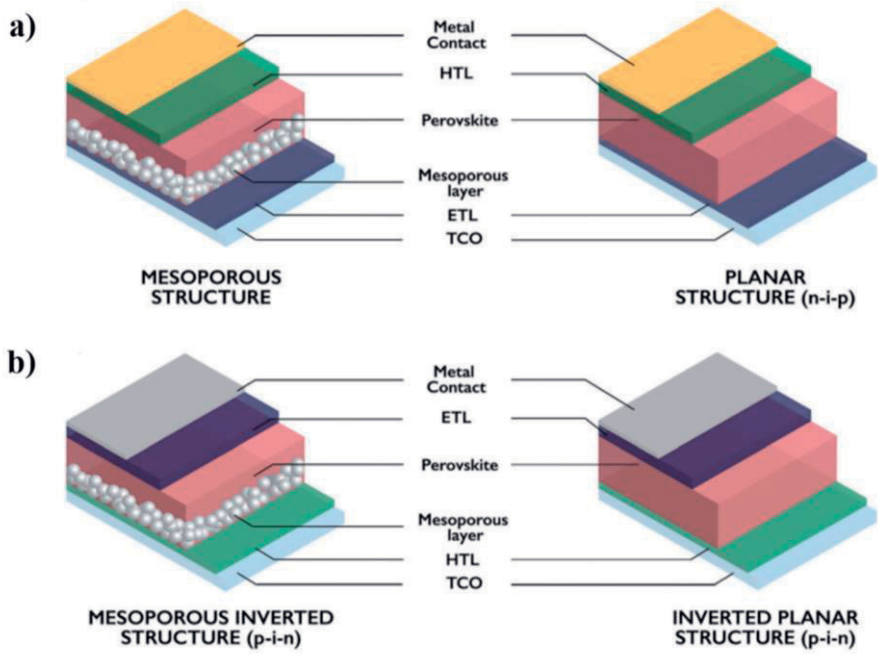


**Figure 2.2.** Schematic illustration of the most common device architectures of PSCs: (a) *n-i-p* mesoporous and planar structures. (b) Inverted *p-i-n* mesoporous and planar structures.[23] Reproduced with permission from [*Chem. Soc. Rev.*, 2018, **47**, 8541–8571] published by Royal Society of Chemistry.

### 2.2.1 Mesoscopic and planar configurations

As shown in Figure 2.2, in the case of mesoscopic structure the perovskite penetrates into a mesoporous n-type or p-type metal oxide, such as $TiO_2$ or $Al_2O_3$. The mesoporous scaffold for perovskite ensures efficient extraction of charges due to the large charge separation at the perovskite/ETM or perovskite/HTM interface in regular or inverted structures, respectively.[26, 27] In addition, the larger particles in the mesoporous layer increase light scattering, enhancing light absorption in the perovskite layer.[28] The initial cells made by using mesoporous $TiO_2$ as an n-type layer and SpiroOMeTAD as the HTM layer exhibited a PCE of around 8% with a 300 nm thick methylammonium lead iodide chloride ($CH_3NH_3PbI_2Cl$) halide perovskite layer.[29] The mesoporous $TiO_2$-based PSCs have been further investigated and to date, a PCE of around 20% has been achieved with this architecture. Furthermore, when another mesoporous oxide ($Al_2O_3$) was employed instead of $TiO_2$, PCE of up to 10% has been achieved.[29] $Al_2O_3$ acts as an insulator

with a wide bandgap of 7–9 eV and cannot transport electrons due to the energy mismatch with the conduction band of the perovskite. Thus, $Al_2O_3$ solely supports the perovskite crystallization.[29] These devices show negligible hysteresis (fluctuations in current-voltage response in forward and reverse directions) as compared to planar structures because of the larger contact areas between the mesoporous and perovskite layer leading to efficient electron transfer and separation. [29,30] However, $TiO_2$ exhibits some disadvantages, such as low electron mobility, charge accumulation at the $TiO_2$/perovskite interface due to its photocatalytic activity, and the presence of trap states, which leads to reduced stability of PSCs under ultraviolet illumination.[31] Furthermore, the fabrication of $TiO_2$ layers requires sintering at high temperature (nearly 500 $^oC$) that causes deformation of the most common polymeric substrates (e.g. polyethylene terephthalate, polyethylene naphthalate) of flexible solar cells, thus hampering the use of $TiO_2$-based devices in flexible electronics. Much effort has been put to substitute the mesoporous-$TiO_2$ layer with e.g $TiO_2$ nanowires synthesized by atomic layer deposition, to improve the absorption coefficient as well as the electron collection.[32] $SnO_2$ has also been used as the mesoporous electron transporting layer due to its excellent qualities, such as 100 times higher electron mobility, deeper conduction band, and wider bandgap (around 4.0 eV) compared to $TiO_2$.[31,33] Zhu *et al.*[34] have demonstrated that, after treating the mesoporous $SnO_2$ with $TiCl_4$, the PCE improved up to 8.54% compared to mesoporous $TiO_2$-based cell with PCE of 7.20%.

Overall, the introduction of a mesoporous layer in PSCs guarantees better control of the morphology of PSCs, high performance and reproducibility, and most importantly negligible hysteresis during the reverse and forward scanning of current-voltage curves, yet it also has some drawbacks.[35,36] Without the mesoporous layer the PSCs structure is simplified, and the device fabrication costs and efforts are reduced.[37]

Typical planar architectures are presented in Figure 2.2. Initially, Snaith *et al.*[29] fabricated a planar PSC, where a mixed halide perovskite film ($MAPbI_{3-x}Cl_x$ with thickness ~150 nm) was sandwiched between a conductive glass covered with compact $TiO_2$ as ETL and a Spiro-OMeTAD HTM layer. The device was completed with an Ag top-electrode and exhibited a PCE of 1.8%. The morphology of planar heterojunction PSCs using $MAPbI_{3-x}Cl_x$ structure was further optimized by carefully controlling the processing conditions, atmosphere, film thickness, and annealing temperature. High photocurrent was achieved when a complete surface

coverage was obtained, leading to a PCE of 11.4% with open-circuit voltage ($V_{oc}$) of 0.89 V, and short-circuit current density ($J_{sc}$) of 20.3 mA/cm$^2$.[36] The performance of planar PSCs was further improved by incorporating a highly uniform vapour-deposited perovskite layer while the other layers, such as $TiO_2$ and the SpiroOMeTAD, were deposited by solution process. The optimized cell structure led to PCEs of over 15% with $V_{oc}$ of 1.07 V, which demonstrates that the use of complex nanostructures is not always a necessary condition to achieve high-performance PSCs.[38] The significant improvement in PCE up to 20.75%, with $V_{oc}$ of 1.12 V, $J_{sc}$ of 23.06 mA/cm$^2$, and FF of 0.80 and with imperceptible hysteresis, excellent reproducibility, and high air stability was achieved after the introduction of a hydrophilic buffer layer onto the non-wetting HTMs.[39] In addition, to reach both high stability and PCE, a novel strategy of incorporating an ionic liquid into the planar inverted structure was introduced.[40] The cell structure consists of an ionic liquid mixed in the triple cation perovskite (FAMACsPbIBr) as the absorbing layer, NiO and [6,6]-phenyl-$C_{61}$-butyric acid methyl ester (PCBM) as HTM and ETM, respectively. The champion device shows an excellent PCE of 19.8% with long-term operational stability.[40] Hairen *et al.* investigated the chlorine-capped $TiO_2$ as a contact passivator to reduce interfacial recombination and enhance the binding at the interface of the perovskite layer.[41] Thus, from a commercialization point of view, the inverted planar (*p-i-n*) structure can have a great potential for the large-scale production due to its moderate fabrication temperature (100 °C), low cost, good air stability, and short processing time.[37,42]

### 2.2.2 Building blocks of PSCs

In addition to the perovskite layer, the main building blocks of the PSCs are the counter electrodes (CE), ETMs, and HTMs. The counter electrodes play an important role in PSCs' performance and stability by collecting electrons or holes. In general, transition and noble metals (e.g. Ni, Cu, Mo, Cr, Ag, and Au) have been used as CE. The CE should efficiently extract, transfer, and collect the charge carriers from the perovskite layer, typically with the help of the ETM/HTM layers. The CE should, thus, have excellent electrical conductivity and suitable work function, *i.e.* the Fermi level of CEs should always lie above the VB and below the CB edge of the perovskite layer.[43] Some studies report that CEs are one of the main causes of cell degradation, either by metal migration or corrosion of the commonly used (Ag, Au) electrodes when in contact with the perovskite materials. Recently, in $MAPbI_3$ solar cells with configuration FTO/$TiO_2$/$MAPbI_3$/HTL/Au, it was found

that Au diffuses into the perovskite layer and causes a significant decrease in the device performance.[44] These issues were addressed by adding buffer interlayers between CEs and HTMs, but this strategy prevents the contact between CEs and the perovskite layer only for a short time-frame. Still, the quest for long-term stability remains, as the perovskite materials tend to diffuse through the interlayer under continuous light illumination, which ultimately degrades the device. To boost the long-term stability, alternative electrodes are employed.[44–48] In one report researchers highlighted copper (Cu) as an alternative stable CE to gold (Au), which can be stable for many years even in direct contact with perovskite in the encapsulated device because of its great corrosion resistance behavior in presence of halogens and non-oxidizing acids (e.g. HCl, HI, HBr). Cu did not show any diffusion or migration into the perovskite layer, due to the absence of any reaction between the perovskite layer and Cu after long-term 1 Sun illumination and thermal annealing.[46] Thus, it is clear that to achieve efficient and stable devices, the long-term stability of CE is a decisive factor.

ETM layers play a key role in PSCs. They not only extract and transport the photogenerated electrons from the perovskite layer to the external circuit while blocking the holes but also help to minimize the charge recombination through the modification of the interface between perovskite and electrode.[49–51] Besides, the uniform and homogeneous ETM layers can improve the air stability of the device by preventing diffusion of oxygen, moisture, and metal particles.[52,53] Majority of ideal ETMs possess characteristics such as *i)* high electron affinity and well-aligned energy levels with the perovskite layer to reduce recombination and enhance charge separation; *ii)* high electron mobility, which is beneficial for extraction of electrons; *iii)* intrinsic hydrophobicity, which helps to prevent moisture infiltration into the perovskite layer, thus improving the stability of the device; *iv)* good chemical stability to avoid any reaction with cathode or the perovskite layer; *v)* low-cost and easy processability.[54–56] The commonly used ETMs are mainly based on inorganic metal oxides (e.g. $TiO_2$, $SnO_2$, ZnO, $WO_3$, $Zn_2SnO_4$, $SrTiO_3$) or organic molecules, such as fullerene derivatives e.g. $C_{60}$, $C_{70}$, [6,6]-phenyl$C_{60}$-butyric acid methyl ester ($PC_{60}BM$).[55,57–63] As discussed above, in most of the high-performing PSCs, a mesoporous ETL has been used because it provides a larger surface area and increases the loading of the absorber, which leads to minimum recombination due to continuous electron transport. Several organic ETMs other than fullerene derivatives have been also employed in high-performing PSCs. These are small molecules, ionic liquids, and polymers, e.g. based on perylene derivatives (due to their good thermal, chemical stability, and high electron mobility > $10^{-3}$ $cm^2V^{-1}s^{-1}$).

The non-fullerene ETMs have some key advantages, such as easily tunable structures, facile processing, high synthetic yield, and large possibility to reduce cost.[64–67] To achieve higher stability as well as good performance, Bai *et al.*[68] introduced an interesting ETM design in which a cross-linkable silanol hydroxy bonded to the carboxylic group of fullerene was functionalized with a hydrophobic $CF_3$ to improve water resistance. The PSCs exhibited a PCE of 19.5% and retained 90% of its original performance after 30 days of storage in ambient conditions. To address the issue of stability, in addition to high-performing ETM designs, several other interesting strategies have been introduced, e.g. the use of fulleropyrrolidinium iodide (bis-$C_{60}$) and amine-functionalized DMAPA-$C_{60}$ interlayers to resist external moisture or oxygen while at the same time leading to high-performing PSCs.[68–73] Despite the significant efforts made to develop novel strategies for effective ETMs, there are still some challenges to be addressed. For example, $SnO_2$ is an excellent ETM leading to devices with very high PCEs. However, the effect of the annealing temperature on $SnO_2$ film characteristics and ultimately on the device performance still needs to be explored.[58] In inverted structures, generally, fullerene derivatives are employed as ETMs but they suffer from problems related to e.g. their poor surface morphology or moisture-induced degradation.

## 2.3 Hole-transporting materials (HTMs)

The HTM layer plays a critical role when targeting high-performance and long-term stable PSCs. The HTM is a prerequisite in all PSC structures for efficient extraction and transporting of holes from the perovskite layer to the metal electrode. A key function of HTMs also includes the protection of the perovskite layer from the diffusion of metal electrodes (Ag, Al, and Au).[74,75] HTMs reduce charge recombination at the HTM/perovskite interface by uniformly covering the perovskite surface. Finally, the HTM can improve perovskite stability via surface passivation through covalent, non-covalent, or ionic interactions.[76–79] To achieve ideal HTMs for high-performing PSCs, several requirements should be fulfilled.[10] The HOMO energy level of the material should be higher than the VB of the perovskite layer to provide a suitable driving force for hole extraction. The closer the HOMO level of the HTM to the perovskite VB, the higher the open-circuit voltage that can be achieved.[10,80] The HTM should also have low-cost, high thermal/chemical stability,[81] high hole mobility for efficient hole transport, and transparency in the visible region to enable optimal light harvesting by the

perovskite absorber. Furthermore, environmentally friendly, easily attainable, and biodegradable HTMs are desirable to achieve green PSCs.[82–84] The first HTM that was deposited by low-temperature processing in PSCs was the polymeric PEDOT:PSS (Figure 2.3.). A PCE of 3.9% in planar device architecture was achieved. The poor performance was due to the un-optimized absorber layer thickness (< 50 nm) and the modest HTM/perovskite interaction.[25] Further, the performance of the PEDOT:PSS-based device increased to 11.7% by tuning the HOMO level of PEDOT:PSS from 4.86 eV to 5.4 eV through perfluorinated isomers.[85] The PEDOT:PSS has several benefits, like high availability and affordability, easy synthesis, and having been extensively investigated in organic photovoltaics. However, it also has some disadvantages, such as *i*) its acidic nature can cause a problem to electrodes, *ii*) its highly hydrophilic and hygroscopic nature can cause degradation and reduce device stability, *iii*) Batch-to-batch variation in electrical and physical properties due to variation in molecular weights, and *iv*) phase segregation of PEDOT and PSS chains in time under the exposure of moisture and oxygen.[42,86,87] Another polymeric HTM PTAA (Figure 2.3) also led to PSCs with excellent performance but, due to its significantly high cost (2000 $/g), batch-to-batch reproducibility issues, difficult purification, poor infiltration into nanostructure materials, and broad dispersity, its large-scale employment in PSCs is impeded.[88,30] Thus, as an alternative to the polymeric PEDOT:PSS, the first solid-state small molecular HTM Spiro-OMeTAD (Figure 2.3) was developed and intensively studied in the context of PSCs. Spiro-OMeTAD is still the most widely used HTM in perovskite devices due to its excellent performance, which is rarely matched by other HTMs.[10]

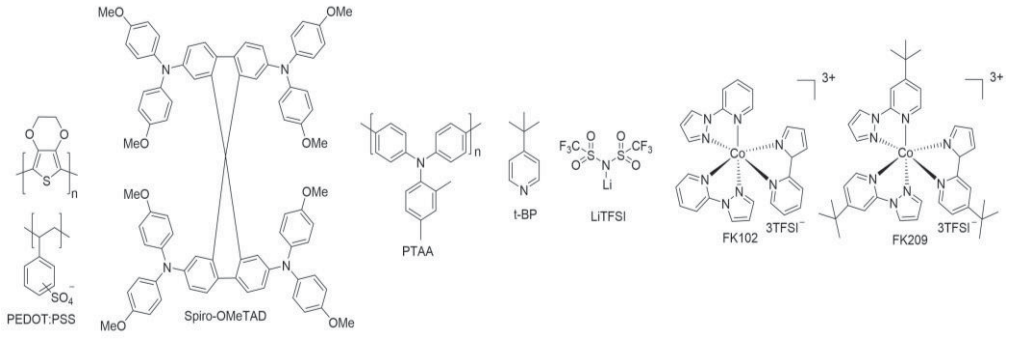


**Figure 2.3.** Conventional hole-transporting materials and dopants employed in high-performing PSCs.

Despite the excellent performance of Spiro-OMeTAD-based solar cells, this HTM suffers from serious disadvantages such as high cost of raw materials (91.67$/g),[83] multistep synthesis (five steps), involving low-temperature processes (-78 °C),[89] and stringent conditions required to carry out synthesis steps. Additionally, synthesis involves sensitive Grignard reactions, cyclization, and bromination with poor yields (total yield less than 50%), purification of final molecule requires costly sublimation process, which increases the overall cost of the material. [90] Also, the Spiro-OMeTAD shows poor hole mobility and conductivity ($1.67 \times 10^{-5}$ $cm^2$ $V^{-1}$ $s^{-1}$ and $3.54 \times 10^{-7}$ S $cm^{-1}$, respectively).[91] To enhance the conductivity and the hole extraction capability, Spiro-OMeTAD requires external dopants, such as 4-tert-butylpyridine (t-BP), lithium bis(trifluoromethansulfonyl)imide salt (LiTFSI), or cobalt(III) complexes (Figure 2.3).[92–94] While the external dopants improve electron injection and reduce the charge recombination in the device, they are detrimental for PSCs stability due to their hygroscopic nature. Hence, their use in HTMs is a critical impediment to the commercialization of PSCs.[95]

To address the above issues, significant efforts have been made in the past few years to design and develop alternative HTMs to the ubiquitous Spiro-OMeTAD based on small organic molecules with various molecular cores for stable and high-performing PSCs. [10, 24, ,88,96–100] Very recently, excellent dopant-free donor-acceptor small-molecule HTMs based on phenylamine as donor and imide-functionalized thiophene as acceptor, were designed for inverted PSCs. These HTMs led to PCE exceeding 21%, negligible hysteresis, and outstanding thermal and photo-stability.[101] These exceptional results are attributed to good hole mobility, suitable energy levels, and good film-forming ability with enough solubility. These examples highlight the importance of small-molecule HTMs in the performance of PSCs.[101] In addition to studying the solar cell performance of small-molecule HTMs, several groups including ourselves have focused on overall cost reduction of HTMs, with the aim of providing a high-performance and low-cost alternative to Spiro-OMeTAD. The first low-cost HTM (EDOT-OMeTPA, 10$/g) was based on ethylenedioxythiophene (EDOT) and was introduced by Petrus and coworkers.[83] The EDOT-OMeTPA was synthesized by using aldehyde derivatives of EDOT and amine of dimethoxy-triphenylamine. When EDOT-OMeTPA was employed in PSC devices, it exhibited comparable PCE (11.0%) to SpiroOMeTAD (11.9%).

**Table 2.1.** Low cost (< 25 $/g) small-molecule organic HTMs and the corresponding PSC parameters reported in the literature.

| HTMs | $J_{sc}$ (mA $cm^{-2}$) | $V_{oc}$ (V) | FF (%) | PCE (%) | Cost ($/g) | Ref |
|---|---|---|---|---|---|---|
| EDOT-OMeTPA | 18.90 | 0.95 | 61 | 11.00 | 10 | 83 |
| SFX-MeOTAD | 21.38 | 0.98 | 59 | 12.40 | 17 | 102 |
| TPA-AZO | 20.72 | 1.12 | 77 | 17.86 | 23 | 103 |
| M114 | 22.24 | 1.05 | 73 | 17.17 | 15 | 104 |
| FBA3 | 22.12 | 1.09 | 79 | 19.27 | 15 | 105 |
| AZO-II | 21.60 | 0.95 | 71 | 14.00 | 12 | Publication II |
| AZO-IV | 19.83 | 1.01 | 58 | 11.62 | 9 | Publication III |
| EDOT-AmideTPA | 22.70 | 1.16 | 77 | 20.3 | 5 | 82 |
| DFH | 22.00 | 1.08 | 81 | 19.3 | 3 | 106 |

Another low-cost HTM was reported based on spiro[fluorene-9,9'-xanthene] (SFX) (16$/g) with PCE of 12.4% compared to reference SpiroOMeTAD of 13%.[102] In these early cases the PCE was limited to 13%. Several other low-cost HTMs such as TPA-AZO[103], M114[104], FBA3[105], EDOT-AmideTPA[82] and DFH[106] were later investigated, to enhance the PCE and simultaneously to further reduce the overall cost presented in Table 2.1. To date, EDOT-Amide-TPA, made by simple condensation reaction of acyl chloride of ethylenedioxythiophene and amine of dimethoxy triphenylamine, is the cheapest (5$/g) and highest-performing (PCE of 20.3%) small-molecular HTM.[82]

Finally, inorganic HTMs are also employed in PSCs, being low-cost, with high hole mobility and good solution processability. Unfortunately, the processing of inorganic materials, e.g. CuI, NiO, and CuSCN, requires highly polar solvents, which partially solubilize the perovskite layer and compromise the long-term device stability. Therefore, to address these issues, several strategies and novel inorganic HTMs have been introduced.[107–110]

### 2.3.1 Phenothiazine and pyrene based HTMs

Due to their monodisperse nature, well-defined structure, high degree of freedom for design and synthesis, UV-stability, high synthesis yield, tunable molecular structures, and high purity, small-molecule HTMs attract great attention in the PSCs community. In particular, here we focus on phenothiazine- and pyrene-based HTMs (Figure 2.4) due to their low-cost, easy availability, high thermal and chemical

stabilities, molecular engineering to fine-tune the energy levels, good solution processability, and high hole mobility.[111–113]

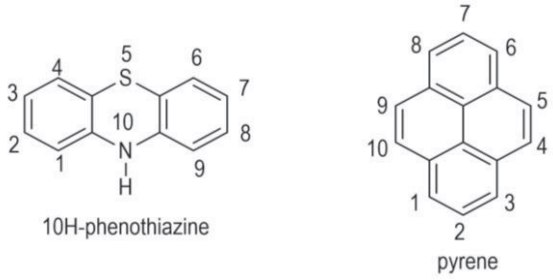


**Figure 2.4.** Molecular structures of phenothiazine and pyrene with respective positional numbering.

10H-phenothiazine, or simply phenothiazine (Figure 2.4), is a yellow water-insoluble solid that has excellent solubility in most organic solvents. It can be easily prepared by reaction of sulfur with diphenylamine and can be further functionalized at the most electrophilic 3 and 7 positions to achieve a large number of organic semiconductors with enhanced solubility via alkylation at N-10 position. Phenothiazines display good optical, electrochemical, thermal, and hole-transporting characteristics, and low environmental impact. Hence, they have been employed in a wide range of organic electronic devices, such as organic light-emitting diodes, organic solar cells, and organic transistors as well as in medicinal chemistry.[114–123] Phenothiazines have been significantly studied in the context of DSSCs as dye molecules by modification at 3 and 7 positions through condensation reactions.[122,124] By virtue of their interesting hole-transporting properties as well as their solution processability, the first examples of phenothiazine-based HTMs were reported by Grisorio et al. in 2017.[125] The authors designed and synthesized two phenothiazine-core derivatives by using Suzuki-Miyaura and Buchwald-Hartwig cross-coupling reactions in which the phenothiazine core was functionalized by dimethoxytriphenyl (PTZ2) and dimethoxydiphenyl (PTZ1) amine derivatives. When these materials were employed in PSCs, a PCE enhancement from 2.1% to 17.6 % was observed when moving from PTZ1 to PTZ2. This is due to the effect of the aryl spacer unit, which helps to achieve energy levels well-aligned with perovskite in the case of PTZ2, leading to cells with comparable performance to that of state-of-the-art conventional Spiro-OMeTAD devices (17.7%). In another report, three high-performing phenothiazine-core derivatives decorated by 4,4-dimethyltriphenyl amine, carbazole, and dimethoxytriphenyl amine were designed

and studied in mixed cation perovskite solar cells as HTMs. The triphenylamine-based HTM exhibited an excellent performance (PCE 19.7%) with higher stability compared to carbazole- and diphenylamine-based HTMs.[126] Thus, the rationale for selecting phenothiazine as the core moiety of this work is based on above discussed literature, in an effort to yield environment friendly synthesis of HTMs and to prevent toxic and expensive transition-metal-catalyzed reactions requiring extensive product purification. We used azomethine (-CH=N-) as conjugated linker introduced via simple Schiff-base condensation reaction. The azomethine bond is isoelectronic to the vinyl bond and shows similar thermal and optoelectronic properties.[83] We envision that eventually, by combining azomethine condensation chemistry with phenothiazine heterocycle, the aim of low-cost and environmentally friendly HTMs can be achieved.

The work reported in **Publication II** in this Thesis provides a new strategy mentioned above that combine the phenothiazine core with azomethine chemistry by designing mono- (AZO-I) and di-substituted (AZO-II) derivatives to achieve the goal of environmentally friendly, easily attainable, and low-cost HTMs. When these materials were utilized in PSCs, a PCE enhancement was observed from 12.6 (AZO-I) to 14% (AZO-II) from mono to di-substitution of phenothiazine core. In another recent work, to improve the stability and performance of PSCs, three novel low-cost phenothiazine-core derivatives were designed and synthesized by functionalization of Lewis basic groups on the corner of the phenothiazine core.[129] These groups played an important role in achieving hydrophobicity, trap passivation, and efficient charge extraction in a single design. In particular, the malononitrile-functionalized derivative exhibited an excellent performance (PCE= 17.3%) comparable to that of conventional Spiro-OMeTAD devices (18%). More importantly, it showed higher device stability as compared to the Spiro-OMeTAD device, which indicates the potential for these phenothiazine HTMs for stable devices.[127] Finally, recently the oxidized form of phenothiazine was used as HTM leading to PSCs with the highest PCE (20.2%) ever reported in the context of phenothiazine derivatives. All the above-mentioned studies demonstrate the enormous potential of phenothiazine core HTMs for PSCs.[128]

Planar fused pyrene-based conjugated materials (small molecules as well as polymers) show impressive charge-transporting and photochemical properties.[129] One of their fascinating benefits is also the availability of reactive sites present on the pyrene-core (Figure 2.4) that can be easily substituted with desired functional groups.[130] Hence, pyrene-core semiconductors have been employed and studied in

different electronic devices, e.g. charge-transporting or emitter layers in OLEDs,[121,131] light-absorbing dyes in DSSCs,[132,133] and electron donors in OPVs.[134-136] The first study regarding the application of low-cost pyrene-based materials as HTM in high-performing PSCs was proposed by Jeon *et al.*[100] They synthesized and controlled the opto-electrochemical properties of three pyrene-core mono (Py-A), tri (Py-B), and tetra (Py-C) substituted derivatives by substitution of N,N- di-p-methoxyphenylamine to pyrene moiety. When these materials were tested in doped PSCs, Py-C showed an excellent performance of PCE of 12.4%, which was comparable to that of Spiro-OMeTAD-based devices (12.7%) measured under similar conditions. The enhancement in the performance of Py-C cell was attributed to its impressive fill factor (FF), which relates to a smaller series resistance (Rs = 51.57 Ω) than Spiro-OMeTAD based device (Rs = 85.87 Ω), as well as the superior electron-blocking ability compared to Spiro-OMeTAD. This report opened a new door of opportunities for developing promising pyrene-core molecular designs as HTMs for PSC devices. Furthermore, the structure of Py-C was modified by Ge *et al.*,[137] upon the incorporation of phenyl-thiophene units to achieve a two dimensional pyrene-core thiophene bridge HTM (OMe-TATPyr).

The newly made pyrene-core HTM not only led to superior hole mobility through improved charge delocalization and intermolecular stacking but also improved the stability due to the presence of sulphur units that passivate the perovskite surface via Pb–S interaction. Finally, upon utilization of doped pyrene-core HTM in PSCs resulted in an exceptional performance (PCE = 20.6%) with good stability, when encapsulated devices stored under room temperature with humidity of 30% compared to the reference spiro-OMeTAD device (PCE was 18.6%).[137] Even though the performance of pyrene-based HTMs improved in just a couple of years from 12.4% to 20.6%, there are still challenges and opportunities to develop dopant-free, low-cost, stable, and high-performing pyrene-based HTMs for future large-scale production of PSCs.

## 2.4 Limitations of PSC technology

Despite the impressive performance and development of PSCs, several critical issues need to be addressed before the commercialization of the technology. In the literature, the control of thin-film growth, the deposition methods, film quality, and the device active area is limited to a few square millimeters. For larger devices, the PCE might drop below 20%. One certified minimodule with an area of 17.277cm$^2$

has demonstrated a PCE of 17.25% tested at Newport, while the larger-area (703 $cm^2$) panel exhibited a PCE of 11.7% measured at AIST.[138]

The stability under standard operational conditions of PSCs is another major critical point of current devices.[139] During the years, the stability of mesoporous PSCs has improved from a few hours to one year, the enhancement in stability to >10,000 hours was observed by interfacial engineering of multilayer 2D/3D perovskite structures.[40,87] The high efficiency obtained mostly in lead-based perovskite opens the issue of toxicity of Pb. Hence, encapsulation of the devices to avoid lead escaping from the structures or the search for alternative solutions to Pb are urgently needed.

Finally, the biggest challenge is to reduce the overall electricity cost. The present goal by US Department of Energy is to achieve as low as 0.09 US$ $kWh^{-1}$ by 2020, and it is expected to be further reduced to 0.05 US$ $kWh^{-1}$ by 2030.[139] Thus, in order to produce large-scale perovskite solar cells, the device constituents should meet certain requirements such as large availability, (i.e. they should be earth-abundant), reduced toxicity, low-cost, and solution processability. The perovskite design should demonstrate high performance, direct bandgap, large absorption coefficient, sufficiently long carrier diffusion length, and good thermal and chemical stability. Many researchers are working on designing alternative perovskite compositions to substitute lead, while also improving the stability. Each limitation of PSC technology is described in detail in subsequent paragraphs.

### 2.4.1 Deposition methods and large area device fabrication

In general, the PCE of large-area perovskite devices mostly depends on the fabrication methods and deposition techniques used to achieve high-quality films over a larger area. Various techniques for device fabrication, such as spin-coating, doctor blading, slot-die coating, printing, soft-cover deposition, vapor deposition, and spray deposition have been developed and employed in organic electronic device fabrication in past years.[141–146] However, in the case of mass production one has to find the techniques that give highly reproducible results, uniform layer deposition, and good perovskite film quality. In the case of solution-processable techniques, e.g. spin-coating, high boiling point organic solvents have been used, which causes defects and pinhole formation and result in poor film quality. Thus, advanced anti-solvent engineering methods[147] have been employed to achieve high-

quality films by a one-step deposition method in which fast crystallization involving spin-coating of perovskite in DMF is followed by the swift dropping of chlorobenzene as antisolvent to achieve large crystalline grains.[148] The use of toxic solvents, however, generates a new obstacle for commercialization. Spin-coating has been popularly used for small to medium area device fabrication and most of the reported results are based on the spin-coating method. But, spin-coating is not compatible with large-area device fabrication due to non-uniform film formation from center to edge, and the large amount of material and solvents wasted, which increases the overall cost of production. The large-area PSCs made by spin-coating show lower performance compared to small-area devices due to enhancement in resistance and poor film quality.[149,150] Thus, large scale production by using spin coating faces challenges in terms of performance as well as cost, though spin coating provides valuable information regarding the selection of the suitable solvent ratio of precursor solutions to achieve high-quality films.[151] Spray-coating allows large-area module fabrication due to its advantage of patternable perovskite materials deposition by masking, demonstrating a PCE of 15.5% with an active area of 40 $cm^2$ under 1 Sun illumination.[152] Screen printing can be a solution for large-area device fabrication and has been used earlier to coat photo-anodes in DSSCs, on the larger area of 31 and 70 $cm^2$. These devices showed PCE of 10.46 and 10.74% with excellent stability, with only a 5% reduction in performance after 2000 h under ambient conditions in unencapsulated devices, indicating potential utility of screen printing for large scale device fabrication.[152] As compared to the above-mentioned solution-processable fabrication processes, chemical or vacuum deposition methods might be more eco-friendly as they do not require toxic solvents. In addition, vacuum deposition allows highly uniform films and chemical vapor deposition already demonstrated modules from 1 to 12 $cm^2$ area with PCE of 14.6 to 9.0%, respectively with higher thermal stability compared to solution-processed films.[145,146] Further enhancement of the efficiency, deposition methods, and cost fabrication should be investigated. Even though high vacuum deposition methods like CVD increase the cost of fabrication and show lower performance compared to solution processable methods, they can be the most suitable techniques to achieve high-quality films without using organic solvents. CVD has been widely employed in industry, thus, if further effort is put in the improvement of the performance of PSCs made by CVD, this technique could become a potential method to achieve up to 1 $m^2$ area PSCs.

### 2.4.2 Stability of PSC devices under operational conditions

Despite the outstanding power conversion efficiencies, PSCs are still lagging in terms of their long-term stability needed for commercialization. A number of different intrinsic and extrinsic factors such as humidity, oxygen, heat, and light are responsible for the degradation and mainly external moisture (i.e. water molecules) causes a lowering in the performance due to its interactions with perovskite as well as other layers. The general chemical transformations of perovskite degradation by moisture are presented in Scheme 2.1.[153–155] Several encapsulation techniques have been investigated to protect perovskite from external moisture degration.[151,152]

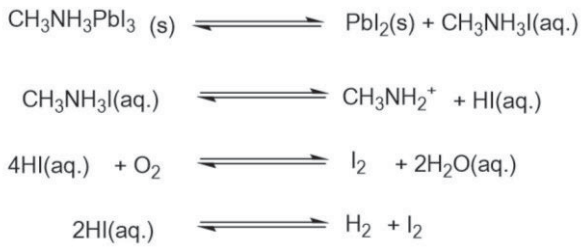


**Scheme 2.1.** Degradation of lead halide perovskite materials in the presence of moisture. Reproduced with permission from [*Adv. Sci.*, 2018, **5**, 1700387], published by John Wiley & Sons, Inc.

In the case of the electron transporting materials, ZnO reacts with perovskite causing instability due to the formation of MA (methylamine) and $PbI_2$ (lead iodide).[158] Thus, more acidic metal oxides, e.g. $TiO_2$, could be an alternative option to achieve thermally stable device.[159] Similarly, another instability issue regards the crystallization of small molecular HTMs at high temperature, which disconnects the electrical contacts with perovskite and electrodes and results in the reduction of performance. In addition, the use of external dopants along with HTMs to improve charge carrier mobility and conductivity causes a serious issue in terms of stability due to their hygroscopic nature. Thus, dopant-free HTMs are highly desirable for stable devices.[160] Polymeric HTMs are also investigated and employed for large scale devices due to their good thermal and chemical properties. They also form an excellent barrier to gold migration. Other interlayer strategies to improve the long-term performance of PSCs have been also investigated.[44,161,162] In most of the high-performing devices generally gold is used as an electrode, especially in the case of *n-i-p* structure. Unfortunately, gold possesses a potential drawback both for the instability issue (due to its migration through the PSC layers) as well as for its high cost.[44] Thus, low-cost carbon electrodes, with outstanding stability and industrially

suitable, have been developed to overcome the mentioned issues. Combining dopant-free HTMs with carbon electrodes could allow improving stability significantly.[163] Also, some inorganic HTMs like NiO have been employed in carbon electrode devices with PCE of 17.02%, and 90% of the initial PCE retained after 1020 h.[164] Also, very recently the devices made by a composite HTM with carbon electrode reached a PCE of 18% with very good stability (after 1680 h the PCE dropped to 15%).[165] Thus, even though carbon electrode cells have lower performance compared to metal electrode cells, the stability of carbon-based devices is much better than the former, indicating the potential of carbon electrode cells for large scale applications.

### 2.4.3 Alternative to toxic lead in PSCs

Pb-based perovskite technology raises the issues regarding possible health and environmental impact, though Pb is allowed in photovoltaic panels according to the European Restrictions on Hazardous Substances.[166] However, it would be beneficial to replace Pb with a more suitable alternative to tackle environmental and health-related issues. In addition, upon contact with water lead halide perovskites form water-soluble compounds of lead which can cause long-term harm to the human body via the food chain.[167] Therefore, it would be desirable to use other non-hazardous elements without compromising the device performance. In order to replace Pb, several requirements must be considered, e.g. the crystal structure formation, the stability of octahedral geometry, as well as the ionic radii of the A, B, and X sites of the perovskite structure. Thus, recently significant efforts have been made to replace Pb with other elements. [168] Tin (Sn)-based perovskites, such as $MASnI_3$, $FASnI_3$, and $CsSnI_3$, [169] are an interesting example of Pb-free perovskites due to the similar ionic radii of Pb and Sn, the easy availability, and the electronic properties close to that of Pb.[170] Despite the potential, Sn has several issues regarding the instability under ambient conditions with the known oxidizing tendency from +2 to +4 oxidation state, requiring the Sn-based device fabrications to be carried out in glove-box.[171] To predict stable and efficient perovskite structures, Volonakis *et al.*[172] carried out a computational screening of different kinds of perovskite structures based on $Cs_2ABi^{+3}X_6$, where A=Cu, Ag, Au, and X= Cl, Br, I. These computationally designed structures showed excellent optical and electrochemical properties and some double perovskites, e.g. $Cs_2BiAgBr_6$ and $Cs_2BiAgCl_6$, have been synthesized with bandgap ranging from 1.8-2.2 eV and 2.2-2.8 eV, respectively, with long recombination lifetimes. In addition, both double-

perovskite structures exhibited outstanding stability compared to lead-based structures in ambient environment with RH of 55%, as investigated by X-ray diffraction analysis.[172–174] There is still a long way to realize the high-performing commercial PSC devices based on double perovskite as well as on other lead-free perovskites and to verify their applicability under operational conditions.

# 3 EXPERIMENTAL

Commercial solvents and reagents were purchased from Sigma-Aldrich and Tokyo Chemical Industry Co. and were used without further purification. If required, chloroform was distilled over potassium carbonate, toluene over sodium metal, dichloromethane over calcium hydride, and triethylamine over potassium hydroxide. All the chemical reactions were carried out by using round bottom flasks and Schlenk tubes under argon or nitrogen environment and monitored by using thin-layer chromatography (TLC). All the crude reaction products were purified by either column chromatography using silica gel 60 (mesh size 40–63 μm) or by recrystallization. $^{1}H$ and $^{13}C$ NMR spectra were recorded on Bruker spectrometer ($^{1}H$ at 400 MHz and $^{13}C$ at 100MHz) in $CDCl_3$ and the chemical shifts were presented in ppm using tetramethyl silane (TMS) as a reference. Mass spectra were recorded with a high-resolution ESI-TOF LCT Premier XE mass spectrometer (Waters Corp). The compounds were dissolved in chloroform:methanol (0.01 mg $mL^{-1}$) and infused at a rate of 15μL $min^{-1}$. Absorption and emission measurements were recorded by using Shimadzu UV-2501PC and Fluorolog Jobin Yvon-SPEX fluorometer, respectively. Differential pulse voltammetry (DPV) of all the materials was performed by using a potentiostat (Compact-Stat, Ivium Technologies) and a three-electrode cell configuration.

## 3.1 Synthesis methods

### 3.1.1 The Suzuki-Miyaura coupling reaction

When designing complex organic molecules, chemists are required to connect carbon atoms, which is difficult due to their stable and not easily reactive nature. Several methods have been proposed, such as Grignard reaction and Wittig for C-C bonds formation,[175] but for the synthesis of complex molecules these approaches produce too many unwanted by-products.

Palladium-catalyzed cross-coupling reactions solved this issue and are an excellent tool for chemists. The cross-coupling reaction between aryl or vinyl-boronic acid or ester derivatives with organic electrophiles, e.g. Ar-X (X= Br, I, Cl, Otriflet, Otosyl), in presence of Pd and a base is commonly called Suzuki coupling reaction.[176] Suzuki coupling is broadly used worldwide, both in academia as well as in commercial production, e.g. in pharmaceutical and electronics industries. The general mechanism of the Suzuki reaction is presented in Scheme 3.1.

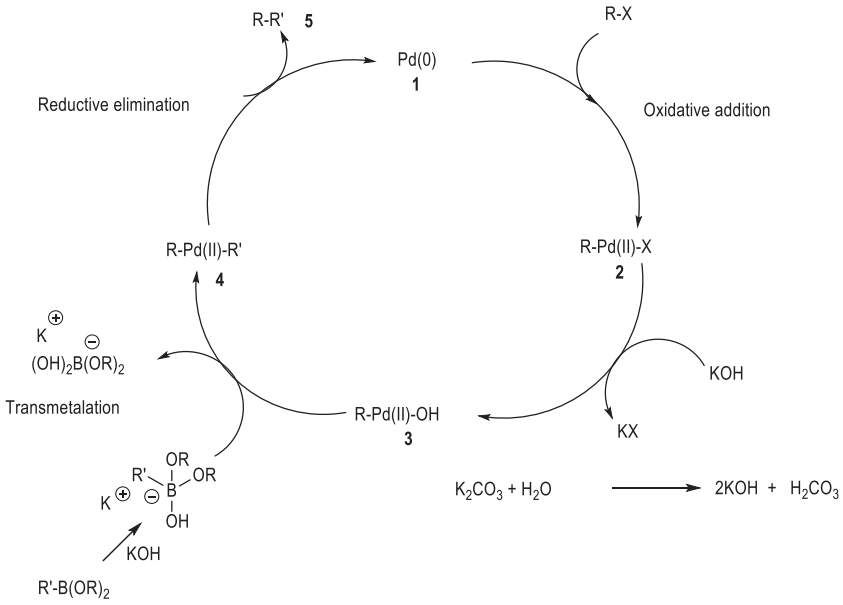


**Scheme. 3.1** Suzuki cross-coupling reaction mechanism.

The general mechanism involves the following steps: *i*) oxidative addition of organic halide to palladium(0) complex, considered as the rate-determining step; *ii*) reaction of a base with intermediate **2** to form intermediate **3**;*iii*) transmetalation between boronic acid/ester with palladium complex, in which nucleophilic organic groups transfer from boron to palladium to form intermediate **4**; *iv*) reductive elimination of complex **4** to regenerate Pd(0) and produce C-C bonded final product R-R' (Scheme 3.1). The reactivity of aryl halides used in Suzuki reactions increase in the order I>Br>>Cl, while electron-deficient aryl halides generally enhance the oxidative addition process compared to electron-rich aryl halides. Aryl triflates are also sometimes used in Suzuki coupling under mild reaction conditions and in presence of efficient catalysts, e.g. $PdCl_2$dppf (dppf = 1,1'-

bis(diphenylphosphinoferrocene)), and nonaqueous basic conditions in polar solvents. Most commonly, tetrakis-triphenylphosphine palladium ( $Pd(PPh_3)_4$ ), or palladium acetate $Pd(OAc)_2$ are used as catalysts in presence of phosphine ligands, such as $P(t\text{-}Bu)_3$ (tritertiary butylphosphine), $PCy_3$ (tricyclohexylphosphine) etc., and potassium/sodium carbonate as a base for these reactions. There are a few drawbacks in Suzuki reactions, such as the formation of undesired by-products due to dehalogenation, homocoupling, and head-to-tail coupling reactions. These drawbacks can be overcome by the optimization of the reaction conditions, e.g. solvent, time, and temperature, before moving to large-scale synthesis.[177]

### 3.1.2 The Ullmann coupling reaction

The coupling reaction of aryl halide and amine to form carbon-nitrogen (C-N) bond in presence of a stoichiometric amount of copper catalyst at high temperature (>180°C) was discovered by Ullmann in 1903.[178] Further modified Ullmann-type coupling reactions were developed in order to achieve the desired products at milder (low temperature) reaction conditions.[179,180] Like palladium-catalyzed carbon-carbon bond formation reactions, Ullmann coupling provides a powerful tool for synthesizing various organic compounds. Due to the easy availability of a range of aryl halides and amines, Ullmann reactions provide many desired aryl amines that have been further employed in the pharmaceutical field and materials science.[181] The most commonly studied mechanisms for Ullmann coupling are represented in the mechanistic pathways of Scheme 3.2.

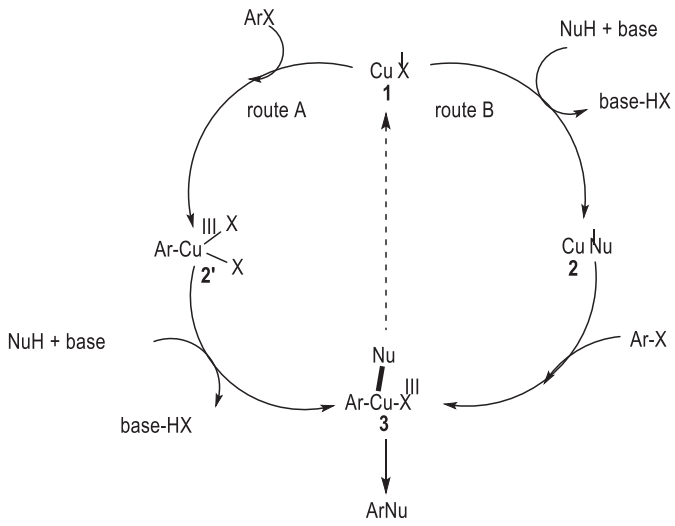


**Scheme. 3.2** Ullmann cross-coupling reaction mechanism.

The Ullman coupling reactions proceed through two possible mechanistic pathways. In the first route, the oxidative addition of aryl halide derivative on copper catalyst takes place to form copper(III) intermediate **2'**, followed by halide exchange with a nucleophile to form intermediate **3** via reductive elimination, which gives ArNu product and regenerates the catalyst. The other route described in the reports begins with Nu reacting with Cu(I) catalyst to form intermediate **2** before the oxidative addition of aryl halide. Then, in the final step, there is the formation of ArNu product with the regeneration of the copper catalyst. In the previously discussed palladium-catalyzed reactions, oxidative addition step is performed first, and then trans-metalation takes place, but in the case of Ullmann coupling these two steps are uncertain, thus two possible mechanistic routes are considered. In general, neutral bidentate chelators containing N-, O- atoms (e.g. 1,10-phenanthroline) are used as ligands, but the most important essential drawback of copper coupling is that the effect of ligands is still not fully understood. Commonly, potassium carbonate, cesium carbonate, or sodium carbonate are employed as bases in Ullmann couplings under mild temperature between 80 to 120 °C using low boiling solvents e.g. toluene, dioxane, NMP, etc. Thus, due to highly air-stability, low-cost, easy accessibility, and the use of low-cost ligands compared to palladium couplings for the preparation of various amines from aryl halides under milder conditions, Ullmann coupling is an effective tool for synthetic chemists to achieve the desired materials.[182]

### 3.1.3 Borylation reaction

Boronic acids and esters are an important class of materials widely employed in C-C cross-coupling Suzuki reactions[176] as well as in molecular recognition,[183] asymmetric chemistry,[184] and medicinal chemistry.[185] Organo-boronates, prepared by simply reacting organo-halide with boronic acid/ester derivatives (e.g. bispinacolatodiboron), are described in the following mechanistic pathway (Scheme 3.3.). The mechanism takes place via three important steps *i*) oxidative addition of organo-halide on palladium to form intermediate 2, *ii*) reaction with a base and then transmetalation between palladium halide complex (Pd-X) and B, and *iii*) reductive elimination of boronic derivative 5 with the regeneration of palladium complex (Scheme 3.3).[186]

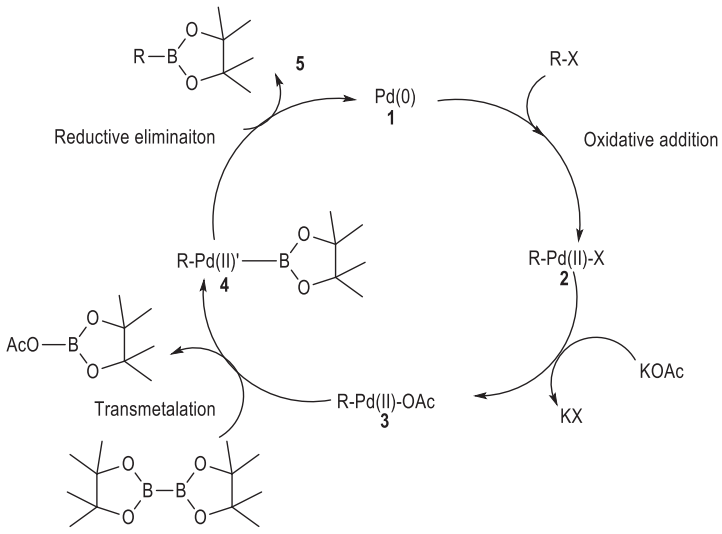


**Scheme. 3.3**. Miyaura borylation reaction mechanism.

In Miyaura reaction, organo-halides with electron-withdrawing groups proceed faster than electron donor groups due to their role in facilitating a rate-determining step. Most commonly, Pd(dppf)$Cl_2$ is used as a catalyst to achieve higher reaction yields compared to Pd($PPh_3$)$_4$ because the latter produces undesired by-products due to the coupling of diboron with phenyl groups in $PPh_3$ especially in the reaction of electron-donating halides. In borylation reaction, generally, polar solvents are employed and the reaction rate varies in order from DMSO>dioxane>toluene, in the presence of weak bases (e.g. potassium acetate (KOAc), triethylamine, and

sodium acetate (NaOAc)) while a strong base (e.g. potassium phosphate) leads to the formation of homocoupling product via Suzuki reaction. In addition, the reactivity of aryl halide varies in order of Ar-I>Ar-Br>Ar-OTf>Ar-Cl. One disadvantage of organoboranes is their tendency towards air oxidation, which reduces the reaction yield as well as limits their application. Thus, complete degassing of solvent and reaction should be done under inert environment.

## 3.2 Characterization techniques

### 3.2.1 Nuclear magnetic resonance spectroscopy

Nuclear magnetic resonance (NMR) spectroscopy was discovered by Isidor Isaac Rabi, who got the Nobel Prize in physics in 1944 for the discovery of NMR, used in magnetic resonance imaging.[187] NMR is a powerful non-selective analytical tool, which allows researchers to elucidate the molecular structures, including respective configuration, comparative concentrations, and even non-covalent interactions. NMR does not only detect and distinguish a range of functional groups but it can also distinguish similar functional groups with different neighboring group substitutions. Electrons, protons, and neutrons can be imagined as spinning around their respective axes. The net spin of the atomic nucleus is determined by the spin quantum number (S) as follows:

1) If the number of protons and neutrons is **even**, there is **no** overall spin, i.e. S = 0.
2) If the number of protons and neutrons is **odd**, the nucleus has an integer spin, i.e. S = 1, 2, 3.
3) If the number of protons **plus** neutrons is **odd**, then the nucleus possesses a half-integer spin (i.e. 1/2, 3/2, 5/2).

The non-zero spin is related to the non-zero magnetic dipole moment (μ) and expressed by

$$\mu = \gamma S \quad \text{.....(3.1)}$$

where $\gamma$ is the gyromagnetic ratio (the ratio of the magnetic moment to the angular momentum of the system, which is unique for each nucleus). In general, the most

commonly used isotopes of interest for organic chemists are $^{1}H$, $^{13}C$, $^{19}F$, and $^{29}Si$ since all of them have S =1/2 and they have 2S+1 possible orientations, i.e. 2 (+1/2 spin-up and -1/2 spin-down). In the absence of an external magnetic field ($B_0$), these orientations have equal energy, while in the presence of $B_0$ the energy levels split and each level has a given magnetic quantum number ($m$), as shown in Figure 3.1.

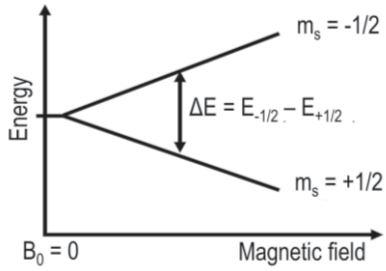


**Figure 3.1.** Splitting pattern of nuclei spin states under an external magnetic field.

The energy of magnetic dipole moment (E) under the magnetic field is given by equation 3.2:

$$E = -\mu B_0 = -\gamma \frac{mh}{2\pi} B_0 \quad \text{.....(3.2)}$$

where $m$ is the magnetic quantum number and h is Planck's constant (6.6 x $10^{-34}$$m^2$kg/s). The energy difference between two states (transition energy) is expressed by equation 3.3:

$$\Delta E = \frac{\gamma h}{2\pi} B_0 \quad \text{.....(3.3)}$$

This shows that the magnetic field $B_0$ increases with energy difference $\Delta E$. If the nucleus has large $\gamma$, $\Delta E$ is correspondingly large.

The resolution of NMR technique mostly depends on the magnitude of the magnetic gradient, thus many efforts have been carried out to develop high field strength often using superconducting materials.[188,189] Representative example of proton NMR interpretation of one of studied molecule is shown in figure 3.2 below.

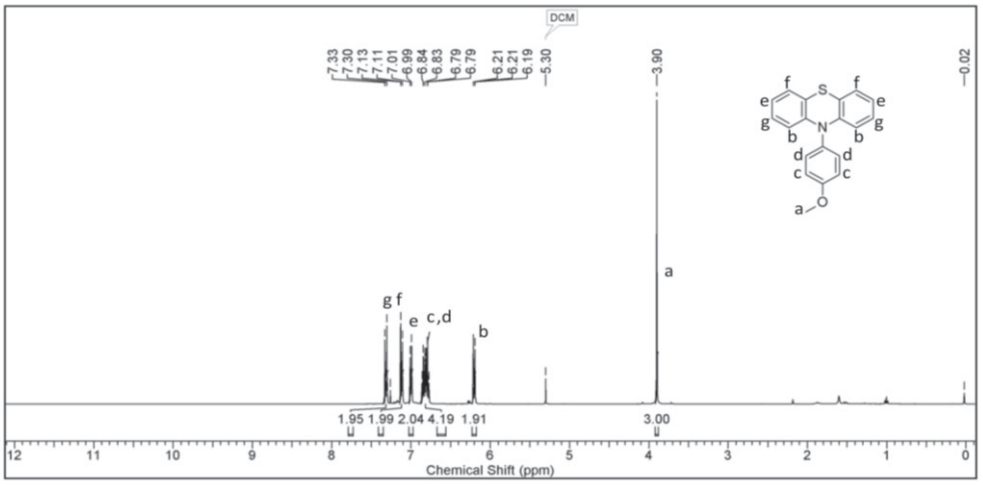


**Figure 3.2.** Representative example of 1H NMR spectra interpretation.

From the above Figure 3.2 it can be observed that the protons (a) associated with methoxy group are upfield and are corresponds to 3.90 ppm, protons (d, c) between 7.01-6.79 ppm are corresponds to aromatic phenyl ring attached to phenothiazine. The least and most downfield protons (b & g) at 6.21 ppm and 7.33 ppm are corresponds to ortho and meta-directing position of nitrogen atom of phenothiazine core. All the NMR data presented in publications I–IV were recorded with a Bruker 400 MHz spectrometer in deuterated chloroform ($CDCl_3$) at room temperature.

### 3.2.2 Mass spectrometry

The molecular structures of compounds reported in the Thesis were measured with electron-spray ionization ESI-TOF or ion-trap mass spectrometry (ESI-TOF LCT Permier XE mass spectrometer, Waters Corp.). Samples were prepared by dissolving the materials in respective solvents with an approximate concentration of 0.01 mg $mL^{-1}$ and infused at a rate of 15 μL/min. The mass spectra were recorded using a standard solution of leucine ekephaline 50 mg/mL as a reference under positive ion mode. During the measurements, the molecules of interest are introduced to the ionization source and, after ionization, the ions travel to the mass analyzer and are collected at different parts of the detector with respect to their mass-to-charge ratio (m/z). Finally, the detector creates a signal that corresponds to

the relative abundance of m/z ratios, which are recorded by computer programs.[190] Representative example of mass fragmentation pattern of one of the studied molecule is depicted in Figure 3.3 below.

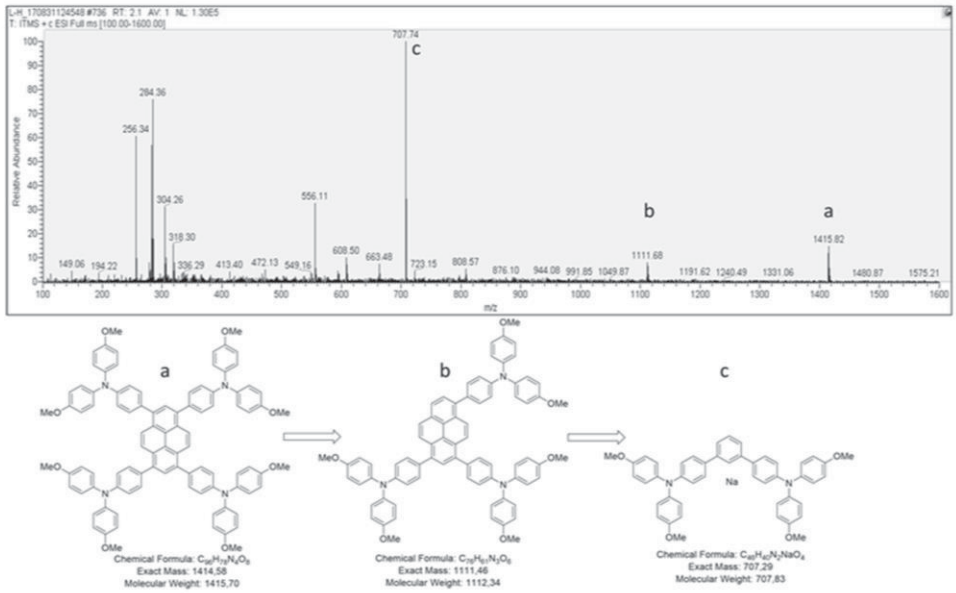


**Figure 3.3.** Mass fragmentation pattern of L-H hole-transport material.

The spectra measured by using ion-trap mass-spectroscopy clearly indicates the main peak at 1415.82 corresponds to compound (a) further the peak at 1111. 68 is corresponds to fragmentation b, finally the peak at 707.29 corelated to sodium adduct of fragment c.

### 3.2.3 Steady-state absorption and emission

Absorption and emission measurements for most of the compounds were carried out by dissolving respective samples in chloroform or dichloromethane. Thin films of the compounds were prepared by spin-coating (WS-400B-6NPP/LITE, Laurell Technologies) from chloroform or dichloromethane solution onto clean glass substrates. The steady-state absorption spectra were measured with a Shimadzu UV-3600 UV/Vis/NIR spectrophotometer both in solution and in thin films. The absorbance of a solution with known concentration was used to determine the extinction coefficient ($\varepsilon$) by using the Beer-Lambert law: $A=\varepsilon lc$,[191] where $A$ is absorbance, $l$ is the path length of the cuvette, and $c$ is the concentration of the

sample. The steady-state emission and the time-resolved photoluminescence decay of perovskite/HTM samples were measured by using the Pico Quant Fluotime 300 (Jobin Yvon) and Edinburgh fluorometers, respectively. The excitation wavelengths were determined from the absorption spectra, and fluorescence was recorded in the range of 400–800 nm by exciting the samples at the respective excitation wavelengths. Measured absorption and emission of the respective functional materials were compared to those of their parent molecules and the effect of different substitutions was studied. Optical characterization was part of all the manuscripts involved in this Thesis. The optical band gap ($E_g$) of each presented material was determined by using the following equation 3.4.

$$E_g = \frac{hc}{\lambda} \quad \text{.....(3.4)}$$

where $h$ is Planck's constant 6.626 x $10^{-34}$ kg $m^2$ /s, $c$ is the speed of light 2.99 x $10^8$ m/s, and λ is the onset absorption wavelength. The optical band gap value was used for the determination of the LUMO level of the investigated compounds.

### 3.2.4 Computational studies

Computational analysis of the compounds presented in the Thesis was carried out by density functional theory (DFT) methods. In **Publications I–III**, geometries and conformational analysis of phenothiazine derivatives, as well as the HOMO-LUMO energy levels and bandgaps, were optimized by PBE1PBE/6-31G** level of theory using dichloromethane solvent. The effect of different substituents on the phenothiazine core was studied at Tampere University by Dr. Nuno R. Candeias. Similarly, the HOMO-LUMO energy levels of pyrene-based compounds were estimated with the help of DFT at B3LYP/LANL2DZ level with a PCM (polarizable continuum model) model of the chloroform solvent in **Publication IV**. All the results were further compared with the experimentally obtained energy levels and bandgaps of molecules.

### 3.2.5 Differential pulse voltammetry

Differential pulse voltammetry (DPV) is used for the electrochemical characterization of organic and inorganic compounds. A periodically applied potential induces a change in the concentration of an electroactive species on the electrode surface associated with an oxidation or reduction process. The reactions

of interest take place at the electron-conducting working electrode. In the DPV technique, the potential perturbation comprises small voltage pulses of the same amplitude (5–250 mV) and the current is sampled twice, before and right after each pulse. The cell current is measured as a function of the potential between the working and reference electrode. The DPV voltammogram shows the differentiation between each detected pulse up to nanoscale.

In this work, the DPV characterization was carried out to determine the HOMO energy levels of the studied compounds. All the DPV experiments were conducted with a potentiostat (Iviumstat Compactstat IEC 61326 Standard) and a three-electrodes cell configuration consisting of working, counter/auxiliary, and reference electrodes. A platinum electrode was the working electrode, a graphite rod the counter electrode, and Ag/AgCl the pseudo reference electrode. A 0.1 M tetrabutylammonium hexafluorophosphate (or tetrabutylammonium tetrafluoroborate) solution in dichloromethane (DCM) was used as supporting electrolyte during the measurements. Ferrocene (Sigma Aldrich, 98%) was the internal standard to scale the obtained potentials against the vacuum level.[192]

For each measurement, first a background was recorded by adding 2.5 ml of the electrolyte solution in the reaction vial and after purging it with nitrogen for about 7 min. The sample solution (50 µl) with 0.05 mM concentration in the supporting electrolyte was introduced in the reaction vial and the system was kept under nitrogen/argon for at least 7 min. The scans were recorded in the range of -2.5 to 2.5 V in both positive and negative directions with a 2.5 mV step. The HOMO level for each compound was calculated from the oxidation potential peak in the DPV voltammogram according to equation 3.5.

$$E_{HOMO}\ (eV) = -(E_{ox} - E_{Fc/Fc+}) - 4.80\ eV \quad \text{.....(3.5)}$$

$$E_{LUMO}\ (eV) = E_g^{opt} - E_{HOMO} \quad \text{.....(3.6)}$$

where $E_{ox}$ is the oxidation potential of the sample, $E_{Fc/Fc+}$ is the standard oxidation potential of ferrocene, -4.80 eV is the energy level of ferrocene against vacuum, and $E_g^{opt}$ is optical bandgap. The LUMO level of the compounds was determined from the optical bandgap and HOMO energy levels using equation 3.6, due to the lack of visible reduction peaks in the voltammograms for all the studied molecules.

### 3.2.6 Time-resolved photoluminescence spectroscopy

Time-resolved photoluminescence (TRPL) is a tool for studying the fast electronic recombination processes that result in the emission of photons. The lifetime of molecules in their lowest excited singlet states ranges from few picoseconds to nanoseconds and it can be influenced by the molecular environment (e.g. solvents, moisture, or temperature) as well as by the interaction with other molecules. In the case of metal-containing complexes, the emission lifetimes range from nano- to milli-seconds after the relaxation of the luminescent species from their excited triplet states called phosphorescence. In this work, TRPL characterization has helped to understand and analyze the charge extraction processes at the perovskite/HTM interface. The fluorescence lifetime at the nanosecond scale was measured by using time-correlated single photon counting (TCSPC) system, which is presented in Figure 3.2.

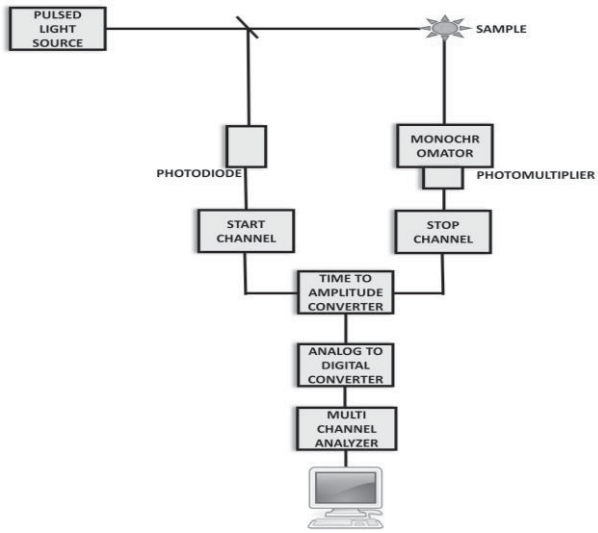


**Figure 3.4** Time-correlated single photon counting (TCSPC) measurement setup.

The TCSPC process involves the detection and measurement of single photons and their arrival time with respect to a reference signal, i.e. the light source. The sample is excited by a pulsed laser source with a high repetition rate. The photons emitted by the sample are directed to a monochromator, which passes the light of a selected wavelength. The detected light is amplified by a photomultiplier tube (PMT) in which the absorption of a photon leads to the emission of an electron. The emitted and reference light signals pass through a constant fraction

discriminator, after which the reference pulse activates a time-to-amplitude converter. In the time-to-amplitude converter, the trigger pulse starts a linearly rising voltage generator and the first emitted photon detected at photomultiplier stops the generator. The output voltage of the generator depends on the time delay between the start and stop pulses. The voltage from the time-to-amplitude converter increases the matching channel count by one and finally the decay profile of the sample is recorded by measuring the arrival of photons at each time interval after the excitation. [193]

The PL decays were fitted with a double exponential. We assign the fast component to the trap-assisted recombination of charge carriers/excitons, and the slow component to the radiative recombination of free charge carriers/excitons in the bulk, respectively.[194] To further simplify the comparison of lifetimes, an effective lifetime i.e. $t_{1/e}$, expressed as $I(t_{1/e}) = I(0)/e$, where $I(t_{1/e})$ is the PL intensity at time $t_{1/e}$.[195] The hole injection yield ($\Phi$h-inj) was determined by using PL decays of perovskite films with HTMs ($t_{1/e(HTM)}$), and without them ($t_{1/e(perov)}$), using equation 3.7.[194,196]

$$\Phi_{\text{h-inj}} = 1 - \left(\frac{1}{t_{1/e(HTM)}} - \frac{1}{t_{1/e(perov)}}\right) \quad \text{.....(3.7)}$$

### 3.2.7 Hole mobility measurements

Charge-carrier mobility is one of the important parameters for realizing high-performing organic electronic or photovoltaic devices. In the case of efficient transistors, it tells how fast they can switch and, in the case of photovoltaics, it tells how quickly the separated charges move away from each other. Hole mobility of the compounds presented in this Thesis was measured by using impedance spectroscopy in **Publication I**, time of flight (TOF) in **Publication II**, and Photo-CELIV in **Publication IV**.

***Impedance spectroscopy for charge-carrier mobility measurement***

Impedance spectroscopy is generally used to evaluate electrochemical systems and solid-state devices. The electrochemical impedance spectroscopy (EIS) is performed in a three-electrode geometry and, in the case of solid-state solar cells, in a two-point or four-point geometry. EIS measurements are conducted on thin films in the frequency range from mega- (microseconds) to sub-hertz (less than seconds). The

measurement is performed by applying an alternating voltage ($V_{ac}$) across the material/sample, and by measuring the alternating current ($I_{ac}$) response. For a constant dc offset, the frequency of $V_{ac}$ is varied and the alternating current is measured at each frequency, giving the transfer function Z.[197] The charge carrier transporting mainly depends on the ohmic resistance of the electrodes, materials, and interfaces as well as defects and grain boundaries present in the bulk of the materials. In the case of solid-state samples, charge-transporting is highly governed by film quality (amorphous/crystalline) as well as the intermolecular interactions present in materials. The most common method for measuring impedance is by applying single-frequency voltage to interfaces and measuring the shifting of amplitude, or real and imaginary parts of the resulting output at a given frequency. All the commercially available instruments in the market can automatically measure the impedance as a function of frequency in the range of 1 MHz to 1 MHz and easily interfaced by computer.[198]

The charge-carrier mobility of all the phenothiazine derivatives (O-1, O-2, and O-3 in **Publication I**) was measured by using an Agilent 4294A impedance analyzer with frequency range 40 Hz to 1.4 MHz applying 0 to 14 V dc bias. The hole only device i.e. at least one electrode injects a hole, while the other blocks the electron transporting, structure ITO/PEDOT:PSS/phenothiazine/$MoO_3$/Au was prepared. All the compounds were dissolved in chlorobenzene of concentration of 65–70 mg $mL^{-1}$ and then spin-coated (300 rpm) on top of PEDOT:PSS, further the layer of $MoO_3$ (5nm) and Au as a top electrode were thermally evaporated on an active area of 8 $mm^2$. First, the transient time ($\tau$) of charge carriers of all the molecules was determined from the peak frequency using the following expression 3.8

$$\tau = k \cdot \tau_p \quad \text{.....(3.8)}$$

where $\tau_p$ is the time constant corresponding to the peak frequency and $k$ is a constant (0.44) for a moderate degree of dispersion used from the literature.[199] The charge carrier mobility was determined by using expression 3.9

$$\mu = d/E\,\tau \quad \text{.....(3.9)}$$

where $\mu$ is the mobility of organic semiconductors, d is the thickness of the film, E is applied electric field, and $\tau$ is transient time. Also, the zero-field mobility and field strength were calculated by using expression 3.9

$$\mu = \mu_0 \exp(\gamma\sqrt{E}) \quad \text{.....(3.10)}$$

where $\mu_0$ denotes the mobility at zero field and $\gamma$ is the parameter describing the field dependence strength. $\gamma$ = 9.9x10$^{-3}$ (V cm$^{-1}$)$^{-1/2}$ for O-2 and $\gamma$ = 6.2x10$^{-3}$ (V cm$^{-1}$)$^{-1/2}$ for O-3.

***Time of flight mobility of charge carriers***

Time of flight (TOF) is the most commonly used technique for charge-carrier mobility measurements. Hole and electron mobility can be measured separately for organic small molecules as well as polymers. TOF is mainly based on carrier transit time, i.e. the time required for photo-generated charge carriers to travel from one electrode to the other electrode in a sample of known thickness (*d*) under an applied electric field ($E=V/d$). In TOF measurements, an organic layer of a few microns thickness is sandwiched between two electrodes, one of which is transparent. During the drift mobility measurement, the material is irradiated by a laser pulse to generate charges. These photogenerated charges migrate towards the second electrode based on the polarity of applied bias and the corresponding electric field. Finally, the current at that electrode is recorded as a function of time.[200]

Hole mobilities of three compounds (AZO-I, AZO-II, and Spiro-OMeTAD in **Publication II**) were measured with the integral mode TOF method. All the compounds were dissolved in chlorobenzene (40 mg/ml for AZO-I or II, and 92 mg/ml for Spiro-OMeTAD) and spin-coated on top of a PEDOT:PSS layer. The top contact was thermally evaporated and included LiF (0.8 nm) and Al (60 nm) films. Samples were irradiated by 355 nm laser pulse to generate charges and the steady-state voltage was applied in reverse bias to extract charges.

The hole or electron mobility of material is calculated by using equation 3.11

$$\mu = \frac{d^2}{V\tau} \text{.....(3.11)}$$

where $\mu$ is the drift mobility of charge carriers, i.e. the average velocity with which charge carriers travel per second under applied voltage (V), and *d* is known thickness, and $\tau$ is transit time. The transit time $\tau$ is derived from the time when photovoltage reaches half of its maximum value $t_{1/2}$ using the following equation 3.12.[201]

$$\tau = \frac{\sqrt{2}}{\sqrt{2}-1}\, t_{1/2} \quad \text{.....(3.12)}$$

In TOF measurements, large film thickness with high optical densities (OD>10) is a requirement to form a thin layer of charge carriers near one of the electrodes. This limits the applicability of TOF in optimized devices.

***Charge extraction by linearly increasing voltage (Photo-CELIV)***

In Photo-CELIV, a linearly increasing voltage is applied at one electrode and the transient current is used to determine the mobility of the photoinduced charge carriers. In materials where the τ is smaller or comparable to the extraction time, the relaxation process can be followed by varying the delay time between extraction and sample irradiation. Thus, by calculating the number of extracted carriers as a function of delay time, the carrier lifetime can be estimated. During measurements, a sample (thickness can be from a few hundred nanometers to micrometers) is sandwiched between an ITO-coated glass and an Al electrode. Upon irradiation of the sample by a laser pulse, the charge carriers are photogenerated through the material. The photogenerated charge carriers either exit the device via the external circuit or undergo recombination. The remaining charges are extracted by adjusting the delay time and by selecting the voltage rise speed A. The current reaches its maximum value at the time corresponding to $t_{max}$. Thus, the mobility can be determined.[202]

All the three compounds (L-H, L-F, and PTAA in **Publication IV**) were dissolved in chlorobenzene (40 mg/ml) and spin-coated (thickness 150–210 nm) on top of PEDOT:PSS layer. Finally, LiF and Al were evaporated to form the following sandwich structure: ITO/PEDOT-PSS/L-H or L-F or PTAA/LiF/Al. The device was illuminated by 355 nm 45 μJ/pulse laser and, after a time delay, a linearly increasing pulse voltage was applied in reverse bias to extract the photo-generated charge carriers and the resulting transient current was recorded. The mobility was determined by using the following expression 3.13[203]

$$\mu = \frac{d^2}{2At_{max}^2}\left[\frac{1}{6.2\left(1+0.002\frac{\Delta j(t_{max})}{j_0}\right)} + \frac{1}{\left(1+0.12\frac{\Delta j(t_{max})}{j_0}\right)}\right]^2 \quad \text{.....(3.13)}$$

where *d* is the thickness of the active layer, $\Delta j(t_{max})$ is the difference between the transient current in dark and in light at $t_{max}$, A is the voltage ramp-up rate, and $j_0 = C_{geo}A$ is a displacement current, and $C_{geo}$ is the geometric capacitance of the device.

### 3.2.8 Solar cell fabrication and characterization

The solar cell fabrication mainly involves planar and mesoporous architectures with regular *n-i-p* or inverted *p-i-n* configuration. In the case of *n-i-p,* the bottom contact is the ETM and the top contact is the HTM. Conversely, in the case of *p-i-n* the HTM is at the bottom. In both cases, light reaches the device through the transparent electrode on a glass substrate. The PSCs fabrication includes the preparation of the precursor solutions, the cleaning of substrates, the bottom/top charge-selective contact depositions, the perovskite film deposition, and finally the metal electrode evaporation. Though the perovskite precursor solution preparation is rather simple, the storing conditions and the formation of coordination geometry in solution highly impact the reproducibility and performance of PSCs. Thus, it is recommended to carry out the solution preparation, as well as the film fabrication, under inert atmosphere, i.e. inside a glovebox.

The substrate cleaning is done by an ultrasonic bath using isopropanol, deionized water, acetone, and finally drying under nitrogen flow. After drying, UV ozone or plasma cleaning is applied for 15 minutes at high power, followed by the deposition of the bottom selective contact according to the respective solar cell architecture ($SnO_2$ or $TiO_2$ in case of regular *n-i-p* architecture and PTAA or Spiro-OMeTAD for the inverted *p-i-n* structure). Subsequently, the perovskite layer is spin-coated and the charge carrier top selective contact is spin-coated atop. Finally, the evaporation of the metal electrode (Au, Cu, or Ag) is performed under high-vacuum. During the evaporation, it is recommended to keep the sample temperature below 60 °C to ensure high-performing devices.

The PSCs in **Publications II** and **III** are planar architectures with ITO/$SnO_2$/CsFAMA/HTM/Au (or Ag) structure, where CsFAMA is a known perovskite with mixed cations composition (Cs, formamidinium FA, and

methylammonium MA). The $SnO_2$ film was prepared by spin-coating an aqueous colloidal dispersion at 4000 rpm for 30 s, followed by thermal annealing at 150 °C for 30 min. The CsFAMA film was spin-coated with a two-step spinning method. The first step was for 10 s with 2000 rpm and the second step was 6000 rpm for 40 s. Chlorobenzene (200 µl) was used as antisolvent during the second spin-coating step and finally the substrate was annealed at 100 °C for 30 min. After cooling the substrate to room temperature, the HTM layer was spin-coated from chlorobenzene or toluene solution. In **Publications II** and **III**, the reference Spiro-OMeTAD was spin-coated on top of the perovskite layer at 4000 rpm for 45 s from a 72.5 mg/ml solution in chlorobenzene. The AZO-I and AZO-II HTMs were deposited with an optimized concentration of 10 mg/ml. In the case of **Publication III**, AZO-III and AZO-IV were deposited on the perovskite layer with an optimized concentration of 10 mg/ml in toluene. All the materials were doped with 17.5 µL Li-TFSI (520 mg/mL), 28.8 µL FK209 (300 mg/mL) and 28.8 µL tBP (300 mg/mL) simultaneously. After the deposition of the HTM layer, a metal electrode was thermally evaporated (100 nm of Ag or Au) with a mask, whose effective area was 7.5 $mm^2$. The current density-voltage (J–V) characterization of the solar cells was performed under dark and solar simulated light illumination (AM 1.5 spectrum, intensity 100 $mW/cm^2$) with a Keithley 2400 source-monitor unit.

In **Publication IV**, PTAA, L-H, or L-F were dissolved in 2 mg/mL (PTAA) and 5 mg/mL (L-H/L-F) of dichlorobenzene and spin-coated onto cleaned ITO substrates at 4000 rpm for 30 s, followed by the thermal annealing at 100 °C for 10 min. The wide-bandgap perovskite precursor solution ($Cs_{0.1}FA_{0.75}MA_{0.15}PbI_{1.5}Br_{1.5}$) was spin-coated onto the substrate using a 2-step spin coating program (2000 rpm for 2 s, and then 4000 rpm for 20 s). During the perovskite deposition, 200 µL anhydrous chlorobenzene antisolvent was dropped onto the spinning substrate, and the as-fabricated perovskite film was annealed at 100 °C for 1 h then PCBM (30 nm) layer was spin-coated. The devices were completed by sequentially thermally evaporating BCP (7.5 nm) and Ag (80 nm) with a mask whose effective area was 8 $mm^2$. The devices were illuminated with a solar simulator (Newport, Oriel class AAA, 94063A) at 100 mW/ $cm^2$ illumination (AM 1.5 G).

The recorded J–V characteristics allow determining the key photovoltaic parameters of solar cells: the maximum power output ($P_{max}$), the power conversion efficiency (PCE), $J_{sc}$, $V_{oc}$, and FF. PCE is defined as the ratio of electrical power produced by a solar cell per unit area divided by incident light per unit area under standard test conditions.[91] The standard test conditions are *i*) irradiance intensity of

1000 W/m², *ii*) AM 1.5 solar reference spectrum, and *iii*) temperature during measurements of 25 °C. The reference AM (air mass) 1.5 spectrum is standardized by the International Organization of Standardization (ISO 9845-1:1992). The sun emits 1353 W/m² energy outside the atmosphere that corresponds to the AM 0 spectrum. AM 1 corresponds to the sun overhead at the zenith, and AM 1.5 refers to the solar zenith angle of 48.2°. For suitability, the flux of AM 1.5 is corrected to 1000 W/m².[201] The general representation of a solar cell J–V curve in dark and under illumination, with the indication of the key photovoltaic parameters, is presented in Figure 3.3.

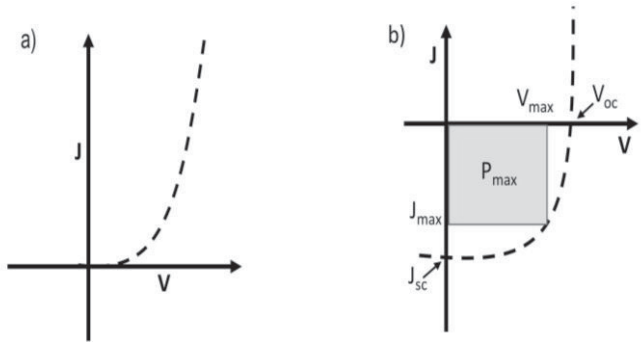


**Figure 3.5**. a) Current density-voltage (J–V) curve for a solar cell in dark, b) J-V curve under illumination. The intersections with abscissa and ordinate are $V_{oc}$ and $J_{sc}$, respectively. The maximum power output ($P_{max}$) is determined by the point at which voltage and current are maximum.

The PCE can be expressed by the following equation:

$$PCE = \frac{P_{out}}{P_{in}} = \frac{J_{sc}\,V_{oc}\,FF}{P_{in}} \quad \text{.....(3.14)}$$

where $P_{out}$ is the output power of the cell, $P_{in}$ is the input power of the cell, $J_{sc}$ is the current at zero applied voltage, i.e. under short-circuit conditions (V = 0), $V_{oc}$ is the voltage at open-circuit conditions, i.e. when no current passes through the device, and FF is the ratio of the maximum power output from the solar cell ($P_{max}$) to the product of $J_{sc}$ and $V_{oc}$, as represented by equation 3.15

$$FF = \frac{P_{max}}{J_{sc}V_{oc}} = \frac{J_{max}V_{max}}{J_{sc}V_{oc}} \quad \text{.....(3.15)}$$

where $J_{max}$ and $V_{max}$ are the maximum current and voltage, respectively. $J_{sc}$ can be affected by the absorption of the photoactive layer, and by the extraction and

transporting efficiency. The $V_{oc}$ is influenced by the charge carrier recombination and by the energy levels of the constituents of the solar cells.

# 4 RESULTS AND DISCUSSION

This Chapter summarizes the most significant results presented in publications I–IV. Firstly, the molecular design, synthesis, optical and electrochemical properties and bulk-hole mobility of phenothiazine compounds are discussed. Secondly, phenothiazine-core HTMs, further modified by using simple condensation chemistry, are discussed. Finally, pyrene-core HTMs are designed and synthesized to study the effect of fluorination on the optical and electrochemical properties, and the photovoltaic performance in PSCs.

## 4.1 Phenothiazine-based charge-transporting materials

One of the aims of the present work was to design and synthesize low-cost and environmentally friendly phenothiazine molecules and to study their charge-carrier (hole) mobility. Furthermore, the molecules were employed as HTM layers in perovskite solar cells to replace the pricey and unstable Spiro-OMeTAD. By tuning the optical and electrochemical properties of the phenothiazine derivatives, an initial screening was carried out to check their applicability as HTMs with the regular mixed cation perovskite structure. When employed as HTMs with an extremely low production cost, they led to good performance and stability of corresponding perovskite devices. After having established the background of molecular design and synthesis of suitable low-cost alternatives to Spiro-OMeTAD HTM, a similar approach was applied for pyrene-based HTM designs.

### 4.1.1 Synthesis of phenothiazine-core materials

According to previous reports, the intramolecular charge transfer (ICT) character of phenothiazines can be tuned by introducing electron donor (ED) or electron acceptor (EA) units at C(3) and C(7) positions, respectively.[122] Also, several studies suggest an enhancement in the charge-carrier mobility by extending the π-conjugation length.[204,205] Thus, to improve the charge-carrier mobility by tuning the molecular energy (HOMO/LUMO) levels[206] and consequently reduce the HOMO-

LUMO energy gap, we introduced strong electron-withdrawing malononitrile group at C(3) position and alkoxy aryl groups at C(7) position of phenothiazine. This was studied in **Publication I**. The synthesis route of the series of phenothiazine compounds presented in **Publication I** is elucidated in Scheme 4.1.

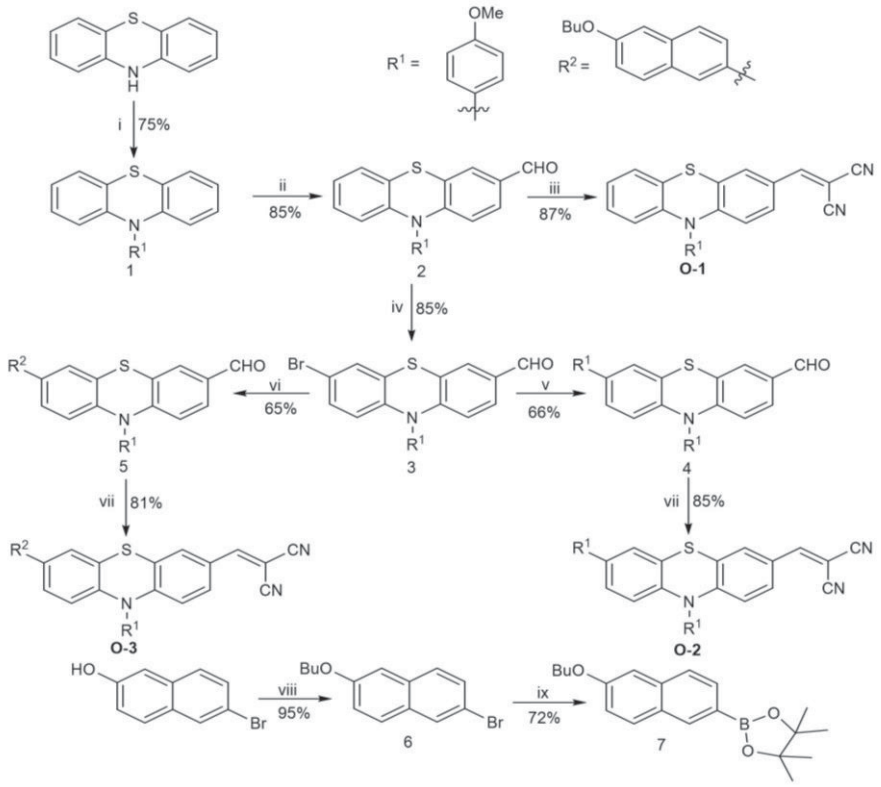


**Scheme 4.1.** Synthesis route for the phenothiazine O-series (**Publication I**). Reagents and conditions: (i) 4-Iodoanisole, Cu, $K_2CO_3$, TEGDME, 180 °C; (ii) $POCl_3$, DMF, $C_2H_4Cl_2$, 80 °C; (iii and vii) $CH_2(CN)_2$, Piperidine, $CHCl_3$, reflux; (iv) N-Bromosuccinimide, $CHCl_3$, rt; (v) 4-methoxyphenyl boronic acid, $Pd(PPh_3)_4$, 2M $K_2CO_3$, THF, reflux; (vi) 2-(6-butoxynaphthalen-2-yl)-4,4,5,5-tetramethyl-1,3,2-dioxoborolane, $Pd(PPh_3)_4$, 2M $K_2CO_3$, THF, reflux; (vii) 1-bromobutane, KOH, DMSO, rt; (ix) bis(pinacolato)diboron, $Pd(dppf)Cl_2$, KOAc, 1,4-dioxane, 80 °C adapted from **Publication I**.

The synthesis of the depicted organic semiconductors was carried out by using a commercially available phenothiazine core. Compound 1 was prepared by a simple one-step Ullman-coupling of 4-iodoanisole and phenothiazine core.[113] Further, a selective mono-formylation was performed by using dimethylformamide (DMF) and the phosphoryl chloride $POCl_3$ complex to produce compound 2 in an 85%

yield. The subsequent condensation of aldehyde 2 with malononitrile resulted in O-1 with an excellent yield of 87%. The synthesis of the corresponding mono-bromo derivative 3 was obtained by reacting N-bromosuccinimide with 2 in chloroform. Furthermore, the Suzuki-coupling reaction using 3 with 4-methoxy phenyl boronic acid afforded 4 in a good yield of 66%. Similarly, compound 3 was reacted with the previously synthesized 2-(6-butoxynaphthalen-2-yl)-4,4,5,5-tetramethyl-1,3,2-dioxaborolane (**7**) to produce 5. Finally, both the intermediates 4 and 5 reacted with malononitrile to give the final compounds O-2 and O-3 with 85 and 81% yield, respectively. All the intermediates, as well as the final compounds were purified by column chromatography and the purity was confirmed with NMR and high-resolution mass spectroscopy.

### 4.1.2 Optical, electrochemical, and computational properties of phenothiazine-core materials

The steady-state absorption of the phenothiazine derivatives O-1, O-2, and O-3 were measured in chloroform solution and films (Figure 4.1). The three molecules exhibit two bands at 320-330 and 450-490 nm. The former band corresponds to the π-π* transition while the latter one is related to the intramolecular charge transfer between the electron-donor moiety (phenothiazine) and the acceptor group (malononitrile).

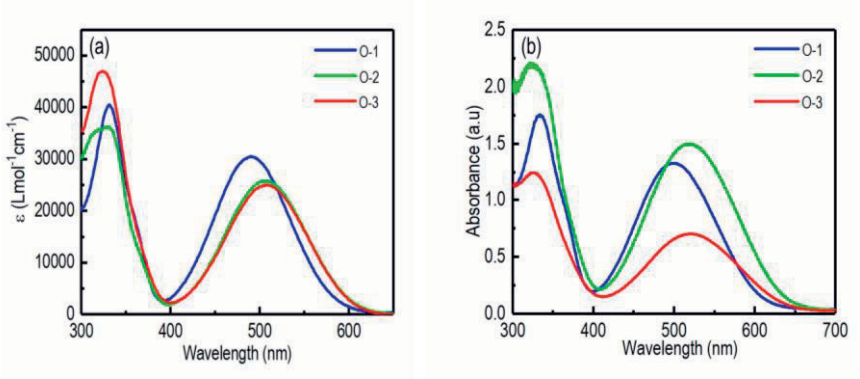


**Figure 4.1.** (a) Attenuation coefficient (ε) of O-1, O-2, and O-3 in chloroform solution; (b) absorption spectra of freshly prepared films of the target compounds on glass, adapted from **Publication I.**

The absorption, molar absorption coefficient (ε), maximum absorption wavelength ( $\lambda_{max}$), and $E_g$ of the three phenothiazine-core molecules are

summarized in Table 4.1. $E_g$ of all the molecules was determined from the absorption edges in films,[118] and the lower $E_g$ of O-3 compared to O-1 and O-2 is ascribed to its extended conjugation. The lowering of ε in the case of O-2 and O-3 compared to O-1 is attributed to the distortion causes in both cases due to the introduction of phenyl and naphthalene units, respectively.

**Table 4.1.** Optical properties of O-1, O-2, and O-3. The absorption measurements were carried out in solution (a) and in film (b), adapted from **Publication I.**

| Compounds | $\lambda_{max}$ (nm)[a] | ε at λmax ($M^{-1}cm^{-1}$) | $\lambda_{max}$ (nm)[b] | $E_g^{opt}$ (eV) |
|---|---|---|---|---|
| O-1 | 330; 490 | 30437 | 333; 500 | 2.06 |
| O-2 | 331; 507 | 25757 | 324; 518 | 2.02 |
| O-3 | 323;509 | 24957 | 325; 521 | 2.00 |

The absorption maxima of O-1 is slightly blue-shifted of about 12-13 nm compared to O-2 and O-3 due to the shorter conjugation length. The solid-state absorption spectra of all the films are red-shifted by 10-12 nm as compared to their solution state counterparts; this can be attributed to solid-state intermolecular interactions.[207]

DFT and DPV were used to determine the energy levels (HOMO, LUMO) of all the molecules presented in this Thesis. Here, the LUMO level of each compound was derived from the HOMO level obtained from DPV and the optical band gap (equation 3.6) The attained HOMO and LUMO energy levels, as well as the band gaps of all the materials were further compared with the computationally determined values. To understand the distribution of electrons between donor-acceptor units, the computed molecular orbitals for O-1, O-2, and O-3 are presented in Figure 4.2.

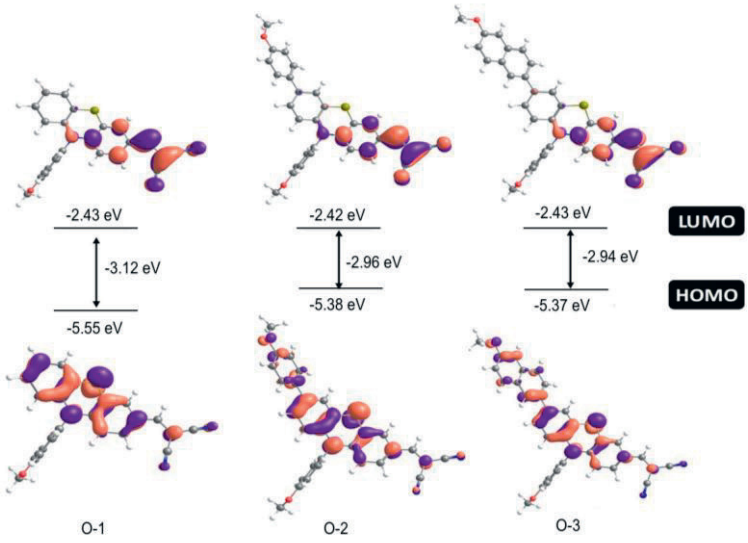


**Figure 4.2.** Energy levels and electron distribution for the frontier molecular orbitals of O-1, O-2, and O-3(Me), calculated with DFT at PBE1PBE/6-31G** level of theory (isosurface value = 0.04), adapted from **Publicaiton I**.

In the case of the HOMO energy levels, the electron distribution is mainly localized over the phenothiazine core as well as over the electron-donating substituents at C(7) position in the case of O-2 and O-3. However, in the case of LUMO, the electron density is distributed on the electron-accepting malononitrile group as well as on the adjacent benzene ring of phenothiazine. The experimental energy levels, measured by using DPV, are presented in Table 4.2. Both the computational and experimentally determined properties showed a similar trend in the energy levels and bandgap, although the absolute values for the excitation energies in the case of the computational results are overestimated by ca. 0.9–1.1 eV. The overestimated energy levels are due to overcorrelation of electrons, which favor delocalized cation radicals at geometry instead of localized unpaired electrons.[208]

**Table 4.2.** [a]HOMO, [a]LUMO, and [a]$E_g$ values based on the computational calculations. [DPV] HOMO values are determined from the electrochemical measurements, [opt]LUMO are derived by using the optical bandgap ([opt]$E_g$), which is calculated from the onset of the absorption spectrum, adapted from **Publicaiton I**.

| Compounds | HOMO (eV) [a] | LUMO (eV) [a] | $E_g$ (eV)[a] | HOMO[DPV] (eV) | LUMO[opt] (eV) | [opt]$E_g$ (eV) |
|---|---|---|---|---|---|---|
| O-1 | -5.55 | -2.43 | 3.12 | -5.29 | -3.16 | 2.06 |
| O-2 | -5.38 | -2.42 | 2.96 | -5.24 | -3.23 | 2.02 |
| O-3 | -5.37 | -2.43 | 2.94 | -5.24 | -3.27 | 2.00 |

All the compounds exhibited similar electrochemical properties and the HOMO level lies in the range of -5.24 to -5.29 eV with no clear reduction peak observed in the DPV measurements. The high HOMO energy level of phenothiazine compounds indicates the further possibility to modify the phenothiazine cores for organic hole-transporting material applications.

### 4.1.3 Bulk-hole-mobility studies of phenothiazine-core materials

The bulk hole mobility of all three-phenothiazine derivatives O-1, O-2, and O-3 was investigated by impedance spectroscopy (Figure 4.3).

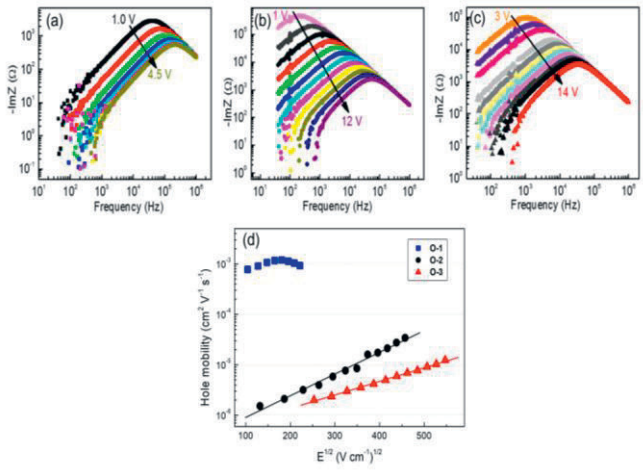


**Figure 4.3**. The imaginary part of the impedance (ImZ) as a function of frequency for hole-only devices made of **O-1** (a), **O-2** (b), and **O-3** (c) films at different DC bias voltage (the arrows indicate increasing voltage). Film thicknesses: 920 nm, 575 nm, and 470 nm for **O-1**, **O-2**, and **O-3**, respectively (upper) and (d) bulk hole mobility of **O-1**, **O-2**, and **O-3** as a function of the square root of the electric field (lower), adapted from **Publicaiton I**.

Hole-only devices were prepared with thermally annealed films at 80 °C for O-1, and at 110 °C for O-2 / O-3. Lower temperature was used to anneal O-1 compared to O-2 and O-3 to overcome the issue of pin-holes and cracking formation.O-1 exhibited excellent bulk-hole mobility of $10^{-3}$ $cm^2V^{-1}s^{-1}$ compared to O-2 and O-3 around $10^{-6}$ $cm^2V^{-1}s^{-1}$. Furthermore, O-2 and O-3 showed a linear trend in mobility data indicated a Poole-Frankel type behavior and thus the hole mobility of O-2 ($\mu_0$ = 3.4x$10^{-7}$ $cm^2$ $V^{-1}$ $s^{-1}$) and O-3 ($\mu_0$ = 4.0x$10^{-7}$ $cm^2$ $V^{-1}$ $s^{-1}$) calculated using equation 3.9.[209,210]

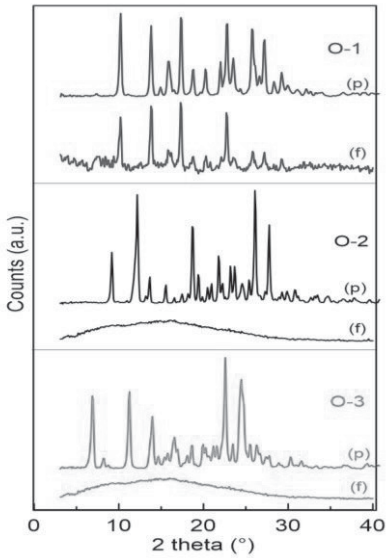


**Figure 4.4.** XRD patterns of powder samples (p) and film samples (f). Film samples were prepared and thermally treated in the same conditions used for the preparation of hole-only devices, adapted from **Publication I**.

The significant enhancement in the bulk hole mobility of O-1 compared to O-2 and O-3 was clarified by carrying out XRD analysis, as presented in Figure 4.4. XRD analysis was conducted in film and powder form. All the powder form samples appeared crystalline. However, while O-2 and O-3 showed amorphous films, surprisingly O-1 was crystalline even in film form. Thus, the enhancement in bulk hole mobility of O-1 is attributed to the presence of a crystalline phase.

## 4.2 Synthesis of phenothiazine-based hole-transporting materials

To provide environmentally friendly, inexpensive, stable, and easily synthesizable hole-transporting materials as an alternative to Spiro-OMeTAD in PSCs, we functionalized the phenothiazine core with an azomethine (-C=N-) bond. Azomethine bonds possess similar optical and thermal characteristics as vinylic double bonds. However, azomethines can be made by a simple condensation reaction of aldehyde and amine under a catalyst-free ambient environment, in which water is the only by-product of the reaction.[211] The synthesis route of the azomethine-based HTMs (AZO-I, AZO-II) used in **Publication II** is presented in scheme 4.2.

The idea of designing the azo-functional materials AZO-I and AZO-II was inspired by the work of Docampo *et al.* on low-cost azomethine-based HTMs and by our earlier work on phenothiazine-based high hole mobility materials.[83] For the synthesis, initially a triarylamine derivative, N, N-bis(4-methoxyphenyl)benzene-1,4-diamine (2), was prepared according to literature procedure by reduction of the nitro-derivative of dimethoxy triarylamine.[212]

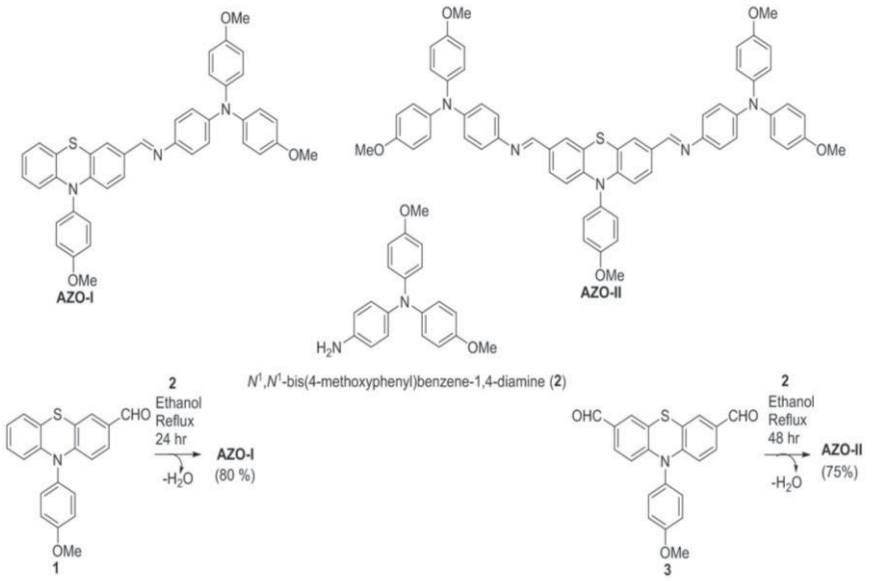


**Scheme 4.2.** Synthesis route for the azomethine functional organic hole-transporting materials, adapted from **Publication II**.

The aim behind the introduction of the methoxy-substituted triarylamine unit was to improve the solubility, tune the energy levels of azomethine derivatives, and ultimately enhance the device performance. Furthermore, both mono- and di-aldehyde functionalized methoxy-substituted phenothiazines were prepared according to the method reported in section 3.1. Finally, the condensation reaction of the amine (2) and the respective aldehydes was carried out to afford the corresponding azo-functional derivatives AZO-I and AZO-II by crystallization. The cost of the azomethine-based HTMs studied in **Publication II** is calculated based on reported cost-models[82,126] and it is presented in Table 4.3.

**Table 4.3.** Calculation of the synthetic cost of AZO-I and AZO-II HTMs, adapted from **Publication II**.

| Chemical name | Price of Chemical ($) | Weight or amount of reagent | Material cost ($) |
|---|---|---|---|
| Phenothiazine | 8.49/100g | 0.76g | 0.06 |
| 4-Iodoanisole | 370/500g | 1.33g | 0.98 |
| 1,2-dichloroethane | 39.82/1000mL | 30mL | 1.19 |
| Cu | 84/500g | 0.243 | 0.04 |
| potassium hydroxide | 3.74/500g | 6.00g | 0.04 |
| DMSO | 26/1000mL | 20mL | 0.52 |
| Ethyl acetate | 1.51/500mL | Step 1. (500 mL) | 1.51 |
| Phosphorus oxychloride | 11.51/250mL | Comp. 1 (3.65 mL), Comp. 3 (10 mL) | 0.168 (1) and 0.460 (3) |
| DMF | 6.91/100mL | Comp. 1 (3.04 mL), Comp. 3 (11 mL) | 0.210 (1) and 0.760 (3) |
| Petroleum ether | 0.94/500mL | Comp. 1 (800 mL), Comp. 3 (1000 mL) | 1.50 (AZO-I) and 1.88 (AZO-II) |
| Dichloromethane | 4.7/500mL | Comp. 1 (200 mL), Comp. 3 (300 mL) | 1.88 (AZO-I) and 2.82 (AZO-II) |
| Compound 2 | 2280/Kg | AZO-I (0.630) and AZO-II (0.86) | 1.38 (AZO-I) and 1.9 (AZO-II) |
| Total cost per gram | | | 9.47 $/gm (**AZO-I**) and 12.16 $/gm (**AZO-II**) |

In order to achieve good solution processability in non-halogenated solvents, minimize the HTM cost, prevent the use of external dopants, and improve the PSC device performance, phenothiazine core was modified by the simple introduction of a π-bridge aryl unit between phenothiazine and azomethine unit (AZO-III). The core was further functionalized with an additional thiol group (AZO-IV) to enhance thiol-iodine interaction and promote the hole transfer at the perovskite/HTM interface.[78]

The synthesis route of AZO-III and AZO-IV is summarized in Scheme 4.3. First, a simple nucleophilic substitution of commercially available phenothiazine, as

well as of 2-thioethyl phenothiazine, was carried out with 4-fluorobenzaldehyde in presence of tripotassium phosphate ($K_3PO_4$) in DMF, according to a previously reported procedure.[213] This led to the intermediates 3 and 4 with 80 and 75% yields, respectively. Furthermore, azomethine condensation reaction of intermediates 3 and 4 with dimethoxy-substituted aryl amine (2) in ethanol leads to the formation of targeted hole-transporting materials AZO-III and AZO-IV, respectively. Final HTMs were purified with recrystallization in ethanol. After purification, an excellent yield of 92% and 87% was estimated for AZO-III and AZO-IV, respectively.

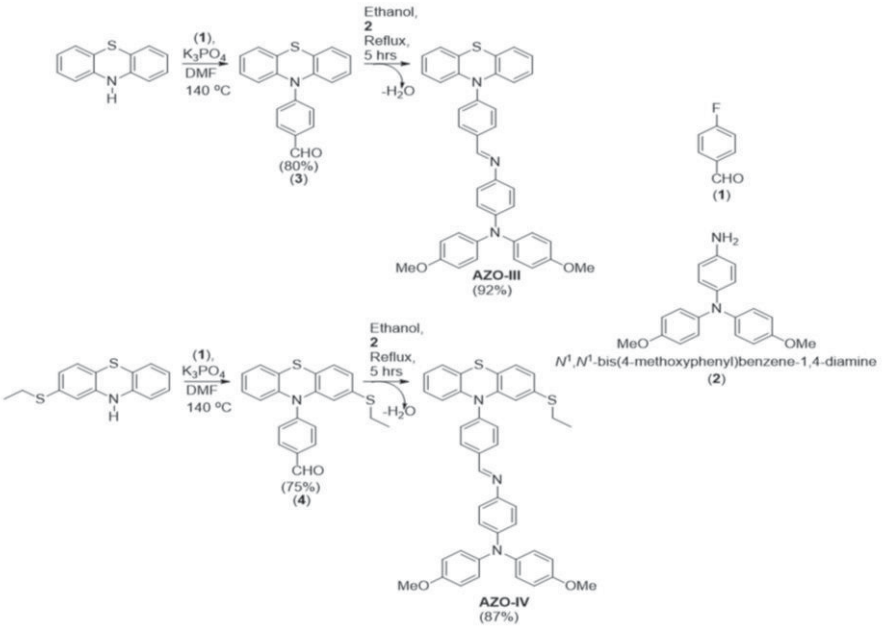


**Scheme 4.3.** Synthesis route for the aryl linker azomethine functional organic hole-transporting materials, adapted from **Publication III**.

Both the synthesized derivatives have good solubility in non-halogenated solvents, e.g. THF (40 mg/ml) or toluene (50 mg/ml), which contributes to a halogen-free solution-processable PSCs fabrication. Synthesis costs of molecules AZO-III and AZO-IV are given in Table 4.4.

**Table 4.4.** Calculation of the synthetic cost of AZO-III and AZO-IV HTMs, adapted from **Publication III**.

| Chemical name | Price of Chemical ($) | Weight or amount of reagent | Material cost ($) |
|---|---|---|---|
| Phenothiazine | 8.49/100g | 1.0g | 0.085 |
| S-ethyl phenothiazine | 30/100g | 1.0g | 0.30 |
| 4-fluorobenzaldehyde | 78/100g | 1.2g (compound 3) and 1.0g (compound 4) | 0.93 (compound 3) and 0.78 (compound 4) |
| Potassium phosphate | 84/500g | 5.3g (compound 3) and 5.0g (compound 4) | 0.89 (compound 3) and 0.84 (compound 4) |
| Ethyl acetate | 1.51/500mL | 500 ml (compound 3) and 500 ml (compound 4) | 1.51 for both 3 and 4 |
| DMF | 6.91/100mL | Comp. 3 (20 mL), Comp. 4 (20 mL) | 1.3 for both 3 and 4 |
| Petroleum ether | 0.94/500mL | Comp. 3 (1000 mL), Comp. 4 (1200 mL) | 1.88 (AZO-III) and 2.2 (AZO-IV) |
| Compound 2 | 2280/Kg | AZO-III (1.16) and AZO-IV (0.96) | 2.64 (AZO-III) and 2.1 (AZO-IV) |
| Total cost per gram | | | 9.23 $/gm (**AZO-III**) and 9.03 $/gm (**AZO-IV**) |

The costs of AZO-III and AZO-IV were decreased by reducing the number of synthetic steps and by improving the synthesis yield. This can be beneficial for large-scale production where cost is one of the important parameters. Furthermore, these materials were characterized and utilized as HTMs upon processing in a non-halogenated solvent (toluene).

### 4.2.1 Optical, electrochemical, computational properties, and hole-mobility of phenothiazine-based HTMs

The absorption spectra of AZO-I and AZO-II, measured in chloroform (concentration $10^{-5}$ M) as well as in solid-state (films spin-coated on glass), are presented in Figure 4.5a. AZO-I exhibited an absorption maximum at 422 nm in solution and 430 nm in solid-state. Similarly, AZO-II exhibited an absorption

maximum at 453 nm in solution and 460 nm in film. The red-shift in the absorption of AZO-II compared to AZO-I can be ascribed to the extended conjugation of AZO-II. The optical bandgaps of 2.3 (AZO-I) and 2.2 eV (AZO-II) were determined based on absorption onsets of 538 nm (AZO-I) and 555 nm (AZO-II) (Figure 4.5a).

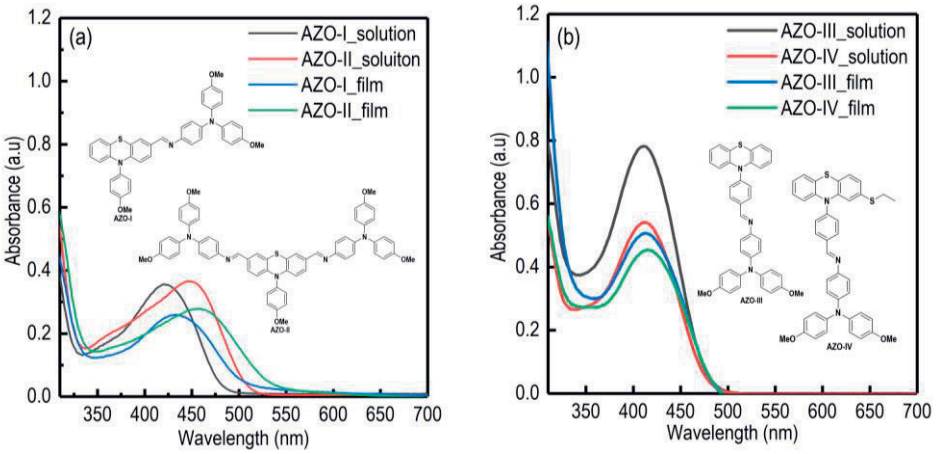


**Figure 4.5.** Absorption of AZO-I and AZO-II in chloroform (1 x $10^{-5}$ mol $L^{-1}$) and in solid-state (a) and absorption of AZO-III and AZO-IV in DCM (1 x $10^{-5}$ mol $L^{-1}$) and in solid-state (b), adapted from **Publication II and III**.

In the case of azomethine derivatives with aryl spacers (AZO-III and AZO-IV), the absorption was measured in DCM (concentration $10^{-5}$ M) as well as in solid-state (spin-coated films), as presented in Figure 4.5b. AZO-III and AZO-IV compounds exhibited absorption maxima at 409 and 412 nm in solution and 412 and 417 nm in solid-state, respectively. The slight red-shift in the absorption of AZO-IV compared to that of AZO-III can be attributed to the introduction of the thio-alkyl group to the phenothiazine chromophore.[214] Also, the slight red-shift in the solid-state absorption properties can be ascribed to the solid-state intermolecular interactions. The optical band-gaps, as determined from the absorption edges, are 2.47 and 2.46 eV for AZO-III and AZO-IV, respectively.

In order to elucidate the perovskite/HTM interactions, photoluminescence (PL) quenching of HTM on top of perovskite and time-resolved photoluminescence (TR-PL) decay analysis were carried out (Figure 4.6 and Table 4.5).

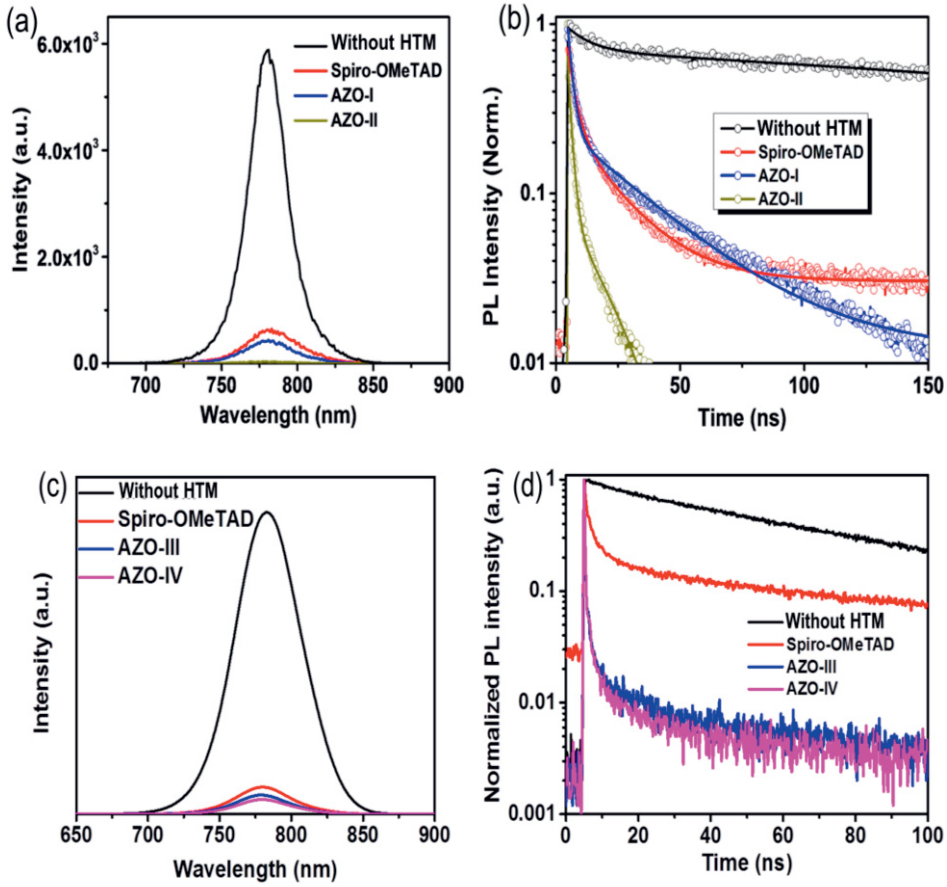


**Figure 4.6.** Steady-state emission spectrum of perovskite (without HTM) and quenching of perovskite emission when an HTM (Spiro-OMeTAD, AZO-I, AZO-II, AZO-III, or AZO-IV ) is deposited atop the perovskite (a & c). Time-resolved photoluminescence decays of perovskite films with and without HTMs on top (b & d), adapted from **Publication II and III**.

Firstly, the HTMs (AZO-I–IV) were deposited on the perovskite surface and steady-state PL was measured at the excitation wavelength of 510 nm with an excitation intensity of 5.8 W $cm^{-2}$. The emission intensity of the perovskite layer was quenched significantly (Figure 4.6a,c) especially in the case of AZO-II, more than in the cases of spiro-OMeTAD and AZO-I, suggesting an efficient hole extraction from perovskite when interfaced with AZO-II. The higher quenching efficiency of AZO-II compared to AZO-I could be attributed to its better film conductivity and enhanced charge transfer from perovskite to HTM (Figure 4.6a). Similarly, both AZO-III and AZO-IV significantly quenched the perovskite emission (Figure 4.6c). In particular, AZO-IV led to excellent quenching compared to AZO-III and

reference Spiro-OMeTAD when deposited on top of the perovskite films. The higher fluorescence quenching in the case of AZO-IV can be attributed to more effective perovskite/HTM interactions (especially the interaction of sulphur atom with $Pb^{+2}$)[78] due to the introduction of the additional thio-alkyl group to the phenothiazine chromophore.

**Table 4.5.** (a) TRPL decay fits of AZO-I, AZO-II, and Spiro-OMeTAD deposited on perovskite films, (b) fitted decay times of perovskite films deposited on AZO-III, AZO-IV, and Spiro-OMeTAD adapted from **Publication II and III**. [a]Effective lifetime, defined as I(t1/e) = I(0) / e, where I (t) is the PL intensity at t time.[196]

**(a)**

| PSCs | $A_1$ (%) | $\tau_1$/ns | $A_2$ (%) | $\tau_2$/ns | Average time/ns |
|---|---|---|---|---|---|
| Without HTL | 12 | 1.69 | 88 | 106.20 | 106.0 |
| Spiro-OMeTAD | 40 | 3.05 | 6.0 | 18.82 | 17.3 |
| AZO-I | 84 | 1.95 | 1.6 | 31.10 | 23.9 |
| AZO-II | 70 | 1.50 | 3.0 | 17.03 | 14.4 |

**(b)**

| PSCs | $A_1$ (%) | $t_1$ | $A_2$ (%) | $t_2$ | $t_{1/e}$[a] |
|---|---|---|---|---|---|
| Without HTL | 9.0 | 8.54 | 91.0 | 69.57 | 68.65 |
| Spiro-OMeTAD | 96.6 | 1.35 | 3.4 | 48.63 | 6.93 |
| AZO-III | 96.5 | 0.19 | 3.5 | 2.40 | 5.45 |
| AZO-IV | 95.8 | 0.22 | 4.2 | 2.59 | 5.23 |

The average carrier lifetimes showed faster decay of AZO-II (14.4 ns) compared to AZO-I (23.9 ns). This was attributed to the efficient hole extraction/transfer at the perovskite/HTM interface (Table 4.5a). The fast decay component ($\tau_1$) is originated from the quenching of charge carriers/excitons at the defects, and the slow decay component ($\tau_2$) is attributed to the radiative recombination lifetime of free charge carriers/excitons in the bulk. In the case of AZO-III and AZO-IV, the contribution factors ($A_1$) for the fast components are more than 95% (Table 4.5b), indicating the dominance of the fast component in the charge recombination dynamics. The hole injection yields of spiro-OMeTAD, AZO-III, and AZO-IV were calculated according to equation 3.7 as 86.0%, 96.0%, and 99.3% respectively, which are consistent with quenching efficiency variations shown in Figure 4.6c. The remarkably accelerated PL decay of AZO-III and IV compared to Spiro-OMeTAD indicates their improved hole-injection dynamics.

To evaluate the applicability of azomethine-based HTMs in perovskite solar cells, we investigated the natural bonding orbitals of AZO-I, AZO-II, AZO-III, and

AZO-IV by using DFT, as presented in Figure 4.7. DPV was used to obtain the experimental energy levels (HOMO, LUMO) of AZO-I–AZO-IV, as shown in Table 4.6. The electron density of the HOMO level in the case of all four molecules is mainly located over the electron-donor/rich and dimethoxytriarylamine moieties. The LUMO level is spread over the electron-withdrawing azomethine bridge and the phenothiazine core in the case of AZO-I and AZO-II, while in the case of AZO-III and AZO-IV, it is spread over the aryl π-spacer and azomethine units, respectively.[83,215]

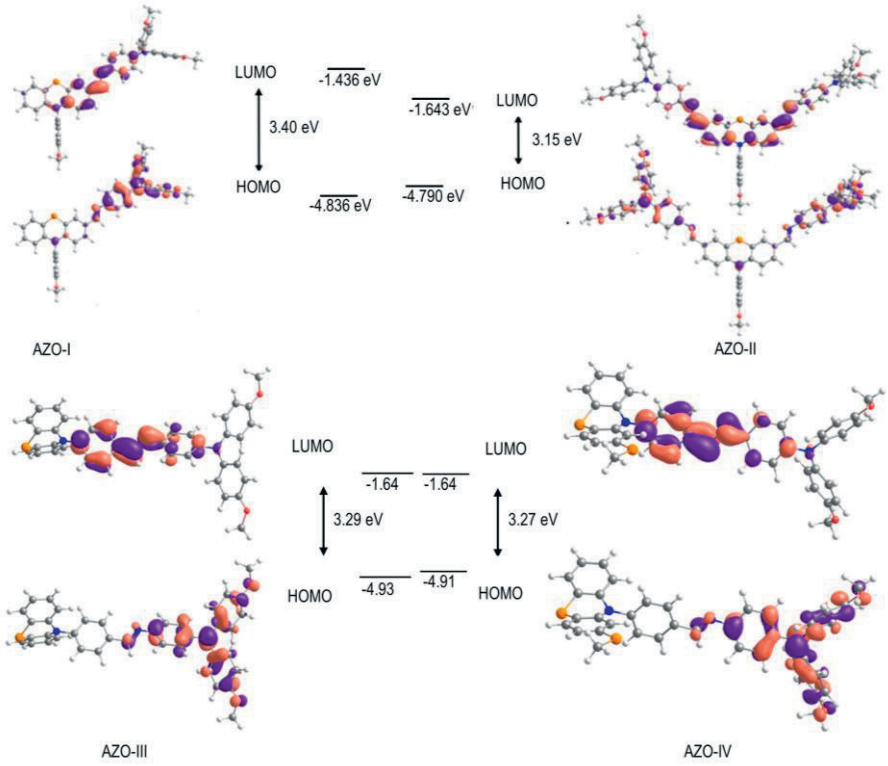


**Figure 4.7.** Energy levels and electron distribution for the frontier molecular orbitals of AZO-I and AZO-II in (a) and AZO-III and AZO-IV in (b) calculated with DFT at PBE1PBE/6-31G** level of theory (isosurface value = 0.04), adapted from **Publication II and III**.

The computed HOMO and LUMO energy levels of AZO-I are -4.84 and -1.44 eV and for AZO-II are -4.79 and -1.64 eV. The slightly higher HOMO energy level for AZO-II compared to AZO-I could be attributed to the extended conjugation in the case of AZO-II due to the introduction of di-substituted methoxytriarylamine. Additionally, AZO-I and II showed HOMO-LUMO energy

gap of 3.40 and 3.15 eV respectively. AZO-III and AZO-IV showed a slight difference in the experimental HOMO energy levels, i.e. -4.99 (AZO-III) and -4.97 eV (AZO-IV).

**Table 4.6.** HOMO[a], LUMO[a], and $E_g$[a] values based on the computational calculations. HOMO$^{DPV}$ values are determined from electrochemical measurements, LUMO$^{opt}$ is calculated from the optical gap ($E_g^{opt}$), and $E_g^{opt}$ is calculated from the onset of the absorption spectrum, adapted from **Publication II and III**.

| Compounds | HOMO (eV) [a] | LUMO (eV) [a] | $E_g$ (eV)[a] | HOMO$^{DPV}$ (eV) | LUMO$^{opt}$ (eV) | $E_g^{opt}$ (eV) |
|---|---|---|---|---|---|---|
| AZO-I | -4.83 | -1.43 | 3.40 | -4.84 | -1.44 | 2.30 |
| AZO-II | -4.79 | -1.64 | 3.15 | -4.79 | -1.64 | 2.20 |
| AZO-III | -4.93 | -1.64 | 3.29 | -4.97 | -2.50 | 2.47 |
| AZO-IV | -4.91 | -1.64 | 3.27 | -4.99 | -2.53 | 2.46 |

Both HTMs exhibited a similar trend in $E_g$ (2.47 and 2.46 eV for AZO-III and AZO-IV, respectively). The computed $E_g$ was 3.29 (AZO-III) and 3.27 eV (AZO-IV), again the computational results are overestimated by ca. 0.9-1.1 eV.[208]

The hole mobilities of AZO-I, AZO-II, and Spiro-OMeTAD (reported in **publication II**) were determined by using integral mode time-of-flight (TOF) method. The transient current (corrected for the steady-state dark current) results of all three compounds are depicted in Figure 4.8.[216] The hole-mobilities of AZO-I and AZO-II, obtained under identical experimental conditions, are $2 \times 10^{-6}$ cm$^2$ /(V s) and $2 \times 10^{-5}$ cm$^2$ /(V s), respectively.

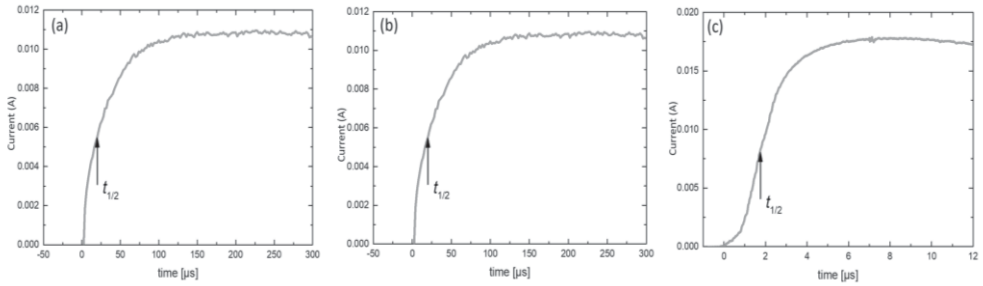


**Figure 4.8**. TOF transient for an AZO-I (a), AZO-II (b), and Spiro-OMeTAD (c) pristine devices, adapted from **Publication II**.

The one order of magnitude higher mobility of AZO-II compared to that of AZO-I can be attributed to the introduction of two electron-donating dimethoxy substituted triarylamine groups in the 3,7-positions of the phenothiazine core.

Under the same experimental conditions, the reference device based on Spiro-OMeTAD exhibited hole mobility of $6 \times 10^{-5}$ $cm^2$ /(V s) higher than both AZO-I and AZO-II.

### 4.2.2 Perovskite solar cells characterization and stability of phenothiazine-core HTMs

In this Section, the most important results regarding the influence of the newly designed low-cost phenothiazine-core hole-transporting materials on the performance and stability of perovskite solar cells are discussed. All the obtained results are reported in **Publications II** and **III**.

To investigate the performance of AZO-I or AZO-II as HTMs in PSCs, devices employing a mixed cation perovskite ($Cs_{0.05}MA_{1-y}FA_yPbI_{3-x}Cl_x$) were constructed. The sample structure was ITO/$SnO_2$/ $Cs_{0.05}MA_{1-y}FA_yPbI_{3-x}Cl_x$/HTM/Au. Both AZO-I, AZO-II, and the reference Spiro-OMeTAD were initially all employed as dopant-free HTMs in PSCs. These devices produced open-circuit voltages ($V_{oc}$) of 0.92, 0.65, and 0.62 V, short-circuit current densities ($J_{sc}$) of 16.07, 7.87, and 8.96 mA $cm^{-2}$, fill factors (FF) of 25, 38, and 45%, and PCEs of 3.83%, 2.03%, and 2.50%, respectively. In PSCs, due to their poor performance without dopants, the HTMs were doped with the conventional Li- and Co-based additives. The J−V curves of the PSCs including one of the two HTMs or the reference Spiro-OMeTAD in doped conditions, were recorded under simulated illumination (AM 1.5 G, 100 mW $cm^{-2}$), as presented in Figure 4.9a. The photovoltaic parameters are summarized in Table 4.7.

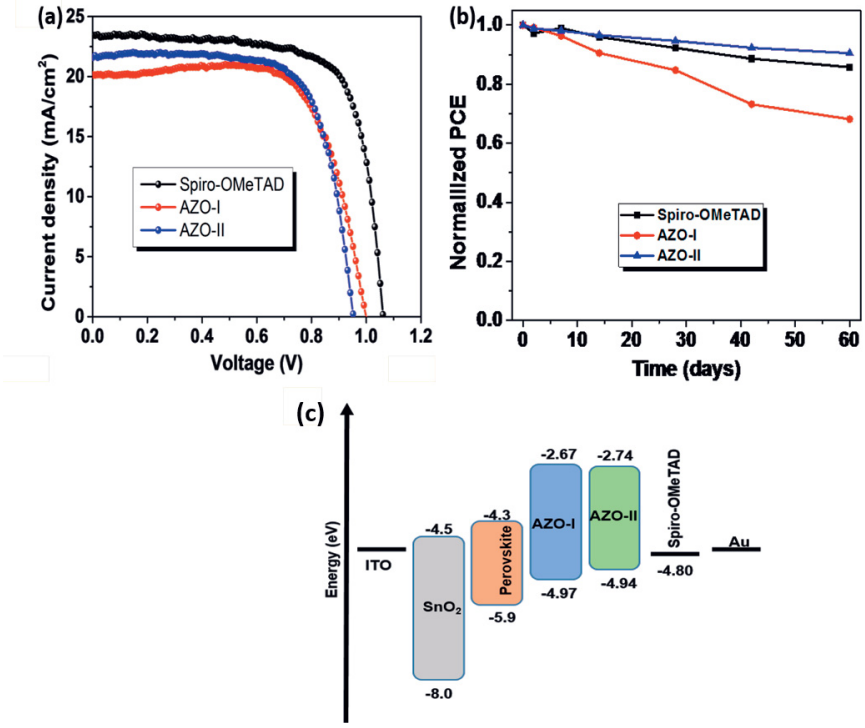


**Figure 4.9.** (a) J–V curves of the perovskite solar cells (reverse scans) measured with a scan rate of 10 mV/s under AM 1.5 G simulated solar light illumination. The device employed Spiro-OMeTAD, AZO-I, or AZO-II as HTMs. (b) Long-time stability of the devices. (c) Energy level diagram for AZO-I, AZO-II, and Spiro-OMeTAD, determined experimentally by DPV and absorption measurements. In addition, the energy levels of the other PSC constituents (values from literature), are reported. Picture adapted from **Publication II**.

The PSC devices based on AZO-I, AZO-II, and Spiro-OMeTAD produced $J_{sc}$ of 20.1, 21.6, and 23.4 mA cm$^{-2}$, $V_{oc}$ of 1.00, 0.95, and 1.04 V, FFs of 0.66, 0.71, and 0.74, and PCEs of 12.6%, 14.0%, and 18.1%, respectively (Table 4.7). The PCEs of champion devices based on AZO-I and AZO-II HTMs were 14.3% and 15.6%, respectively. The lower performance of AZO-I compared to the other two HTMs can be ascribed to its lower hole mobility in the undoped form ($2 \times 10^{-6}$ cm$^2$ V$^{-1}$ s$^{-1}$) compared to those of AZO-II ($2 \times 10^{-5}$ cm$^2$ V$^{-1}$ s$^{-1}$) and Spiro-OMeTAD ($6 \times 10^{-5}$ cm$^2$ V$^{-1}$ s$^{-1}$).[217] The lower PCE of AZO-II compared to Spiro-OMeTAD is due to its lower $J_{sc}$ and hole mobility compared to Spiro-OMeTAD (Figure 4.8c and Table 4.7).[218] These results showed a similar trend to that of the earlier mentioned results in dopant-free conditions.

**Table 4.7**. Photovoltaic Parameters Obtained from J−V Curves Based on Different HTMs.[II]

| HTMs | Jsc (mA/cm2) | Voc (V) | FF (%) | PCE (%) | PCEmax (%) |
|---|---|---|---|---|---|
| AZO-I | 20.1 | 1.00 | 66 | 12.6 | 14.3 |
| AZO-II | 21.6 | 0.95 | 71 | 14.0 | 15.6 |
| Spiro-OMeTAD | 23.4 | 1.04 | 74 | 18.1 | 19.3 |

For both the HTMs the $V_{oc}$ values are smaller than that for spiro-OMeTAD-based devices, which may be caused due by their thinner films compared to Spiro-OMeTADY (films spin-coated from a 10 mg/ml chlorobenzene solution in case of AZO-I and AZO-II and 72.5 mg/ml for Spiro-OMeTAD). In fact, earlier studies showed that thinner films result into incomplete coverage of the substrate (ITO), leading to the direct contact with the perovskite layer, in turn causing interface recombination and reduction in $V_{oc}$.[219] It is worth noting that the correlation between the energy levels of HTMs in presence of additives and the charge-recombination (and its implications on $V_{oc}$) is still topic of debate and needs further understanding.[220–222] The higher $J_{sc}$ and FFs of AZO-II-based devices compared to AZO-I can be ascribed to the higher hole mobility of AZO-II, which is responsible for efficient charge extraction and hole transporting.

The unencapsulated devices were under ~30% RH to study their stability over time, as shown in Figure 4.9b. After 60 days, the devices based on AZO-II retained 91% of their initial PCE, while those employing spiro-OMeTAD and AZO-I retained 86% and 68%, respectively. The stability results showed that AZO-II, or more generally the materials design concept combining phenothiazine core and azomethine bridging, is promising for fabricating low-cost and high-performance HTMs for PSCs.

Keeping the long-term goal of making environmentally friendly PSCs in mind, AZO-III and AZO-IV were designed and investigated in mixed halide perovskite devices with structure ITO/$SnO_2$/ $Cs_{0.05}MA_{1-y}FA_yPbI_3$−$xCl_x$/HTM/Au. Initially, halogenated solvent processed devices were fabricated and the best performing device data presented in Table 4.8. In dopant-free conditions, both HTMs exhibited higher performance (AZO-III = 5.76% and AZO-IV = 10.91%) compared to reference Spiro-OMeTAD (3.31%)-based devices. In particular, the three times higher performance of AZO-IV compared to Spiro-OMeTAD can be ascribed to its good solubility, better HTM/perovskite interactions, and well-aligned energy levels (Table 4.8). The higher $J_{sc}$ and FF of AZO-IV compared to that of AZO-III

and Spiro-OMeTAD can be attributed to its efficient charge extraction, which in turn relates due to the effective perovskite/AZO-IV interactions demonstrated by the significant quenching of perovskite emission in Figure 4.6c.

**Table 4.8.** Photovoltaic parameters obtained from J–V curves based on different HTMs processed with chlorobenzene without dopants with a concentration of 10 mg/ml, **Publication III**.

| HTMs | $J_{sc}$ (mA/cm$^2$) | $V_{oc}$ (V) | FF (%) | $PCE_{max}$ (%) |
|---|---|---|---|---|
| Spiro-OMeTAD | 16.01 | 0.90 | 23 | 3.31 |
| AZO-III | 13.50 | 0.84 | 50 | 7.68 |
| AZO-IV | 18.75 | 0.97 | 60 | 10.91 |

Similar PSCs were fabricated by using non-halogenated solvents for AZO-III/AZO-IV processing and without additional dopants. However, unfortunately, all the devices exhibited a mediocre performance because of the poor film quality observed even by naked eyes. Thus, to improve the performance, the HTMs processed by a non-halogenated solvent (toluene, concentration 10 mg/ml) were doped (Li-TFSi, FK209, and t-BP). The J–V characteristics of champion PSCs (reverse scans) are presented in Figure 4.10. The photovoltaic parameters of the champion device, as well as the averaged photovoltaic parameters from 20 independent devices, are summarized in Table 4.9. The very low standard deviations demonstrate the high reproducibility of these experiments.

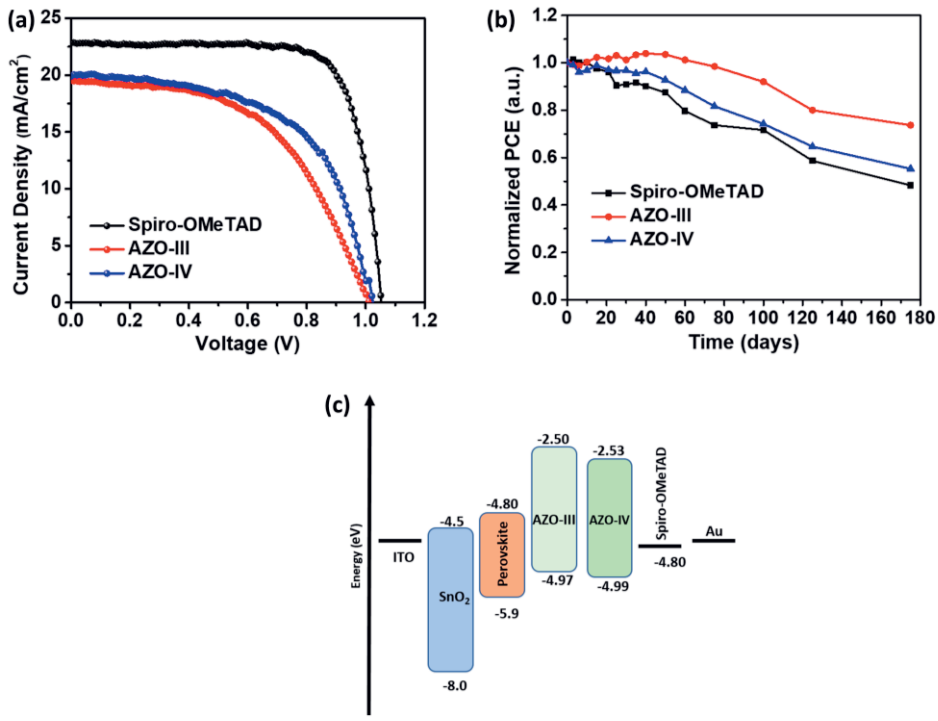


**Figure 4.10.** (a) J–V curves for perovskite solar cells (reverse scans) measured with a scan rate of 10 mV/s under AM 1.5G simulated solar light illumination by using Spiro-OMeTAD, AZO-III, and AZO-IV as HTMs. (b) Long-time stability of the devices based on Spiro-OMeTAD, AZO-III, and AZO-IV as HTM. (c) Energy level diagram, as determined experimentally with DPV, for the HTMs used in PSC devices in this work, adapted from **Publication III**.

The champion PSCs based on AZO-III and AZO-IV exhibited short-circuit current densities ($J_{sc}$) of 19.75 mA cm$^{-2}$ and 19.83 mA cm$^{-2}$, respectively. Both HTMs showed the same $V_{oc}$ of 1.01 V and the resulting PCE was 9.77% and 11.62% for AZO-III and AZO-IV cells, respectively. The reference Spiro-OMeTAD films were made by using an optimized concentration of 72.5 mg/ml in chlorobenzene since its solubility in toluene is modest.[7,78] The corresponding devices based on Spiro-OMeTAD exhibited a PCE of 18.63%. The lower performance of AZO derivatives compared to Spiro-OMeTAD was mainly caused by lower FF and $J_{sc}$, since both newly made HTMs showed higher hole injection yields compared to spiro-OMeTAD. The lower $J_{sc}$ can be ascribed to poor charge transfer, probably due to low hole-mobility, which has been reported in case of similar phenothiazine core azomethine (AZO-I) in earlier studies. To investigate the reason behind the lower FF of AZO derivatives, we extracted shunt ($R_{sh}$) and series ($R_s$) resistance of the devices using 1-diode model from the J–V curves of the backward scan (Table

4.9). The reference device displayed the lowest $R_s$ and the highest $R_{sh}$, hence showed higher FF compared to AZO-III and AZO-IV.

**Table 4.9**. Photovoltaic parameters of the champion devices obtained from J - V curves based on different HTMs. The averaged parameters are also reported together with the standard deviations, adapted from **Publication III.**

| HTMs | | $J_{sc}$(mA/cm$^2$) | $V_{oc}$(V) | FF(%) | $PCE_{max}$ (%) | Rs (Ω·cm2) | Rsh (kΩ·cm$^2$) |
|---|---|---|---|---|---|---|---|
| AZO-III | champion | 19.75 | 1.01 | 49 | 9.77 | 15.63 | 0.68 |
| | average | 18.98± 0.81 | 1.01± 0.01 | 0.46± 0.02 | 8.75± 0.72 | 15.75± 0.12 | 0.65± 0.08 |
| AZO-IV | champion | 19.83 | 1.01 | 58 | 11.62 | 5.23 | 0.74 |
| | average | 18.09± 1.62 | 1.01± 0.01 | 55± 0.04 | 10.04± 0.87 | 5.32± 0.09 | 0.69± 0.11 |
| Spiro-OMeTAD | champion | 22.69 | 1.08 | 76 | 18.63 | 3.95 | 4.42 |
| | average | 22.78± 0.34 | 1.06± 0.01 | 0.76± 0.01 | 18.38± 0.14 | 3.98± 0.03 | 4.37± 0.04 |

To understand the stability of the above-mentioned PSC devices, we kept 20 unencapsulated cells employing reference Spiro-OMeTAD, AZO-III, and AZO-IV in air with a relative humidity of 30% for 6 months (Figure 4.10b). After the initial two months, the PCE of AZO-III was unchanged and outperformed the previously made AZO-I and AZO-II (that retained 68 and 91% of the initial PCE, respectively). After 6 months, the AZO-III based devices showed the highest stability and maintained 75% of their initial performance compared to AZO-IV (56%) and Sprio-OMeTAD (48%). Furthermore, the water contact angle (CA) of the HTMs was measured (Figure 4.11) to get further insight on the hydrophobicity, since this plays a key role in protecting perovskite against moisture. Both AZO-III (86.6°) and AZO-IV (92°) films exhibited higher CAs compared to Spiro-OMeTAD (77.3°), showing a highly hydrophobic nature.

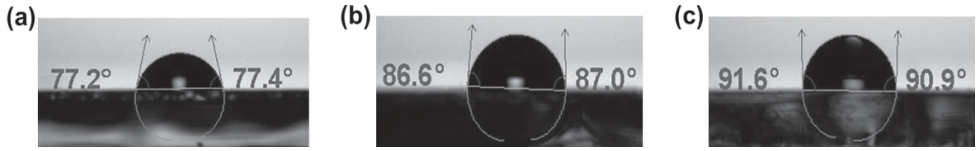


**Figure 4.11.** The water contact angles (CA) of a) Spiro-OMeTAD_CAaverage = 77.3°, b) AZO-III_CAaverage = 86.6°, and c) AZO-IV_CAaverage = 92.0°, adapted from **Publication III**.

Though AZO-IV exhibited higher CA compared to AZO-III, its lower stability can be explained by the rapid oxidative degradation in the presence of p-type

dopants. This is in turn caused by the strong charge localization in the radical cation state of AZO-IV (compared to AZO-III) due to additional thioalkyl substitution in 2-position, as shown in earlier reports. [126,223] Thus, despite the lower performance of doped AZO-IV (11.62%) cells compared to Spiro-OMeTAD-based reference device (18.63%), the significantly lower cost, good stability, and the environmentally friendly synthesis and processing make AZO-IV a rather competitive HTM.

## 4.3 Synthesis of pyrene-core HTMs

As mentioned earlier, due to their low-cost, good stability, easy availability, and freedom of functionalization, pyrene-core molecules have been utilized in a range of organic electronic devices such as transistors, light-emitting diodes, and solar cells.[136] Motivated by this, we synthesized a low-cost, pyrene-based, and fluorine-substituted HTM (L-F) and compared its performance with a non-fluorinated pyrene derivative (**Publication IV**).

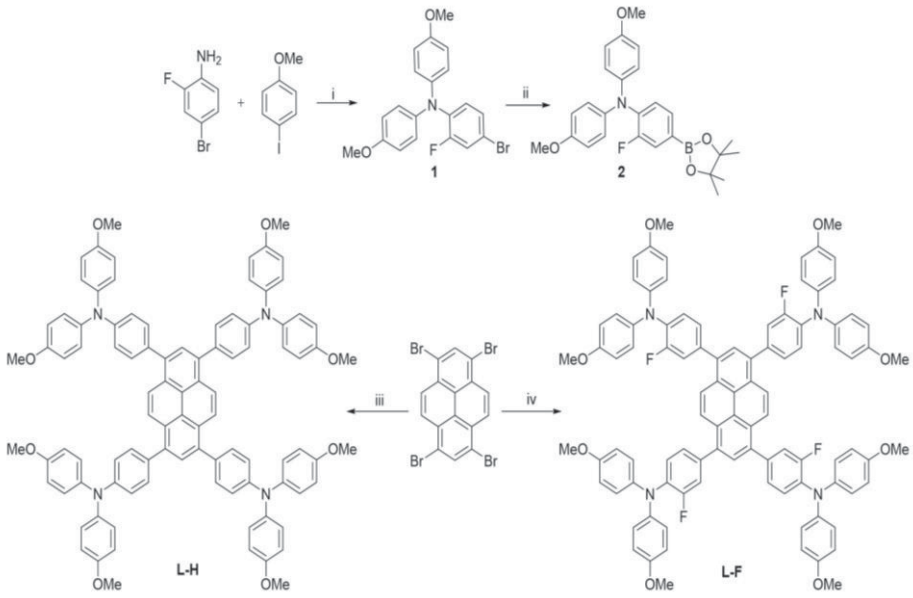


**Scheme 4.4.** Synthesis route for the pyrene-based hole-transporting materials L-H and L-F. Reagents: i) CuI, 1, 10-Phenanthroline, KOH, Toluene, reflux, 48 hr, 80%. ii) Bis(pinacolato)diboron, potassium acetate, $PdCl_2$(dppf), 1,4-dioxane, reflux, 12 hr, 78%. iii) 4-methoxy-N-(4-methoxyphenyl)-N-(4-(4,4,5,5-tetramethyl-1,3,2-dioxaborolan-2-yl) phenyl) aniline), $Pd(PPh_3)_4$, 2M $K_2CO_3$, toluene:THF (30:70), reflux, 12 hr, 75%. (iv) 2-fluoro-N,N-bis(4-methoxyphenyl)-4-(4,4,5,5-tetramethyl-1,3,2-dioxaborolan-2-yl)aniline, $Pd(PPh_3)_4$, 2M $K_2CO_3$, toluene:THF (30:70), reflux, 12 hr, 71%, adapted from **Publication IV**.

The synthesis of both the pyrene-core HTMs is shown in Scheme 4.4. L-H was prepared by Suzuki-coupling of the previously reported 4-methoxy-N-(4-methoxyphenyl)-N-(4-(4,4,5,5-tetramethyl-1,3,2-dioxaborolan-2-yl) phenyl)aniline (L)[218] and the commercially available tetra-bromo-pyrene with good synthesis yield (73%). L-F was made by first synthesizing a fluoro-substituted triarylamine (4-bromo-2-fluoro-N,N-bis(4-methoxyphenyl)aniline) (1) via Ullman coupling of commercially available precursors, namely 4-bromo-2-fluoroaniline and 1-iodo-4-methoxybenzene, in very good yield (80%). Furthermore, Miyaura borylation of 1 afforded its boronic ester 2-fluoro-N,N-bis(4-methoxyphenyl)-4-(4,4,5,5-tetramethyl-1,3,2-dioxaborolan-2-yl)aniline (2) with good yield (78%). Finally, 2 reacted with tetrabromopyrene via a Suzuki-coupling reaction giving L-F with good yield (71%). The synthesis cost of pyrene-core derivatives is calculated based on earlier reports, as presented in Table 4.10.

**Table 4.10**. Calculation of the synthetic cost of L-H and L-F HTMs, adapted from **Publication IV**.

| Chemical name | Weight reagent (g/g) | Weight solvent (mL) | Weight workup (g/g) | Price of chemical (US$/kg) | Chemical cost (US$/g product) | Cost per step (US$/step) |
|---|---|---|---|---|---|---|
| 4-iodoanisole | 4.0/ 2.8 | | | 389 | 1.59 | |
| 4-bromoaniline or 4-bromo-2-fluoroaniline | 1.0 | | | 195/213 | 0.20/0.213 | |
| 1,10-phenanthroline | 0.04/0.189 | | | 326 | 0.01/0.06 | |
| Copper Iodide | 0.02/0.20 | | | 230 | 0.004/0.04 | |
| Potassium hydroxide | 2.61/2.2 | | | 4.9 | 0.012/0.010 | |
| Toluene | | 20/25 | | 3.7 | 0.074/0.092 | |
| Dichloromethane | | | 200 | 2.6 | 0.52 | |
| Sodium sulphate | | | 0.5 | 2.6 | 0.0013 | |
| Hexane | | | 1000 | 3.5 | 3.5 | |
| Silica gel | | | 100 | 5.4 | 0.54 | |
| Ethyl acetate | | | 200 | 2 | 0.40 | 1st step |
| Product_bromoamine/ 1 | | | | | | 6.85 (1.50 g)/ 7.96 (1.70 g) |
| Bromoamine or 1 used in 2nd step | 2.00/2.00 | | | | 9.13/9.36 | |
| Product step 2 (triarylamine of LH or LF) | | | | | | 15.62 (1.76 g) / 15.05 (1.73 g) |
| Triarylamine used in LH or LF | 0.832/0.866 | | | | 7.38/7.53 | |
| Product L-H or L-F | | | | | | L-H, 12.52 (0.410 g) = 30.53 US$/g and L-F, 12.68 (0.408 g) = 31.07 US$/g |

The synthesized molecules L-H and L-F have good solubility (20mg/ml) in common organic solvents (e.g. THF, dichloromethane), and all the intermediates, as well as the final compounds, were characterized by using $^{1}$H NMR, $^{13}$C NMR,

and mass spectroscopies. L-H and L-F were further employed as HTMs in perovskite solar cells.

### 4.3.1 Optical, electrochemical, computational properties and hole-mobility of pyrene-core HTMs

Absorption and emission of both L-H and L-F were measured in chloroform solution (concentration $10^{-5}$ M) and are presented in Figure 4.12. Both materials exhibited absorption maxima between 415–418 nm corresponding to π-π* transition. The red-shift in absorption around 80 nm compared to pristine pyrene (338 nm) is attributed to the extended conjugation.[224] The band at 370–372 nm is attributed to the n-π* transition and the band at 300 nm to the π-π* transition of the triphenylamine moieties.[225]

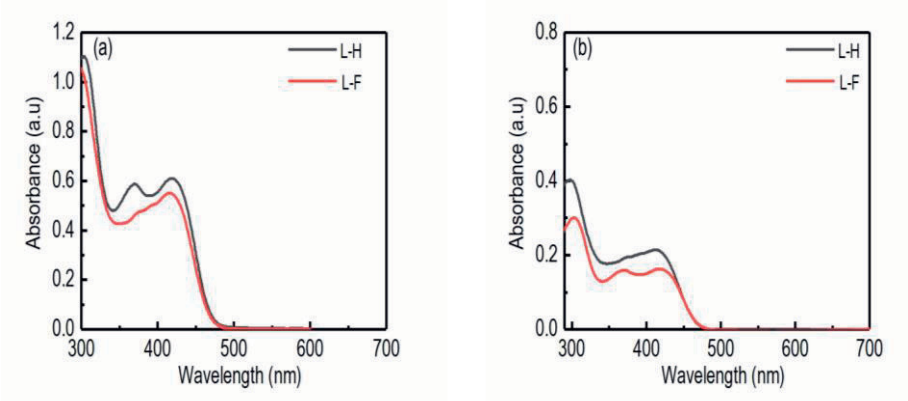


**Figure 4.12.** Absorbance spectra of L-H and L-F in a9 chloroform ( $10^{-5}$ M), and b) in the solid state (spin-coated films), adapted from **Publication IV**.

In addition, L-H and L-F showed emission maxima at 500 and 539 nm, respectively and red-shift in the emission by 107 and 146 nm as compared to pristine pyrene (393 nm).[226] The solid-state emission of L-H and L-F was red-shifted by 30 and 17 nm compared to solution due to the more pronounced intermolecular interactions in the solid-state.[227] Finally, $E_g$ for L-H (2.71 eV) and L-F (2.66 eV) was determined from the intersection of the normalized absorption and emission spectra in solution.

The experimental energy levels were determined by using photoelectron spectroscopy in air (PESA) (Figure 4.13a) by spin-coating the materials on ITO-coated glass. The sample is scanned with a range of energies (4.4–6.4 eV), the photogenerated electrons are detected at the anode and correlated to the photoelectron yield of the sample.

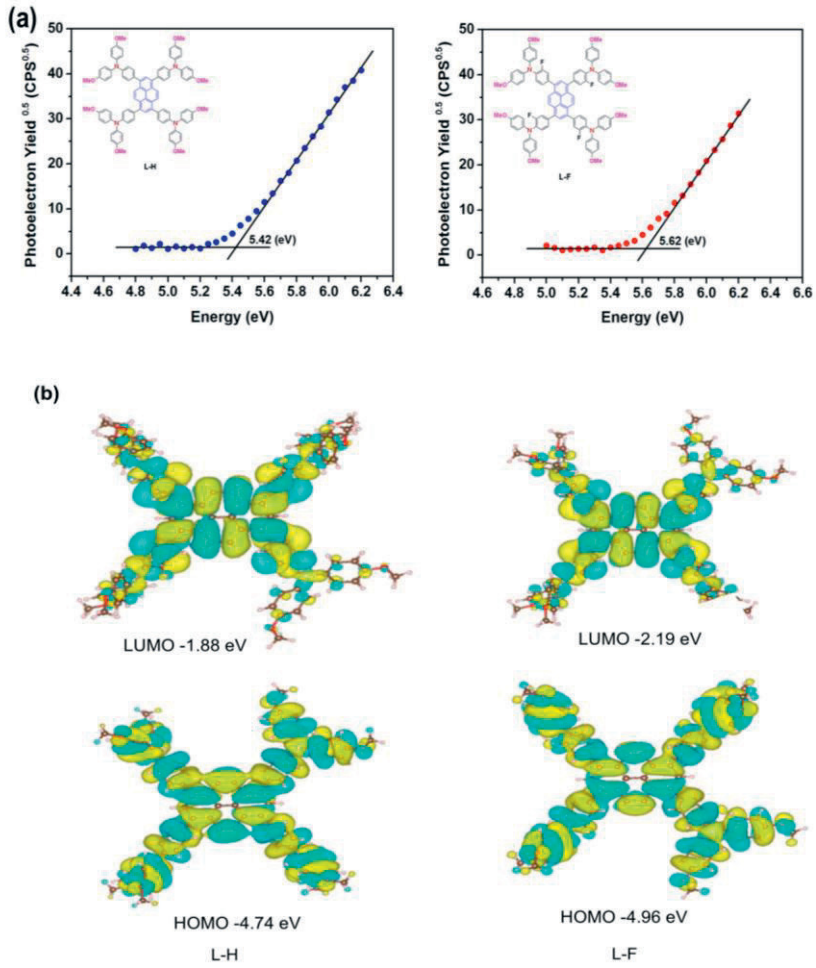


**Figure 4.13**. (a) Photoelectron spectroscopy in air (PESA) analysis of L-H and L-F thin films. (b) Energy levels and electron distribution for the frontier molecular orbitals of L-H and L-F were calculated with DFT at B3LYP/LANL2DZ level with a polarizable continuum model (PCM) model of the chloroform solvent, adapted from **Publication IV**.

The HOMO level was determined by taking the slope of the applied UV-energy versus the photoelectron yield.[228] HOMO values for L-H and L-F are -5.42 and -5.62 eV, respectively. The corresponding LUMO values, determined from the difference between the optical band gaps and the HOMO values, are -2.71 eV for

L-H and -2.96 eV for L-F. The deeper HOMO level of L-F can be attributed to the inductive electron-withdrawing character of the meta-fluorine, which is in good agreement with the red-shifted absorption and emission spectra.

On the other hand, the computational energy levels obtained by DFT are presented in Figure 4.13b. In both cases, the electron distribution of the HOMO level is mainly delocalized over the whole molecular system. The LUMO is delocalized over the central pyrene and partially on the triarylamine units. The computed HOMO/LUMO energy levels are -4.74/-1.88 eV for L-H and -4.96/-2.19 eV for L-F and the corresponding bandgaps are 2.86 eV(L-H) and 2.77 eV(L-F). Both experimental and computational levels and bandgaps showed a similar trend. The lower HOMO/LUMO levels of L-F as compared to L-H are due to the inductive electron-withdrawing behavior of the fluorinated core.

The hole mobility of pyrene-based hole-transporting materials reported in article IV (L-H and L-F), as well as reference PTAA, were measured by using charge extraction by linearly increasing voltage (Photo-CELIV)[229] method. The Photo-CELIV curves of all the compounds are presented in Figure 4.12.

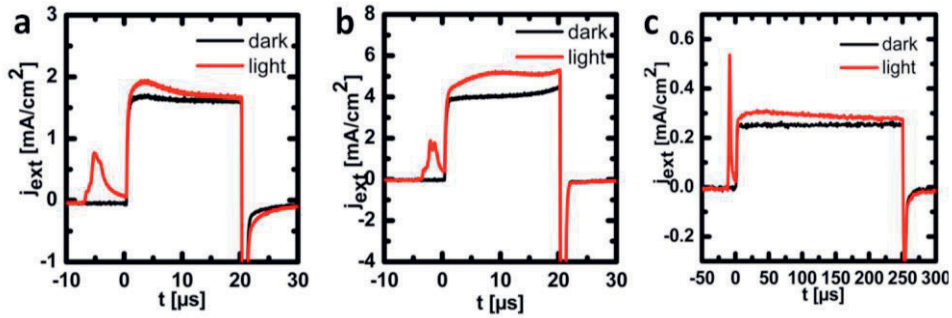


**Figure 4.14.** Photo-CELIV curves for L-H (a), L-F (b), and PTAA (c), adapted from **Publication IV**.

The obtained hole-mobilities of L-H, L-F, and reference PTAA are 1.9 x $10^{-4}$, 7.0 x $10^{-6}$, and 8.1 x $10^{-6}$ cm$^2$/(V s), respectively. The two orders of magnitude lower hole mobility of L-F compared to L-H can be attributed to the presence of electron-withdrawing fluorine atoms that increase the ionization potential and the electron affinity, thus reducing the hole mobility.[230,231] Additionally, the poor hole mobility of PTAA is attributed to the photodegradation behavior. Hence, PTAA requires the addition of external dopants to improve its hole mobility.[232]

### 4.3.2 Solar cell fabrication and characterization of pyrene-core HTMs

The aim behind the design of pyrene-based HTMs was to enhance the performance of dopant-free PSCs by employing fluorination strategy keeping low-cost synthesis approach. To investigate the performance of pyrene-based HTMs, low-cost and undoped L-H and L-F (~30$/g) were employed in mixed perovskite ($Cs_{0.1}FA_{0.75}MA_{0.15}Pb(Br_{0.5}I_{0.5})_3$ devices with ITO/HTM/perovskite/PCBM/BCP /Ag configuration (Figure 4.15a).

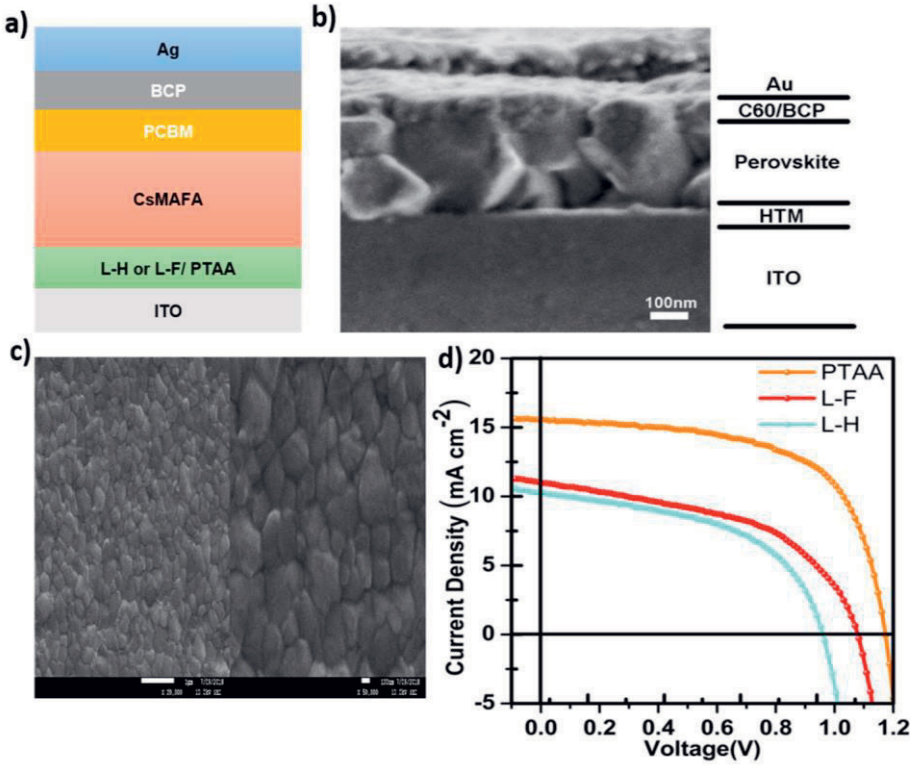


**Figure 4.15.** (a) Perovskite solar cells structure; (b) SEM cross-section image showing the different composition layers; (c) SEM images showing the morphology of perovskite layers at 1µm and 100 nm scales, and (d) J–V curves of mixed perovskite (CsMAFA) solar cells based on the various dopant-free hole-transportingmaterials, adapted from **Publication IV**.

The well-known and extremely pricey polymeric HTM, PTAA (2238 $/g), was used to build a reference device. The scanning electron microscopy cross-section image in Figure 4.15b illustrates the layer structure of the investigated PSCs, while the morphology of perovskite thin films is shown in Figure 4.15c. The J–V

characteristics, measured under simulated sunlight, are presented in Figure 4.15d and Table 4.11. The champion devices, using L-H or LF as dopant-free HTMs, exhibited a $V_{oc}$ of 0.87 and 1.07 V, a $J_{sc}$ of 10.25 and 10.98 mA/cm$^2$, and PCE of 5.03 and 5.93% for L-H and L-F, respectively. The higher $V_{oc}$ of L-F cell compared to that including L-H can be attributed to its lower HOMO energy level tuned by the introduction of the electron-withdrawing fluoro-substituted triarylamine.[233]

**Table 4.11**. Photovoltaic parameters obtained from J−V curves of PSCs based on different HTMs.[III]

| HTMs | $J_{sc}$ (mA/cm$^2$) | $V_{oc}$ (V) | FF (%) | PCE (%) |
|---|---|---|---|---|
| L-H | 10.25 | 0.879 | 55.7 | 5.03 |
| L-F | 10.98 | 1.074 | 50.3 | 5.93 |
| PTAA | 15.57 | 1.179 | 61.8 | 11.35 |

Under similar conditions, the reference polymeric PTAA-based PSC exhibited a $V_{oc}$ of 1.17 V, a $J_{sc}$ of 15.57 mA/cm$^2$, and PCE of 11.35%. Even though the performance of pyrene-based solar cells is lower compared to that of PTAA devices, their low-cost renders them competitive to the costly HTMs, at least for indoor applications (e.g. Internet-of-Things sensors) where a high PCE is not the main requirement. Our study showed that fluorination is a useful tool to achieve dopant-free and low-cost HTMs.

# 5 CONCLUSIONS AND FUTURE OUTLOOK

The main results of this Thesis are summarized as follows:

In **Publication I**, the molecular design and synthesis, and the spectroscopic, electrochemical, and bulk hole mobility properties of a series of phenothiazine derivatives with electron-accepting and electron-donating functionalities at C(7)/C(3) positions were studied. Suzuki and Ullman coupling reactions were optimized and carried out using corresponding boronic ester and organohalide derivatives with excellent synthetic yields. Finally, the condensation reactions of aldehydes and malononitrile were carried out to achieve donor-acceptor phenothiazine compounds. From the optical characterization, a red-shift in the absorption was observed upon the introduction of electron-donating substituents at C(7) position. Moreover, the electron-donating group slightly reduces the optical bandgap, resulting in the HOMO energy levels being raised, while the LUMO levels were mostly unaffected. The bulk hole mobility was significantly enhanced in the case of O-1 due to the higher crystallinity in the films.

In **Publication II** and **III**, the phenothiazine core was further modified by introducing azomethine functionality to achieve environmentally friendly and low-cost HTMs (AZO-I, -II, -III, and IV) for PSCs. All the azomethine-based HTMs were synthesized by using non-halogenated solvents, low-cost precursors, and simple condensation of an aldehyde with arylamine in high synthesis yields. After the investigation of optical, electrochemical, and hole mobility properties, the quenching of perovskite photoluminescence at the perovskite/HTM interface was studied. These experiments showed an efficient charge-transfer for all the azomethine compounds that were further employed as HTMs in PSCs. Firstly the performance, as well as the lifetime, of the devices including doped AZO-I and AZO-II processed with chlorobenzene were compared with the reference Spiro-OMeTAD cell. In the case of AZO-I and AZO-II the PCE improved from 12.6 (AZO-I) to 14% (AZO-II) and the ehnanced performance was correlated to the higher hole mobility and better-aligned HOMO level of AZO-II. The stability of the unencapsulated devices was studied over 2 months. Despite a small loss in the PCE of AZO-II compared to reference cell (18.1%), it exhibited excellent stability

(90% of the initial PCE retained after 60 days), as well as the lower cost (12 $/g) compared to Spiro-OMeTAD (91 $/g). In **Publication III**, the azomethine core was modified, with an aryl bridge introduced in AZO-III and AZO-IV, to ensure halogen-free solvent processing for the HTMs. When AZO-III and AZO-IV were spin-coated from a chlorobenzene (halogenated solvent) solution, the corresponding PSCs employing undoped AZO-III and AZO-IV exhibited an excellent PCE of 7.68 and 10.98% compared to that of the reference Spiro-OMeTAD device (3.31%). When the HTMs were processed in non-halogenated solvents (toluene) and doped, AZO-IV exhibited a higher PCE of 11.62% compared to AZO-III (9.77%), whereas the reference (Spiro-OMeTAD) cell showed a PCE of 18.63%. Even though in this case the PCEs of the AZO-based devices are lower compared to the reference, the very good stability (75% of the initial PCE is retained after 6 months), the simple synthesis, and very low-cost (~9 $/g) makes AZO-III remarkably competitive to the commercial Spiro-OMeTAD. Therefore these azomethines with eco-friendly synthesis hold great potential for the development of HTMs with minimal environmental impact.

In **Publication IV**, to achieve solution processability, high hole mobility, well-aligned energy HOMO levels, and low-cost, two pyrene-based HTMs, namely L-H and L-F, were synthesized by Suzuki-coupling reactions. The optical, electrochemical, and electrical properties of L-H were tuned via fluorination. When these materials were employed as dopant-free HTMs in mixed perovskite devices, L-F exhibited a higher PCE than L-H (5.93% and 5.03% for L-F and L-H, respectively). Further molecular and device engineering of fluorinated pyrene-based semiconductors is a plausible route towards future dopant-free HTMs for PSCs.

The results reported in this Thesis provide a step forward in the realization of low-cost, high-performing, and environmentally friendly perovskite solar cells. PSCs have a wide range of applications due to their solution processability that allows their deposition also on flexible substrates, the low-cost, and the excellent power conversion efficiency. Nevertheless, there are still some open issues left that have to be addressed, e.g. the significant degradation of PSCs under ambient conditions, the replacement of toxic lead in the perovskite composition, the device fabrication in air, and the environmental impact of each constituent of the solar cells. The highest PCE presented in this work is 14.0 % for the ITO/$SnO_2$/ $Cs_{0.05}MA_{1-y}FA_yPbI_3{-}xCl_x$/HTM/Au structure with doped AZO-II HTM. This device retained 91 % of the initial PCE after 2 months of storage in air, as discussed in **Publication II**.

The main drawbacks of spiro-OMeTAD-based PSCs are *i)* this HTM is highly expensive with a raw-material price of 91.62 $/g because of the complex synthesis and purification steps involved; *ii)* low-performance without external dopants due to its poor hole mobility and conductivity; *iii)* reduced long-term stability, mostly due to the presence hygroscopic dopants. Several key design rules can be employed to improve the stability of PSCs via molecular engineering, such as *i)* fluorination of HTMs to provide hydrophobic protection to perovskite surface, *ii)* non-covalently interacting HTMs to address defects and passivation of PSCs, *iii)* introduction of a functional interlayer between HTM/perovskite and ETM/perovskite surfaces, *iv)* thermally cross-linkable small molecules, as well as polymers, designed by using siloxane chemistry or simple acrylate functionalization, *v)* thermally stable polyazomethines, polyimides, and polyamides-based donor-acceptor ETMs or HTMs synthesized by simple condensation chemistry, and *vi)* self-assembled monolayers to circumvent the disadvantage of vacuum deposition or spin-coating and to improve the film uniformity.

# BIBLIOGRAPHY


1 C. James, *https://www.investopedia.com/terms/n/nonrenewableresource.asp, Investopedia*, 2019.

2 T. Kazarina, https://tass.ru/spec/climate?fbclid=IwAR38cyQzCrtEIk0snHtDkUsdbEzNyrucRB9nm7lFZyqNlynOT12k7k0smQc, *NCASI Spec. Rep.*, 2019.

3 J. S. Pal and E. A. B. Eltahir, *Nat. Clim. Chang.*, 2016, **6**, 197–200.

4 https://gulfnews.com/uae/environment/gulf-will-be-too-hot-for-humans-by-2070-study-1.1608055, 2015.

5 https://www.businessinsider.com/solar-power-potential-how-much-energy-does-sun-have-2017-3?r=US&IR=T, 2017.

6 Renewable capacity statistics, International Renewable Energy Agency (IRENA), Abu Dhabi, 2019.

7 Urban Renewable Energy on the Upswing: A Spotlight on Renewable Energy in Cities in REN21's *"Renewables 2019 Global Status Report"*, 2019.

8 https://www.nrel.gov/pv/assets/pdfs/best-research-cell-efficiencies, 2020.

9 A. K. Jena, A. Kulkarni, and T. Miyasaka, *Chem. Rev.* 2019, **119**, 3036–3103

10 L. Calió, S. Kazim, M. Grätzel and S. Ahmad, *Angew. Chem. Int. Ed*, 2016, **55**, 14522–14545.

11 Q. Wali, F. J. Iftikhar, M. E. Khan, A. Ullah, Y. Iqbal and R. Jose, *Org. Electron.*, 2020, **78**, 105590.

12 H. Lu, B. He, Y. Ji, Y. Shan, C. Zhong, J. Xu, J. LiuYang, F. Wu and L. Zhu, *Chem. Eng. J.*, 2020, **385**, 123976.

13 A. R. Chakhmouradian and P. M. Woodward, *Phys. Chem. Miner.*, 2014, **41**, 387–391.

14 A. Kojima, K. Teshima, Y. Shirai and T. Miyasaka, *J. Am. Chem. Soc.*, 2009, **131**, 6050–6051.

15 H. Kim, C. Lee, J. Im, K. Lee, T. Moehl, A. Marchioro, S. Moon, R. Humphry-baker, J. Yum, J. E. Moser and M. Gra, *Sci. Rep.*, 2012, **2**, 591.

16 P. Liu, W. Wang, S. Liu, H. Yang and Z. Shao, *Adv. Energy Mater.*, 2019, **9**, 1803017.

17 F. Hao, C. C. Stoumpos, D. H. Cao, R. P. H. Chang and M. G. Kanatzidis, *Nat. Photonics*, 2014, **8**, 489–494.

18 J. Woong Jung, J. Woong Jo, C.-C. Chueh, F. Liu, W. Ho Jo, T. P. Russell, A. K-Y Jen, J. W. Jung, C. Chueh, A. K-Y Jen, J. W. Jo, W. H. Jo, F. Liu and T. P. Russell, *Adv. Mater.*, 2015, **27**, 3310–3317.

19 W. S. Yang, J. H. Noh, N. J. Jeon, Y. C. Kim, S. Ryu, J. Seo and S. I. Seok, *Science*, 2015, **348**, 1234–1237.

20 J. H. Noh, S. H. Im, J. H. Heo, T. N. Mandal and S. Il Seok, *Nano Lett.*, 2013, **13**, 1764−1769.

21 S. D. Stranks, G. E. Eperon, G. Grancini, C. Menelaou, M. J. P. Alcocer, T. Leijtens, L. M. Herz, A. Petrozza and H. J. Snaith, *Science* , 2013, **342**, 341–344.

22 S. Kazim, M. K. Nazeeruddin, M. Grätzel and S. Ahmad, *Angew. Chem. Int. Ed*, 2014, **53**, 2812–2824.

23 J. Urieta-Mora, I. García-Benito, A. Molina-Ontoria and N. Martín, *Chem. Soc. Rev.*, 2018, **47**, 8541–8571.

24 N. J. Jeon, H. Na, E. H. Jung, T. Yang, Y. G. Lee, G. Kim, H. Shin, S. Il Seok, J. Lee and J. Seo, *Nat. Energy*, 2018, **3**, 682–689.

25 J. Y. Jeng, Y. F. Chiang, M. H. Lee, S. R. Peng, T. F. Guo, P. Chen and T. C. Wen, *Adv. Mater.*, 2013, **25**, 3727–3732.

26 H. S. Kim, I. Mora-Sero, V. Gonzalez-Pedro, F. Fabregat-Santiago, E. J. Juarez-Perez, N. G. Park and J. Bisquert, *Nat. Commun.*, 2013, **4**, 1–7.

27 Y. Chen, Z. Yang, X. Jia, Y. Wu, N. Yuan, J. Ding, W. H. Zhang and S. (Frank) Liu, *Nano Energy*, 2019, **61**, 148–157.

28 M. Che, L. Zhu, Y. L. Zhao, D. S. Yao, X. Q. Gu, J. Song and Y. H. Qiang, *Mater. Sci. Semicond. Process.*, 2016, **56**, 29–36.

29 M. M. Lee, J. Teuscher, T. Miyasaka, T. N. Murakami, and H. J. Snaith, *Science.*, 2012, **338**, 643–648.

30 W. S. Yang, B.-W. Park, E. H. Jung and N. J. Jeon, *Science.*, 2017, **356**, 1376–1379.

31 B. Roose, J. P. C. Baena, K. C. Gödel, M. Graetzel, A. Hagfeldt, U. Steiner and A. Abate, *Nano Energy*, 2016, **30**, 517–522.

32 Y. Yu, J. Li, D. Geng, J. Wang, L. Zhang, T. L. Andrew, M. S. Arnold and X. Wang, *ACS Nano*, 2015, **9**, 564–572.

33 L. Xiong, M. Qin, C. Chen, J. Wen, G. Yang, Y. Guo, J. Ma, Q. Zhang, P. Qin, S. Li and G. Fang, *Adv. Funct. Mater.*, 2018, **28**, 1–10.

34 Z. Zhu, X. Zheng, Y. Bai, T. Zhang and Z. Wang, *Phys. Chem. Chem. Phys.*, 2015, **17**, 18265–18268.

35 W. Li, J. Liu and D. Zhao, *Nat. Rev. Mater.*, 2016, **1**, 16023.

36 G. E. Eperon, V. M. Burlakov, P. Docampo, A. Goriely and H. J. Snaith, *Adv. Funct. Mater.*, 2014, **24**, 151–157.

37 Z. Zhou, X. Li, M. Cai, F. Xie, Y. Wu, Z. Lan, X. Yang, Y. Qiang, A. Islam and L.

Han, *Adv. Energy Mater.*, 2017, **7**, 1700763.

38 M. Liu, M. B. Johnston and H. J. Snaith, *Nature*, 2013, **501**, 395–8.

39 X. Liu, Y. Cheng, C. Liu, T. Zhang, N. Zhang, S. Zhang, J. Chen, Q. Xu, J. Ouyang and H. Gong, *Energy Environ. Sci.*, 2019, **12**, 1622–1633.

40 S. Bai, P. Da, C. Li, Z. Wang, Z. Yuan, F. Fu, M. Kawecki, X. Liu, N. Sakai, J. T.-W. Wang, S. Huettner, S. Buecheler, M. Fahlman, F. Gao and H. J. Snaith, *Nature*, 2019, **571**, 245–250.

41 J. Z. Fan, S. Hoogland, Y. Zhao, M. Yuan, H. Tan, E. H. Sargent, F. Fan, P. Li, R. Quintero-Bermudez, L. N. Quan, Y. Zhao, A. Jain, X. Lan, O. Voznyy, Z. Yang, Z. Lu, B. Zhang and F. P. García de Arquer, *Science*, 2017, **355**, 722–726.

42 L. Yang, F. Cai, Y. Yan, J. Li, D. Liu, A. J. Pearson and T. Wang, *Adv. Funct. Mater.*, 2017, **27**, 1702613.

43 W. Ming, D. Yang, T. Li, L. Zhang and M. H. Du, *Adv. Sci.*, 2018, **5**, 1700662.

44 K. Domanski, J. P. Correa-Baena, N. Mine, M. K. Nazeeruddin, A. Abate, M. Saliba, W. Tress, A. Hagfeldt and M. Grätzel, *ACS Nano*, 2016, **10**, 6306–6314.

45 Y. Kato, L. K. Ono, M. V. Lee, S. Wang, S. R. Raga and Y. Qi, *Adv. Mater. Interfaces*, 2015, **2**, 2–7.

46 J. Zhao, X. Zheng, Y. Deng, T. Li, Y. Shao, A. Gruverman, J. Shield and J. Huang, *Energy Environ. Sci.*, 2016, **9**, 3650–3656.

47 Y. Deng, Q. Dong, C. Bi, Y. Yuan and J. Huang, *Adv. Energy Mater.*, 2016, **6**, 1600372.

48 Q. Jiang, X. Sheng, B. Shi, X. Feng and T. Xu, *J. Phys. Chem. C*, 2014, **118**, 25878–25883.

49 Y. Wang, Y. Yue, X. Yang and L. Han, *Adv. Energy Mater.*, 2018, **8**, 1–25.

50 W. Zhang, Y. C. Wang, X. Li, C. Song, L. Wan, K. Usman and J. Fang, *Adv. Sci.*, 2018, **5**, 1800159.

51 X. Tong, F. Lin, J. Wu and Z. M. Wang, *Adv. Sci.*, 2015, **3**, 1500201.

52 E. Bi, H. Chen, F. Xie, Y. Wu, W. Chen, Y. Su, A. Islam, M. Grätzel, X. Yang and L. Han, *Nat. Commun.*, 2017, **8**, 1–7.

53 N. Arora, M. I. Dar, A. Hinderhofer, N. Pellet, P. Yadav, F. Schreiber, S. M. Zakeeruddin, M. Gratzel, *Science*, 2017, **358**, 768–771.

54 L. Huang and Z. Ge, *Adv. Energy Mater.*, 2019, **31**, 1900248.

55 J. Lian, B. Lu, F. Niu, P. Zeng and X. Zhan, *Small Methods*, 2018, **2**, 1800082.

56 E. J. Juarez-Perez, M. Wußler, F. Fabregat-Santiago, K. Lakus-Wollny, E. Mankel, T. Mayer, W. Jaegermann and I. Mora-Sero, *J. Phys. Chem. Lett.*, 2014, **5**, 680–685.

57 A. Bera, A. D. Sheikh, M. A. Haque, R. Bose, E. Alarousu, O. F. Mohammed and T. Wu, *ACS Appl. Mater. Interfaces*, 2015, **7**, 12404–12411.

58 A. J. Yun, J. Kim, T. Hwang and B. Park, *ACS Appl. Energy Mater.*, 2019, **2**, 3554–3560.

59 A. Bera, K. Wu, A. Sheikh, E. Alarousu, O. F. Mohammed and T. Wu, *J. Phys. Chem. C*, 2014, **118**, 28494–28501.

60 C. Zhen, T. Wu, R. Chen, L. Wang, G. Liu and H. M. Cheng, *ACS Sustain. Chem. Eng.*, 2019, **7**, 4586–4618.

61 H. Sun, Y. Zhou, Y. Xin, K. Deng, L. Meng, J. Xiong and L. Li, *Adv. Funct. Mater.*, 2019, **29**, 1808667.

62 D. Liu and T. L. Kelly, *Nat. Photonics*, 2014, **8**, 133–138.

63 P. Zhang, J. Wu, T. Zhang, Y. Wang, D. Liu, H. Chen, L. Ji, C. Liu, W. Ahmad, Z. D. Chen and S. Li, *Adv. Mater.*, 2018, **30**, 1703737.

64 M. W. Hua Zhang, Lingwei Xue, Junbo Han, Yong Qing Fu, Yan Shen, Zhiguo Zhang, Yongfang Li, *J. Mater. Chem. A*, 2016, **4**, 8724–8733.

65 J. Huang, Z. Gu, L. Zuo, T. Ye and H. Chen, *Sol. Energy*, 2016, **133**, 331–338.

66 D. Yang, R. Yang, X. Ren, X. Zhu, Z. Yang, C. Li and S. F. Liu, *Adv. Mater.*, 2016, **28**, 5206–5213.

67 Z. Zhu, J. Q. Xu, C. C. Chueh, H. Liu, Z. Li, X. Li, H. Chen and A. K. Y. Jen, *Adv. Mater.*, 2016, **28**, 10786–10793.

68 Y. Bai, Q. Dong, Y. Shao, Y. Deng, Q. Wang, L. Shen, D. Wang, W. Wei and J. Huang, *Nat. Commun.*, 2016, **7**, 12806.

69 H. Azimi, T. Ameri, H. Zhang, Y. Hou, C. O. R. Quiroz, J. Min, M. Hu, Z. G. Zhang, T. Przybilla, G. J. Matt, E. Spiecker, Y. Li and C. J. Brabec, *Adv. Energy Mater.*, 2015, **5**, 1401692.

70 Z. Zhu, C. C. Chueh, F. Lin and A. K. Y. Jen, *Adv. Sci.*, 2016, **3**, 1600027.

71 P. Y. Gu, N. Wang, C. Wang, Y. Zhou, G. Long, M. Tian, W. Chen, X. W. Sun, M. G. Kanatzidis and Q. Zhang, *J. Mater. Chem. A*, 2017, **5**, 7339–7344.

72 P. Y. Gu, N. Wang, A. Wu, Z. Wang, M. Tian, Z. Fu, X. W. Sun and Q. Zhang, *Chem. - An Asian J.*, 2016, **11**, 2135–2138.

73 Y. Lin, L. Shen, J. Dai, Y. Deng, Y. Wu, Y. Bai and X. Zheng, *Adv. Mater.*, 2017, **29**, 1604545.

74 L. Zhao, R. A. Kerner, Z. Xiao, Y. L. Lin, K. M. Lee, J. Schwartz and B. P. Rand, *ACS Energy Lett.*, 2016, **1**, 595–602.

75 E. M. Sanehira, B. J. Tremolet De Villers, P. Schulz, M. O. Reese, S. Ferrere, K. Zhu,

L. Y. Lin, J. J. Berry and J. M. Luther, *ACS Energy Lett.*, 2016, **1**, 38–45.

76 S. S. Reddy, V. M. Arivunithi, V. G. Sree, H. Kwon, J. Park, Y. C. Kang, H. Zhu, Y. Y. Noh and S. H. Jin, *Nano Energy*, 2019, **58**, 284–292.

77 Y. Yue, N. T. Salim, Y. Wu, X. Yang, A. Islam, W. Chen, J. Liu, E. Bi, F. Xie, M. Cai and L. Han, *Adv. Mater.*, 2016, **28**, 10738–10743.

78 M. Saliba, S. Orlandi, T. Matsui, S. Aghazada, M. Cavazzini, J.-P. Correa-Baena, P. Gao, R. Scopelliti, E. Mosconi, K.-H. Dahmen, F. Dengelis, A. Abate, A. Hagfeldt, G. Pozzi, M. Graetzel and M. K. Nazeeruddin, *Nat. Energy*, 2016, **1**, 15017.

79 I. García-Benito, I. Zimmermann, J. Urieta-Mora, J. Aragó, J. Calbo, J. Perles, A. Serrano, A. Molina-Ontoria, E. Ortí, N. Martín and M. K. Nazeeruddin, *Adv. Funct. Mater.*, 2018, **28**, 1801734.

80 S. Ryu, J. H. Noh, N. J. Jeon, Y. Chan Kim, W. S. Yang, J. Seo and S. Il Seok, *Energy Environ. Sci.*, 2014, **7**, 2614–2618.

81 Z. Yu and L. Sun, *Adv. Energy Mater.*, 2015, **5**, 1500213.

82 M. L. Petrus, K. Schutt, M. T. Sirtl, E. M. Hutter, A. C. Closs, J. M. Ball, J. C. Bijleveld, A. Petrozza, T. Bein, T. J. Dingemans, T. J. Savenije, H. Snaith and P. Docampo, *Adv. Energy Mater.*, 2018, **8**, 1801605.

83 M. L. Petrus, T. Bein, T. J. Dingemans and P. Docampo, *J. Mater. Chem. A*, 2015, **3**, 12159–12162.

84 D. Vaitukaityte, Z. Wang, T. Malinauskas, A. Magomedov, G. Bubniene, V. Jankauskas, V. Getautis and H. J. Snaith, *Adv. Mater.*, 2018, **30**, 1803735.

85 K. Lim, H. Kim, J. Jeong, H. Kim, J. Y. Kim and T. Lee, *Adv. Mater.*, 2014, **26**, 6461–6466.

86 P. Docampo, J. M. Ball, M. Darwich, G. E. Eperon and H. J. Snaith, *Nat. Commun.*, 2013, **4**, 1–6.

87 Z. H. Bakr, Q. Wali, A. Fakharuddin, L. Schmidt-mende, M. Brown and R. Jose, *Nano Energy*, 2017, **34**, 271–305.

88 P. Vivo, J. K. Salunke and A. Priimagi, *Materials,* 2017, **10**, 1087.

89 P. Gratia, A. Magomedov, T. Malinauskas, M. Daskeviciene, A. Abate, S. Ahmad, M. Grätzel, V. Getautis and M. K. Nazeeruddin, *Angew. Chem. Int. Ed*, 2015, **54**, 11409–11413.

90 A. T. Murray, J. M. Frost, C. H. Hendon, C. D. Molloy, D. R. Carbery and A. Walsh, *Chem. Commun.*, 2015, **51**, 8935–8938.

91 B. Xu, Doctoral Thesis, *Advanced Organic Hole Transport Materials for Solution-Processed Photovoltaic Devices,* 2015.

92 P. Ganesan, K. Fu, P. Gao, I. Raabe, K. Schenk, R. Scopelliti, J. Luo, L. H. Wong, M.

Grätzel and M. K. Nazeeruddin, *Energy Environ. Sci.*, 2015, **8**, 1986–1991.

93 J. H. Noh, N. J. Jeon, Y. C. Choi, M. K. Nazeeruddin, M. Grätzel and S. Il Seok, *J. Mater. Chem. A*, 2013, **1**, 11842–11847.

94 H. Li, K. Fu, A. Hagfeldt, M. Grätzel, S. G. Mhaisalkar and A. C. Grimsdale, *Angew. Chem. Int. Ed*, 2014, **53**, 1–5.

95 D. Bi, G. Boschloo and A. Hagfeldt, *Nano*, 2014, **9**, 21–23.

96 A. Gheno, S. Vedraine, B. Ratier and J. Bouclé, *Metals*, 2016, **6**, 21.

97 J. Liu, Y. Wu, C. Qin, X. Yang, T. Yasuda, A. Islam, K. Zhang, W. Peng, W. Chen and L. Han, *Energy Environ. Sci.*, 2014, **7**, 2963–2967.

98 Z. Zhu, Y. Bai, H. K. H. Lee, C. Mu, T. Zhang, L. Zhang, J. Wang, H. Yan, S. K. So and S. Yang, *Adv. Funct. Mater.*, 2014, **24**, 7357–7365.

99 J. H. Heo, S. H. Im, J. H. Noh, T. N. Mandal, C.-S. Lim, J. A. Chang, Y. H. Lee, H.-J. Kim, A. Sarkar, K. Nazeeruddin, M. Grätzel and S. Il Seok, *Nat. Photonics*, 2013, **7**, 486.

100 N. J. Jeon, J. Lee, J. H. Noh, K. Nazeeruddin, M. Grätzel, S. Il Seok, N. J. Jeon, J. Lee, J. H. Noh, M. K. Nazeeruddin and M. Grätzel, *J. Am. Chem. Soc.*, 2013, **135**, 19087–19090.

101 Y. Wang, W. Chen, L. Wang, B. Tu, T. Chen, B. Liu, K. Yang, C. W. Koh, X. Zhang, H. Sun, G. Chen, X. Feng, H. Y. Woo, A. B. Djurišić, Z. He and X. Guo, *Adv. Mater.*, 2019, **31**, 1902781.

102 M. Maciejczyk, A. Ivaturi, and N. Robertson, *J. Mater. Chem. A,* 2016, **4**, 4855.

103 B. Pashaei, S. Bellani, H. Shahroosvand, and F. Bonaccorso, *Chem. Sci.,* 2020, **11**, 2429.

104 M. Li, Z. Wang, M. Liang, L. Liu, X. Wang, Z. Sun, and S. Xue, *J. Phys. Chem. C,* 2018, **122**, 24014-24024.

105 X. Sun, F. Wu, C. Zhong, L. Zhu, and Z. Li, **Chem. Sci.**, 2019, **10**, 6899.

106 Y. Cao, Y. Li, T. Morrissey, B. Lam, B. O. Patrick, D. J. Dvorak, Z. Xia, T. L. Kelly, and C. P. Berlinguette, *Energy Environ. Sci.,* 2019, **12**, 3502.

107 O. Malinkiewicz, A. Yella, Y. H. Lee, G. M. Espallargas, M. Graetzel, M. K. Nazeeruddin and H. J. Bolink, *Nat. Photonics*, 2014, **8**, 128.

108 Y. Chen, Z. Yang, S. Wang, X. Zheng, Y. Wu, N. Yuan, W. H. Zhang and S. Liu, *Adv. Mater.*, 2018, **30**, 1805660.

109 W. Y. Chen, L. L. Deng, S. M. Dai, X. Wang, C. B. Tian, X. X. Zhan, S. Y. Xie, R. Bin Huang and L. S. Zheng, *J. Mater. Chem. A*, 2015, **3**, 19353–19359.

110 A. S. Subbiah, A. Halder, S. Ghosh, N. Mahuli, G. Hodes and S. K. Sarkar, *J. Phys. Chem. Lett.*, 2014, **5**, 1748–1753.

111 B. Xu, E. Sheibani, P. Liu, J. Zhang, H. Tian, N. Vlachopoulos, G. Boschloo, L. Kloo, A. Hagfeldt and L. Sun, *Adv. Mater.*, 2014, **26**, 6629–6634.

112 X. Liang, C. Wang, M. Wu, Y. Wu, F. Zhang, Z. Han, X. Lu, K. Guo and Y. M. Zhao, *Tetrahedron*, 2017, **73**, 7115–7121.

113 J. Huang and K. Lee, *ACS Appl. Mater. Interfaces*, 2014, **10**, 4–9.

114 X. Qiu, R. Lu, H. Zhou, X. Zhang, T. Xu, X. Liu and Y. Zhao, *Tetrahedron Lett.*, 2008, **49**, 7446–7449.

115 C. S. Kramer, K. Zeitler and T. J. J. Muller, *Org. Lett.*, 2000, **2**, 3723–3726.

116 R. Y. Lai, E. F. Fabrizio, L. Lu, S. A. Jenekhe and A. J. Bard, *J. Am. Chem. Soc.*, 2001, **123**, 9112–9118.

117 X. Kong, A. P. Kulkarni and S. A. Jenekhe, *Macromolecules*, 2003, **36**, 8992–8999.

118 W. Zhou, Y. Wen, L. Ma, Y. Liu and X. Zhan, *Macromolecules*, 2012, **45**, 4115–4121.

119 J. H. Kim, Y. H. Seo, W. H. Lee, Y. Hong, S. K. Lee, W. S. Shin, S. J. Moon and I. N. Kang, *Synth. Met.*, 2011, **161**, 72–78.

120 L. I. N. Lin, Y. Morisaki and Y. Chujo, *J. Polym. Sci. Part A*, 2010, **48**, 4823–4834.

121 J. K. Salunke, F. L. Wong, K. Feron, S. Manzhos, M. F. Lo, C. S. Shinde, D., Patil A., Lee, V. A. L. Roy and P. P. Sonar, P., Wadgaonkar, *J. Mater. Chem. C*, 2016, **4**, 1009–1018.

122 Z. S. Huang, H. Meier and D. Cao, *J. Mater. Chem. C*, 2016, **4**, 2404–2426.

123 S. P. Massie, *Chem. Rev.*, 1954, **54**, 797–833.

124 C. J. Yang, Y. J. Chang, M. Watanabe, Y. S. Hon and T. J. Chow, *J. Mater. Chem.*, 2012, **22**, 4040–4049.

125 R. Grisorio, B. Roose, S. Colella, A. Listorti, G. P. Suranna and A. Abate, *ACS Energy Lett.*, 2017, **2**, 1029–1034.

126 F. Zhang, S. Wang, H. Zhu, X. Liu, H. Liu, X. Li, Y. Xiao, S. M. Zakeeruddin and M. Gratzel, *ACS Energy Lett.*, 2018, **3**, 1145–1152.

127 C. Lu, M. Paramasivam, K. Park, C. H. Kim and H. K. Kim, *ACS Appl. Mater. Interfaces*, 2019, **11**, 14011–14022.

128 X. Ding, C. Chen, L. Sun, H. Li, H. Chen, J. Su, H. Li, H. Li, L. Xu and M. Cheng, *J. Mater. Chem. A*, 2019, **7**, 9510–9516.

129 H. Cho, S. Lee, N. S. Cho, G. E. Jabbour, J. Kwak, D.-H. Hwang and C. Lee, *ACS Appl. Mater. Interfaces*, 2013, **5**, 3855–3860.

130 X. Yao, K. Zhang, K. Müllen and X. Y. Wang, *Asian J. Org. Chem.*, 2018, **7**, 2233–2238.

131 H. Y. Oh, C. Lee and S. Lee, *Org. Electron.*, 2009, **10**, 163–169.

132 S. S. Li, K. J. Jiang, C. C. Yu, J. H. Huang, L. M. Yang and Y. L. Song, *New J. Chem.*, 2014, **38**, 4404–4408.

133 A. Baheti, C. P. Lee, K. R. J. Thomas and K. C. Ho, *Phys. Chem. Chem. Phys.*, 2011, **13**, 17210–17221.

134 C. C. Yu, K. J. Jiang, J. H. Huang, F. Zhang, X. Bao, F. W. Wang, L. M. Yang and Y. Song, *Org. Electron.*, 2013, **14**, 445–450.

135 S. Y. Liu, W. Q. Liu, J. Q. Xu, C. C. Fan, W. F. Fu, J. Ling, J. Y. Wu, M. M. Shi, A. K. Y. Jen and H. Z. Chen, *ACS Appl. Mater. Interfaces*, 2014, **6**, 6765–6775.

136 T. M. Figueira-Duarte and K. Müllen, *Chem. Rev.*, 2011, **111**, 7260–7314.

137 Q. Q. Ge, J. Y. Shao, J. Ding, L. Y. Deng, W. K. Zhou, Y. X. Chen, J. Y. Ma, L. J. Wan, J. Yao, J. S. Hu and Y. W. Zhong, *Angew. Chem. Int. Ed*, 2018, **57**, 10959–10965.

138 M. A. Green, E. D. Dunlop, D. H. Levi, J. Hohl-Ebinger, M. Yoshita and A. W. Y. Ho-Baillie, *Prog. Photovoltaics Res. Appl.*, 2019, **27**, 565–575.

139 Q. Wang, N. Phung, D. D. Girolamo, P. Vivo, and A. Abate, *Energy Environ. Sci.*, 2019, **12**, 865-886.

140 S. Chu, Y. Cui and N. Liu, *Nat. Mater.*, 2016, **16**, 16–22.

141 K. Hwang, Y. S. Jung, Y. J. Heo, F. H. Scholes, S. E. Watkins, J. Subbiah, D. J. Jones, D. Y. Kim and D. Vak, *Adv. Mater.*, 2015, **27**, 1241–1247.

142 A. Priyadarshi, L. J. Haur, P. Murray, D. Fu, S. Kulkarni, G. Xing, T. C. Sum, N. Mathews and S. G. Mhaisalkar, *Energy Environ. Sci.*, 2016, **9**, 3687–3692.

143 A. T. Barrows, A. J. Pearson, C. K. Kwak, A. D. F. Dunbar, A. R. Buckley and D. G. Lidzey, *Energy Environ. Sci.*, 2014, **7**, 2944–2950.

144 T. Liu, K. Chen, Q. Hu, R. Zhu and Q. Gong, *Adv. Energy Mater.*, 2016, **6**, 1600457.

145 L. K. Ono, M. R. Leyden, S. Wang and Y. Qi, *J. Mater. Chem. A*, 2016, **4**, 6693–6713.

146 M. R. Leyden, Y. Jiang and Y. Qi, *J. Mater. Chem. A*, 2016, **4**, 13125–13132.

147 N. Ahn, D. Y. Son, I. H. Jang, S. M. Kang, M. Choi and N. G. Park, *J. Am. Chem. Soc.*, 2015, **137**, 8696–8699.

148 M. Xiao, F. Huang, W. Huang, Y. Dkhissi, Y. Zhu, J. Etheridge, A. Gray-Weale, U. Bach, Y. B. Cheng and L. Spiccia, *Angew. Chem. Int. Ed*, 2014, **53**, 9898–9903.

149 M. Yang, Y. Zhou, Y. Zeng, C. S. Jiang, N. P. Padture and K. Zhu, *Adv. Mater.*, 2015, **27**, 6363–6370.

150 B. Ding, Y. Li, S. Y. Huang, Q. Q. Chu, C. X. Li, C. J. Li and G. J. Yang, *J. Mater. Chem. A*, 2017, **5**, 6840–6848.

151 M. Yang, Z. Li, M. O. Reese, O. G. Reid, D. H. Kim, S. Siol, T. R. Klein, Y. Yan, J. J.

Berry, M. F. A. M. Van Hest and K. Zhu, *Nat. Energy*, 2017, **2**, 1–9.

152 J. H. Heo, M. H. Lee, M. H. Jang and S. H. Im, *J. Mater. Chem. A*, 2016, **4**, 17636–17642.

153 J. M. Frost, K. T. Butler, F. Brivio, C. H. Hendon, M. Van Schilfgaarde and A. Walsh, *Nano Lett.*, 2014, **14**, 2584–2590.

154 S. Ahmad, P. K. Kanaujia, W. Niu, J. J. Baumberg and G. V. Prakash, *ACS Appl. Mater. Interfaces*, 2014, **6**, 10238–10247.

155 Q. Fu, X. Tang, B. Huang, T. Hu, L. Tan, L. Chen and Y. Chen, *Adv. Sci.*, 2018, **5**, 1700387.

156 Z. Song, A. Abate, S. C. Watthage, G. K. Liyanage, A. B. Phillips, U. Steiner, M. Graetzel and M. J. Heben, *Adv. Energy Mater.*, 2016, **6**, 1600846.

157 F. Bella, G. Griffini, J. P. Correa-Baena, G. Saracco, M. Grätzel, A. Hagfeldt, S. Turri and C. Gerbaldi, *Science*, 2016, **354**, 203–206.

158 J. Yang, B. D. Siempelkamp, E. Mosconi, F. De Angelis and T. L. Kelly, *Chem. Mater.*, 2015, **27**, 4229–4236.

159 Y. Dkhissi, S. Meyer, D. Chen, H. C. Weerasinghe, L. Spiccia, Y. B. Cheng and R. A. Caruso, *ChemSusChem*, 2016, **9**, 687–695.

160 C. Huang, W. Fu, C.-Z. Li, Z. Zhang, W. Qiu, M. Shi, P. Heremans, A. K.-Y. Jen and H. Chen, *J. Am. Chem. Soc.*, 2016, **138**, 2528–2531.

161 E. H. Jung, N. J. Jeon, E. Y. Park, C. S. Moon, T. J. Shin, T. Y. Yang, J. H. Noh and J. Seo, *Nature*, 2019, **567**, 511–515.

162 L. Liu, A. Mei, X. Li, H. Han, Y. Dkhissi, A. D. Scully, R. A. Caruso, Y. B. Cheng, I. Jeong, J. Lee, M. J. Ko, K. Yong, B. S. Richards, T. L. Kelly, N. Pellet, M. Levi, S. Turri, M. Levi and S. Turri, *Science* , 2016, **354**, 206–209.

163 S. N. Habisreutinger, R. J. Nicholas and H. J. Snaith, *Adv. Energy Mater.*, 2017, **7**, 1601839.

164 S. Liu, W. Huang, P. Liao, N. Pootrakulchote, H. Li, J. Lu, J. Li, F. Huang, X. Shai, X. Zhao, Y. Shen, Y. B. Cheng and M. Wang, *J. Mater. Chem. A*, 2017, **5**, 22952–22958.

165 Q. Q. Chu, B. Ding, J. Peng, H. Shen, X. Li, Y. Liu, C. X. Li, C. J. Li, G. J. Yang, T. P. White and K. R. Catchpole, *J. Mater. Sci. Technol.*, 2019, **35**, 987–993.

166 M. A. Green, A. Ho-Baillie and H. J. Snaith, *Nat. Photonics*, 2014, **8**, 506–514.

167 A. Abate, *Joule*, 2017, **1**, 659–664.

168 W. Ke, and M. G. Kanatzidis, *Nat. Comm.*, 2019, **10**, 965.

169 E. Jokar, C. H. Chien, C. M. Tsai, A. Fathi, and E. W. Diau, *Adv. Mater.* 2019, **31** 1804835.

170 F. Giustino and H. J. Snaith, *ACS Energy Lett.*, 2016, **1**, 1233–1240.

171 N. K. Noel, S. D. Stranks, A. Abate, C. Wehrenfennig, S. Guarnera, A. A. Haghighirad, A. Sadhanala, G. E. Eperon, S. K. Pathak, M. B. Johnston, A. Petrozza, L. M. Herz and H. J. Snaith, *Energy Environ. Sci.*, 2014, **7**, 3061–3068.

172 G. Volonakis, M. R. Filip, A. A. Haghighirad, N. Sakai, B. Wenger, H. J. Snaith and F. Giustino, *J. Phys. Chem. Lett.*, 2016, **7**, 1254–1259.

173 A. H. Slavney, T. Hu, A. M. Lindenberg and H. I. Karunadasa, *J. Am. Chem. Soc.*, 2016, **138**, 2138–2141.

174 E. T. McClure, M. R. Ball, W. Windl and P. M. Woodward, *Chem. Mater.*, 2016, **28**, 1348–1354.

175 D. Seyferth, D. E. Welch and J. K. Heeren, *J. Am. Chem. Soc.*, 1964, **86**, 1100–1105.

176 A. Suzuki, *Pure Appl. Chem.*, 1991, **63**, 419–422.

177 A. Suzuki, *J. Organomet. Chem.*, 1998, **576**, 147–168.

178 F. Ullmann, *Berichte der Dtsch. Chem. Gesellschaft*, 1903, **36**, 2382–2384.

179 D. Ma, Q. Cai and H. Zhang, *Org. Lett.*, 2003, **5**, 2453–2455.

180 F. Monnier and M. Taillefer, *Angew. Chem. Int. Ed*, 2009, **48**, 6954–6971.

181 A. S. Travis, *Chemistry of Anilines, Z. Rapaport, Ed. (John Wiley & Sons, New York, 2007),* 2007, vol. 1, pp. 1–73.

182 I. P. Beletskaya and A. V. Cheprakov, *Coord. Chem. Rev.*, 2004, **248**, 2337–2364.

183 I. Hamachi, Y. Tajiri and S. Shinkai, *J. Am. Chem. Soc.*, 1994, **116**, 7437–7438.

184 D. S. Matteson, *J. Org. Chem.*, 2013, **78**, 10009–10023.

185 J. N. Cambre and B. S. Sumerlin, *Polymer (Guildf).*, 2011, **52**, 4631–4643.

186 A. J. J. Lennox and G. C. Lloyd-Jones, *Chem. Soc. Rev.*, 2014, **43**, 412–443.

187 The Nobel Prize in Physics 1994, https://www.nobelprize.org/prizes/physics/1944/summary.

188 H. Gunther, *NMR Spectroscopy: Basic Principles, Concepts and Applications in Chemistry, 3rd Edition*, Wiley, 2013.

189 J. Keeler, *Understanding NMR spectroscopy, 1st Edition*, Wiley, 2005.

190 C. S. Ho, C. W. K. Lam, M. H. M. Chan, R. C. K. Cheung, L. K. Law, L. C. W. Lit, K. F. Ng, M. W. M. Suen and H. L. Tai, *Clin. Biochem. Rev.*, 2003, **24**, 3–12.

191 https://www.sciencedirect.com/topics/engineering/beer-lambert-law

192 Robert R. Gagne, Carl A. Koval, and G. C. Lisensky, *Inorg. Chem.*, 1980, **19**, 2854–

2855.

193 N. V. Tkachenko, *Optical spectroscopy: methods and instrumentaitons, Elsevier Science*, 2006.

194 S. Makuta, M. Liu, M. Endo, H. Nishimura, A. Wakamiya and Y. Tachibana, *Chem. Commun.*, 2016, **52**, 673–676.

195 P. Ch, N. H. Pbi, C. Applications, Y. Yamada, T. Nakamura, M. Endo, A. Wakamiya and Y. Kanemitsu, *J Am Chem Soc*, 2014, **136**, 11610–11613.

196 M. Liu, M. Endo, A. Shimazaki, A. Wakamiya and Y. Tachibana, *ACS Appl. Energy Mater.*, 2018, **1**, 3722–3732.

197 E. Von Hauff, *J. Phys. Chem. C*, 2019, **123**, 11329–11346.

198 Barsoukov, E., Macdonald, J. R., *Impedance Spectroscopy: Theory, Experiment, and Applications, 3rd Edition, Wiley,* 2018.

199 D. C. Tripathi, A. K. Tripathi and Y. N. Mohapatra, *Appl. Phys. Lett.*, 2011, **98**, 033304.

200 V. Coropceanu, J. Cornil, Y. da Silva Filho, Demetrio A, Olivier, R. Silbey and J. L. Bredas, *Chem. Rev.*, 2007, **107**, 926–952.

201 A. Pivrikas, Doctoral Thesis, *Charge transport and recombination in bulk-heterojunction solar cells,* 2006.

202 R. C. H. Meera Stephen, K. Genevicius, G. Juska, K. Arlauskas, *Polym. Int.*, 2017, **66**, 13–25.

203 N. Nekrasas, *Thin Solid Films*, 2004, **452**, 290–293.

204 A. A. Bakulin, A. Rao, V. G. Pavelyev, P. H. M. van Loosdrecht, M. S. Pshenichnikov, D. Niedzialek, J. Cornil, D. Beljonne, and R. H. Friend., *Science* , 2012, **335**, 1340–1344.

205 S. Shoaee, T. M. Clarke, C. Huang, S. Barlow, S. R. Marder, M. Heeney, I. McCulloch and J. R. Durrant, *J. Am. Chem. Soc.*, 2010, **132**, 12919–12926.

206 R. Oshi, S. Abdalla and M. Springborg, *Eur. Phy. J. D*, 2019, **73**, 1–9.

207 F. Würthner, T. E. Kaiser and C. R. Saha-Möller, *Angew. Chem. Int. Ed*, 2011, **50**, 3376–3410.

208 T. Bally and G. N. Sastry, *J. Phys. Chem. A*, 1997, **101**, 7923–7925.

209 J. Frenkel, *Phys. Rev.*, 1938, **54**, 647–648.

210 H. H. Poole, *London, Edinburgh, and Dublin Philosophical Magazine and Journal of Science,* 1916, **32**, 112–129.

211 M. L. Petrus, R. K. M. Bouwer, U. Lafont, S. Athanasopoulos, N. C. Greenham and T. J. Dingemans, *J. Mater. Chem. A*, 2014, **2**, 9474–9477.

212 G. S. Liou and C. W. Chang, *Macromolecules*, 2008, **41**, 1667–1674.

213 N. Duvva, K. Sudhakar, D. Badgurjar, R. Chitta and L. Giribabu, *J. Photochem. Photobiol. A Chem.*, 2015, **312**, 8–19.

214 K. B. and E. A. Braude, *J. Chem. Soc.,* 1952, 1068–1077.

215 T. Skalski, Y. Gautier and W. G. Skene, *J. Phys. Chem. C*, 2016, **120**, 9081–9087.

216 A. Pivrikas, N. S. Sariciftci, G. Juska, and R. ¨Osterbacka, *Prog. Photovoltaics Res. Appl*, 2007, **15**, 677–696.

217 F. Zhang, X. Liu, C. Yi, D. Bi, J. Luo, S. Wang, X. Li, Y. Xiao, S. M. Zakeeruddin and M. Grätzel, *ChemSusChem*, 2016, **9**, 2578–2585.

218 M. Kasparas Rakstys, Antonio Abate, M. Ibrahim Dar, Peng Gao, Vygintas Jankauskas, Gwénolé Jacopin,⊥ Egidijus Kamarauskas, Samrana Kazim, Shahzada Ahmad, and M. K. N. Kasparas Rakstys, Antonio Abate, M. Ibrahim Dar, Peng Gao, Vygintas Jankauskas, Gwénolé Jacopin, Egidijus Kamarauskas, Samrana Kazim, Shahzada Ahmad, Michael Grätzel and and M. K. N. Gwénolé Jacopin, Egidijus Kamarauskas, Samrana Kazim, Shahzada Ahmad, Michael Grätzel, *J. Am. Chem. Soc.*, 2015, **137**, 16172–16178.

219 A. Magomedov, A. Al-ashouri, E. Kasparavic, S. Strazdaite, G. Niaura, M. Jošt, T. Malinauskas and S. Albrecht, *Adv. Energy Mater.*, 2018, 1801892.

220 M. Stolterfoht, P. Caprioglio, C. M. Wolff, J. A. Márquez, J. Nordmann, D. Rothhardt, U. Hörmann, A. Redinger, L. Kegelmann, S. Albrecht, M. Saliba, T. Unold and D. Neher, *http//arxiv.org/abs/1810.01333.*, 2018, 1–28.

221 W. Yan, Y. Li, S. Ye, Y. Li, H. Rao, Z. Liu, S. Wang, Z. Bian and C. Huang, *Nano Res.*, 2016, **9**, 1600–1608.

222 J. Chen and N. G. Park, *Adv. Mater.*, 2019, **31**, 1–56.

223 J. Karpińska, B. Starczewska and H. Puzanowska-Tarasiewicz, *Anal. Sci.*, 1996, **12**, 161–170.

224 F. Babudri, G. M. Farinola, F. Naso and R. Ragni, *Chem. Commun.*, 2007, 1003–1022.

225 Z. Li, Z. Wu, W. Fu, P. Liu, B. Jiao, D. Wang, G. Zhou and X. Hou, *J. Phys. Chem. C*, 2012, **116**, 20504–20512.

226 P. Sonar, M. S. Soh, Y. H. Cheng, J. T. Henssler and A. Sellinger, *Org. Lett.*, 2010, 2008–2011.

227 D. Chercka, S.-J. Yoo, M. Baumgarten, J.-J. Kim and K. Müllen, *J. Mater. Chem. C*, 2014, **2**, 9083–9086.

228 J. Jasieniak, M. Califano and S. E. Watkins, *ACS Nano*, 2011, **5**, 5888–5902.

229 J. Lorrmann, B. H. Badada, O. Inganäs, V. Dyakonov and C. Deibel, *J. Appl. Phys.*, 2010, **108**, 113705.

230 A. R. Chaudhry, R. Ahmed, A. Irfan, A. Shaari and A. G. Al-sehemi, *Sci. Adv. Mater.*,

2014, **6**, 1–13.

231 R. Zhou, B. Xia, H. Li, Z. Wang, Y. Yang and J. Zhang, *Front. Chem.*, 2018, **6**, 1–10.

232 T. Maksudov, A. Panagiotopoulos, E. Serpetzoglou, I. Konidakis, M. M. Stylianakis, E. Stratakis and E. Kymakis, *Nanoscale Adv.*, 2019, **1**, 3107–3118.

233 R. Sandoval-Torrientes, I. Zimmermann, J. Calbo, J. Aragó, J. Santos, E. Ortí, N. Martín and M. K. Nazeeruddin, *J. Mater. Chem. A*, 2018, **6**, 5944–5951.

# PUBLICATIONS

I Durgaprasad B. Shinde, Jagadish K. Salunke, Nuno R. Candeias, Francesca Tinti, Massimo Gazzano, Prakash Wadgaonkar, Arri Priimagi, Nadia Camaioni, Paola Vivo. Crystallisation-enhanced bulk hole mobility in phenothiazine-based organic semiconductors. *Scientific Reports* **2017**, 7, 46268.

II Jagadish K. Salunke, Xing Guo, Zhenhua Lin, João R Vale, Nuno R. Candeias, Mathias Nyman, Staffan Dahlström, Ronald Österbacka, Arri Priimagi, Jingjing Chang, Paola Vivo. Phenothiazine-based hole-transporting materials toward eco-friendly perovskite solar cells. *ACS Applied Energy Materials* **2019**, 2, 5, 3021-3027.

III Jagadish K. Salunke, Xing Guo, Maning Liu, Zhenhua Lin, Nuno R. Candeias, Arri Priimagi, Jingjing Chang, Paola Vivo. N-substituted phenothiazines as environmentally friendly hole-transporting materials for low-cost and highly stable halide perovskite solar cells. *ACS Omega* **2020**, 5, 23334-23342.

IV Jagadish K. Salunke, Amandeep Singh, Dongxu He, Hong Duc Pham, Yang Bai, Lianzhou Wang, Staffan Dahlström, Mathias Nyman, Sergei Manzhos, Krishna Feron, Ronald Österbacka, Arri Priimagi, Paola Vivo, Prashant Sonar. Fluorination of pyrene-based organic semiconductors enhances the performance of light-emitting diodes and halide perovskite solar cells. *Organic Electronics* **2019**, 77:105524.

# PUBLICATION I

Crystallisation-enhanced bulk hole mobility in phenothiazine-based organic semiconductors.

Durgaprasad B. Shinde, Jagadish K. Salunke, Nuno R. Candeias, Francesca Tinti, Massimo Gazzano, Prakash Wadgaonkar, Arri Priimagi, Nadia Camaioni, Paola Vivo.

*Scientific Reports* 2017, 7, 46268.
DOI: https://doi.org/10.1038/srep46268

SCIENTIFIC REPORTS

OPEN

# Crystallisation-enhanced bulk hole mobility in phenothiazine-based organic semiconductors

Received: 26 January 2017
Accepted: 14 March 2017
Published: 12 April 2017

D. B. Shinde[1,2,*], Jagadish K. Salunke[3,*], Nuno R. Candeias[3], Francesca Tinti[4], Massimo Gazzano[4], P. P. Wadgaonkar[1,2], Arri Priimagi[3], Nadia Camaioni[4] & Paola Vivo[3]

**A series of three novel donor-acceptor systems based on C(3)-malononitrile-substituted phenothiazines was synthesised in good overall yields and their thermal, spectroscopic, and electrochemical properties were characterised. The compounds were prepared through a sequence of Ullmann-coupling, Vilsmeier-Haack formylation and Knoevenagel-condensation, followed by Suzuki-coupling reactions for introduction of aryl substitutents at C(7) position of the phenothiazine. The introduction of a donor unit at the C(7) position exhibited a weak impact on the optical and electrochemical characteristics of the compounds and led to amorphous films with bulk hole mobilities in the typical range reported for phenothiazines, despite the higher charge delocalisation as attested by computational studies. In contrast, highly ordered films were formed when using the C(7)-unsubstituted 3-malononitrile phenothiazine, exhibiting an outstanding mobility of $1 \times 10^{-3}$ cm$^2$ V$^{-1}$ s$^{-1}$, the highest reported for this class of compounds. Computational conformational analysis of the new phenothizanes suggested that free rotation of the substitutents at the C(7) position suppresses the ordering of the system, thereby hampering suitable packing of the new materials needed for high charge carrier mobility.**

The charge carrier mobility plays a significant role when designing new materials for organic electronic applications as it correlates with several key characteristics determining the performance of organic electronic devices. For instance, charge carrier transport directly affects the switching of organic field effect transistors (OFETs), and lower turn-on voltages are observed for organic light emitting diodes (OLEDs) based on materials with high mobility[1,2]. The mobility also influences charge carrier dynamics in organic photovoltaics (OPVs)[3,4]. A large number of π-conjugated small molecules have been designed and synthesised for OPVs[5–8], OLEDs[9,10], and OFETs[11]. With respect to their polymeric counterparts, the benefits of solution-processable small-molecule-based organic semiconductors arise from their high structural flexibility, easy availability, simple preparation and purification, well-defined structure, and batch-to-batch reproducibility[12–14].

Phenothiazine heterocycle is a well-known electron-rich compound due to the presence of nitrogen and sulphur hetero atoms[15]. Phenothiazines are good electron-donors in photo-excited charge transfer transitions, and display a low and reversible oxidation potential for the generation of a stable radical cation[16–21]. Their ability to suppress molecular aggregation due to butterfly conformation of phenothiazine[22], together with their attractive hole-transport characteristics have resulted in their use in dye sensitized solar cells (DSSCs) as photosensitizers[22–31], as well as in organic thin film transistors and OLEDs[32–35]. Molecular aggregation and the degree of disorder in phenothiazine films has a strong impact on their optical properties[36] and better film-forming properties are usually observed in systems for which aggregate formation is less likely to occur[37,38].

The state-of-the-art phenothiazines possess, however, fairly low bulk mobilities[32–35], which represents one key reason of the few reports existing on phenothiazines for organic photovoltaics[32,39–43]. To the best of our knowledge, as the only counter-example, high mobility values for charge-transfer complexes of iodine with N-methylphenothiazine (2:3 donor acceptor ratio) have been reported by Matsunaga in 1960s, where a complex cation radical of phenothiazine was proposed as the conductive species[44–50]. Finding a phenothiazine derivative

[1]Polymer Science and Engineering Division, CSIR-National Chemical Laboratory, Dr Homi Bhabha Road, Pune 411008, India. [2]Academy of Scientific and Innovative Research, 110025, New Delhi, India. [3]Laboratory of Chemistry and Bioengineering, Tampere University of Technology, P.O. Box 541, FI-33101 Tampere, Finland. [4]Istituto per la Sintesi Organica e la Fotoreattività, Consiglio Nazionale delle Ricerche, via P. Gobetti 101, I-40129 Bologna, Italy. *These authors contributed equally to this work. Correspondence and requests for materials should be addressed to J.S. (email: jagadish.salunke@tut.fi) or N.C. (email: nadia.camaioni@isof.cnr.it) or P.V. (email: paola.vivo@tut.fi)

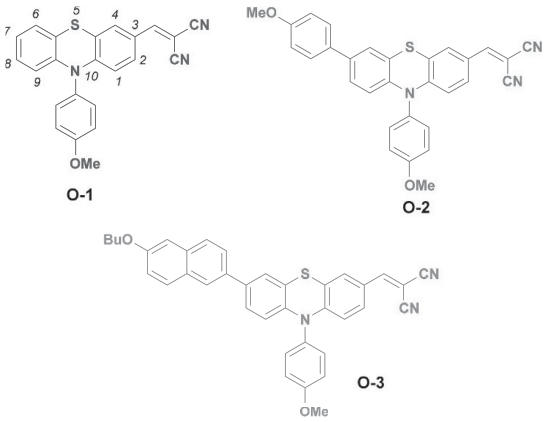


**Figure 1. Chemical structures of the phenothiazine derivatives O-1, O-2, and O-3.**

combining high mobility, good film-forming properties and high light-harvesting capabilities would therefore be highly desired for various organic electronic applications.

Herein, we report the synthesis and characterisation of three newly designed push-pull *para*-methoxyphenyl *N*-substituted phenothiazine-based organic semiconductors (**O-1**, **O-2** and **O-3**) presented in Fig. 1. Based on previous mobility data for *para*-methoxyphenyl *N*-substituted phenothiazines[29,31], the intramolecular charge transfer (ICT) character of phenothiazines can be improved by introducing substituents at C(3) and C(7) positions[28]. Extending the π-system of the phenothiazine increases ICT and consequently improves its charge transport properties[51,52]. Despite the several reports on such approach, the *para*-methoxyphenyl *N*-substituted phenothiazines already studied usually bear a cyanoacrylic moiety at C(3) position[53–57]. We envisioned that the substitution of such group with a stronger electron acceptor such as malononitrile would increase the ICT. In order to increase the electron density at the phenothiazine core, alkoxyaryl groups were added at the C(7) position; *para*-methoxyphenyl unit into **O-2** and 6-butoxynaphthalene into **O-3,** to induce solution processability due to bulkier molecular structure. We thoroughly investigated the effect of the donor unit at the C(7) position of 3-malononitrile *para*-methoxyphenyl *N*-substituted phenothiazines on the electrochemical, spectro scopic, and charge-transport properties. To our surprise, molecule **O-1** exhibited not only higher hole-mobility in comparison to **O-2** and **O-3** but, to the best of our knowledge, the highest bulk hole-mobility ever reported in the context of phenothiazine-based small molecules. The relation between the molecular structure, structural (X-ray) analysis, and the outstanding bulk mobility of **O-1** with respect to the other two proposed phenothiazines (**O-2**, **O-3**) is also discussed in detail.

## Results and Discussion

**Synthesis.** The synthesis route of **O-1**, **O-2**, and **O-3** is depicted in Fig. 2. 10-(4-Methoxyphenyl)-10*H*-phenothiazine 1 was prepared (75% yield) in one-step reaction via Ullmann-coupling of 4-iodoanisole and commercially available phenothiazine, according to a previously reported procedure[9]. The subsequent Vilsmeier-Haack formylation of 1 in 1,2-dichloroethane produced its mono-formyl derivative 2 in 85% yield. The Knoevenagel-condensation reaction of 2 with an excess amount of malononitrile in the presence of piperidine and chloroform afforded **O-1** in 87% yield. Bromination of 2 using *N*-bromosuccinimide (NBS) in chloroform produced its bromo-derivative 3 in 85% yield. Furthermore, Suzuki-coupling reaction of 3 with two different electron donors, 4-methoxyphenyl boronic acid and previously synthesized 2-(6-butoxynaphthalen-2-yl)-4,4,5,5-tetramethyl-1,3,2-dioxaborolane 7 in presence of catalyst $Pd(PPh_3)_4$ in inert atmosphere afforded compounds 4 and 5 in 66 and 65% of yields, respectively.

Finally, introduction of malononitrile to obtain **O-2** and **O-3** was achieved as described above for **O-1** in 85 and 81% yields, respectively. All the compounds were easily soluble in common organic solvents, which allowed their purification by column chromatography. All the reaction intermediates, as well as the final products, were characterized and confirmed by $^1$H NMR, $^{13}$C NMR and high-resolution mass spectroscopy (see Supplementary Information, SI, Figs S1–S11).

**UV-vis spectroscopy.** The UV-vis absorption spectra (in units of molar absorptivity, ε) of **O-1**, **O-2**, and **O-3** in chloroform solution (concentration $10^{-5}$ M), together with the absorption spectra of thin films normalised at the Soret-transition (S0-S2) absorption maximum, are shown in Fig. 3 and summarised in Table 1. The absorption spectra of the three molecules show two distinct bands: one at 320–330 nm and another at 490–510 nm. The former corresponds to π-π* electronic transition of the chromophores (Soret band). The latter is attributed to the intra- molecular charge transfer (ICT) from the donor to the acceptor moieties (Q band). As can be seen from Fig. 3, the Soret and Q bands are comparable, with slightly higher intensity for the Soret bands. Furthermore,

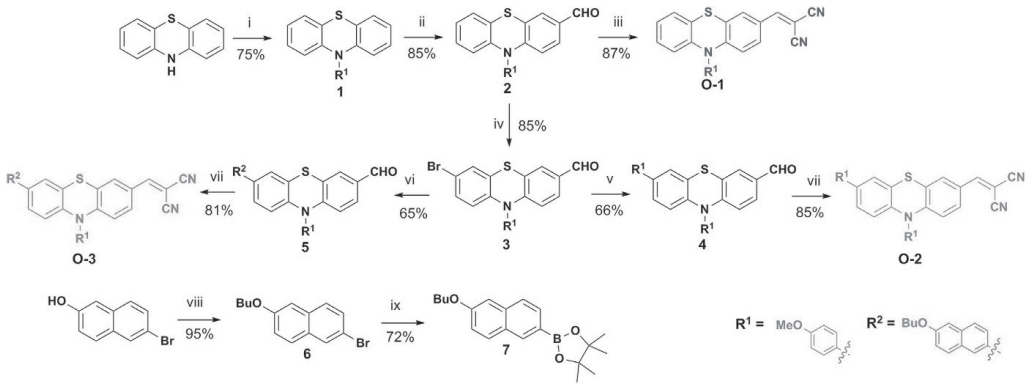


**Figure 2. Synthesis of push-pull organic semiconductors O-1, O-2 and O-3.** Reagents: (i) 4-Iodoanisole, Cu, $K_2CO_3$, TEGDME, 180 °C; (ii) $POCl_3$, DMF, $C_2H_4Cl_2$, 80 °C; (iii and (vii) $CH_2(CN)_2$, Piperidine, $CHCl_3$, reflux; (iv) N-Bromosuccinimide, $CHCl_3$, rt; (v) 4-methoxyphenyl boronic acid, $Pd(PPh_3)_4$, $K_2CO_3$ (2M), THF; (vi) 2-(6-butoxynaphthalen-2-yl)-4,4,5,5-tetramethyl-1,3,2-dioxoborolane, $Pd(PPh_3)_4$, $K_2CO_3$ (2M), THF; (viii) 1-bromobutane, KOH, DMSO, rt; (ix) bis(pinacolato)diboron, $Pd(dppf)Cl_2$, KOAc, 1,4-dioxane, 80 °C.

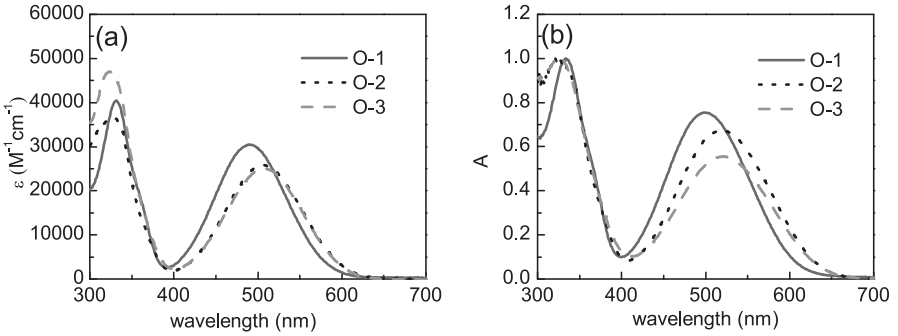


**Figure 3.** (**a**) molar absorptivity (ε) of **O-1**, **O-2** and **O-3** in chloroform solution; (**b**) absorption spectra of freshly prepared films of the target compounds.

| Compound | $\lambda_{max}$ (nm)[a] | ε at $\lambda_{max}$ ($M^{-1}cm^{-1}$) | $\lambda_{max}$ (nm)[b] | $E_g^{opt}$ (eV) | $E_g$ (eV) | $HOMO^{DPV}$ (eV)[c] | $LUMO^{opt}$ (eV)[d] | $T_d/T_m$ (°C)[e] |
|---|---|---|---|---|---|---|---|---|
| **O-1** | 330, 490 | 30 437 | 333, 500 | 2.06 | 2.09 | −5.29 | −3.16 | 302/199 |
| **O-2** | 331, 507 | 25 757 | 324, 518 | 2.02 | 2.08 | −5.24 | −3.23 | 386/194 |
| **O-3** | 523, 509 | 24 957 | 325, 521 | 2.00 | 2.08 | −5.24 | −3.27 | 404/163 |

**Table 1. Optical, electrochemical, and thermal characterisation of O-1, O-2, and O-3.** Wavelengths corresponding to the absorption maxima in [a]$10^{-5}$ M chloroform solution and in [b]film samples, spin-coated from chloroform solution. [c]$HOMO^{DPV}$ values were determined experimentally by DPV measurements. [d]$LUMO^{opt}$ is derived from optical bandgap (Eg), *i.e.* from the onset of the absorption spectrum ($E = hc/\lambda$). $LUMO^{opt} = E_g^{opt} - HOMO^{DPV}$. [e]$T_d$ is determined from TGA (see SI), $T_m$ measured with open capillary method.

for compounds **O-2** and **O-3**, the absorption maxima are overlapping (shift in $\lambda_{max}$ of 2 nm), while **O-1** absorption peaks are slightly blue-shifted by 12–13 nm. The red-shift of the absorption maxima of **O-2** and **O-3** with respect to **O-1** can be attributed to their slightly more extended conjugation. The absorption spectra of the films spin-coated onto glass substrates are bathocromically-shifted by 10–12 nm as compared to the spectra measured in solution, most likely due to chromophore-chromophore intermolecular interactions[58].

**Electrochemical analysis.** The electrochemical properties of **O-1**, **O-2**, and **O-3** were determined by differential pulse voltammetry (DPV) in dichloromethane solution. The voltammograms, *i.e.* changes in current-voltage curves, are presented in SI with respect to the ferrocene couple (Fig. S13). The highest occupied molecular orbital (HOMO) levels, corresponding to the ionization potentials of the materials, were derived from

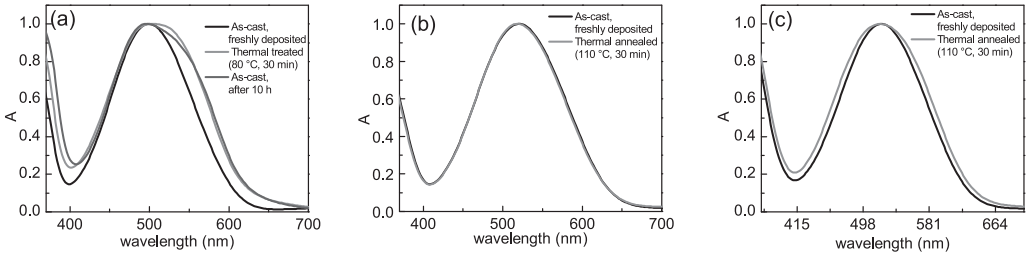


**Figure 4.** Normalised absorption spectra of **O-1** (**a**), **O-2** (**b**) and **O-3** (**c**) films, spin-coated from chlorobenzene solutions. Spectra of as-cast freshly deposited films, of as-cast films after 10 h at room temperature, and of thermally annealed films are shown.

DPV and are presented in Table 1. All the compounds exhibited similar electrochemical properties: the HOMO values lie in the range of −5.24 to −5.29 eV. Since no clear reduction peaks were appreciated from the voltammograms of Fig. S12, the LUMO values were derived from the optical bandgap ($E_g^{opt}$) reported in Table 1, as explained in the Methods section.

**Thermal analysis.** The thermal properties of **O-1**, **O-2**, and **O-3** were investigated with differential scanning calorimetry (DSC) and thermogravimetric analysis (TGA). Interestingly, given its lowest molecular weight in the series, DSC data in Fig. S13a (SI) showed a higher melting point for **O-1** (199 °C) compared to **O-2** (194 °C) and **O-3** (163 °C). This can be attributed to its molecular packing and tendency towards crystallisation, as detailed later on. In case of **O-3**, large drop in the melting point was observed as compared to **O-2**, probably due to the presence of the butyl chain. The thermal decomposition temperatures ($T_d$) of the compounds were obtained from the TGA curves shown in Fig. S13b (SI), with an increasing trend with increasing molecular weight, *i.e.* **O-1** < **O-2** < **O-3**. The results of the thermal characterisation, summarized in Table 1, support the suitability of these materials for organic electronic device fabrication[59].

**Hole mobility characterisation.** The bulk hole mobility in films of **O-1**, **O-2**, and **O-3** was investigated by means of impedance spectroscopy[60] applied to hole-only devices. Upon injecting charge carriers, by applying a dc bias superimposed to small harmonic voltage modulation, dramatic changes were observed in the impedance spectra[61,62]. The transit time of charge carriers $\tau$ can be inferred from the peak frequency of the negative differential subsceptance[61,62] or from the peak frequency of the imaginary part of impedance (ImZ)[63]. For dispersive charge transport, the latter method is considered more convenient. Indeed, even in high dispersion conditions, clear peaks are observed in the ImZ spectrum[63].

The phenothiazine films for impedance spectroscopy measurements were deposited by spin-coating from chlorobenzene solutions. Differently from **O-2** and **O-3**, the optical properties of **O-1** films underwent a clear and spontaneous variation even at room temperature, leading in some hours to a change of colour visible to the naked eye. Moreover, the spectral variation of **O-1** films was greatly accelerated by the thermal treatment applied to remove the excess solvent. In Fig. 4a the absorption spectrum of a freshly deposited **O-1** film is compared with that obtained after thermal annealing at 80 °C for 30 min (in an Ar-filled glove-box) and with that of a film stored at ambient temperature for around 10 h. In the latter two cases, the spectra are similar and broader compared to the spectrum of the freshly deposited **O-1** film, with an enhanced absorption toward lower energies. The spontaneous change in the spectral properties of **O-1** films at room temperature and upon thermal annealing indicates enhanced intermolecular electronic interactions, possibly due to evolution towards a more ordered arrangement of **O-1** molecules in the solid state. The described behaviour was not observed for **O-2** and **O-3** films, which preserved to a large extent the original spectral features upon thermal treatment at 110 °C for 30 min (Fig. 4b and c). It should be noted that a lower temperature (80 °C), was applied for the thermal annealing of **O-1** films. That choice was motivated by the deterioration of **O-1** film compactness (appearance of pin-holes and cracks) upon heating above 80 °C, making them useless in the preparation of sandwich-type devices.

Hole-only devices for charge carrier mobility investigation were prepared with thermally annealed films, at 80 °C for **O-1**, and at 110 °C for **O-2** and **O-3**. The frequency dependence of ImZ for typical hole-only devices is shown in Fig. 5 for different values of the dc voltage. Clear peaks were observed for all molecules, shifting towards higher frequencies as the voltage increased. The transit time of charge carriers was obtained from the peak frequency through $\tau = k \cdot \tau_p$, where $\tau_p$ is the time constant corresponding to the peak frequency and $k$ a constant dependent on the dispersion degree[63]. The value of 0.44 was assumed for $k$, reported for a moderate degree of dispersion[63].

The hole mobility $\mu$ was calculated by using the well-known expression $\mu = d/E\ \tau$, where $d$ is the film thickness and $E$ the electric field. The obtained values are displayed in Fig. 6 as a function of $E^{1/2}$. An outstanding bulk mobility of positive charge carriers was achieved for **O-1** films, with values around $1 \times 10^{-3}$ cm$^2$ V$^{-1}$ s$^{-1}$. For **O-2** and **O-3**, $\mu$ dropped dramatically, by three orders of magnitude, as compared to **O-1** films, with values on the order of $10^{-6}$ cm$^2$ V$^{-1}$ s$^{-1}$ in the same field range. The linear trend of mobility data for **O-2** and **O-3** shown in Fig. 6 indicates a Poole-Frenkel-type behaviour of mobility[64,65]:

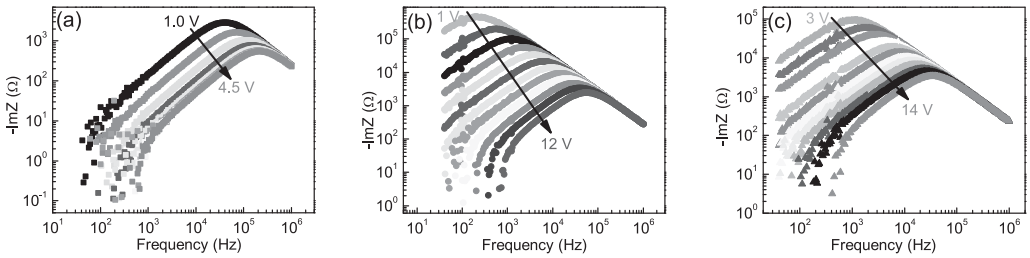


**Figure 5.** ImZ as a function of frequency for hole-only devices made of **O-1** (**a**), **O-2** (**b**) and **O-3** (**c**) films at different values of the dc voltage (the arrows indicate increasing voltage). Film thickness: 920 nm, 575 nm and 470 nm for **O-1**, **O-2** and **O-3**, respectively.

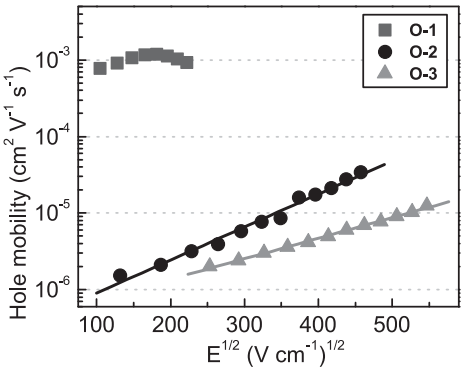


**Figure 6. Bulk hole mobility of O-1, O-2 and O-3 as a function of the square root of electric field.** For **O-2** and **O-3** the lines indicate the linear fit to the experimental data.

$$\mu = \mu_0 \exp(\gamma\sqrt{E}) \quad (1)$$

where $\mu_0$ denotes the mobility at zero field and $\gamma$ is the parameter describing how strong is the field dependence. The parameters for the Poole-Frenkel fit to the mobility data of **O-2** film are $\mu_0 = 3.4 \times 10^{-7}$ cm$^2$ V$^{-1}$ s$^{-1}$ and $\gamma = 9.9 \times 10^{-3}$ (V cm$^{-1}$)$^{-1/2}$, while $\mu_0 = 4.0 \times 10^{-7}$ cm$^2$ V$^{-1}$ s$^{-1}$ and $\gamma = 6.2 \times 10^{-3}$ (V cm$^{-1}$)$^{-1/2}$ were obtained for **O-3**.

To clarify the significant difference in charge transport properties of **O-1** with respect to **O-2** and **O-3**, we performed powder x-ray diffraction (XRD) analysis. The XRD patterns recorded on (i) film samples, prepared and treated in the same conditions used for the preparation of hole-only devices, and (ii) powder samples are compared in Fig. 7. The sharp peaks of the XRD patterns of the powder samples indicate a high degree of crystallinity for each of the three phenothiazines. For film samples, on the other hand, the XRD pattern of **O-1** indicates the presence of crystalline material also in the film, in the same phase as in the powder, while amorphous patterns were obtained for the **O-2** and **O-3** films. The presence of crystalline phase is well in line with the annealing-induced spectral changes observed in **O-1** films (Fig. 4a) and the absence of such changes for **O-2** and **O-3**.

XRD investigations of the films confirm that the outstanding bulk hole mobility in **O-1** films can be ascribed to the presence of crystalline phases, completely absent in the layers deposited from the other two phenothiazines. The high degree of ordering of **O-1** is probably due to its more compact and less twisted molecular structure as compared to **O-2** and **O-3.** The latter ones have bulkier substituents in the C(7) position, which are able to freely rotate (see the computational analysis), thereby decreasing the system order. Despite some exceptions on increased charge mobility with decreased π-π stacking[66], shorter π-π stacking distances typically leads to higher charge carrier mobility[1,67,68]. Hence, a better π-π stacking in case of **O-1** could be responsible for its high hole mobility (*ca.* $10^{-3}$ cm$^2$ V$^{-1}$ s$^{-1}$) whereas the more twisted nature of **O-2** and **O-3** leads to poor mobilities (*ca.* $10^{-6}$ cm$^2$ V$^{-1}$ s$^{-1}$). These low mobility values are comparable to those reported in the literature for other solution-deposited[32–35,69] and thermally evaporated[70] phenothiazine derivatives. To the best of our knowledge, the mobility of **O-1** is the highest reported for phenothiazine-based small molecules, without complexation with iodine.

**Computational analysis.** In order to get further insight into the electronic nature of the newly synthesised phenothiazines and to support our suggestion for the higher hole mobility of **O-1**, the compounds were studied

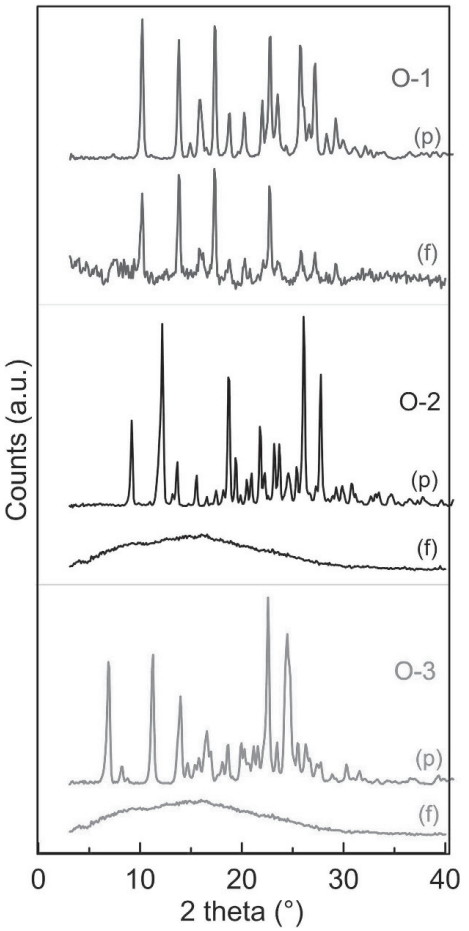


**Figure 7. XRD patterns of powder samples (p) and film samples (f).** All patterns are subtracted for the background of the substrates in order to enhance the presence of halos due to the amorphous component. The recorded patterns are reported in Figure S14. Film samples were prepared and thermally treated in the same conditions used for the preparation of hole-only devices.

by Density Functional Theory methods. Compounds **O-1** and **O-2** were optimised at the PBE1PBE/6-31G** level of theory, as well as **O-3**, simplified by replacement of the *n*-butyl chain with a methyl (**O-3(Me)**), and a detailed computational analysis can be found in the SI. The conformational analysis of the three phenothiazines studied showed that in the ground state the preferential conformations of the compounds are slightly bent in the phenothiazine heterocyclic ring and adopt a butterfly shape. The presence of different substituents at the C(7) position of the phenothiazine has little or no effect on the dihedral angles made by the two aromatic rings, being about 19–20° for the three molecules studied. The introduction of aryl substituents at C(7) position of phenothiazines **O-2** and **O-3(Me)** does not encumber the resonance between the substituents and the phenothiazine ring, although such substituents are preferentially placed ca. 34° out of the plane. The rotation of these substituents about the C-C bonds requires only 3.4 kcal/mol, which might explain the above-mentioned disorder of these systems and the absence of π-π stacking suggested for **O-1**.

The electronic distribution in HOMO and LUMO levels are presented in Fig. 8. The electron density distribution in the LUMO of the phenothiazines is mainly localised on the malononitrile end group and the adjacent benzene ring, while in **O-2** and **O-3(Me)** the HOMO orbitals are delocalised over the phenothiazine moiety and its C(7) substituents. Clearly, introduction of electron-rich substituents in the C(7) position of the phenothiazine increases their HOMO energy while keeping the energy of LUMO orbitals localised on the acceptor end. The $\lambda_{max}$ found reflects the observed experimental trends, although the absolute values for the excitation energies are overestimated by the method (by *ca.* 0.9–1.1 eV). As similar electronic features were determined for these three

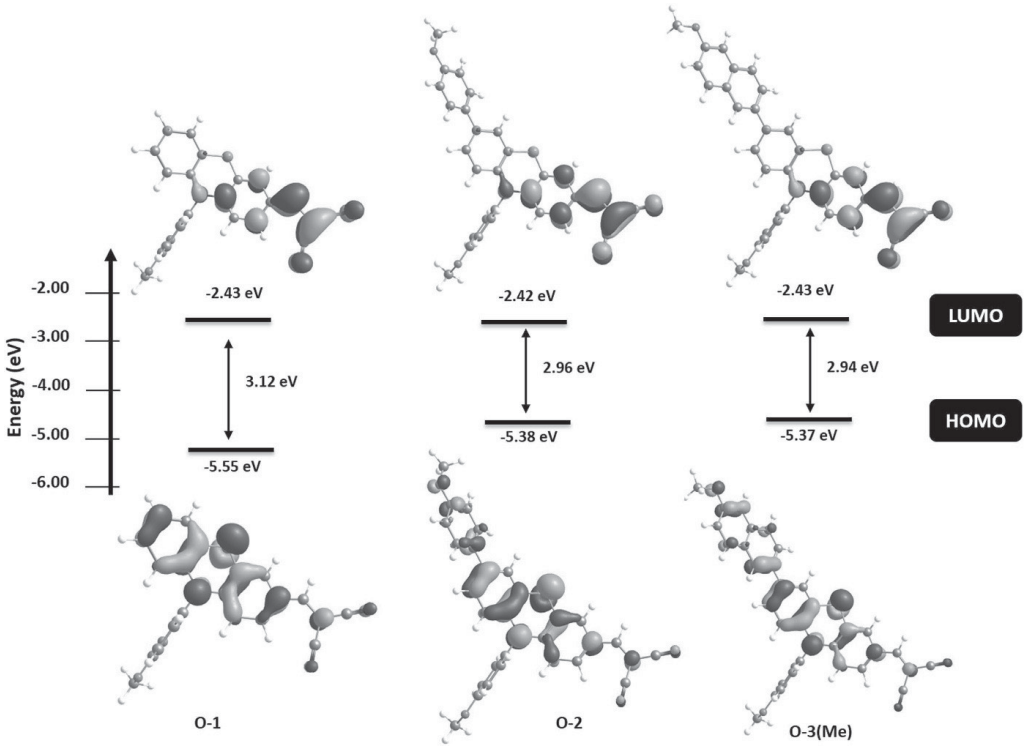


**Figure 8. Energy levels and electron distribution for frontier molecular orbitals of O-1, O-2 and O-3(Me) calculated with DFT at PBE1PBE/6-31G** level of theory (isosurface value = 0.04).**

phenothiazines, the higher charge mobility of **O-1** should not be attributed to the modification of the electron density by introduction of substituents at C(7), but to the lower degrees of freedom of **O-1**.

**Conclusions.** A series of new donor-acceptor systems based on C(7)-substituted phenothiazine derivatives was synthesised with good overall yields. The presence of crystalline phases in spin-coated films prepared with the unsubstituted phenothiazine **O-1**, arising from the chemical structure of the compound, likely leads to excellent π-π stacking. While the introduction of bulky *para*-methoxyphenyl and 6-butoxynaphthyl terminal groups in C(7) position of **O-2** and **O-3** has a weak impact on the optical and electrochemical characteristics of the compounds, it has a strong influence on the structural properties of the related spin-coated thin films. In fact, disorder is introduced into **O-2** and **O-3** compounds, by making them more twisted, as the rotation of the bulky substituents requires as little as 3.4 kcal/mol. This explains the observed amorphous nature of **O-2** and **O-3** films. The values of the bulk hole mobility of **O-2** and **O-3** samples (in order of $10^{-6}$ $cm^2$ $V^{-1}$ $s^{-1}$) lie in the typical range of state-of-the-art phenothiazines, while **O-1** shows an outstanding mobility in the order of $10^{-3}$ $cm^2$ $V^{-1}$ $s^{-1}$, the highest reported for phenothiazine-based materials. The achievements of this study provide a strong motivation to further design phenothiazine-based donor-acceptor systems with high bulk mobility, to be adopted as hole-transport materials for organic electronics. Work in this direction is underway and will be reported in future publications.

## Methods

**Synthesis.** All chemicals were purchased from Sigma Aldrich and were used without further purification. The chemical reactions were carried out using round-bottom flasks and Schlenk tubes under argon or nitrogen environment. $^1$H NMR and $^{13}$C NMR spectra were recorded on Bruker spectrometer ($^1$H, 400 MHz and $^{13}$C, 100 MHz) in $CDCl_3$. Chemical shifts were given in ppm with reference to tetramethyl silane (TMS). Molecular mass was determined by using Thermo Scientific Q-Exactive Accela 1250 pump mass spectrometer. Purification of the products was carried out by column chromatography on silica gel 60 (Sigma Aldrich) with mesh size 0.040–0.063 mm. The complete details on the synthesis of **O-1**, **O-2**, **O-3** and their intermediate products are provided in SI.

**Spectroscopic measurements.** The steady-state absorption spectra were measured with a Shimadzu UV-3600 UV/Vis/NIR spectrophotometer both in solution and in thin films. Thin films of the three compounds were deposited by spin-coating (WS-400B-6NPP/LITE, Laurell Technologies) from $CHCl_3$ solution (1700 rpm, 1 min) onto clean glass substrates.

**Electrochemical Measurements.** Differential pulse voltammetry (DPV), for HOMO/LUMO determination of the target compounds, was performed by employing a potentiostat (Compact-Stat, Ivium Technologies) and a three-electrode cell configuration. Dry tetrabutyl ammonium tetrafluoroborate in dichloromethane (0.1 M) was the supporting electrolyte, glass platinum electrode the working electrode, Pt wire the counter-electrode, and Ag/AgCl wire the pseudo-reference electrode. Ferrocene/ferrocenium (Fc/Fc+) couple was used as an internal standard reference to scale the measured potentials against the vacuum level[17]. All solutions were deoxygenated with $N_2$ prior to each experiment. The measurements were carried out between −2.2 V and 2.0 V, scanning in both directions with scan rate of 50 mV/s The HOMO energy levels were calculated from the oxidation potentials observed from the DPV curves according to the equation:

$$E_{HOMO}(eV) = -(E_{ox} - E_{Fc/Fc+}) - 4.80\ eV \quad (2)$$

where $E_{ox}$ is the oxidation potential of the sample and $E_{Fc/Fc+}$ the potential of ferrocene. $E_{ox}$ and $E_{Fc/Fc+}$ are both referred against the Ag/AgCl reference electrode. The value −4.80 eV is the energy level of ferrocene against vacuum[71]. The LUMO levels were derived from the optical bandgap, since no clear reduction peaks could be appreciated from the DPV curves:

$$E_{LUMO}(eV) = E_g^{opt} - E_{HOMO} \quad (3)$$

**Charge carrier mobility measurements.** Hole-only devices were prepared in the sandwiched structure ITO/PEDOT:PSS/phenothiazine/$MoO_3$/Au, where ITO is indium tin oxide and PEDOT:PSS is poly(3, 4-ethylenedioxythiophene)/polystyrene sulphonic acid (CLEVIOS P VP AI 4083, H.C. Starck). ITO-coated glass substrates were first cleaned in detergent and water, then ultrasonicated in acetone and isopropyl alcohol for 15 min each. The layer of PEDOT:PSS (~40 nm) was spin-coated at 4000 rpm onto the ITO-glass substrates, and baked in an oven at 120 °C for 10 min. The phenothiazine layers were deposited under ambient conditions by spin-coating (300 rpm) from chlorobenzene solutions (65–70 g/l). After the deposition, the films were transferred in an Ar-filled glove-box, where a thermal treatment was applied to remove the excess solvent before the top contact deposition. The $MoO_3$ layer (5 nm) and the Au top electrode (100 nm) were thermally evaporated at a base pressure of $4 \times 10^{-6}$ mbar through a shadow mask defining a device active area of 8 $mm^2$.

The electrical characterization of the devices was carried out at room temperature in glove-box. Impedance spectroscopy measurements were conducted using an Agilent 4294A impedance analyzer. The impedance measurements were done in the frequency range 40 Hz–1.4 MHz, with an amplitude of the harmonic voltage modulation of 20 mV. The dc bias was varied in the range 0 V–14 V.

**XRD investigation.** The powder samples were analysed in an aluminium sample-holder 0.2 mm deep. The film samples were deposited on quartz plates by using the same conditions used for the preparation of the phenothiazine layers for hole-only devices. After the deposition, the film samples were thermally annealed in the same conditions used for the related devices. The XRD scans were performed in the interval 5–60° (2theta) with a PANalytical X'Pert diffractometer in reflection geometry equipped with a copper anode (λmean = 1.5418 Å) and a fast X'Celerator detector.

**Computational Calculations.** Full geometrical optimizations were performed by Density Functional Theory[72] using PBE1PBE/6-31G** hybrid functional and influence of solvent ($CHCl_3$) was taken into account by the application of the polarized continuum model using the Gaussian09 program. The vertical excitations of the optimized ground state geometries were further calculated with the time-dependent DFT (TDDFT)[73] method and the linear response PCM ($CHCl_3$ as solvent) to determine the first-six transitions. A full account on the computational details and the corresponding reference list are presented as SI.

## References


1. Coropceanu, V. *et al.* Charge transport in organic semiconductors. *Chem. Rev.* **107,** 926–952 (2007).
2. Sirringhaus, H., Tessler, N. & Friend, R. H. Integrated optoelectronic devices based on conjugated polymers. *Science* **280,** 1741–1744 (1998).
3. Mandoc, M. M., Koster, L. J. A. & Blom, P. W. M. Optimum charge carrier mobility in organic solar cells. *Appl. Phys. Lett.* **90.** 133504 (2007).
4. Yoshikawa, S., Saeki, A., Saito, M., Osaka, I. & Seki, S. On the role of local charge carrier mobility in the charge separation mechanism of organic photovoltaics. *Phys. Chem. Chem. Phys.* **17,** 17778–17784 (2015).
5. Mishra, M. & Bäuerle, P. Small molecule organic semiconductors on the move: promises for future solar energy technology. *Angew. Chemie Int. Ed.* **51,** 2020–2067 (2012).
6. Liu, Y. *et al.* Solution-processed small-molecule solar cells: breaking the 10% power conversion efficiency. *Sci. Rep.* **3,** 3356 (2013).
7. Roncali, J., Leriche, P. & Blanchard, P. Molecular Materials for Organic Photovoltaics: Small is Beautiful. *Adv. Mater.* **26,** 3821 (2014).
8. Mohamed, S., Demeter, D., Laffitte, J.-A., Blanchard, P. & Roncali, J. Structure-properties relationships in triarylamine-based donor-acceptor molecules containing naphtyl groups as donor material for organic solar cells. *Sci. Rep.* **5,** 9031 (2015).
9. Salunke, J. K. *et al.* Phenothiazine and carbazole substituted pyrene based electroluminescent organic semiconductors for OLED devices. *J. Mater. Chem. C* **4,** 1009–1018 (2016).
10. Yu, T. C., Liu, L. L., Xie, Z. Q. & Ma, Y. G. Progress in small-molecule luminescent materials for organic light-emitting diodes. *Sci. China-Chemistry* **58,** 907–915 (2015).

11. Wu, W., Liu, Y. & Zhu, D. π-Conjugated molecules with fused rings for organic field-effect transistors: design, synthesis and applications. *Chem. Soc. Rev.* **39,** 1489–1502 (2010).
12. Yan, H. *et al.* A high-mobility electron-transporting polymer for printed transistors. *Nature* **457,** 679–686 (2009).
13. Yu, G., Gao, J., Hummelen, J. C., Wudl, F. & Heeger, A. J. Polymer Photovoltaic Cells: Enhanced Efficiencies via a Network of Internal Donor-Acceptor Heterojunctions. *Science* **270,** 1789–1791 (1995).
14. Bazan, G. & Bryce, M. R. Themed issue on small molecules and monodisperse oligomers for organic electronics. *J. Mater. Chem. C* **4,** 3675–3676 (2016).
15. Wu, T. Y. *et al.* Synthesis, Characterization and Photovoltaic Properties of Di-Anchoring Organic Dyes. *J. Braz. Chem. Soc.* **22,** 780–789 (2011).
16. Krämer, C. S., Zeitler, K. & Müller, T. J. J. First Synthesis and Electronic Properties of (Hetero)aryl Bridged and Directly Linked Redox Active Phenothiazinyl Dyads and Triads. *Tetrahedron Lett.* **42,** 8619–8624 (2001).
17. Sailer, M., Franz, A. W. & Müller, T. J. J. Synthesis and Electronic Properties of Monodisperse Oligophenothiazines. *Chem. - A Eur. J.* **14,** 2602–2614 (2008).
18. Memminger, K., Oeser, T. & Müller, T. J. J. Phenothiazinophanes: Synthesis, Structure, and Intramolecular Electronic Communication. *Org. Lett.* **10,** 2797–2800 (2008).
19. Oka, H. Synthesis and through-bond spin interaction of stable 1,3-phenylene linked poly(phenothiazine cation radical). *J. Mater. Chem.* **18,** 1927–1934 (2008).
20. Hong, B. C., Dange, N. S., Ding, C. F. & Liao, J. H. Organocatalytic Michael–Knoevenagel–Hetero-Diels–Alder Reactions: An Efficient Asymmetric One-Pot Strategy to Isochromene Pyrimidinedione Derivatives. *Org. Lett.* **14,** 448–451 (2012).
21. Okamoto, T. *et al.* Remarkable Structure Deformation in Phenothiazine Trimer Radical Cation. *Org. Lett.* **6,** 3493–3496 (2004).
22. Wu, W. *et al.* Efficient and stable dye-sensitized solar cells based on phenothiazine sensitizers with thiophene units. *J. Mater. Chem.* **20,** 1772 (2010).
23. Kim, M. J. *et al.* Tuning of spacer groups in organic dyes for efficient inhibition of charge recombination in dye-sensitized solar cells. *Dye. Pigment.* **95,** 134–141 (2012).
24. Qiu, X. *et al.* Synthesis of phenothiazine-functionalized porphyrins with high fluorescent quantum yields. *Tetrahedron Lett.* **49,** 7446–7449 (2008).
25. Tian, H. *et al.* Phenothiazine derivatives for efficient organic dye-sensitized solar cells. *Chem. Commun.* (*Camb.*) **36,** 3741–3743 (2007).
26. Liang, M. & Chen, J. Arylamine organic dyes for dye-sensitized solar cells. *Chem. Soc. Rev.* **42,** 3453–3488 (2013).
27. Kim, S. H. *et al.* Effect of Five-Membered Heteroaromatic Linkers to the Performance of Phenothiazine-Based Dye-Sensitized Solar Cells. *Org. Lett.* **13,** 5784–5787 (2011).
28. Huang, Z.-S., Meier, H. & Cao, D. Phenothiazine-based dyes for efficient dye-sensitized solar cells. *J. Mater. Chem. C* **4,** 2404–2426 (2016).
29. Kim, S. H. *et al.* The effect of N-substitution and ethylthio substitution on the performance of phenothiazine donors in dye-sensitized solar cells. *Dyes Pigments* **97,** 262–271 (2013).
30. Cao, D. *et al.* Enhanced Performance of the Dye-Sensitized Solar Cells with Phenothiazine-Based Dyes Containing Double D−A Branches. *Org. Lett.* **13,** 1610–1613 (2011).
31. Park, S. S., Won, Y. S., Choi, Y. C. & Kim, J. H. Molecular Design of Organic Dyes with Double Electron Acceptor for Dye-Sensitized Solar Cell. *Energy and Fuels* **23,** 3732–3736 (2009).
32. Huang, J. H. & Lee, K. C. Highly Stable, Solution-Processable Phenothiazine Derivative as Hole Collection Material for Organic Solar Cells. *ACS Appl. Mater. Interfaces* **6,** 7680–7685 (2014).
33. Li, Z. *et al.* Design and synthesis of solution processable small molecules towards high photovoltaic performance. *J. Mater. Chem.* **21,** 2159–2168 (2011).
34. Kumar, S., Singh, M., Jou, J.-H. & Ghosh, S. Trend breaking substitution pattern of phenothiazine with acceptors as a rational design platform for blue emitters. *J. Mater. Chem. C* **4,** 6769–6777 (2016).
35. Ahn, Y. *et al.* Electroluminescence Characteristics of a New Green-Emitting Phenylphenothiazine Derivative with Phenylbenzimidazole Substituent. *Bull. Korean Chem. Soc.* **34,** 107–111 (2013).
36. Fidder, H., Knoester, J. & Wiersma, D. A. Optical properties of disordered molecular aggregates: A numerical study. *J. Chem. Phys.* **95,** 7880–7890 (1991).
37. Spano, F. C. The Spectral Signatures of Frenkel Polarons in H- and J-Aggregates. *Acc. Chem. Res.* **43,** 429–439 (2010).
38. Chang, J.-F. *et al.* Molecular-weight dependence of interchain polaron delocalization and exciton bandwidth in high-mobility conjugated polymers. *Phys. Rev. B* **74,** 115318 (2006).
39. Sun, X. *et al.* Novel Electroactive and Photoactive Molecular Materials Based on Conjugated Donor−Acceptor Structures for Optoelectronic Device Applications. *J. Phys. Chem. B* **109,** 10786–10792 (2005).
40. Sang, G., Zou, Y. & Li, Y. Two Polythiophene Derivatives Containing Phenothiazine Units: Synthesis and Photovoltaic Properties. *J. Phys. Chem. C* **112,** 12058–12064 (2008).
41. Siu, C. H. *et al.* Synthesis and Characterization of Phenothiazine-Based Platinum(II)–Acetylide Photosensitizers for Efficient Dye-Sensitized Solar Cells. *Chem. - A Eur. J.* **22,** 3750–3757 (2016).
42. Blanco, G. D. *et al.* Syntheses, Charge Separation, and Inverted Bulk Heterojunction Solar Cell Application of Phenothiazine–Fullerene Dyads. *ACS Appl. Mater. Interfaces* **8,** 8481–8490 (2016).
43. Tan, Q. *et al.* Application of Small Molecule Donor Materials Based on Phenothiazine Core Unit in Bulk Heterojunction Solar Cells. *J. Phys. Chem. C* **118,** 16851–16855 (2014).
44. Matsunaga, Y. Some new organic semiconductors : thiazineiodine complexes. *Helv. Phys. Acta* **36,** 800–802 (1963).
45. Matsunaga, Y. Infrared spectra in the characterization of some molecular complexes of the dative type. *J. Chem. Phys.* **41,** 1609–1613 (1964).
46. Kan, K. & Matsunaga, Y. The Electrical Properties of Iodine Complexes of N-Methyl-and N-Ethyl-phenothiazines and Their Mixtures. *Bull. Chem. Soc. Jpn.* **45,** 2096–2100 (1972).
47. Matsunaga, Y. & Suzuki, Y. Electrical and Optical Properties of the Iodine Complexes of Phenoxazine, Phenoselenazine, and Benzophenothiazines. *Bull. Chem. Soc. Jpn.* **45,** 3375–3379 (1972).
48. Matsunaga, Y. & Suzuki, Y. The Cation-radical Salts Derived from Benzo- and Dibenzo-phenothiazines. *Bull. Chem. Soc. Jpn.* **46,** 719–722 (1973).
49. Matsunaga, Y. *Energy and Charge Transfer in Organic Semiconductors*, Springer US: Boston, MA, (1974).
50. Doi, S., Inabe, T. & Matsunaga, Y. Electrical Properties and Constitution of the Phenothiazine–Iodine and Related Complexes. *Bull. Chem. Soc. Jpn.* **50,** 837–841 (1977).
51. Bakulin, A. A. *et al.* The role of driving energy and delocalized States for charge separation in organic semiconductors. *Science* **335,** 1340–1344 (2012).
52. Shoaee, S. *et al.* Acceptor Energy Level Control of Charge Photogeneration in Organic Donor/Acceptor Blends. *J. Am. Chem. Soc.* **132,** 12919–12926 (2010).
53. Chang, Y. J. *et al.* Organic dyes containing oligo-phenothiazine for dye-sensitized solar cells. *J. Mater. Chem.* **22,** 21704–21712 (2012).

54. Iqbal, Z. *et al.* Phenothiazine-based dyes with bilateral extension of π-conjugation for efficient dye-sensitized solar cells. *Dyes Pigments* **96,** 722–731 (2013).
55. Hua, Y. *et al.* Co-sensitization of 3D bulky phenothiazine-cored photosensitizers with planar squaraine dyes for efficient dye-sensitized solar cells. *J. Mater. Chem. A* **3,** 13848–13855 (2015).
56. Lin, R. Y.-Y. *et al.* High-Performance Aqueous/Organic Dye-Sensitized Solar Cells Based on Sensitizers Containing Triethylene Oxide Methyl Ether. *ChemSusChem* **8,** 2503–2513 (2015).
57. Bejan, A., Shova, S., Damaceanu, M.-D., Simionescu, B. C. & Marin, L. Structure-Directed Functional Properties of Phenothiazine Brominated Dyes: Morphology and Photophysical and Electrochemical Properties. *Cryst. Growth Des.* **16,** 3716–3730 (2016).
58. Würthner, F., Kaiser, T. E. & Saha-Möller, C. R. J-Aggregates: From Serendipitous Discovery to Supramolecular Engineering of Functional Dye Materials. *Angew. Chemie - Int. Ed.* **50,** 3376–3410 (2011).
59. Heeger, A. J. 25th Anniversary Article: Bulk Heterojunction Solar Cells: Understanding the Mechanism of Operation. *Adv. Mater.* **26,** 10–28 (2014).
60. Macdonald, J. R. & Kenan, W. R. *Impedance Spectroscopy: Emphasizing Solid Materials and Systems*, Wiley-Interscience: New York, (1987).
61. Tanase, C., Meijer, E. J., Blom, P. W. M. & De Leeuw, D. M. Unification of the Hole Transport in Polymeric Field-Effect Transistors and Light-Emitting Diodes. *Phys. Rev. Lett.* **91,** 216601 (2003).
62. Kassing, R. Calculation of the frequency dependence of the admittance of SCLC diodes. *Phys. status solidi* **28,** 107–117 (1975).
63. Tripathi, D. C., Tripathi, A. K. & Mohapatra, Y. N. Mobility determination using frequency dependence of imaginary part of impedance (Im Z) for organic and polymeric thin films. *Appl. Phys. Lett.* **98,** 033304 (2011).
64. Frenkel, J. On Pre-Breakdown Phenomena in Insulators and Electronic Semi-Conductors. *Phys. Rev.* **54,** 647–648 (1938).
65. Poole, H. H. On the dielectric constant and electrical conductivity of mica in intense fields. *Philos. Mag. Ser.* **32,** 112–129 (1916).
66. Dou, J. H. *et al.* Systematic Investigation of Side-Chain Branching Position Effect on Electron Carrier Mobility in Conjugated Polymers. *Adv. Funct. Mater.* **24,** 6270–6278 (2014).
67. Ma, Z., Geng, H., Wang, D. & Shuai, Z. Influence of alkyl side-chain length on the carrier mobility in organic semiconductors: herringbone vs. pi–pi stacking. *J. Mater. Chem. C* **4,** 4546–4555 (2016).
68. Anthony, J. E. Functionalized Acenes and Heteroacenes for Organic Electronics. *Chem. Rev.* **106,** 5028–5048 (2006).
69. Laurinaviciute, R., Ostrauskaite, J., Skuodis, E., Grazulevicius, G. V. & Jankauskas, V. *Synth. Met.* **192,** 50–55 (2014).
70. Cheng, Y.-J. *et al.* A phenothiazine/dimesitylborane hybrid material as a bipolar transport host of red phosphor. *J. Mater. Chem. C* **4,** 9499–9508 (2016).
71. D'Andrade, B. W. *et al.* Relationship between the ionization and oxidation potentials of molecular organic semiconductors. *Org. Electron. physics, Mater. Appl.* **6,** 11–20 (2005).
72. Parr, R. G. & Yang, W. *Density-functional theory of atoms and molecules*, Oxford University Press, New York, (1989).
73. Casida, M. E. *Recent Advances in Density Functional Methods*, ed. D. P. Chong, World Scientific: Singapore (1995).


## Acknowledgements

Academy of Finland is gratefully acknowledged for funding (Decisions No. 268672, 277091, 284553, 287954 and 294067). A.P. also acknowledges the financial support of the Emil Aaltonen Foundation. DBS is thankful to University Grants Comission (UGC), New Delhi, for the research fellowship.

## Author Contributions

D.B.S. synthesized the 3 molecules. J.S. designed the materials and participated to the spectroscopic/electrochemical characterization. N.R.C. took care of the computational analysis. F.T. carried out the bulk mobility measurements. M.G. carried out the X-ray analysis. P.P.W., N.C., and A.P. supervised the experimental work. P.V. coordinated the experiments and the writing, and participated to the spectroscopic/electrochemical work. All the authors contributed to the writing of the manuscript.

## Additional Information

**Supplementary information** accompanies this paper at http://www.nature.com/srep

**Competing Interests:** The authors declare no competing financial interests.

**How to cite this article**: Shinde, D. B. *et al.* Crystallisation-enhanced bulk hole mobility in phenothiazine-based organic semiconductors. *Sci. Rep.* **7**, 46268; doi: 10.1038/srep46268 (2017).

**Publisher's note:** Springer Nature remains neutral with regard to jurisdictional claims in published maps and institutional affiliations.

# PUBLICATION II

Phenothiazine-Based Hole-Transporting Materials toward Eco-friendly Perovskite Solar Cells

Jagadish Salunke, Xing Guo, Zhenhua Lin, Joaõ R. Vale, Nuno R. Candeias, Mathias Nyman, Staffan Dahlströ̈m, Ronald Ö̈sterbacka, Arri Priimagi, Jingjing Chang, and Paola Vivo

*ACS Appl. Energy Mater. 2019, 2, 3021-3027.*
DOI: 10.1021/acsaem.9b00408

ACS APPLIED ENERGY MATERIALS

Letter

Cite This: ACS Appl. Energy Mater. 2019, 2, 3021−3027

www.acsaem.org

# Phenothiazine-Based Hole-Transporting Materials toward Eco-friendly Perovskite Solar Cells

Jagadish Salunke,*[,†] Xing Guo,[‖] Zhenhua Lin,[‖] João R. Vale,[†,§] Nuno R. Candeias,[†] Mathias Nyman,[‡] Staffan Dahlström,[‡] Ronald Österbacka,[‡] Arri Priimagi,[†] Jingjing Chang,*[,‖] and Paola Vivo*[,†]

[†]Faculty of Engineering and Natural Sciences, Tampere University, P. O. Box 541, 33101 Tampere, Finland

[‡]Physics, Faculty of Science and Engineering and Center for Functional Materials, Åbo Akademi University, Porthansgatan 3, 20500 Turku, Finland

[§]Instituto de Investigação do Medicamento (iMed.ULisboa), Faculdade de Farmácia, Universidade de Lisboa, Avenida Professor Gama Pinto, 1649-003 Lisboa, Portugal

[‖]State Key Discipline Laboratory of Wide Band Gap Semiconductor Technology, Shaanxi Joint Key Laboratory of Graphene, School of Microelectronics, Xidian University, 2 South Taibai Road, Xi'an 710071, People's Republic of China

*Supporting Information*

**ABSTRACT:** Organic hole-transporting materials (HTMs), AZO-I and AZO-II, were synthesized via Schiff base chemistry by functionalizing a phenothiazine core with triarylamine(s) through azomethine bridges. Substantial enhancements in the power conversion efficiency (PCE = 12.6% and 14% for AZO-I and AZO-II, respectively) and stability (68% or 91% of PCE retained after 60 days for AZO-I or AZO-II, respectively) of perovskite solar cells (PSCs) were achieved when switching from mono- (AZO-I) to disubstituted (AZO-II) HTMs. The extremely low production costs (9 and 12 $/g for AZO-I and AZO-II, respectively), together with the Pd-catalyst-free synthesis, make these materials excellent candidates for low-cost and eco-friendly PSCs.

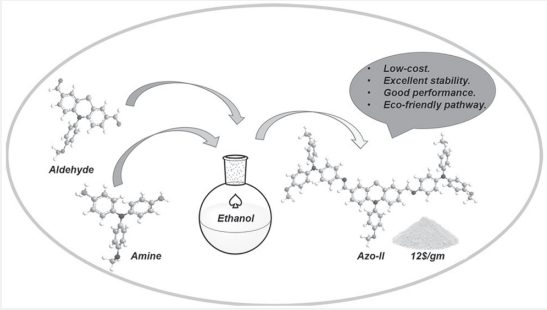


**KEYWORDS:** *phenothiazine, azomethine, hole-transporting materials, perovskite solar cells, eco-friendly, low-cost, stability*

Halide perovskite solar cells (PSCs) have recently received tremendous attention, due to their low-cost, high flexibility, low-temperature processing, and the skyrocketing rise of their power conversion efficiency (PCE), from 3.8% to 23.7%, in just less than a decade.[1,2] The excellent performance, together with the above-mentioned key features of PSCs, make them an attractive alternative to conventional photovoltaic technologies. PSCs consist of hole-transporting material (HTM), a light-absorbing layer (perovskite), and electron-transporting material (ETM), between two electrodes. The HTM layer plays a key role in PSCs as it facilitates the hole transfer from perovskite to the electrode and suppresses recombination, and also protects the perovskite surface against degradation due to moisture/oxygen.[3]

To date, most high-performance PSCs are based on either small molecular 2,2′,7,7′-tetrakis(*N*,*N*-di-*p*-methoxyphenylamine)-9,9′-spirobifluorene (spiro-OMeTAD) or polymeric poly[bis(4-phenyl)(2,4,6-trimethylphenyl)amine] (PTAA) HTM.[3] However, these materials are tremendously pricey (91.67 $/g (raw material cost)[4] and 2190 $/g (retail price)[5] for spiro-OMeTAD and PTAA, respectively) and also have major drawbacks such as low hole mobility, complex multistep synthesis, and difficult purification.[3] Thus, small-molecule HTMs based on pyrene,[6] carbazole,[7] phenothiazine,[8,9] dissymmetric fluorene−dithiophene (FDT),[10] fluorene terminated molecules,[14] and several others have been proposed as alternatives to spiro-OMeTAD.[3]

Almost all of the above-mentioned HTMs are synthesized in modest overall yields by means of toxic and expensive palladium-catalyzed cross-coupling reactions. The required stringent conditions and purification, hampers their low-cost large-scale production.[11] In addition, the presence of catalyst traces can prevent batch-to-batch reproducibility of solar cell performance.[12] Hence, designing simple, low-cost, and environmentally friendly HTMs, with high mobility and good stability, would be highly important toward commercialization of PSCs. Green HTMs based on, e.g., azomethine,[4] enamine,[13] hydrazone,[14] amide,[15] and aniline,[16] with good solar cell performance, have been reported.

Received: February 27, 2019
Accepted: April 8, 2019
Published: April 8, 2019

  

DOI: 10.1021/acsaem.9b00408
ACS Appl. Energy Mater. 2019, 2, 3021−3027

**Scheme 1. Molecular Design and Synthetic Route for AZO-I and AZO-II**

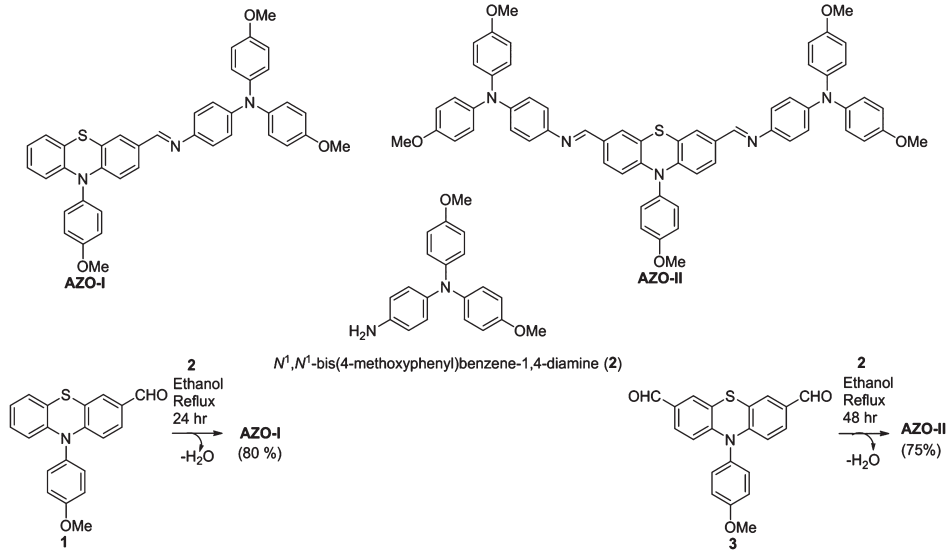


In particular, Docampo et al. have reported an azomethine-based 3,4-ethylenedioxythiophene (EDOT) core HTM EDOT-OMeTPA, demonstrating that Schiff base condensation chemistry is a viable route to achieve low-cost HTMs for high-performance PSCs, with reduced environmental impact.[4] In their design, EDOT was used as the central core, which, even if providing good performance, requires the use of chlorinated solvents, inert atmosphere, and acidic conditions for HTM synthesis. Moreover, the EDOT core presents additional challenges regarding solubility of the HTM and less freedom for functionalization, limiting the development of its soluble derivatives. To address these drawbacks, there is a need for combining the attractive azomethine-based chemistry with other cores.

Phenothiazine is a well-known electron-rich heterocycle, which has been extensively used in the context of organic transistors,[17] photovoltaics,[18] and light emitting diodes.[19] Recently phenothiazine has also proven to be an excellent building block for high-performing and cost-effective HTM in PSCs.[8,9] Its potential benefits are numerous. Phenothiazine is a cheap building block that possesses several possibilities for further functionalization. It is chemically stable and can exhibit very high hole mobilities.[20] It is also well-soluble in common organic solvents and has good film-forming properties. For all these reasons, we foresee phenothiazine as a particularly promising core unit for designing low-cost, environmentally friendly HTMs for high-performance PSCs.

Herein, we report on two new phenothiazine-based HTMs functionalized with azomethine moieties, AZO-I and AZO-II, shown in Scheme 1. Both materials are synthesized in excellent yields from cheap and readily available precursors, via a simple Pd-free synthetic route with only water as byproduct. To the best of our knowledge, AZO-I and AZO-II are among the cheapest phenothiazine core HTMs reported, amounting to 9 and 12 $/g, respectively (see the Supporting Information (SI) for details). Compared to the ubiquitous spiro-OMeTAD (raw material cost 91.67 $/g), these compounds provide a significant gain in cost and a greener synthesis pathway. When employed in PSCs, disubstitution of dimethoxy triarylamine groups yields improved properties as compared to monosubstitution in terms of both PCE and stability, the average PCEs being 12.6%, 14.0%, and 18.1% for AZO-I-, AZO-II-, and spiro-OMeTAD-based devices, respectively. Moreover, the devices comprising AZO-II were markedly stable, maintaining >90% of the PCE even after 2 months of storage of unencapsulated devices in ambient conditions with 30% relative humidity (RH).

The molecular design for AZO-I and AZO-II was inspired by the work of Docampo et al. on low-cost azomethine-based HTMs,[4] as well as the recent breakthroughs on phenothiazine-based HTMs.[8,9] We would especially like to mention the HTMs PTZ2 and Z30, reported by Abate and co-workers[8] and the Grätzel group,[9] respectively (see SI Figure S1 for the chemical structures of PTZ2 and Z30). Both PTZ2 and Z30 are very similar in molecular design to that of AZO-II, and they yield PCEs comparable to spiro-OMeTAD in PSC devices. However, they have been synthesized in modest overall yields (24.9% and 27.7% for PTZ2 and Z30, respectively) via multistep Pd-catalyzed Suzuki coupling reactions with challenging purification steps, rendering them relatively costly. In contrast, syntheses of AZO-I and AZO-II are straightforward, Pd-free, and significantly more efficient with overall yields of 51% (AZO-I) and 40% (AZO-II), as detailed further in the Supporting Information. Table S1 presents comparative details between the previously studied HTMs relevant for this study (EDOT-OMeTPA, PTZ2, Z30, and spiro-OMeTAD) and HTMs AZO-I and AZO-II. We note that methoxy-substituted triarylamine units are introduced to the phenothiazine core to increase the solubility, fine-tune the energy levels of the HTMs well-aligned to perovskite valence band, and ultimately boost the solar cell efficiency.[4]

To evaluate the applicability of these organic semiconductors in PSCs, we investigated the natural bond orbital (NBO) analysis of the optimized geometries of the azomethine compounds calculated with density functional theory (DFT) at PBE1PBE/6-31G**, followed by time-dependent calculations


DOI: 10.1021/acsaem.9b00408
ACS Appl. Energy Mater. 2019, 2, 3021−3027

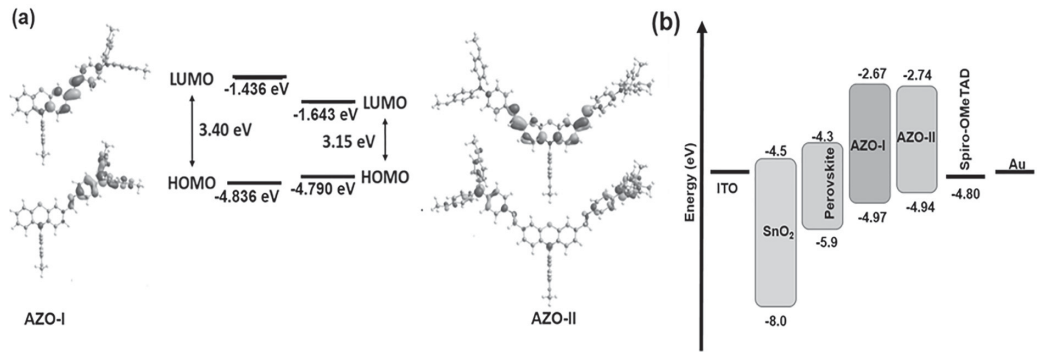


**Figure 1.** (a) Energy levels and electron distribution for frontier molecular orbitals of AZO-I and AZO-II calculated with DFT at PBE1PBE/6-31G** level of theory (isosurface value = 0.04). Energy values are presented in italics (eV). Details in SI and Figure S2. (b) Energy level diagram, as determined experimentally with DPV, for the HTMs used in PSC devices in this work.

**Table 1. Optical, Electrochemical, Thermal Characterization, and Hole Mobility of AZO-I and AZO-II HTMs**

| | $\lambda_{max}$ (nm) Abs/Emi | | | | | | | | |
|---|---|---|---|---|---|---|---|---|---|
| HTM | DCM | Film | HOMO (eV) | LUMO (eV) | $E_g$ (eV) | $T_d$ (°C) | $T_g$ (°C) | $T_m$ (°C) | $\mu$ ($cm^2\ V^{-1}\ s^{-1}$) |
| AZO-I | 422/534 | 430/544 | −4.97[a], −4.83[b] | −1.43[b] | 2.30[c], 3.40[b] | 392 | 85 | 232 | $2 \times 10^{-6}$ |
| AZO-II | 453/548 | 460/554 | −4.94[a], −4.79[b] | −1.64[b] | 2.20[c], 3.15[b] | 405 | 120 | 288 | $2 \times 10^{-5}$ |

[a]HOMO level determined by DPV. [b]Energy levels and $E_g$ determined by TDDFT analysis. [c]$E_g$ determined from optical bandgap.

(Figure 1a, Table S2). For AZO-II, the conjugation length is increased due to the disubstitution of dimethoxytriarylamine as compared to the monosubstitution in AZO-I, which is anticipated to lead to the enhancement of hole transport in AZO-II through the hopping mechanism.[21] The electron density of the HOMO level for both HTMs is located on the peripheral electron-rich dimethoxytriarylamine moieties, while the LUMO is spread over the phenothiazine unit including the electron-withdrawing azomethine bridge between the phenothiazine core and the triarylamine(s).[22,4] The calculated HOMO and LUMO energy levels are −4.84 and −1.44 eV for AZO-I and −4.79 and −1.64 eV for AZO-II (see Figure 1b). The small increase in HOMO level of AZO-II with respect to AZO-I can be ascribed to the slightly extended conjugation length in AZO-II due to the presence of two azomethine bridges.[23]

The absorption and emisssion spectra of the HTMs were measured in solution ($1.0 \times 10^{-5}$ M dichloromethane (DCM); Figure S4a) and in solid state (spin-coated films; Figure S4b). AZO-I and AZO-II show absorption maxima ($\lambda_{max}$) at 422/430 nm and 453/460 nm in solution/solid state, respectively, coresponding to the intramolecular charge transfer (ICT) of the $\pi-\pi^*$ transition.[24] The red shift of $\lambda_{max}$ for AZO-II with respect to AZO-I can be ascribed to the more extended conjugation. The absorption onsets are 538 nm (AZO-I) and 555 nm (AZO-II), and the corresponding optical bandgaps, 2.3 and 2.2 eV, respectively, also in line with the more extended conjugation of AZO-II.[18] The photoluminescene maxima were at 534 nm (solution) and 544 nm (solid) for AZO-I and 548 nm (solution) and 554 nm (solid) for AZO-II (Figure S4).

The experimental determination of the energy levels was carried out through differential pulse voltammetery (DPV; Figure S5). The data are presented in Figure 1b and summarized in Table 1. The obtained HOMO levels of AZO-I and AZO-II are −4.97 and −4.94 eV, respectively, following a trend similar to those achieved by DFT calculations. The experimental HOMO level for spiro-OMeTAD in similar conditions was determined to be −4.80 eV (Figure S5). The relatively small energy difference in the HOMO levels as compared to spiro-OMeTAD (0.17 and 0.14 eV for AZO-I and AZO-II, respectively) indicates their potential applicability in PSCs based on mixed cation and halide perovskites ($Cs_{0.05}MA_{1-y}FA_yPbI_{3-x}Cl_x$), whose valence band is located at 5.9 eV.

The decomposition temperatures, corresponding to 5% weight loss ($T_d$) for AZO-I and AZO-II are 392 and 405 °C, respectively, as determined by thermogravimetric analysis (TGA; Figure S6 and Table 1), comparable to spiro-OMeTAD (424 °C). The glass transition temperatures ($T_g$) and the melting temperatures ($T_m$) were measured with differential scanning calorimetry (DSC; Figure S6). It was found that AZO-I showed $T_g$ at 85 °C and $T_m$ at 232 °C, whereas AZO-II exhibits $T_g$ at 120 °C and $T_m$ at 288 °C. We attribute the higher $T_g/T_m$ of the latter to its larger molecular weight and stiffness.[9] Note also that the $T_g$ of AZO-II is comparable to those of spiro-OMeTAD (120 °C) and the previously reported phenothiazine-based HTM Z30 (125.7 °C), which is important for the stability of the PSC devices.[4] The bulk hole mobility of the pristine HTMs was determined by integral mode time-of-flight (Q-TOF) method (Figure S7 and related discussion). The obtained hole mobilities for AZO-I and AZO-II are $2 \times 10^{-6}$ $cm^2/(V\ s)$ and $2 \times 10^{-5}$ $cm^2/(V\ s)$, respectively (Figure S7, Table 1). The fact that AZO-II displays 1 order of magnitude higher mobility than AZO-I can be attributed to the introduction of two electron-donating triarylamine groups in the 3,7-positions of the electron-rich phenothiazine core.[25] As a reference, under identical experimental conditions the mobility of spiro-OMeTAD ($6 \times 10^{-5}$ $cm^2/(V\ s)$; Figure S7) is comparable, though somewhat higher, than for AZO-II.

We also carried out steady-state photoluminescence (PL) and time-resolved photoluminescence (TR-PL) analysis to


DOI: 10.1021/acsaem.9b00408
ACS Appl. Energy Mater. 2019, 2, 3021−3027

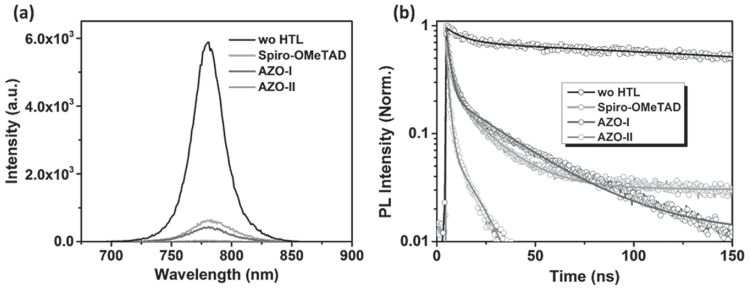


**Figure 2.** (a) Steady-state and (b) time-resolved photoluminescence spectra of spiro-OMeTAD, AZO-I, and AZO-II deposited on perovskites.

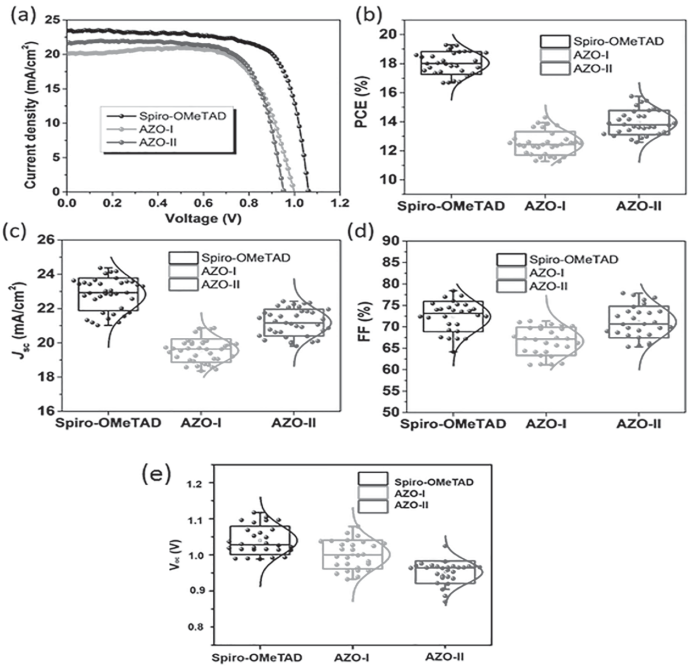


**Figure 3.** (a) Current density−voltage ($J$−$V$) curves for perovskite solar cells (reverse scans) measured with scan rate of 10 mV/s under AM 1.5G simulated solar light illumination by using spiro-OMeTAD, AZO-I, and AZO-II as HTMs. PCE (b), $J_{SC}$ (c), FF (d), and $V_{oc}$ (e) distributions of PSC devices based on different HTMs.

understand the charge extraction process at the perovskite/HTM interface. As shown in Figure 2a, when films of spiro-OMeTAD, AZO-I, or AZO-II were deposited on perovskite surface, the steady-state photoluminescence of the perovskite layer was quenched severely, as expected. The PL intensity of AZO-II was much lower than that of spiro-OMeTAD and AZO-I, suggesting that AZO-II could more efficiently extract the photogenerated holes from the perovskite layer. The higher quenching efficiency of AZO-II compared to AZO-I could be attributed to better film conductivity and enhanced charge transfer from perovskite to HTM. The TR-PL measurement was used to further analyze the hole-extraction process, as shown in Figure 2b. The carrier lifetimes were obtained by fitting the TR-PL curves with a double-exponential decay model presented in Table S6. The significantly faster decay of AZO-II allows us to conclude that the hole injection process from the valence band of perovskite to the HOMO level of the HTM is more efficient as compared to both AZO-I and spiro-OMeTAD. This is also consistent with the steady-state PL results (see in SI and Table S5).

In order to investigate the performance AZO-I and AZO-II in PSC devices and compare them to spiro-OMeTAD, we fabricated mixed cation and halide PSC devices (ITO/$SnO_2$/$Cs_{0.05}MA_{1-y}FA_yPbI_{3-x}Cl_x$/HTM/Au; see device fabrication details in the SI). The perovskite film quality was evaluated by field emission scanning electron microscope (FESEM) and X-ray powder diffraction (XRD) techniques (see Figure S8). As shown in Figure S8, the perovskite film exhibited a smooth and dense polycrystalline surface with large grain size (800−1200 nm). The XRD spectrum of the perovskite film further confirmed that good crystallinity was achieved. Current density−voltage ($J$−$V$) curves of the PSC devices employing the three HTMs, collected under simulated illumination (AM 1.5G, 100 mW $cm^{-2}$), are presented in Figure 3, and the photovoltaic parameters are summarized in Table 2. The HTMs were first employed in pristine form, with the aim of


DOI: 10.1021/acsaem.9b00408
ACS Appl. Energy Mater. 2019, 2, 3021−3027

**Table 2. Photovoltaic Parameters Obtained from *J*−*V* Curves Based on Different HTMs**

| HTM | $J_{SC}$ (mA/cm$^2$) | $V_{oc}$ (V) | FF (%) | PCE (%) | $PCE_{max}$ (%) |
|---|---|---|---|---|---|
| AZO-I | 20.1 | 1.00 | 66 | 12.6 | 14.3 |
| AZO-II | 21.6 | 0.95 | 71 | 14.0 | 15.6 |
| spiro-OMeTAD | 23.4 | 1.04 | 74 | 18.1 | 19.3 |

fabricating dopant-free PSC devices. However, due to the poor performance of devices based on undoped HTMs (Table S3), we used conventional Li- and Co-based dopants and made doped PSCs (see device fabrication details in the SI). The thicknesses of the HTMs were also optimized by using different solution concentrations. The devices based on AZO-I, AZO-II, and spiro-OMeTAD produced averaged short-circuit current densities ($J_{SC}$) of 20.1, 21.6, and 23.4 mA cm$^{-2}$, open-circuit voltages ($V_{oc}$) of 1.00, 0.95, and 1.04 V, and fill factors (FFs) of 0.66, 0.71, and 0.74, resulting in average PCEs of 12.6%, 14.0% and 18.1%, respectively (Table 2). The PCEs of champion devices based on AZO-I and AZO-II HTMs are 14.3% and 15.6%, respectively.

The poorer performance of AZO-I compared to the other two HTMs can be partly attributed to its lower hole mobility ($2 \times 10^{-6}$ cm$^2$ V$^{-1}$ s$^{-1}$) compared to those of AZO-II ($2 \times 10^{-5}$ cm$^2$ V$^{-1}$ s$^{-1}$) and spiro-OMeTAD ($6 \times 10^{-5}$ cm$^2$ V$^{-1}$ s$^{-1}$).[26,27] Even though AZO-II showed better hole injection compared to spiro-OMeTAD based on the TR-PL quenching data, its lower performance in solar cells can be related to the lower $J_{SC}$, most likely due to its lower HOMO level.[28,29] The low HOMO level of AZO-I was beneficial for a larger built-in field for charge extraction/collection, resulting in larger $V_{oc}$ compared to that of AZO-II. However, for both HTMs the $V_{oc}$ values are smaller than that for spiro-OMeTAD-based devices, which may be caused by charge-recombination-induced voltage loss.[30] The higher $J_{SC}$ and FFs of AZO-II-based devices compared to AZO-I can be ascribed to its higher hole mobility, responsible for efficient charge extraction and hole transport. All of the devices showed good reproducibility, as evident from the distribution of the photovoltaic data depicted in Figure 3.

To provide further insights into the interaction between perovskite and AZO-I/AZO-II in comparison to spiro-OMeTAD, we recorded *J*−*V* forward scans to evaluate the hysteresis (Figure S9) and measured the EQE spectra (Figure S10). Devices including AZO-I show the largest hysteresis, thus confirming the worst interaction with perovskite with respect to cells based on spiro-OMeTAD and AZO-II. On the other hand, the *J*−*V* characteristics of solar cells employing spiro-OMeTAD or AZO-II display a similar hysteresis behavior. The EQE spectra (Figure S10) of AZO-I and AZO-II devices show a sudden drop in the EQE around the absorption maxima wavelengths of the materials. With bandgaps around 2.2 eV, both AZO-I and AZO-II, may absorb a significant amount of light, thus partially justifying a detrimental effect on $J_{SC}$ with respect to spiro-OMeTAD cells. However, the reduced performance of AZO-I-/AZO-II-based devices should be mostly related to HOMO level alignment (discussed above) and HTMs' conductivity issues, since the HTMs do not contribute to the EQE spectra as does the key light harvesting layer, the perovskite itself.

Finally, the unencapsulated devices based on spiro-OMeTAD, AZO-I, and AZO-II HTMs were stored in ambient conditions with ∼30% RH to evaluate their temporal stability, as shown in Figure 4. The devices based on AZO-II displayed

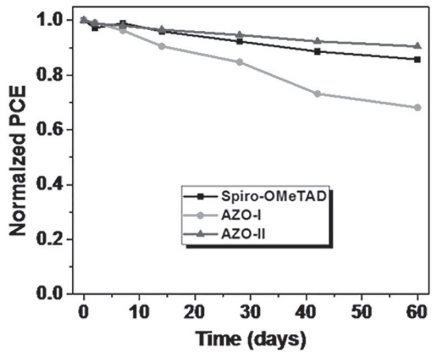


**Figure 4.** Long-time stability of the devices based on spiro-OMeTAD, AZO-I, and AZO-II as HTM.

remarkably long lifetimes over a prolonged time period. In fact, after 60 days, the devices based on AZO-II retained 91% of their initial PCE, while those employing spiro-OMeTAD and AZO-I retained 86% and 68%, respectively. These values are averaged from 15 independent devices. The poor performance of the devices based on AZO-I might also partly be caused by reduced encapsulation due to its lower thickness that minimizes the device series resistance (see the experimental details in the SI), together with its lower $T_g$.[12] The stability results further underpin that AZO-II, or more generally the materials design concept combining phenothiazine core and azomethine bridging, is promising for fabricating low-cost, eco-friendly, and high-performance HTMs for PSCs.

In conclusion, we designed and synthesized two phenothiazine-based HTMs, AZO-I and AZO-II, using simple, eco-friendly, and low-cost Schiff base chemistry and inexpensive precursors. When employed in PSC devices, AZO-II afforded an average PCE of 14.0% with excellent stability, maintaining >90% of the PCE even after 2 months' storage in ambient conditions with ∼30% RH. In addition to the relatively high performance, the production cost of AZO-II is extremely low, only 12 $/g. Given the low price and high stability, AZO-II, in spite of a small loss in the overall PSC performance as compared to that of spiro-OMeTAD-based reference devices (18.1% average PCE), is rather competitive with respect to state-of-the-art HTMs, demonstrating that phenothiazine-based low-cost derivatives synthesized by Schiff base chemistry hold a great potential for eco-friendly HTMs with minimal environmental impact. Further modification of the phenothiazine core can be conducted via N-substitution, in order to tune the energy levels, improve solubility in green solvents, and enhance the charge-carrier mobility, while retaining the low cost of production, hence paving the way toward green, phenothiazine-based PSCs with ever-improving performance.

## ■ ASSOCIATED CONTENT

### Ⓢ Supporting Information

The Supporting Information is available free of charge on the ACS Publications website at DOI: 10.1021/acsaem.9b00408.

Details on synthetic procedures, DFT calculations, device fabrication procedures, hysteresis *J*−*V* scans, EQE spectra, fundamental characterization of all new



DOI: 10.1021/acsaem.9b00408
ACS Appl. Energy Mater. 2019, 2, 3021−3027

compounds, energy level calculations from differential pulse voltammetry, and cost analysis of the HTMs (PDF)

## AUTHOR INFORMATION


### Corresponding Authors

*(J.S.) E-mail: jagadish.salunke@tuni.fi.
*(J.C.) E-mail: jjingchang@xidian.edu.cn.
*(P.V.) E-mail: paola.vivo@tuni.fi.

### ORCID

Jagadish Salunke: 0000-0002-7075-8066
Nuno R. Candeias: 0000-0003-2414-9064
Mathias Nyman: 0000-0002-1250-7111
Ronald Österbacka: 0000-0003-0656-2592
Arri Priimagi: 0000-0002-5945-9671
Jingjing Chang: 0000-0003-3773-182X
Paola Vivo: 0000-0003-2872-6922


### Notes

The authors declare no competing financial interest.

## ACKNOWLEDGMENTS

We thank Dr. Maning Liu for fruitful discussions and Mr. Arto Hiltunen for helping with the TGA measurements. J.S. is grateful to the Fortum Foundation (Grant 201800260) for funding. P.V., M.N., and R.Ö. acknowledge the Jane & Aatos Erkko Foundation (Project "ASPIRE"), and A.P. the Academy of Finland (Decision No. 311142), for financial support. This work is part of the Academy of Finland Flagship Programme, Photonics Research and Innovation (PREIN), Decision No. 320165.

## REFERENCES


(1) Jena, A.; Kulkarni, A.; Miyasaka, T. Halide perovskite photovoltaics status, and future prospects. *Chem. Rev.* **2019**, *119*, 3036−3103.

(2) NREL. Best Research-Cell Efficiency Chart; https://www.nrel.gov/pv/assets/pdfs/best-reserch-cell-efficiencies.20190327.pdf, accessed: Mar. 27, 2019.

(3) Vivo, P.; Salunke, J. K.; Priimagi, A. Hole-Transporting Materials for Printable Perovskite Solar Cells. *Materials* **2017**, *10* (9), 1087.

(4) Petrus, M. L.; Bein, T.; Dingemans, T. J.; Docampo, P. A low cost azomethine-based hole transporting material for perovskite photovoltaics. *J. Mater. Chem. A* **2015**, *3*, 12159−12162.

(5) Sigma Aldrich.https://www.sigmaaldrich.com/technical-service-home/product-catalog.html, retrieved on Feb. 26, 2019.

(6) Jeon, N. J.; Lee, J.; Noh, J. H.; Nazeeruddin, M. K.; Grätzel, M.; Seok, S. Il Efficient Inorganic−Organic Hybrid Perovskite Solar Cells Based on Pyrene Arylamine Derivatives as Hole-Transporting Materials. *J. Am. Chem. Soc.* **2013**, *135*, 19087−19090.

(7) Xu, B.; Sheibani, E.; Liu, P.; Zhang, J.; Tian, H.; Vlachopoulos, N.; Boschloo, G.; Kloo, L.; Hagfeldt, A.; Sun, L. Carbazole-Based Hole-Transport Materials for Effi cient Solid-State Dye-Sensitized Solar Cells and Perovskite Solar Cells. *Adv. Mater.* **2014**, *26* (38), 6629−6634.

(8) Grisorio, R.; Roose, B.; Colella, S.; Listorti, A.; Suranna, G. P.; Abate, A. Molecular Tailoring of Phenothiazine-Based Hole-Transporting Materials for High-Performing Perovskite Solar Cells. *ACS Energy Lett.* **2017**, *2* (5), 1029−1034.

(9) Zhang, F.; Wang, S.; Zhu, H.; Liu, X.; Liu, H.; Li, X.; Xiao, Y.; Zakeeruddin, S. M.; Grätzel, M. Impact of Peripheral Groups on Phenothiazine-Based Hole-Transporting Materials for Perovskite Solar Cells. *ACS Energy Lett.* **2018**, *3*, 1145−1152.

(10) Saliba, M.; Orlandi, S.; Matsui, T.; Aghazada, S.; Cavazzini, M.; Correa-Baena, J.-P.; Gao, P.; Scopelliti, R.; Mosconi, E.; Dahmen, K.-H.; De Angelis, F.; Abate, A.; Hagfeldt, A.; Pozzi, G.; Graetzel, M.; Nazeeruddin, M. K. A molecularly engineered hole-transporting material for efficient perovskite solar cells. *Nat. Energy.* **2016**, *1* (2), 15017.

(11) Petrus, M. L.; Schlipf, J.; Li, C.; Gujar, T. P.; Giesbrecht, N.; Müller-buschbaum, P.; Thelakkat, M.; Bein, T.; Hüttner, S.; Docampo, P. Capturing the Sun: A Review of the Challenges and Perspectives of Perovskite Solar Cells. *Adv. energy Mater.* **2017**, *7*, 1700264.

(12) Nikiforov, M. P.; Lai, B.; Chen, W.; Chen, Si.; Schaller, R. D.; Strzalka, J.; Maser, J.; Darling, S. B. Detection and role of trace impurities in high-performance organic solar cells. *Energy Environ. Sci.* **2013**, *6*, 1513−1520.

(13) Daskeviciene, M.; Paek, S.; Wang, Z.; Malinauskas, T.; Jokubauskaite, G.; Rakstys, K.; Cho, K. T.; Magomedov, A.; et al. Carbazole-based enamine: Low-cost and efficient hole transporting material for perovskite solar cells. *Nano Energy* **2017**, *32*, 551−557.

(14) Petrus, M. L.; Sirtl, M. T.; Closs, A. C.; Bein, T.; Docampo, P. Hydrazone-based hole transporting material prepared via condensation chemistry as alternative for cross-coupling chemistry for perovskite solar cells. *Mol. Syst. Des. Eng.* **2018**, *3*, 734−740.

(15) Petrus, M. L.; Schutt, K.; Sirtl, M. T.; Hutter, E. M.; Closs, A. C.; Ball, J. M.; Bijleveld, J. C.; Petrozza, A.; Bein, T.; Dingemans, T. J.; Savenije, T. J.; Snaith, H.; Docampo, P. New Generation Hole Transporting Materials for Perovskite Solar Cells: Amide-Based Small-Molecules with Nonconjugated Backbones. *Adv. Energy Mater.* **2018**, *8*, 1801605.

(16) Vaitukaityte, D.; Wang, Z.; Malinauskas, T.; Magomedov, A.; Bubniene, G.; Jankauskas, V.; Getautis, V.; Snaith, H. J. Efficient and Stable Perovskite Solar Cells Using Low-Cost Aniline-Based Enamine Hole-Transporting Materials. *Adv. Mater.* **2018**, *30*, 1803735.

(17) Zhou, W.; Wen, Y.; Ma, L.; Liu, Y.; Zhan, X. Conjugated Polymers of Rylene Diimide and Phenothiazine for n-Channel Organic Field-Effect Transistors. *Macromolecules* **2012**, *45*, 4115−4121.

(18) Maglione, C.; Carella, A.; Centore, R.; Chavez, P.; Leveque, P.; Fall, S.; Leclerc, N. Novel low bandgap phenothiazine functionalized DPP derivatives prepared by direct heteroarylation: Application in bulk heterojunction organic solar cells. *Dyes Pigm.* **2017**, *141*, 169−178.

(19) Salunke, J. K.; Wong, F. L.; Feron, K.; Manzhos, S.; Lo, M. F.; Shinde, D.; Patil, A.; Lee, C. S.; Roy, V. A. L.; Sonar, P.; Wadgaonkar, P. P. Phenothiazine and carbazole substituted pyrene based electroluminescent organic semiconductors for OLED devices. *J. Mater. Chem. C* **2016**, *4*, 1009−1018.

(20) Shinde, D. B.; Salunke, J. K.; Candeias, N. R.; Tinti, F.; Gazzano, M.; Wadgaonkar, P. P.; Priimagi, A.; Camaioni, N.; Vivo, P. Crystallisation-enhanced bulk hole mobility in phenothiazine-based organic semiconductors. *Sci. Rep.* **2017**, *7*, 46268.

(21) Saeki, A.; Koizumi, Y.; Aida, T.; Seki, S. Comprehensive Approach to Intrinsic Charge Carrier Mobility in Conjugated Organic Molecules, Macromolecules, and Supramolecular Architectures. *Acc. Chem. Res.* **2012**, *45* (8), 1193−1202.

(22) Tremblay, M.-H.; Skalski, T.; Gautier, Y.; Pianezzola, G.; Skene, W. G. Investigation of Triphenylamine−Thiophene−Azomethine Derivatives: Toward Understanding Their Electrochromic Behavior. *J. Phys. Chem. C* **2016**, *120*, 9081−9087.

(23) Bolduc, A.; Al Ouahabi, A.; Mallet, C.; Skene, W. G. Insight into the Isoelectronic Character of Azomethines and Vinylenes Using Representative Models: A Spectroscopic and Electrochemical Study. *J. Org. Chem.* **2013**, *78*, 9258−9269.

(24) Karthikeyan, C. S.; Thelakkat, M. Key aspects of individual layers in solid-state dye-sensitized solar cells and novel concepts to improve their performance. *Inorg. Chim. Acta* **2008**, *361*, 635−655.

(25) Bi, D.; Xu, B.; Gao, P.; Sun, L.; Grätzel, M.; Hagfeldt, A. Facile synthesized organic hole transporting material for perovskite solar cell with efficiency of 19.8%. *Nano Energy* **2016**, *23*, 138−144.

(26) Zhang, F.; Liu, X.; Yi, C.; Bi, D.; Luo, J.; Wang, S.; Li, X.; Xiao, Y.; Zakeeruddin, S. M.; Grätzel, M. Dopant-Free Donor (D)−$\pi$−




DOI: 10.1021/acsaem.9b00408
*ACS Appl. Energy Mater.* 2019, 2, 3021−3027

D−π−D Conjugated Hole-Transport Materials for Efficient and Stable Perovskite Solar Cells. *ChemSusChem* **2016**, *9* (18), 2578−2585.

(27) Guo, J. J.; Bai, Z. C.; Meng, X. F.; Sun, M. M.; Song, J. H.; Shen, Z. S.; Ma, N.; Chen, Z. L.; Zhang, F. Novel dopant-free metallophthalocyanines based hole transporting materials for perovskite solar cells: The effect of core metal on photovoltaic performance. *Sol. Energy* **2017**, *155*, 121−129.

(28) Rakstys, K.; Abate, A.; Dar, M. I.; Gao, P.; Jankauskas, V.; Jacopin, G.; Kamarauskas, E.; Kazim, S.; Ahmad, S.; Grätzel, M.; Nazeeruddin, M. K. Triazatruxene-Based Hole Transporting Materials for Highly Efficient Perovskite Solar Cells. *J. Am. Chem. Soc.* **2015**, *137* (51), 16172−16178.

(29) Planells, M.; Abate, A.; Hollman, D. J.; Stranks, S. D.; Bharti, V.; Gaur, J.; Mohanty, D.; Chand, S.; Snaith, H. J.; Robertson, N. Diacetylene bridged triphenylamines as hole transport materials for solid state dye sensitized solar cells. *J. Mater. Chem. A* **2013**, *1*, 6949−6960.

(30) Stolterfoht, M.; Caprioglio, P.; Wolff, C. M.; Márquez, J. A.; Nordmann, J.; Rothhardt, D.; Hörmann, U.; Redinger, A.; Kegelmann, L.; Albrecht, S.; Saliba, M.; Unold, T.; Neher, D. The perovskite/transport layer interfaces dominate non-radiative recombination in efficient perovskite solar cells. 2018, arXiv:1810.01333. *arXiv.org ePrint archive*. http//arxiv.org/abs/1810.01333.



DOI: 10.1021/acsaem.9b00408
*ACS Appl. Energy Mater.* 2019, 2, 3021−3027

# PUBLICATION III

N-Substituted Phenothiazines as Environmentally Friendly Hole-Transporting Materials for Low-Cost and Highly Stable Halide Perovskite Solar Cells

Jagadish Salunke, Xing Guo, Maning Liu, Zhenhua Lin, Nuno R. Candeias, Arri Priimagi, Jingjing Chang, and Paola Vivo

*ACS Appl. Energy Mater. 2019, 2, 3021-3027.*
DOI: 10.1021/acsaem.9b00408

ACS OMEGA

http://pubs.acs.org/journal/acsodf

Article

# N-Substituted Phenothiazines as Environmentally Friendly Hole-Transporting Materials for Low-Cost and Highly Stable Halide Perovskite Solar Cells

Jagadish Salunke,* Xing Guo, Maning Liu, Zhenhua Lin, Nuno R. Candeias, Arri Priimagi, Jingjing Chang,* and Paola Vivo*

Cite This: https://dx.doi.org/10.1021/acsomega.0c03184

Read Online

ACCESS | Metrics & More | Article Recommendations | Supporting Information

**ABSTRACT:** Most of the high-performing halide perovskite solar cells (PSCs) leverage toxic chlorinated solvents (e.g., *o*-dichlorobenzene or chlorobenzene) for the hole-transporting material (HTM) processing and/or antisolvents in the perovskite film fabrication. To minimize the environmental and health-related hazards, it is highly desirable, yet at the same time demanding, to develop HTMs and perovskite deposition processes relying on nonhalogenated solvents. In this work, we designed two small molecules, **AZO-III** and **AZO-IV**, and synthesized them via simple and environmentally friendly Schiff base chemistry, by condensation of electron-donating triarylamine and phenothiazine moieties connected through an azomethine bridge. The molecules are implemented as HTMs in PSCs upon processing in a nonchlorinated (toluene) solvent, rendering their synthesis and film preparation eco-friendly. The enhancement in the power conversion efficiency (PCE) was achieved when switching from **AZO-III** (9.77%) to **AZO-IV** (11.62%), in which the thioethyl group is introduced in the 2-position of the phenothiazine ring. Additionally, unencapsulated PSCs based on **AZO-III** displayed excellent stabilities (75% of the initial PCEs is retained after 6 months of air exposure for **AZO-III** to be compared with a 48% decrease of the initial PCE for Spiro-OMeTAD-based devices). The outstanding stability and the extremely low production cost (**AZO-III** = 9.23 $/g and **AZO-IV** = 9.03 $/g), together with the environmentally friendly synthesis, purification, and processing, make these materials attractive candidates as HTMs for cost-effective, stable, and eco-friendly PSCs.

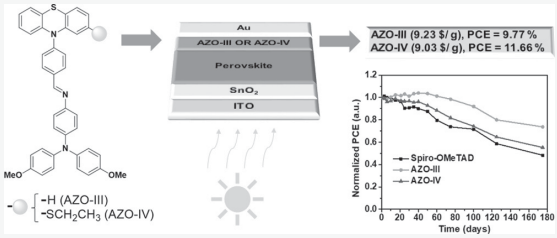


## 1. INTRODUCTION

Over the last decade, organic small molecules have received tremendous attention as hole-transporting materials (HTMs) in halide perovskite solar cells (PSCs) because of their reproducible synthesis, low-temperature solution processability, and large freedom of functionalization[1−6] To date, 2,2,7,7-tetrakis(*N*,*N*-dipmethoxyphenylamine) 9,9-spirobifluorene (Spiro-OMeTAD) is by far the most commonly used small-molecular HTM in conventional n−i−p PSC structures. Spiro-OMeTAD-based devices exhibit impressive power conversion efficiencies (PCEs) in the range of 20−22%[7−10] close to the existing record of 25.2%[11] reached by PSCs. However, the multistep synthesis, difficult purification, high-cost (91.67 $/g, raw material cost), and poor hole-mobility of Spiro-OMeTAD limit its large-scale production.[12,13] Furthermore, all the Spiro-OMeTAD-based high-performing devices require the addition of external dopants for enhancing the mediocre hole-mobility of pristine Spiro-OMeTAD. Nevertheless, because of their hygroscopic nature, these dopants cause moisture-induced degradation pathways in PSCs, thus reducing their long-term stability.[14−17] Therefore, to overcome the limitations of Spiro-OMeTAD, various types of organic small molecular HTMs based on fluorene,[2,18] carbazole,[12,19] pyrene,[20,21] and several others functional groups have been widely investigated.[1,6]

However, all the above-mentioned high-performing HTMs were either synthesized by using toxic and expensive palladium catalysts via multistep synthesis or were processed with hazardous halogenated solvents with severe acute toxicity, which can not only harm the environment but also hamper the large-scale production and commercialization of PSCs.[3,22−26] Hence, when designing new HTMs, one should ideally account for a good solubility of the materials in nonhalogenated solvents, in addition to the other obvious characteristics such as well-aligned energy levels with the perovskite conduction/valence band (VB), high hole-mobility, and cost-effective facile synthesis with high overall conversion yields. There are very

Received: July 2, 2020
Accepted: August 19, 2020

**Scheme 1. Molecular Design and Synthetic Route for AZO-III and AZO-IV; Previously Reported AZO-I and AZO-II Molecules Are Also Added for Comparison; Scheme Adapted with Permission from *ACS Appl. Energy Mater.* 2019, *2*, 3021−3027; Copyright 2019 American Chemical Society**

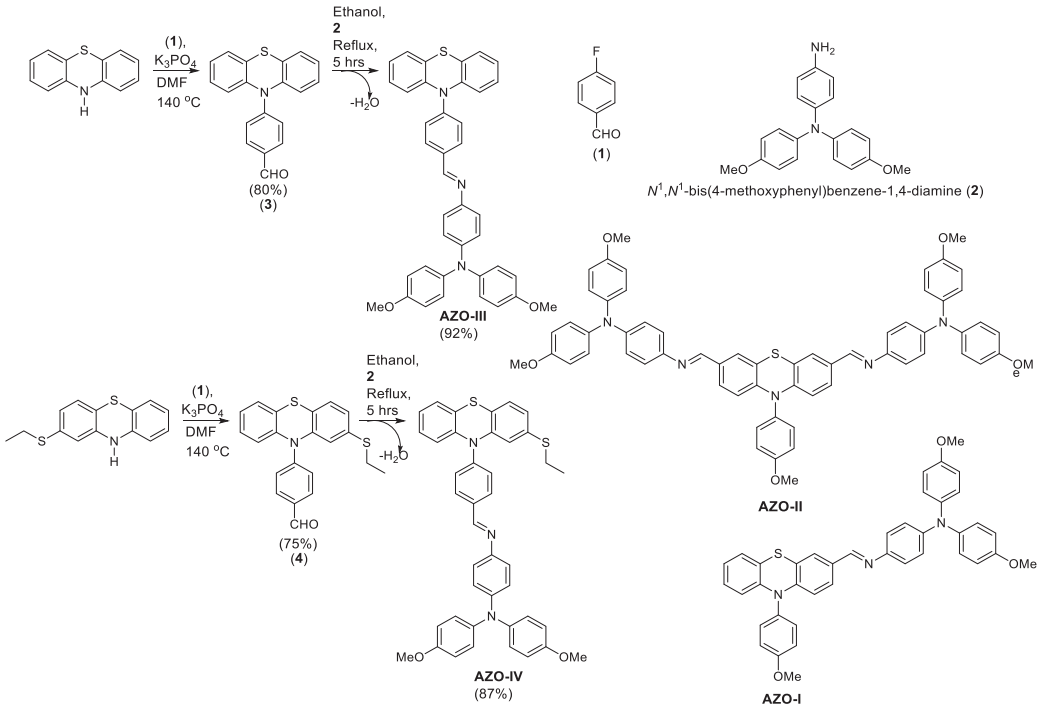


few reports regarding HTMs processed in nonhalogenated solvents.[24−28] Nevertheless, in all the reported examples, the HTMs were mostly synthesized in modest overall yields via onerous multistep syntheses employing costly and toxic palladium catalysts and were purified via stringent and long procedures that limit their scalability.[24−28] Thus, HTMs that combine green solvents processability with cost-effective and eco-friendly synthesis and purification are still lacking.

Because of their easy availability, chemical stability, low-cost, good solubility in common organic solvents, large freedom of functionalization, and excellent hole-mobility,[29] phenothiazine-based small molecules have been extensively studied in organic electronics.[30−32] Recently, they have also been considered as low-cost and effective HTMs for PSCs.[33−37] In our previous work,[37] we designed two phenothiazine-core, azomethine-based HTMs (**AZO-I** and **AZO-II**) via an environmentally friendly Schiff base chemistry approach, starting from low-cost precursors. Even though **AZO-I** and **AZO-II** provided a high-performing, stable, and low-cost alternative to Spiro-OMeTAD, their insolubility in nonhalogenated solvents limited their eco-friendliness as regarding their processing in the device fabrication.[37]

Here, we report on two new azomethine-based phenothiazines, **AZO-III** and **AZO-IV**, whose synthesis routes are presented in Scheme 1 and details are mentioned in Section 2 and in Supporting Information. Both were synthesized by using low-cost precursors and simple Schiff base chemistry with only water as a byproduct. Upon the utilization of **AZO-III** and **AZO-IV** in mixed perovskite (CsFAMA)-based devices, the thioethyl-substituted **AZO-IV** exhibited an improved PCE of 11.62% compared to that of **AZO-III** (9.77%). Additionally, the **AZO-III**-based PSCs provided stable power output after the unencapsulated devices were kept in ambient conditions (relative humidity, RH = 30%, at 25 °C) for 6 months. **AZO-III** and **AZO-IV** are the cheapest phenothiazine-core HTMs processed in nonhalogenated solvents (**AZO-III** = 9.23 $/g and **AZO-IV** = 9.03 $/g; in comparison, the raw material cost of conventional Spiro-OMeTAD is 91.67 $/g. See Table S1 in Supporting Information).

## 2. RESULTS AND DISCUSSION

To ensure the solubility in nonhalogenated solvents while guaranteeing the maximum HTM loading capacity on the perovskite surface and at the same time minimizing the synthesis steps, we modified our previously reported structures (**AZO-I**, **AZO-II**, Scheme 1)[37] by (i) making them smaller in size, (ii) introducing an aryl spacer between the phenothiazine and the azomethine bridge (**AZO-III**), and (iii) further adding a thioethyl (**AZO-IV**) group in the 2-position of the phenothiazine unit to enhance the solubility, and possibly also the HTM/perovskite interactions.[2]

Furthermore, the methoxy-substituted triarylamine group was introduced to the phenothiazine core to ensure good alignment between the highest occupied molecular orbital (HOMO) levels of the HTMs and the VB of the perovskite. These design principles combined good solubility (20 mg/mL) in toluene, reduction in cost/synthesis steps (in comparison, the cost of **AZO-I** and **AZO-II** was 9 and 12 $/g, respectively), and excellent synthesis yields of 92% (**AZO-III**) and 87% (**AZO-IV**). Further details on the cost analysis of HTMs


https://dx.doi.org/10.1021/acsomega.0c03184
*ACS Omega* XXXX, XXX, XXX−XXX

**Table 1. Optical and Electrochemical Characterization of AZO-III and AZO-IV**

| | $\lambda_{max}$ Abs/Emi (nm) | | | | | |
|---|---|---|---|---|---|---|
| HTMs | DCM | film | HOMO (eV) | LUMO (eV) | $^{b}E_g$ (eV) | $^{d}E_g$ (eV) |
| **AZO-III** | 409/565 | 412/567 | −4.97[a], −4.93[b] | −2.41[c], −1.64[b] | 3.29[b] | 2.56[d] |
| **AZO-IV** | 412/565 | 417/576 | −4.99[a], −4.91[b] | −2.45[c], −1.64[b] | 3.27[b] | 2.54[d] |

[a]HOMO level determined by DPV. [b]Energy levels and $^{b}E_g$ determined by NBO analysis. [c]LUMO level by using optical band gap. [d]Optical bandgap.

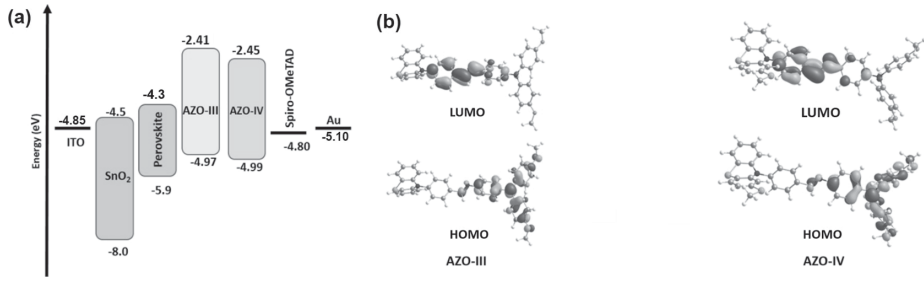


**Figure 1.** (a) Energy level diagram for **AZO-III**, **AZO-IV**, and Spiro-OMeTAD, based on DPV experiments, and the reported values for ITO, $SnO_2$, and Au [37]. (b) Optimized geometries, selected molecular orbitals, and frontier molecular orbitals energies of **AZO-III** and **AZO-IV**, calculated with DFT at PBE1PBE/6-31G** level of theory in DCM.

calculated based on previously reported cost models[34,38] and on the chemical characterization of the synthesized products are provided in Table S1 and Figures S1−S4 in Supporting Information.

The UV−vis absorption spectra of **AZO-III** and **AZO-IV** were measured in chloroform ($1 \times 10^{-5}$ M) and in thin films and presented in Table 1 and Figure S5 in Supporting Information. The absorption peaks ($\lambda_{max}$) are at 409 and 412 nm for **AZO-III** and at 412 and 417 nm for **AZO-IV** in solution and film phases, respectively. These bands correspond to the intramolecular charge transfer from the electron-donating methoxy-substituted triarylamine to the azomethine unit(s). The slight increase in the $\lambda_{max}$ of **AZO-IV** compared to **AZO-III** is ascribed to the presence of the additional electron-rich thioethyl group in **AZO-IV**.[39] The minor red-shift in the absorption maxima in the case of thin films for both compounds is attributed to intermolecular interactions in the solid state.[40] The absorption onsets of **AZO-III** and **AZO-IV** in films are at 484 and 488 nm, and the corresponding optical bandgaps ($E_g$) are 2.56 eV and 2.54 eV, respectively. The steady-state photoluminescence (PL) spectra of **AZO-III** and **AZO-IV** show the peak positions at 565 nm and 567 nm for **AZO-III** and at 565 and 576 nm for **AZO-IV** in chloroform ($1 \times 10^{-5}$ M) and in thin films, respectively (Figure S5, Table 1).

To determine the energy levels of the two HTMs, as well as that of the reference HTM Spiro-OMeTAD, differential pulse voltammograms have been recorded (see Figure S6) with the key results summarized in Table 1. Because the HOMO levels correspond to the ionization potentials of the materials, both **AZO-III** and **AZO-IV** display similar electrochemical properties, with their HOMO levels lying at −4.97 and −4.99 eV, respectively. The HOMO level of **AZO-III** is similar to that of the previously reported **AZO-I** because it possesses a similar core with the only difference being the position of the electron-donating methoxy-substituted triarylamine units.[37] The HOMO level of Spiro-OMeTAD, as determined by differential pulse voltammetry (DPV) in identical conditions, is −4.82 eV. Because of the small difference between the HOMO levels of **AZO-III** (0.15 eV) or **AZO-IV** (0.17 eV) with respect to Spiro-OMeTAD, both new HTMs show high compatibility with the triple-cation halide perovskite (e.g., $Cs_{0.05}MA_{1-y}FA_yPbI_{3-x}Cl_x$) employed in this work, whose VB lies at −5.9 eV.[37] The corresponding energy level diagram, comprising all the materials used in our solar cell structures, is depicted in Figure 1a. Because no clear reduction peaks are detected in DPV curves, the lowest unoccupied molecular orbital (LUMO) levels are derived from the optical $E_g$ and the corresponding values for **AZO-III** and **AZO-IV** are −2.41 eV and −2.45 eV, respectively (in Table 1).

**AZO-III** and **AZO-IV** were further studied with density functional theory (DFT), at the PBE1PBE/6-31G** level, followed by time-dependent calculations (Figure 1b, Tables S2 and S3 in Supporting Information). For the computational analysis, the ethyl substituent in the thioether group of **AZO-IV** has been replaced by a methyl for simplicity, and the further details are described in Section 4.4. A comparison of the unoccupied frontier orbital energies calculated by DFT (−1.64 eV) and determined by using the optical band gap (−2.41 and −2.45 eV) clearly shows that the computational method used overestimates the energy of the orbitals. The absolute excitation energies are overestimated by the method by ca 0.6−0.9 eV, although the simulated energies of the occupied frontier orbitals (−4.91 to −4.93 eV) are close to the values determined experimentally (−4.97 to −4.99 eV) differing less than 0.1 eV. The electron density in the case of HOMO energy levels of both the compounds is located on the electron-donating triarylamine units, while the LUMO energy levels are spread over the electron-withdrawing azomethine linkage and the aryl spacer unit between phenothiazine and azomethine(s).[41,42] Simulations of the vertical excitations of **AZO-III** and **AZO-IV** indicate that the first transition refers to the HOMO−LUMO transitions (Tables S2 and S3) through intramolecular charge transfer.

To investigate the hole extraction process at the perovskitel HTM interface, we carried out PL quenching experiments, as presented in Figure 2a. Upon deposition of **AZO-III**, **AZO-IV**,


https://dx.doi.org/10.1021/acsomega.0c03184
ACS Omega XXXX, XXX, XXX−XXX

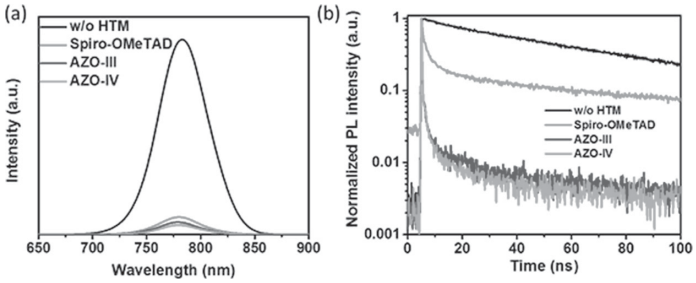


**Figure 2.** (a) Steady-state and (b) time-resolved PL spectra of Spiro-OMeTAD, **AZO-III**, and **AZO-IV** deposited on the perovskite surface, excited at 510 nm with an excitation intensity of 5.8 W $cm^{-2}$.

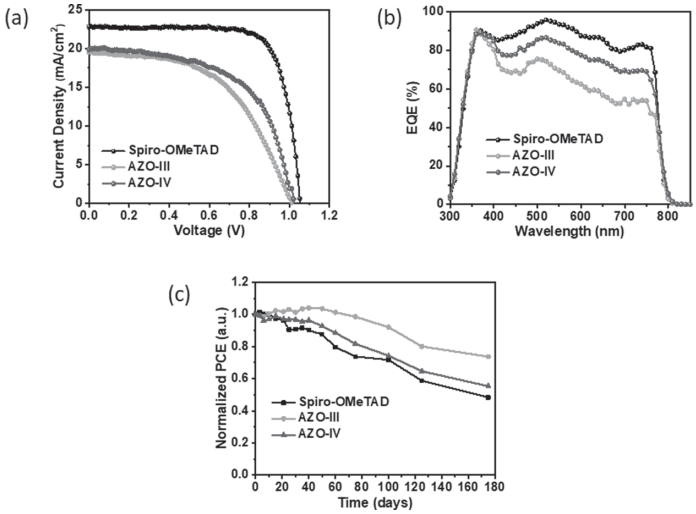


**Figure 3.** (a) Current density−voltage ($J$−$V$) curves measured with a scan rate of 10 mV/s in a backward scan, under AM 1.5 simulated solar light illumination, (b) EQE spectra, and (c) long-term stability of PSCs employing Spiro-OMeTAD, **AZO-III**, and **AZO-IV** as HTM.

and Spiro-OMeTAD films on top of the perovskite layer, the steady-state PL spectra of the pristine perovskite layer on glass quench significantly, indicating that the holes can be effectively injected from the VB of the perovskite layer to the HOMO level of the HTMs. By comparing the amplitude of the PL spectra before and after HTM deposition, the quenching efficiency, that is, hole injection yield, can be calculated as 92.2, 94.6, and 95.8% for Spiro-OMeTAD, **AZO-III**, and **AZO-IV**, respectively. The improved hole injection yields for **AZO-III** and **AZO-IV** compared to the reference Spiro-OMeTAD can be attributed to the better energy level alignment because the HOMO levels of both **AZO-III** and **AZO-IV** are effectively deepened toward the VB of the perovskite, which favors an efficient hole extraction'.[43] We also assign even the higher PL quenching efficiency of **AZO-IV** to the presence of additional sulfur atoms as compared to **AZO-III**, which has been previously suggested to enhance the adhesion and the interaction between the HTM and the perovskite surface.[2,44]

The hole transfer dynamics have been further investigated with the perovskite excited state and the hole injection from the VB of the perovskite to the HOMO level of HTMs have been investigated with time-resolved PL (TR-PL) measurements (Figure 2b). All PL decays can be fitted well with a single-exponential function with two components, and the fitting results are summarized in Table S4 (Supporting Information). We assign the fast component to the trap-assisted recombination of charge carriers/excitons and to the hole injection dynamics from perovskite to HTMs and the slow component to the radiative recombination of free charge carriers/excitons in the bulk, respectively.[45] The contribution factors (A1) for the fast components of all the HTMs are more than 95%, indicating that the fast component indeed dominates the charge recombination dynamics (Table S4 in Supporting Information).

To simplify the comparison of lifetimes, we here define an effective lifetime, that is, $t_{1/e}$,[46] expressed as $I(t_{1/e}) = I(0)/e$, where $I(t_{1/e})$ is the PL intensity at time $t_{1/e}$. From the effective lifetimes for the PL decays of the perovskite films without ($t_{1/e(perov)}$) and with HTMs ($t_{1/e(HTM)}$), we can work out the hole injection yield ($\Phi_{h\text{-}inj}$) using the following equation[45,47]

$$\Phi_{h\text{-}inj} = 1 - \left( \frac{1}{t_{1/e(HTM)}} - \frac{1}{t_{1/e(perov)}} \right) \quad (1)$$

Accordingly, the hole injection yields for spiro-OMeTAD, **AZO-III**, and **AZO-IV** are 86.0, 96.0, and 99.3%, respectively, which is consistent with the trend of quenching efficiency variations shown in Figure 2a. The remarkably accelerated PL


https://dx.doi.org/10.1021/acsomega.0c03184
ACS Omega XXXX, XXX, XXX−XXX

Table 2. Photovoltaic Parameters of the Champion Devices Obtained from $J-V$ Curves Based on Different HTMs[a]

| HTMs | | $J_{SC}$ (mA/cm$^2$) | $V_{OC}$ (V) | FF (%) | PCE (%) | $R$ (Ω·cm$^2$) | $R_{Sh}$ (kΩ·cm$^2$) |
|---|---|---|---|---|---|---|---|
| Spiro-OMeTAD | champion | 22.69 | 1.08 | 0.76 | 18.63 | 3.95 | 4.42 |
| | average | 22.78 ± 0.34 | 1.06 ± 0.01 | 0.76 ± 0.01 | 18.38 ± 0.14 | 3.98 ± 0.03 | 4.37 ± 0.04 |
| **AZO-III** | champion | 19.75 | 1.01 | 0.49 | 9.77 | 15.63 | 0.68 |
| | average | 18.98 ± 0.81 | 1.01 ± 0.01 | 0.46 ± 0.02 | 8.75 ± 0.72 | 15.75 ± 0.12 | 0.65 ± 0.08 |
| **AZO-IV** | champion | 19.83 | 1.01 | 0.58 | 11.62 | 5.23 | 0.74 |
| | average | 18.09 ± 1.62 | 1.01 ± 0.01 | 0.55 ± 0.04 | 10.04 ± 0.87 | 5.32 ± 0.09 | 0.69 ± 0.11 |

[a]The averaged parameters are also reported together with the standard deviations.

decays for both **AZO-III** and **AZO-IV** compared to spiro-OMeTAD clearly demonstrate their improved hole-injection dynamics for the newHTMs.

To investigate the performance of **AZO-III** and **AZO-IV** in PSCs, we fabricated devices using mixed halide perovskite as light-harvester (complete structure: ITO/$SnO_2$/$Cs_{0.05}MA_{1-y}FA_yPbI_{3-x}Cl_x$/HTM/Au, see device fabrication details in Section 4.3). The **AZO-III** and **AZO-IV** films were first cast from toluene with a concentration of 60, 40, and 20 mg/mL. However, the corresponding PSCs displayed a very low $J_{SC}$, probably due to the low conductivity of the HTMs. Hence, we focused on the optimized concentration of 10 mg/mL. In addition, both HTMs possessed good solubility in tetrahydrofuran (THF), but because of the poor film quality, we did not test the THF-casted films in solar cells.

Initially, all the HTMs were used to fabricate dopant-free PSCs, but because of poor PCEs (Table S5), conventional dopants (see details in Section 2.2) were added to the HTMs to improve the PCEs The reference Spiro-OMeTAD films were deposited from a chlorobenzene solution with a much higher concentration of 72.5 mg/mL (corresponding to the known optimized concentration for HTM),[37] because its solubility in toluene is modest.[2] It has been shown that the use of different solvents for Spiro-OMeTAD films has a minimal impact on the corresponding device performance.[48] Importantly, the use of toluene in less concentrated (10 mg/mL) **AZO-III** and **AZO-IV** solutions, compared to that of the chlorobenzene (72.5 mg/mL) solution of Spiro-OMeTAD with higher concentration, removes the necessity of utilization of toxic-halogenated solvent and at the same time reduces the overall device fabrication costs.[28]

The current density−voltage ($J-V$) curves of each HTM's champion PSCs under 1 sun simulated illumination (AM 1.5G, 100 mW/cm$^2$) are presented in Figure 3a. The photovoltaic parameters extracted from the $J-V$ characteristics are summarized in Table 2. In Table 2, both the results of the champion devices and the averaged photovoltaic parameters obtained from 20 independent devices are reported. The very low standard deviations demonstrate the high reproducibility of these experiments.

The performance gap for **AZO-III/IV** devices versus Spiro-OMeTAD cells is mainly caused by the lower short-circuit current ($J_{SC}$) and fill factor (FF). Because both new HTMs show higher hole injection yields than that of spiro-OMeTAD, the decrease in $J_{SC}$ can be attributed to the poor charge transfer within **AZO-III** or **AZO-IV**, probably in relation to the low hole mobility, which has been reported for similar phenothiazine core azomethine compounds (e.g., **AZO-I**) in earlier studies.[37,49−52] To clarify the reasons for the lower FF, we have extracted the series ($R_S$) and shunt ($R_{Sh}$) resistance of the devices, according to the 1-diode model,[53] from the $J-V$ curves in a backward scan (Table 2). The control Spiro-OMeTAD devices show the lowest $R_S$ and highest $R_{Sh}$, thus leading to higher FF than those of **AZO-III**- and **AZO-IV**-based PSCs. It is interesting to observe a nearly three times larger $R_S$ of the **AZO-III** device compared to that of the **AZO-IV** device, indicating that the charge recombination can be effectively hindered in the case of **AZO-IV**. We further carried out the external quantum efficiency (EQE) measurements for all the champion devices (Figure 3b). The reference device shows the expected highest EQE value of 95.6% at around 520 nm, while the **AZO-III** and **AZO-IV** devices display the highest EQE values of 74.5 and 85.0%, respectively, which are consistent with their demonstrated lower $J_{SC}$. This indicates that the internal quantum efficiency (IQE) of the Spiro-OMeTAD-based devices is much higher than those of AZO-based devices because the absorbance of all the cells at 520 nm is nearly identical, close to 1. This results in a much higher charge collection efficiency in the reference devices compared to those of AZO-based devices based on the equation of IQE = charge separation efficiency × charge collection efficiency.[54] The higher charge collection efficiency in the reference devices further confirms that the bulk hole mobility for the doped Spiro-OMeTAD is higher than that of doped **AZO-III** or **AZO-IV**, mainly responsible for the poorer performance of the new HTM-based solar cells.

This again supports the enhancement of charge separation/collection upon the additional thioethyl attachment in the case of **AZO-IV**. Finally, we have monitored the stability of unencapsulated devices employing **AZO-III**, **AZO-IV**, and Spiro-OMeTAD (20 cells) upon storing them in air with relative humidity (RH) ∼ 30% over six months (Figure 3c). The **AZO-III** devices exhibited high stability and maintained 75% of their initial performance over 180 days (six-months) period, while **AZO-IV** and Spiro-OMeTAD cells retained 56 and 48% of the initial PCEs, respectively.

If we focus on the performance after the first two months of storage, **AZO-III** (PCE unchanged or, in other words, 100% of its initial PCE is retained) also outperforms the previously reported **AZO-I** and **AZO-II**, which retained 68 and 91% of the initial PCEs, respectively, under identical conditions and storage time.[37] To understand the reason behind the superior stability of **AZO-III** and **AZO-IV** devices compared to that of Spiro-OMeTAD cells, we measured water contact angle (CA) of HTMs shown in Figure 4 to study their hydrophobicity because this plays an important role in protecting the PSC

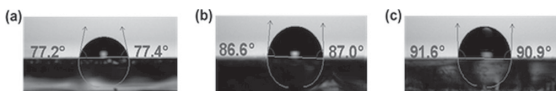


**Figure 4.** Water CAs of (a) Spiro-OMeTAD_$CA_{average}$ = 77.3°, (b) **AZO-III**_$CA_{average}$ = 86.6°, and (c) **AZO-IV**_$CA_{average}$ = 92.0°.


https://dx.doi.org/10.1021/acsomega.0c03184
ACS Omega XXXX, XXX, XXX−XXX

layer against moisture. Both **AZO-III** (86.6°) and **AZO-IV** (92.0°) films exhibited higher CAs compared to Spiro-OMeTAD (77.3°), showing a highly hydrophobic nature. Such enhanced hydrophobicity for both **AZO-III** and **AZO-IV** arises from the reduced number of hydrophilic methoxy groups compared to Spiro-OMeTAD (three methoxy groups in AZOs vs eight methoxy groups in Spiro-OMeTAD).[54]

Even though **AZO-IV** exhibited higher CA (92°) than **AZO-III** (86.2°), the lower stability of **AZO-IV** can be explained by its rapid oxidative degradation in the presence of p-type dopants caused by the strong charge localization in the radical cation state of **AZO-IV** (compared to **AZO-III**) because of additional thioalkyl substitution in 2-position, as shown in earlier reports.[34,55]

## 3. CONCLUSIONS

In summary, we have designed and synthesized two low-cost azomethine-functionalized phenothiazine-core HTMs, **AZO-III** and **AZO-IV**, via simple Schiff base chemistry with excellent synthesis yields. Upon the processing of these HTMs in nonhalogenated solvents, the champion **AZO-IV**-based corresponding device yielded a PCE of 11.62% with an inherently high hydrophobicity (water CA = 91.96°) and an extremely low production cost of 9.03 $/g. On the other hand, **AZO-III** HTM displayed excellent stability, retaining 75% of its initial performance after 6 months shelf-storage in 30% RH environment. Hence, despite the lower performance of **AZO-III** and **AZO-IV** (9.77 and 11.62%, respectively) cells compared to Spiro-OMeTAD-based reference device (18.63%), the significantly lower cost, good stability, and the environmentally friendly synthesis and processing make them rather competitive HTMs. Further optimization of these eco-friendly HTM designs may include the introduction of alkyl chains, as well as electron-rich units, in the phenothiazine core to ensure high hole-transportability, solution processability, and tunable energy levels.

## 4. EXPERIMENTAL SECTION

**4.1. Synthesis.** All the chemical precursors, namely, 4-iodoanisole, 4-nitroaniline, Cu powder, $K_2CO_3$, 18-Crown-6, Pd/C (10%), KOH, 1,10-phenanthroline, CuI, and phenothiazine, as well as the solvents, were purchased form Sigma-Aldrich and used without further purification. Compound **3** and **4** were synthesized according to previously reported methods.[56,57] All the reactions were carried out under an inert environment in Schleck tube. $^1$H and $^{13}$C NMR spectra were recorded with 500 MHz JEOL spectrometer in $CDCl_3$ against tetramethylsilane as reference. Mass spectroscopy was carried out using a high-resolution ESI-TOF LCT Premier XE mass spectrometer (Waters Corp.). The analyte was dissolved in chloroform/methanol ($c \approx 0.01$ mg/mL). More details on the synthesis are in the Supporting Information.

**4.2. Characterization.** The steady-state absorption spectra were recorded with a Shimadzu UV-2501PC spectrophotometer both in solution and in thin films. The solid-state films of **AZO-III** and **AZO-IV** were deposited by spin-coating (WS-400B-6NPP/LITE, Laurell Technologies) from $CHCl_3$ solution (1000 rpm, 1 min) onto clean glass substrates. Steady PL and TR-PL were measured by using the Pico Quant FluoTime 300 with a 510 nm picosecond pulsed laser. DPV measurements of the target HTMs and the reference Spiro-OMeTAD were performed by employing a potentiostat (Compact-Stat, Ivium Technologies) and a three-electrode cell configuration. Dry tetrabutyl ammonium tetrafluoroborate in dichloromethane (DCM) (0.1 M) was the supporting electrolyte, glass platinum was the electrode the working electrode, Pt wire was the the counter-electrode, Ag/AgCl wire was the the pseudo-reference electrode, and ferrocene/ferrocenium ($Fc/Fc^+$) couple the internal standard reference to scale the measured potentials against the vacuum level.

**4.3. Device Fabrication and Stability Test Measurements.** All the devices were prepared by using mixed perovskite with ITO/$SnO_2$/$Cs_{0.05}MA_{1-y}FA_yPbI_{3-x}Cl_x$/HTM/Au (or Ag) device structure. The substrates were cleaned by detergent, deionized water, acetone, and isopropyl alcohol, successively, and then, the substrates were further cleaned by UV ozone treatment for 15 min. The $SnO_2$ film as an ETM was prepared by spin-coating the $SnO_2$ aqueous colloidal dispersion at 4000 rpm for 30 s followed by thermal annealing at 150 °C for 30 min. The $Cs_{0.05}MA_{1-y}FA_yPbI_{3-x}Cl_x$ film was deposited by a two-step method according to a previous report.[58] 1.36 M $PbI_2$, 0.24 M $PbCl_2$, and 0.08 M CsI were dissolved in the dimethylformamide (DMF) and stirred for 3 h at 70 °C. 70 mg of MAI and 30 mg of FAI were dissolved in 1 mL of IPA with 10 $\mu$L of DMF added. After that, around 70 $\mu$L of $PbX_2$ precursor solution was spin-coated onto $SnO_2$ or $SnO_2$/LiF substrates at 3000 rpm for 45 s. Then, 200 $\mu$L of MAI/FAI solution was spin-coated onto the $PbX_2$ at 3000 rpm for 45 s. Then, the samples were thermally annealed on a hot plate at 100 °C for 10 min. The spiro-OMeTAD film as an HTM was prepared by spin-coating 72.5 mg/mL solution on the perovskite layer at 4000 rpm for 45 s. **AZO-III** and **AZO-IV** were prepared by dissolving the powders in toluene or chlorobenzene with concentrations 20, 15, 10, and 5 mg/mL. Both the HTMs along with Spiro-OMeTAD were first used without dopants, but because of the poor performance of the corresponding PSCs, doped devices were fabricated by doping the HTMs with 17.5 $\mu$L of Li-TFSI (520 mg/mL in acetonitrile), 28.8 $\mu$L of FK209 (300 mg/mL in acetonitrile), and 28.8 $\mu$L of tbp. Furthermore, the films of **AZO-III** and **AZO-IV** were deposited on perovskite layers by spin-coating at 3000 rpm for 45 s. The devices were finished by thermally evaporated 100 nm Ag or Au. All the devices had an effective area of 7.5 mm$^2$. All current density−voltage ($J$−$V$) curves were recorded using a Kethley 2400 source meter unit under simulated AM 1.5G illumination at an intensity of 100 mW/cm$^2$ with an XES-70S1 solar simulator. The system was calibrated using a NREL-certified monocrystal Si photodiode detector before device testing. Steady PL and TR-PL were measured by using the Pico Quant FluoTime 300 with a 510 nm picosecond pulsed laser. The stability test is averaged based on 20 devices, and for both the HTMs, the chosen concentration was 10 mg/mL.

**4.4. Computational Details.** All calculations were carried out using the Gaussian 09[59] software package without symmetry constraints. DFT[60] and time-dependent DFT[61] were used for computation of the ground state and vertical excitations (considering the six lower-lying transitions) of **AZO-III** and **AZO-IV**. Solvent effects (DCM) were considered in every calculation using the polarizable continuum model initially devised by Casida[62] and further studied by Tomasi and co-workers[63−65] as implemented on Gaussian 16, with radii and non-electrostatic terms for Truhlar and co-workers' SMD solvation model.[65] All calculations have been performed using the PBE1PBE functional and 6-31G(d,


https://dx.doi.org/10.1021/acsomega.0c03184
ACS Omega XXXX, XXX, XXX−XXX

p)[66−70] basis set. This functional uses a hybrid generalized gradient approximation, including 25% mixture of Hartree−Fock[71] exchange with DFT exchange−correlation, given by Perdew, Burke, and Ernzerhof functional (PBE).[72,73] Frequency calculations were performed to confirm the nature of the stationary points, yielding nonimaginary frequency for the optimized geometries. Natural population analysis[74,75] was performed as implemented on Gaussian 09 to study the electronic structure of the optimized species.[76−81]

## ■ ASSOCIATED CONTENT

### Supporting Information

The Supporting Information is available free of charge at https://pubs.acs.org/doi/10.1021/acsomega.0c03184.

Cost analysis of the newly designed materials and details on their synthesis and characterization (optical, electrochemical, and computational) (PDF)

## ■ AUTHOR INFORMATION


### Corresponding Authors

**Jagadish Salunke** − *Faculty of Engineering and Natural Sciences, Tampere University, FI-33014 Tampere, Finland*; Email: jagdishsalunke.nmu@gmail.com

**Jingjing Chang** − *State Key Discipline Laboratory of Wide Band Gap Semiconductor Technology, Shaanxi Joint Key Laboratory of Graphene, School of Microelectronics, Xidian University, 710071 Xi'an, P. R. China*; orcid.org/0000-0003-3773-182X; Email: jjingchang@xidian.edu.cn

**Paola Vivo** − *Faculty of Engineering and Natural Sciences, Tampere University, FI-33014 Tampere, Finland*; orcid.org/0000-0003-2872-6922; Email: paola.vivo@tuni.fi

### Authors

**Xing Guo** − *State Key Discipline Laboratory of Wide Band Gap Semiconductor Technology, Shaanxi Joint Key Laboratory of Graphene, School of Microelectronics, Xidian University, 710071 Xi'an, P. R. China*

**Maning Liu** − *Faculty of Engineering and Natural Sciences, Tampere University, FI-33014 Tampere, Finland*; orcid.org/0000-0001-9875-0966

**Zhenhua Lin** − *State Key Discipline Laboratory of Wide Band Gap Semiconductor Technology, Shaanxi Joint Key Laboratory of Graphene, School of Microelectronics, Xidian University, 710071 Xi'an, P. R. China*; orcid.org/0000-0002-2965-1769

**Nuno R. Candeias** − *Faculty of Engineering and Natural Sciences, Tampere University, FI-33014 Tampere, Finland; LAQV-REQUIMTE, Department of Chemistry, University of Aveiro, 3810-193 Aveiro, Portugal*; orcid.org/0000-0003-2414-9064

**Arri Priimagi** − *Faculty of Engineering and Natural Sciences, Tampere University, FI-33014 Tampere, Finland*; orcid.org/0000-0002-5945-9671

Complete contact information is available at: https://pubs.acs.org/10.1021/acsomega.0c03184


### Author Contributions

J.S. and X.G. contributed equally. The manuscript was written through contributions of all authors. All authors have given approval to the final version of the manuscript.

### Notes

The authors declare no competing financial interest.

## ■ ACKNOWLEDGMENTS

J.S. is grateful to the Fortum Foundation (201800260) and Finnish Foundation for Technology Promotion. A.P. is grateful to the Academy of Finland (Decision number 311142). P.V. acknowledges Jane & Aatos Erkko foundation (project ASPIRE) for financial support. This work is part of the Academy of Finland Flagship Programme, Photonics Research and Innovation (PREIN, Decision number 320165).

## ■ REFERENCES


(1) Calió, L.; Kazim, S.; Grätzel, M.; Ahmad, S. Hole-transport materials for perovskite solar cells. *Angew. Chem., Int. Ed.* **2016**, *55*, 14522−14545.

(2) Saliba, M.; Orlandi, S.; Matsui, T.; Aghazada, S.; Cavazzini, M.; Correa-Baena, J.-P.; Gao, P.; Scopelliti, R.; Mosconi, E.; Dahmen, K.-H.; Angelis, F. De.; Abate, A.; Hagfeldt, A.; Pozzi, G.; Graetzel, M.; Nazeeruddin, M. K. A molecularly engineered hole-transporting material for efficient perovskite solar cells. *Nat. Energy* **2016**, *1*, 15017.

(3) Bakr, Z. H.; Wali, Q.; Fakharuddin, A.; Schmidt-mende, L.; Brown, T. M.; Jose, R. Advances in hole transport materials engineering for stable and efficient perovskite solar cells. *Nano Energy* **2017**, *34*, 271−305.

(4) Azmi, R.; Nam, S. Y.; Sinaga, S.; Akbar, Z. A.; Lee, C.-L.; Yoon, S. C.; Jung, I. H.; Jang, S.-Y. High-performance dopant-free conjugated small molecule-based hole-transport materials for perovskite solar cells. *Nano Energy* **2018**, *44*, 191−198.

(5) Chen, H.; Bryant, D.; Troughton, J.; Kirkus, M.; Neophytou, M.; Miao, X.; Durrant, J. R.; McCulloch, I. One-step facile synthesis of a simple hole transport material for efficient perovskite solar cells. *Chem. Mater.* **2016**, *28*, 2515−2518.

(6) Vivo, P.; Salunke, J. K.; Priimagi, A. Hole-transporting materials for printable perovskite solar cells. *Materials* **2017**, *10*, 1087.

(7) Bi, D.; Yi, C.; Luo, J.; Decoppet, J. D.; Zhang, F.; Zakeeruddin, S. M.; Li, X.; Hagfeldt, A.; Grätzel, M. Polymer-templated nucleation and crystal growth of perovskite films for solar cells with efficiency greater than 21%. *Nat. Energy* **2016**, *1*, 16142.

(8) Jiang, Q.; Chu, Z.; Wang, P.; Yang, X.; Liu, H.; Wang, Y.; Yin, Z.; Wu, J.; Zhang, X.; You, J. Planar-structure perovskite solar cells with efficiency beyond 21%. *Adv. Mater.* **2017**, *29*, 1703852.

(9) Mahmoudi, T.; Wang, Y.; Hahn, B. $SrTiO_3/Al_2O_3$-Graphene electron transport layer for highly stable and efficient composites-based perovskite solar cells with 20.6% efficiency. *Adv. Energy Mater.* **2020**, *10*, 1903369.

(10) Hu, M.; Zhang, L.; She, S.; Wu, J.; Zhou, X.; Li, X.; Wang, D.; Miao, J.; Mi, G.; Chen, H.; Tian, Y.; Xu, B.; Cheng, C. Electron transporting bilayer of $SnO_2$ and $TiO_2$ nanocolloid enables highly efficient planar perovskite solar cells. *Sol. RRL* **2020**, *4*, 1900331.

(11) NREL. Efficiency chart. https://www.nrel.gov/pv/assets/pdfs/best-research-cell-efficiencies (accessed 10 March, 2020).

(12) Xu, B.; Sheibani, E.; Liu, P.; Zhang, J.; Tian, H.; Vlachopoulos, N.; Boschloo, G.; Kloo, L.; Hagfeldt, A.; Sun, L. Carbazole-based hole-transport materials for efficient solid-state dye-sensitized solar cells and perovskite solar cells. *Adv. Mater.* **2014**, *26*, 6629−6634.

(13) Gratia, P.; Magomedov, A.; Malinauskas, T.; Daskeviciene, M.; Abate, A.; Ahmad, S.; Grätzel, M.; Getautis, V.; Nazeeruddin, M. K. A methoxydiphenylamine-substituted carbazole twin derivative : An efficient hole-transporting material for perovskite solar cells. *Angew. Chem., Int. Ed.* **2015**, *54*, 11409−11413.

(14) Zhang, J.; Xu, B.; Johansson, M. B.; Hadadian, M.; Correa Baena, J. P.; Liu, P.; Hua, Y.; Vlachopoulos, N.; Johansson, E. M. J.; Boschloo, G.; Sun, L.; Hagfeldt, A. Constructive effects of alkyl chains: A strategy to design simple and non-Spiro hole transporting materials for high-efficiency mixed-Ion perovskite solar cells. *Adv. Energy Mater.* **2016**, *6*, 1502536.

(15) Krüger, J.; Plass, R.; Cevey, L.; Piccirelli, M.; Grätzel, M.; Bach, U. High efficiency solid-state photovoltaic device due to inhibition of interface charge recombination. *Appl. Phys. Lett.* **2001**, *79*, 2085−2087.
(16) Magomedov, A.; Kasparavičius, E.; Rakstys, K.; Paek, S.; Gasilova, N.; Genevičius, K.; Juška, G.; Malinauskas, T.; Nazeeruddin, M. K.; Getautis, V. Pyridination of hole transporting material in perovskite solar cells questions the long-term stability. *J. Mater. Chem. C* **2018**, *6*, 8874−8878.
(17) Juarez-Perez, E. J.; Leyden, M. R.; Wang, S.; Ono, L. K.; Hawash, Z.; Qi, Y. The role of the dopants on the morphological and transport properties of Spiro-MeOTAD hole transport layer. *Chem. Mater.* **2016**, *28*, 5702−5709.
(18) Jeon, N. J.; Na, H.; Jung, E. H.; Yang, T.-Y.; Lee, Y. G.; Kim, G.; Shin, H.-W.; Il Seok, S.; Lee, J.; Seo, J. A fluorene-terminated hole-transporting material for highly efficient and stable perovskite solar cells. *Nat. Energy* **2018**, *3*, 682−689.
(19) Zhang, J.; Xu, B.; Johansson, M. B.; Vlachopoulos, N.; Boschloo, G.; Sun, L.; Johansson, E. M. J.; Hagfeldt, A. Strategy to boost the efficiency of mixed-ion perovskite solar cells: changing geometry of the hole transporting material. *ACS Nano* **2016**, *10*, 6816−6825.
(20) Ge, Q.-Q.; Shao, J. Y.; Ding, J.; Deng, L. Y.; Zhou, W. K.; Chen, Y. X.; Ma, J. Y.; Wan, L. J.; Yao, J.; Hu, J. S.; Zhong, Y. W. A two-dimensional hole-transporting material for high-performance perovskite solar cells with 20 % average efficiency. *Angew. Chem., Int. Ed.* **2018**, *57*, 10959−10965.
(21) Jeon, N. J.; Lee, J.; Noh, J. H.; Nazeeruddin, M. K.; Grätzel, M.; Seok, S. I., II; Jeon, N. J.; Lee, J.; Nazeeruddin, M. K.; Grätzel, M. Efficient inorganic−organic hybrid perovskite solar cells based on pyrene arylamine derivatives as hole-transporting materials. *J. Am. Chem. Soc.* **2013**, *135*, 19087−19090.
(22) Petrus, M. L.; Schlipf, J.; Li, C.; Gujar, T. P.; Giesbrecht, N.; Müller-Buschbaum, P.; Thelakkat, M.; Bein, T.; Hüttner, S.; Docampo, P. Capturing the Sun: A Review of the challenges and perspectives of perovskite solar cells. *Adv. Energy Mater.* **2017**, *7*, 1700264.
(23) Kim, G.-W.; Lee, J.; Kang, G.; Kim, T.; Park, T. Donor − acceptor type dopant-free, polymeric hole transport material for planar perovskite solar cells ( 19 . 8 %). *Adv. Energy Mater.* **2018**, *8*, 1701935.
(24) Lee, J.; Malekshahi Byranvand, M.; Kang, G.; Son, S. Y.; Song, S.; Kim, G.-W.; Park, T. Green-solvent-processable, dopant-free hole-transporting materials for robust and efficient perovskite solar cells. *J. Am. Chem. Soc.* **2017**, *139*, 12175−12181.
(25) Zhang, M.; Wang, Z.; Zhou, B.; Jia, X.; Ma, Q.; Yuan, N.; Zheng, X.; Ding, J.; Zhang, W. Green anti-solvent processed planar perovskite solar cells with efficiency beyond 19%. *Sol. RRL* **2018**, *2*, 1700213.
(26) Jiang, K.; Wu, F.; Zhang, G.; Zhu, L.; Yan, H. Efficient perovskite solar cells based on dopant-free spiro-OMeTAD processed with halogen-free green solvent. *Sol. RRL* **2019**, *3*, 1900061.
(27) Lu, H.; He, B.; Ji, Y.; Shan, Y.; Zhong, C.; Xu, J.; LiuYang, J.; Wu, F.; Zhu, L. Dopant-free hole transport materials processed with green solvent for efficient perovskite solar cells. *Chem. Eng. J.* **2020**, *385*, 123976.
(28) Lee, J.; Kim, G. W.; Kim, M.; Park, S. A.; Park, T. Nonaromatic green-solvent-processable, dopant-free, and lead-capturable hole transport polymers in perovskite solar cells with high efficiency. *Adv. Energy Mater.* **2020**, *10*, 1902662.
(29) Shinde, D. B.; Salunke, J. K.; Candeias, N. R.; Tinti, F.; Gazzano, M.; Wadgaonkar, P. P.; Priimagi, A.; Camaioni, N.; Vivo, P. Crystallisation-enhanced bulk hole mobility in phenothiazine-based organic semiconductors. *Sci. Rep.* **2017**, *7*, 46268.
(30) Zhou, W.; Wen, Y.; Ma, L.; Liu, Y.; Zhan, X. Conjugated polymers of rylene diimide and phenothiazine for n-channel organic field-effect transistors. *Macromolecules* **2012**, *45*, 4115−4121.
(31) Maglione, C.; Carella, A.; Centore, R.; Chávez, P.; Lévêque, P.; Fall, S.; Leclerc, N. Novel low bandgap phenothiazine functionalized DPP derivatives prepared by direct heteroarylation: Application in bulk heterojunction organic solar cells. *Dyes Pigm.* **2017**, *141*, 169−178.
(32) Salunke, J. K.; Wong, F. L.; Feron, K.; Manzhos, S.; Lo, M. F.; Shinde, D.; Patil, A.; Lee, C. S.; Roy, V. A. L.; Sonar, P.; Wadgaonkar, P. P. Phenothiazine and carbazole substituted pyrene based electroluminescent organic semiconductors for OLED devices. *J. Mater. Chem. C* **2016**, *4*, 1009−1018.
(33) Grisorio, R.; Roose, B.; Colella, S.; Listorti, A.; Suranna, G. P.; Abate, A. Molecular tailoring of phenothiazine-based hole-transporting materials for high-performing perovskite solar cells. *ACS Energy Lett.* **2017**, *2*, 1029−1034.
(34) Zhang, F.; Wang, S.; Zhu, H.; Liu, X.; Liu, H.; Li, X.; Xiao, Y.; Zakeeruddin, S. M.; Grätzel, M. Impact of peripheral groups on phenothiazine-based hole-transporting materials for perovskite solar cells. *ACS Energy Lett.* **2018**, *3*, 1145−1152.
(35) Liang, X.; Wang, C.; Wu, M.; Wu, Y.; Zhang, F.; Han, Z.; Lu, X.; Guo, K.; Zhao, Y.-M. Effects of core moiety and substituted positions in phenothiazine-based hole transporting materials towards high thermal stability and good hole mobility. *Tetrahedron* **2017**, *73*, 7115−7121.
(36) Sivanadanam, J.; Mandal, S. S.; Aidhen, I. S.; Ramanujam, K. Design of cone-shaped hole transporting material organic structures for perovskite solar cells applications. *ChemistrySelect* **2018**, *3*, 8159−8166.
(37) Salunke, J.; Guo, X.; Lin, Z.; Vale, J. R.; Candeias, N. R.; Nyman, M.; Dahlström, S.; Österbacka, R.; Priimagi, A.; Chang, J.; Vivo, P. Phenothiazine-based hole-transporting materials toward eco-friendly perovskite solar cells. *ACS Appl. Energy Mater.* **2019**, *2*, 3021−3027.
(38) Petrus, M. L.; Schutt, K.; Sirtl, M. T.; Hutter, E. M.; Closs, A. C.; Ball, J. M.; Bijleveld, J. C.; Petrozza, A.; Bein, T.; Dingemans, T. J.; Savenije, T. J.; Snaith, H.; Docampo, P. New generation hole transporting materials for perovskite solar cells: amide-based small-molecules with nonconjugated backbones. *Adv. Energy Mater.* **2018**, *8*, 1801605.
(39) Bowden, K.; Braude, E. A. Studies in light absorption. part X. further observations on ultra-violet auxochromes. A survey of the effects of xome of the less common elements. *J. Chem. Soc.* **1952**, 1068−1077.
(40) Karthikeyan, C. S.; Thelakkat, M. Key aspects of individual layers in solid-state dye-sensitized solar cells and novel concepts to improve their performance. *Inorg. Chim. Acta* **2008**, *361*, 635−655.
(41) Tremblay, M.-H.; Skalski, T.; Gautier, Y.; Pianezzola, G.; Skene, W. G. Investigation of Triphenylamine-Thiophene-Azomethine Derivatives: Toward Understanding Their Electrochromic Behavior. *J. Phys. Chem. C* **2016**, *120*, 9081−9087.
(42) Petrus, M. L. Azomethine-based Donor Materials for Organic Solar Cells. Ph.D. Thesis, Delft University of Technology, 2014.
(43) Wang, Q.-K.; Wang, R.-B.; Shen, P.-F.; Li, C.; Li, Y.-Q.; Liu, L.-J.; Duhm, S.; Tang, J.-X. Energy level offsets at lead halide perovskite/organic hybrid interfaces and their impact on charge separation. *Adv. Mater. Interfaces* **2015**, *2*, 1400528.
(44) Zhang, H.; Liu, M.; Yang, W.; Judin, L.; Hukka, T. I.; Priimagi, A.; Deng, Z.; Vivo, P. Thionation enhances the performance of polymeric dopant-free hole-transporting materials for perovskite solar cells. *Adv. Mater. Interfaces* **2019**, *6*, 1901036.
(45) Makuta, S.; Liu, M.; Endo, M.; Nishimura, H.; Wakamiya, A.; Tachibana, Y. Photo-excitation intensity dependent electron and hole injections from lead iodide perovskite to nanocrystalline $TiO_2$ and spiro-OMeTAD. *Chem. Commun.* **2016**, *52*, 673−676.
(46) Yamada, Y.; Nakamura, T.; Endo, M.; Wakamiya, A.; Kanemitsu, Y. Photocarrier recombination dynamics in perovskite $CH_3NH_3PbI_3$ for solar cell applications. *J. Am. Chem. Soc.* **2014**, *136*, 11610−11613.
(47) Liu, M.; Endo, M.; Shimazaki, A.; Wakamiya, A.; Tachibana, Y. Identifying an optimum perovskite solar cell structure by kinetic analysis: planar, mesoporous based, or extremely thin absorber structure. *ACS Appl. Energy Mater.* **2018**, *1*, 3722−3732.


https://dx.doi.org/10.1021/acsomega.0c03184
*ACS Omega* XXXX, XXX, XXX−XXX

(48) Isabelli, F.; Di Giacomo, F.; Gorter, H.; Brunetti, F.; Groen, P.; Andriessen, R.; Galagan, Y. Solvent systems for industrial-scale processing of spiro-OMeTAD hole transport layer in perovskite solar cells. *ACS Appl. Energy Mater.* **2018**, *1*, 6056−6063.
(49) Zhang, F.; Liu, X.; Yi, C.; Bi, D.; Luo, J.; Wang, S.; Li, X.; Xiao, Y.; Zakeeruddin, S. M.; Grätzel, M. Dopant-free donor (D)−$\pi$−D−$\pi$−D conjugated hole-transport materials for efficient and stable perovskite solar cells. *ChemSusChem* **2016**, *9*, 2578−2585.
(50) Guo, J.-J.; Bai, Z.-C.; Meng, X.-F.; Sun, M.-M.; Song, J.-H.; Shen, Z.-S.; Ma, N.; Chen, Z.-L.; Zhang, F. Novel dopant-free metallophthalocyanines based hole transporting materials for perovskite solar cells: The effect of core metal on photovoltaic performance. *Sol. Energy* **2017**, *155*, 121−129.
(51) Rakstys, K.; Abate, A.; Dar, M. I.; Gao, P.; Jankauskas, V.; Jacopin, G.; Kamarauskas, E.; Kazim, S.; Ahmad, S.; Grätzel, M.; Nazeeruddin, M. K. Triazatruxene-based hole transporting materials for highly efficient perovskite solar cells. *J. Am. Chem. Soc.* **2015**, *137*, 16172−16178.
(52) Planells, M.; Abate, A.; Hollman, D. J.; Stranks, S. D.; Bharti, V.; Gaur, J.; Mohanty, D.; Chand, S.; Snaith, H. J.; Robertson, N. Diacetylene bridged triphenylamines as hole transport materials for solid state dye sensitized solar cells. *J. Mater. Chem. A* **2013**, *1*, 6949−6960.
(53) Yoo, S.; Domercq, B.; Kippelen, B. Intensity-dependent equivalent circuit parameters of organic solar cells based on pentacene and C60. *J. Appl. Phys.* **2005**, *97*, 103706.
(54) Liu, M.; Endo, M.; Shimazaki, A.; Wakamiya, A.; Tachibana, Y. Light intensity dependence of performance of lead halide perovskite solar cells. *J. Photopolym. Sci.* **2017**, *30*, 577−582.
(55) Xu, B.; Zhang, J.; Hua, Y.; Liu, P.; Wang, L.; Ruan, C.; Li, Y.; Boschloo, G.; Johansson, E. M. J.; Kloo, L.; Hagfeldt, A.; Jen, A. K.-Y.; Sun, L. Tailor-making low-cost spiro [fluorene-9, 9'-xanthene]-based 3D oligomers for perovskite solar cells. *Chem* **2017**, *2*, 676−687.
(56) Karpinska, J.; Starczewska, B.; Puzanowska-Tarasiewicz, H. Analytical properties of 2- and 10-disubstituted phenothiazine derivatives. *Anal. Sci.* **1996**, *12*, 161−170.
(57) Petrus, M. L.; Bein, T.; Dingemans, T. J.; Docampo, P. A low cost azomethine-based hole transporting material for perovskite photovoltaics. *J. Mater. Chem. A* **2015**, *3*, 12159−12162.
(58) Duvva, N.; Sudhakar, K.; Badgurjar, D.; Chitta, R.; Giribabu, L. Spacer controlled photo-induced intramolecular electron transfer in a series of phenothiazine-boron dipyrromethene donor-acceptor dyads. *J. Photochem. Photobiol., A* **2015**, *312*, 8−19.
(59) Guo, X.; Zhang, B.; Lin, Z.; Su, J.; Yang, Z.; Zhang, C.; Chang, J.; Liu, S.; Hao, Y. Highly efficient perovskite solar cells based on a dopant-free conjugated DPP polymer hole transport layer: influence of solvent vapor annealing. *Sustainable Energy Fuels* **2018**, *2*, 2154−2159.
(60) Frisch, M. J.; Trucks, G. W.; Schlegel, H. B.; Scuseria, G. E.; Robb, M. A.; Cheeseman, J. R.; Scalmani, G.; Barone, V.; Mennucci, B.; Petersson, G. A.; Nakatsuji, H.; Caricato, M.; Li, X.; Hratchian, H. P.; Izmaylov, A. F.; Bloino, J.; Zheng, G.; Sonnenberg, J. L.; Hada, M.; Ehara, M.; Toyota, K.; Fukuda, R.; Hasegawa, J.; Ishida, M.; Nakajima, T.; Honda, Y.; Kitao, O.; Nakai, H.; Vreven, T.; Montgomery, J. A.; Peralta, J. E.; Ogliaro, F.; Bearpark, M.; Heyd, J. J.; Brothers, E.; Kudin, K. N.; Staroverov, V. N.; Keith, T.; Kobayashi, R.; Normand, J.; Raghavachari, K.; Rendell, A.; Burant, J. C.; Iyengar, S. S.; Tomasi, J., Cossi, M.; Rega, N.; Millam, J. M.; Klene, M.; Knox, J. E.; Cross, J. B.; Bakken, V.; Adamo, C.; Jaramillo, J.; Gomperts, R.; Stratmann, R. E.; Yazyev, O.; Austin, A. J.; Cammi, R.; Pomelli, C.; Ochterski, J. W.; Martin, R. L.; Morokuma, K.; Zakrzewski, V. G.; Voth, G. A.; Salvador, P.; Dannenberg, J. J.; Dapprich, S.; Daniels, A. D.; Farkas, O.; Foresman, J. B.; Ortiz, J. V.; Cioslowski, J.; Fox, D. J. *Gaussian 09*, Revision D.01; Gaussian Inc.: Wallingford CT, 2013.
(61) Parr, R. G.; Yang, W. *Density Functional Theory of Atoms and Molecules*; Oxford University Press: New York, 1989.
(62) Casida, M. E. *Time-Dependent Density-Functional Response Theory for Molecules*; Chong, D. P., Ed.; World Scientific: Singapore, 1995; Vol. *1*, pp 155−192.
(63) Cancès, E.; Mennucci, B.; Tomasi, J. A new integral equation formalism for the polarizable continuum model: Theoretical background and applications to isotropic and anisotropic dielectrics. *J. Chem. Phys.* **1997**, *107*, 3032−3041.
(64) Mennucci, B.; Tomasi, J. Continuum solvation models: A new approach to the problem of solute's charge distribution and cavity boundaries. *J. Chem. Phys.* **1997**, *106*, 5151−5158.
(65) Cossi, M.; Barone, V.; Mennucci, B.; Tomasi, J. Ab initio study of ionic solutions by a polarizable continuum dielectric model. *Chem. Phys. Lett.* **1998**, *286*, 253−260.
(66) Marenich, A. V.; Cramer, C. J.; Truhlar, D. G. Universal solvation model based on solute electron density and on a continuum model of the solvent defined by the bulk dielectric constant and atomic surface tensions. *J. Phys. Chem. B* **2009**, *113*, 6378−6396.
(67) Ditchfield, R.; Hehre, W. J.; Pople, J. A. Self-consistent molecular-orbital methods. IX. An extended gaussian-type basis for molecular-orbital studies of organic molecules. *J. Chem. Phys.* **1971**, *54*, 724−728.
(68) Hehre, W. J.; Ditchfield, R.; Pople, J. A. Self—consistent molecular orbital methods. XII. Further extensions of gaussian—type basis sets for use in molecular orbital studies of organic molecules. *J. Chem. Phys.* **1972**, *56*, 2257−2261.
(69) Hariharan, P. C.; Pople, J. A. Accuracy of AHnequilibrium geometries by single determinant molecular orbital theory. *Mol. Phys.* **1974**, *27*, 209−214.
(70) Gordon, M. S. The isomers of silacyclopropane. *Chem. Phys. Lett.* **1980**, *76*, 163−168.
(71) Hariharan, P. C.; Pople, J. A. The influence of polarization functions on molecular orbital hydrogenation energies. *Theor. Chim. Acta* **1973**, *28*, 213−222.
(72) Hehre, W. J.; Radom, L.; Schleye, P. V. R.; Pople, J. *Ab Initio Molecular Orbital Theory*; John Wiley & Sons: NewYork, 1986.
(73) Perdew, J. P. density-functional approximation for the correlation energy of the inhomogeneous electron gas. *Phys. Rev. B: Condens. Matter Mater. Phys.* **1986**, *33*, 8822−8824.
(74) Carpenter, J. E. Extension of Lewis structure concepts to open-shell and excited-state molecular species. Ph.D. Thesis, University of Wisconsin, Madison WI, 1987.
(75) Carpenter, J. E.; Weinhold, F. Analysis of the geometry of the hydroxymethyl radical by the different hybrids for different spins natural bond orbital procedure. *J. Mol. Struct.* **1988**, *169*, 41−62.
(76) Foster, J. P.; Weinhold, F. Natural hybrid orbitals. *J. Am. Chem. Soc.* **1980**, *102*, 7211−7218.
(77) Reed, A. E.; Weinhold, F. Natural bond orbital analysis of near-Hartree-Fock water dimer. *J. Chem. Phys.* **1983**, *78*, 4066−4073.
(78) Reed, A. E.; Weinhold, F. Natural localized molecular orbitals. *J. Chem. Phys.* **1985**, *83*, 1736−1740.
(79) Reed, A. E.; Weinstock, R. B.; Weinhold, F. Natural population analysis. *J. Chem. Phys.* **1985**, *83*, 735−746.
(80) Reed, A. E.; Curtiss, L. A.; Weinhold, F. Intermolecular interactions from a natural bond orbital, donor-acceptor viewpoint. *Chem. Rev.* **1988**, *88*, 899−926.
(81) Weinhold, F.; Carpenter, J. E. *The Structure of Small Molecules and Ions*; Plenum Press, 1988.


https://dx.doi.org/10.1021/acsomega.0c03184
*ACS Omega* XXXX, XXX, XXX−XXX

# PUBLICATION IV

Fluorination of pyrene-based organic semiconductors enhances the performance of light emitting diodes and halide perovskite solar cells

Jagadish Salunke, Amandeep Singh, Dongxu He, Hong DucPham, Yang Bai, Lianzhou Wang, Staffan Dahlström, Mathias Nyman, Sergei Manzhos, Krishna Feron, Ronald Österbacka, Arri Priimagi, Paola Vivo, and Prashant Sonar

*Organic Electronics* 2020, 77, 105524.
DOI.org/10.1016/j.orgel.2019.105524

Organic Electronics 77 (2020) 105524

Contents lists available at ScienceDirect

Organic Electronics

journal homepage: http://www.elsevier.com/locate/orgel

# Fluorination of pyrene-based organic semiconductors enhances the performance of light emitting diodes and halide perovskite solar cells

Jagadish Salunke [a,**,1], Amandeep Singh [b,1], Dongxu He [c], Hong Duc Pham [b], Yang Bai [c], Lianzhou Wang [c], Staffan Dahlström [d], Mathias Nyman [d], Sergei Manzhos [e], Krishna Feron [f,g], Ronald Österbacka [d], Arri Priimagi [a], Paola Vivo [a,***], Prashant Sonar [b,*]

[a] Faculty of Engineering and Natural Sciences, Tampere University, P.O. Box 541, FI-33015, Tampere, Finland
[b] School of Chemistry, Physics and Mechanical Engineering, Molecular Design and Synthesis, Queensland University of Technology (QUT), Brisbane, Australia
[c] Australian Institute for Bioengineering and Nanotechnology and School of Chemical Engineering, University of Queensland, Brisbane, Australia
[d] Physics, Faculty of Science and Engineering and Center for Functional Materials, Åbo Akademi University, Porthansgatan 3, 20500, Turku, Finland
[e] Centre Énergie Matériaux Télécommunications, Institut National de la Recherche Scientifique, 1650 Boulevard Lionel-Boulet, Varennes, QC, J3X1S2, Canada
[f] CSIRO Energy Centre, NSW, 2304, Australia
[g] Centre for Organic Electronics, University of Newcastle, Callaghan, NSW, 2308, Australia

ARTICLE INFO

*Keywords:*
Pyrene
Triphenylamine
Dopant-free
Fluorination
Organic light emitting diodes
Hole transporting material
Perovskite solar cells

ABSTRACT

In this work, a fluorinated pyrene-based organic semiconductor (**L-F**) has been designed and synthesized starting from a low-cost pyrene core functionalized with triphenylamine substituents at 1,3,6,8 positions (**L-H**), obtained via Suzuki coupling reactions. Its performance when used as green emitter in organic light emitting diodes (OLEDs) or as dopant-free hole-transporting material (HTM) in halide perovskite solar cells (PSCs) is higher than that of the **L-H** counterpart, in spite of its lower bulk hole-mobility ($7.0 \times 10^{-6}$ cm$^2$/V) to **L-H** ($1.9 \times 10^{-4}$ cm$^2$/V). In fact, the OLED devices based on a **L-F** active layer showed excellent green emission (brightness and current efficiency were 1759.8 cd/m$^2$ and 3.7 cd/A, respectively) at a 4.5 V turn-on voltage. When the molecules were employed as a dopant-free HTM in PSCs, **L-F** led to a power conversion efficiency (PCE) and open circuit voltage ($V_{oc}$) of 5.9% and 1.07 V, respectively, thus outperforming those of corresponding devices based on **L-H** (PCE = 5.0% and $V_{oc}$ = 0.87 V) under similar experimental conditions (AM 1.5G and 100 mW cm$^2$). We attribute the enhancements of **L-F**-based optoelectronic devices (OLEDs and PSCs) to the observed better quality of the **L-F** films. The promising performance of **L-F** indicates that fluorination of small molecules can be an effective strategy to achieve low-cost and high-performing materials for energy harvesting and display-based organic electronic devices.

## 1. Introduction

Small-molecule organic semiconductors (SMOS) have been extensively investigated in several types of organic electronic devices, such as organic light emitting diodes (OLEDs) [1,2], organic field effect transistors (OFETs) [3,4], organic solar cells (OSCs) [5,6], dye sensitized solar cells (DSSCs) [7,8], and, recently, perovskite solar cells (PSCs) [9–11]. Compared to conventional inorganic semiconducting materials, SMOS have numerous advantages in terms of solution processability, low-temperature processing, roll-to-roll printing on flexible substrates, tunability of the optoelectronic properties by functionalization [12,13], easy scalability, and high purity, which make them highly suitable for electronic applications [14–18]. Even though SMOS are intensively investigated for a wide range of organic electronic applications, only few studies report the application of versatile low-cost SMOS that could be used in multiple types of devices, and particularly in both OLEDs and PSCs [19,20].

A large number of solution processable SMOS have been successfully

* Corresponding author.
** Corresponding author.
*** Corresponding author.
*E-mail address:* sonar.prashant@qut.edu.au (P. Sonar).
[1] Both authors contributed equally.

https://doi.org/10.1016/j.orgel.2019.105524
Received 10 July 2019; Received in revised form 18 October 2019; Accepted 23 October 2019
Available online 9 November 2019

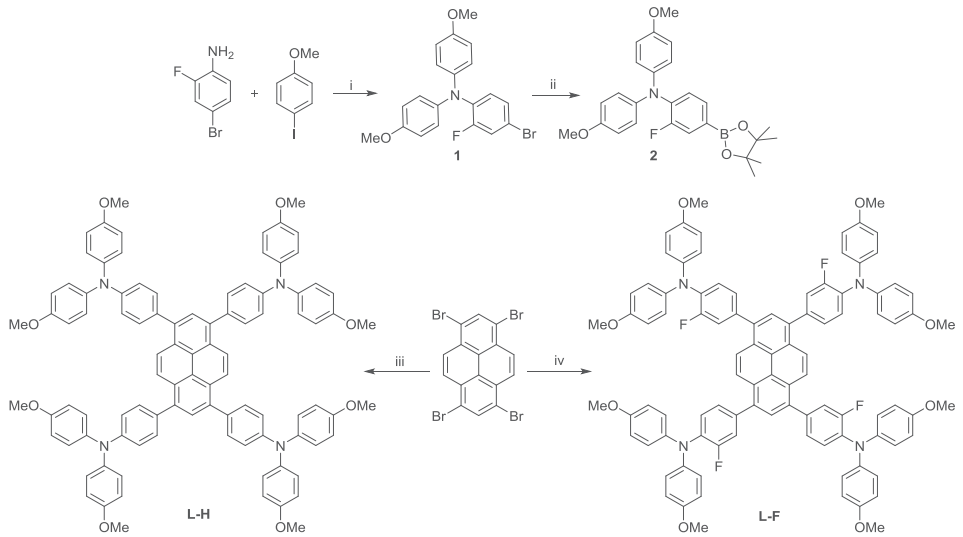


**Scheme 1.** Molecular design and synthetic route for **L-H** and **L-F**.
Reagents: i) CuI, 1,10-Phenanthroline, KOH, Toluene, reflux, 48 h, 80%. ii) Bis(pinacolato)diboron, Potassium acetate, $PdCl_2$(dppf), 1,4-dioxane, reflux, 12 h, 78%. iii) 4-methoxy-*N*-(4-methoxyphenyl)-*N*-(4-(4,4,5,5-tetramethyl-1,3,2-dioxaborolan-2-yl)phenyl)aniline, $Pd(PPh_3)_4$, 2 M $K_2CO_3$, toluene:THF (30:70), reflux, 12 h, 75%. (iv) 2-fluoro-*N*,*N*-bis(4-methoxyphenyl)-4-(4,4,5,5-tetramethyl-1,3,2-dioxaborolan-2-yl)aniline, $Pd(PPh_3)_4$, 2 M $K_2CO_3$, toluene:THF (30:70), reflux, 12 h, 71%.

employed for the production of low cost, scalable, and high-performance OLEDs [21–23]. Even though red/orange light emitting SMOS are commercially available, obtaining efficient and low-cost green/blue SMOS with high color purity is still a big challenge [24–26]. Thus, molecular design and engineering approaches for novel green/blue emitting SMOS still attract considerable attention of molecular designers/researchers in the area of OLEDs [27–30].

Another area of demand for low-cost SMOS is the design of novel high-performance hole-transporting materials (HTMs) for PSCs applications. PSCs have recently attracted tremendous attention because of their outstanding power conversion efficiencies (PCEs) up to 25.2% achieved in just a decade of research [31–36]. However, the poor stability of PSCs and the cost of some of their building blocks are among the main impediments to their future commercialization [37–41]. Typically, the most efficient and widely adopted organic HTMs in perovskite-based photovoltaics are 2,2′,7,7′-tetrakis(*N*,*N*-di-p-methoxyphenylamine)-9, 9′-spirobifluorene (Spiro-OMeTAD) and poly-[bis(4-phenyl)(2,4, 6-trimethylphenyl)amine] (PTAA). Nonetheless, these materials are not only very costly (retail prices for Spiro-OMeTAD and PTAA are 300 $/g and 2238 $/g, respectively) [42,43], but they also require corrosive or hygroscopic dopants to enhance their poor mobility and conductivity [11,44]. Unfortunately, such dopants are very detrimental for the stability of the device. To date, the key requirements of HTMs such as high stability, high hole-mobility, easy synthesis, and cost-effectiveness, have not been effectively addressed [45,46], thus making their fulfilment an important challenge in PSC research.

Pyrene is a well-known polycyclic aromatic hydrocarbon (PAH) with several impressive properties such as good stability, high fluorescence quantum yield, excimer formation tendency, and easily modifiable chemical structure [47–49]. Due to these characteristics, pyrene derivatives have been widely studied in the context of OLEDs, OFETs, fluorescence probes, and organic electronics in general [69]. However, only few works are reported pyrene-based materials as promising molecular frameworks for PSCs [50–52], and all pyrene-based HTMs proposed in such framework require the addition of dopants such as 4-*tert*-butylpyridine (*t*-BP) or bis(trifluoromethane)sulfonimide lithium salt in order to achieve devices with reasonable performance [50–53]. Furthermore, while there are several reports on pyrene-based functional organic semiconductors for either OLEDs or transistors [54–56] to the best of our knowledge there are no reports using the same materials for OLED and PSCs applications.

In this work, we synthesized two pyrene-based SMOS, namely 4,4′,4″,4‴-(pyrene-1,3,6,8-tetrayl)tetrakis(*N*,*N*-bis(4-methoxyphenyl) aniline (coded as **L-H**) and 4,4′,4″,4‴-(pyrene-1,3,6,8-tetrayl)tetrakis(2-fluoro-*N*,*N*-bis(4-methoxyphenyl)aniline) (coded as **L-F**) from cheap precursors via simple two-to-three steps synthetic routes in high yields. Their chemical structures are shown in Scheme 1. While **L-H** has been very recently reported as doped HTM in planar PSCs architectures [52], we herein modify the **L-H** design by fluorination of the TPA end-capping group (yielding the **L-F** material). Our work demonstrates that, upon fluorination, the performance of OLEDs and PSCs based on **L-F** pyrene SMOS outperforms that of devices based on non-fluorinated **L-H** material. In fact, the OLED devices based on **L-F** and **L-H** show current efficiency of 3.7 cd/A and 1.3 cd/A, respectively at a 4.5 V turn-on voltage. When **L-F** and **L-H** are employed as dopant-free HTMs in *p-i-n* PSCs, they lead to a PCE of 5.93% and 5%, respectively. We attribute the enhanced performance of OLEDs and PSCs based on **L-F** to the fluorination-induced tuning of energy level alignment and to the observed better film quality of **L-F**.

## 2. Experimental

### 2.1. Materials

All the compounds (palladium catalyst, N-bromosuccinimide, potassium acetate, 1,3,6,8-tetrabromopyrene, 4-iodoanisole, KOH, 1,10-phenanthroline, CuI, bis(pinacolato)diboron and 4-bromo-2-fluoro-N, N-bis(4-methoxyphenyl)aniline) and solvents were purchased form Aldrich Chemicals and were used without further purification. All the reactions were carried out under inert environment in a Schlenk tube. $^1H$ and $^{13}C$ NMR spectra were recorded with a Varian Mercury 300 MHz spectrometer (Varian Inc.) in $CDCl_3$ against tetramethylsilane as reference. The differential scanning calorimetry (DSC) signals were recorded using a Mettler Toledo DSC 1 apparatus, while thermogravimetric

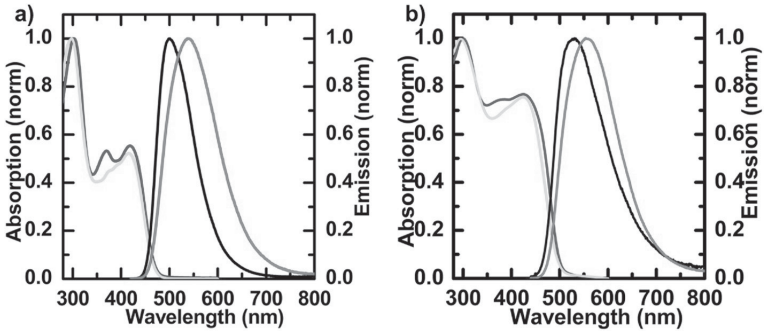


**Fig. 1.** (a) Normalized absorption (blue for **L-H** and green for **L-F**) and emission (black for **L-H** and red for **L-F**) spectra in chloroform solution ($10^{-5}$M). (b) Normalized absorption (blue for **L-H** and green for **L-F**) and emission (black for **L-H** and red for **L-F**) spectra of spin-coated **L-H** (black) and **L-F** (red) films. (For interpretation of the references to color in this figure legend, the reader is referred to the Web version of this article.)

analysis (TGA) measurements were conducted on a STAR TGA850 analyzer. The absorption and emission measurements were carried out by means of UV-2501PC spectrophotometer and Fluorolog Yobin Yvon-SPEX fluorometer, respectively.

For solar cells fabrication, $C_{60}$ (95%) was purchased from Solenne BV. PTAA (Mn = 7000–10000 g $mol^{-1}$), cesium iodide (99.99%), cesium bromide, lead iodide (99.99%), lead bromide (99.99%), and bathocuproine (BCP) (96%) were purchased from Sigma-Aldrich. Formamidinium iodide (FAI), formamidinium bromide (FABr), methylammonium bromide (MABr), and methylammonium iodide (MAI) were purchased from GreatCell Solar.

### 2.2. Synthesis of *L-H* and *L-F*

#### 2.2.1. Synthesis of 4-bromo-2-fluoro-N,N-bis(4-methoxyphenyl)aniline (1)

4-Bromo-2-fluoroaniline (2 g, 10 mmol), 4-iodoanisole (5.6 g, 24 mmol), 1,10-phenanthroline (0.38 g, 2.1 mmol), and 25 mL toluene were added into a Schlenck tube under nitrogen atmosphere. The reaction mixture was heated to 100 °C, then CuI (0.40 g, 2.1 mmol) and KOH (4.41 g, 78.9 mmol) were added and the reaction mixture was refluxed for 48 h. The reaction mixture was cooled to room temperature and poured into 200 mL of ice cold water, after which the organic phase was extracted using dichloromethane, dried over anhydrous sodium sulphate, and filtered. After evaporation of the solvent, the crude product was purified by column chromatography using a 5% ethyl acetate:pet ether solvent, giving 3.4 g of white solid in a 80% yield.

$^1$H NMR (300 MHz, $CDCl_3$) $\delta$ ppm 3.78 (s, 1 H) 6.77–6.85 (m, 4 H) 6.89–6.95 (m, 4 H) 6.95 (dd, $J$ = 8.70, 0.50 Hz, 1 H) 7.15 (dd, $J$ = 8.70, 0.50 Hz, 1 H) 7.22 (dd, $J$ = 1.60, 0.50 Hz, 1 H). $^{13}$C NMR (75 MHz, $CDCl_3$) $\delta$ ppm 55.06, 114.09, 119.83, 120.14, 123.71, 127.43, 128, 134.67, 140.38, 155.06, 158.12.

#### 2.2.2. Synthesis of 2-fluoro-N,N-bis(4-methoxyphenyl)-4-(4,4,5,5-tetramethyl-1,3,2-dioxaborolan-2-yl)aniline (2)

Compound **1** (3 g, 7.46 mmol), bis(pinacolato)diboron (2.08 g, 8.2 mmol), $Pd(dppf)Cl_2$ (0.273 g. 0.37 mmol), KOAc (2.19 gm, 22.38 mmol), were added to a Schlenk flask under inert atmosphere. The flask was evacuated and stirred at room temperature for 20 min, and 1,4-dioxane (25 mL) was added to the reaction mixture under nitrogen flow. The solution was refluxed under nitrogen environment for 12 h. The reaction mixture was quenched by adding 100 mL water and then extracted by using 200 mL dichloromethane. The organic phase was dried over sodium sulphate and filtered. The evaporation of the organic solvent by a rotary evaporator gave the crude product, which was further purified by column chromatography using a 3–5% ethyl acetate: pet ether solvent, affording 2.6 g of white solid in 78% yield.

$^1$H NMR (300 MHz, $CDCl_3$) $\delta$ ppm 1.34 (s, 12 H) 3.79 (s, 6 H) 6.72–6.86 (m, 4 H) 6.88–6.99 (m, 4 H) 7.01 (dd, $J$ = 8.30, 0.50 Hz, 1 H) 7.43 (dd, $J$ = 8.30, 1.50 Hz, 1 H) 7.47 (dd, $J$ = 1.50, 0.50 Hz, 1 H). $^{13}$C NMR (75 MHz, $CDCl_3$) $\delta$ ppm 24.82, 55.45, 83.85, 114.42, 122.71, 124.49, 125.87, 131.05, 138.38, 141.01, 154.54, 155.50, 157.86.

#### 2.2.3. Synthesis of 4,4′,4″,4‴-(pyrene-1,3,6,8-tetrayl)tetrakis(N,N-bis(4-methoxyphenyl)aniline) (L-H) done according to a reported procedure [52]

$^1$H NMR (300 MHz, $CDCl_3$) $\delta$ = 8.26 (s, 4 H), 8.00 (s, 2 H), 7.48 (d, $J$ = 8.2 Hz, 8 H), 7.26 - 7.14 (m, 16 H), 7.09 (d, $J$ = 8.8 Hz, 8 H), 7.01 -

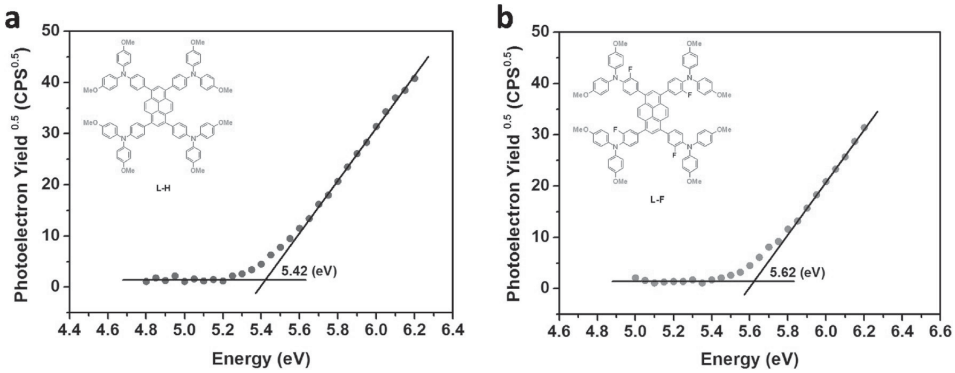


**Fig. 2.** Photoelectron spectroscopy in air analysis of (a) **L-H** and (b) **L-F** thin films.

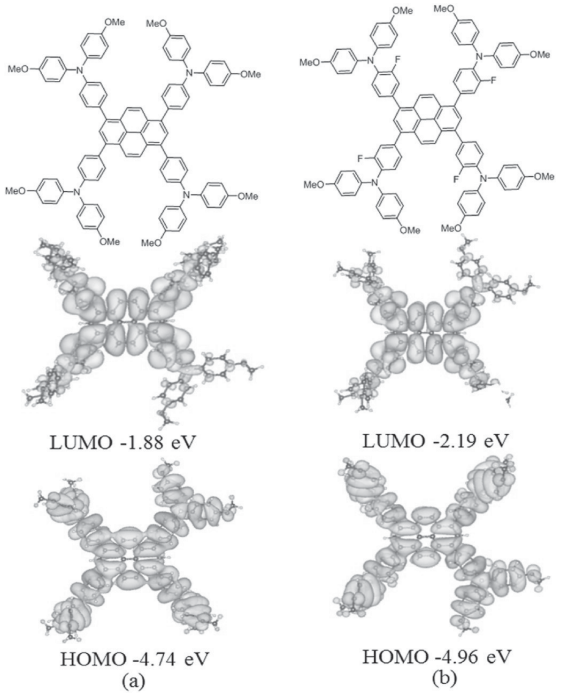


**Fig. 3.** The computed energy levels and electron distributions of HOMO and LUMO of **L-H** (a) and **L-F** (b) (visualization of orbitals here and elsewhere by VESTA).

6.77 (m, 16 H), 3.83 (s, 24 H). $^{13}$C NMR (75 MHz, $CDCl_3$) $\delta = 155.8$, 147.9, 141.0, 136.8, 133.1, 131.2, 129.4, 127.8, 126.6, 125.0, 120.3, 114.7, 55.5. ESI-MS: $C_{96}H_{78}N_4O_8^+ m/z$ 1415.82 (calculated $m/z$ 1414.58).

*2.2.4. Synthesis of 4,4′,4″,4‴-(pyrene-1,3,6,8-tetrayl)tetrakis(2-fluoro-N, N-bis(4-methoxyphenyl)aniline (L-F)*

Compound **2** (0.87 g, 1.93 mmol), 1, 3, 6, 8-tetrabromopyrene (0.2 g, 0.38 mmol), 2 M $K_2CO_3$ (5 ml), and $Pd(PPh_3)_4$ (0.04 g, 0.04 mmol) were added into a Schlenk tube under nitrogen environment. 20 mL of toluene: THF (3:7) mixture was added into the flask and the reaction mixture was refluxed for 12 h. After confirming the reaction completion by TLC, the reaction mixture was poured into 100 mL of water, and the organic phase was extracted by using 100 mL of dichloromethane. The organic phase was dried over sodium sulphate and filtered. After evaporation of the organic solvent, the crude reaction mixture was further purified by column chromatography (5–7% DCM: pet ether), which afforded 0.41 g of **L-F** as a yellow solid in 71% yield.

$^1$H NMR (300 MHz, $CDCl_3$) $\delta = 8.31$ (s, 4 H), 8.04 (s, 2 H), 7.50 - 7.30 (m, 8 H), 7.30 - 7.17 (m, 6 H), 7.08 (d, $J = 8.8$ Hz, 15 H), 6.87 (d, $J = 8.2$ Hz, 15 H), 3.83 (s, 24 H), $^{19}$F NMR (282 MHz, $CDCl_3$) $\delta = -118.94$. $^{13}$C NMR (75 MHz, $CDCl_3$) $\delta = 158.5$, 155.4, 141.2, 137.0, 135.2, 129.4, 128.1, 127.0, 125.4, 124.2, 123.3, 119.0, 114.5, 110.0, 55.5. ESI-MS: $C_{96}H_{74}F_4N_4O_8^+ m/z$ 1487.76 (calculated $m/z$ 1486.54).

### 2.3. Computational modeling

To compute the molecular structures and energy levels, density functional theory (DFT) [57] calculations were performed in Gaussian 09 [58], to determine the energies of frontier orbitals and their localization (Fig. 3. Table 1) as well as absorption and emission spectra (Fig. S9, ESI†). The optical spectra were computed with time-dependent DFT (TD-DFT) [59].The B3LYP [60]exchange correlation functional, LANL2DZ basis set and polarizable continuum model [61]of chloroform solvent were used. In addition, effect of fluorination on the inter-molecular interaction was studied on **L-H** and **L-F** dimers; in this case, Grimme D3 dispersion corrections [62] were included.

**Table 1**
Photoluminescence quantum yield & full width half maximum (FWHM) of **L-H** and **L-F**.

| Small Molecule | FWHM (nm) | Quantum Yield (QY) % |
|---|---|---|
| L-H | 67 | 75.45 |
| L-F | 93 | 80.72 |

### 2.4. Quantum yield measurements

Rhodamine B in water (literature quantum yield 31%) was chosen as standards to measure the photoluminescence quantum yield (PLQY) of newly synthesized materials. Absolute values are calculated using the standard reference sample that has a fixed and known fluorescence quantum yield value, according to the following equation 1.

Where, $\phi\_ref$ = Quantum yield of the reference dye, (0.27) $\phi$ = Quantum yield of the sample, subscript S is for sample and R is for reference sample. In order to minimize re-absorption effects, absorption in the 10-mm fluorescence cuvette was kept under 0.05 at the excitation wavelength.

$$\frac{\Phi}{\Phi_{ref}} = \frac{\frac{\int A_1}{1-10^{-Abs}} S}{\frac{\int A_2}{1-Abs} R} \tag{1}$$

$$\Phi = \Phi_{Ref}\, X\, \frac{\frac{\int A_1}{1-10^{-Abs}} S}{\frac{\int A_2}{1-10^{-Abs}} R} \tag{2}$$

### 2.5. Hole-mobility measurements

The hole-mobility of **L-H**, **L-F**, and PTAA (as a reference) was determined by the photo-induced charge carrier extraction in a linearly increasing voltage (Photo-CELIV) [63,64] method with an active layer thickness of 150–210 nm (see below). To study the hole-mobility of the samples, first each material was dissolved in chlorobenzene in concentration 40 mg/mL and then spin-coated on an ITO substrate coated with PEDOT:PSS layer with a thickness of around 30 nm. Finally, LiF and aluminium were vacuum-evaporated. The sandwich-type structure hence consists of an ITO/PEDOT-PSS (30 nm)/**L-H** (190 nm) or **L-F** (150 nm) or PTAA (210 nm)/LiF (0.8 nm)/Al cathode (active area of~3 mm$^2$, thickness 60 nm). The device was mounted in a cryostat and illuminated from the ITO side by a 355 nm, 45μJ/pulse laser for bulk photo-generation of charge carriers and after a time delay, a linearly increasing voltage pulse was applied in reverse bias to extract the photo-generated charges. The resulting extraction current transient was recorded and the mobility was calculated at maximum current transient ($t_{max}$) from the following equation [63]:

$$\mu = \frac{d^2}{2At_{max}^2}\left[\frac{1}{6.2\left(1+0.002\frac{\Delta j(t_{max})}{j_0}\right)} + \frac{1}{1+0.12\frac{\Delta j(t_{max})}{j_0}}\right]^2 \tag{3}$$

where $d$ is the thickness of the active semiconductor layer, $A$ *is* the voltage ramp-up rate, $\Delta j(t_{max})$ is the difference between the current transient in light and in dark at $t_{max}$ and $j_0 = C_{geo}A$ is the displacement current, where $C_{geo}$ the geometric capacitance of the device.

### 2.6. Fabrication of OLED devices

OLED devices using both **L-H** and **L-F** were fabricated using pre-patterned ITO-coated glass substrates (Xianyan Technology). The pre-fabrication step involves repeatedly washing the ITO substrates with Alconox and deionised water. The substrates were rinsed several times in deionised water before ultra-sonicating them in acetone, ethanol, and isopropanol consecutively for 10 min each. The substrates were blow-dried with compressed air, before spin-coating PEDOT:PSS (Heraeus). PEDOT:PSS was filtered with a 0.45 μm PVDF filter before spin coating (5000 rpm, 30 s, Laurell Technologies). The spin coated PEDOT:PSS films were removed from contact pads and then annealed at 150 °C for 15 min, before transferring them to a glove box system with low moisture and oxygen ($O_2 < 0.1$ ppm, $H_2O < 0.1$ ppm). The emitters (**L-H** and **L-F**) were dissolved in chloroform (6 mg/ml) and magnetically stirred for 24 h, inside glovebox, before spin coating them over the PEDOT:PSS layer. The emitter layer was spin-coated using a Speciality Coating Systems spin coater (1500 rpm, 30 s) to obtain a thickness of ~50 nm, followed by thermal annealing at 70 °C. After the emitter deposition, the samples were transferred to another glove box fitted with a torpedo thermal evaporator, without breaking the vacuum. 50 nm of TBPi [2,2′,2″-(1,3,5-benzinetriyl)-tris(1-phenyl-1-H-benzimidazole] (Ossila), 2 nm of LiF (Sigma Aldrich), and 100 nm of Ag (Sigma Aldrich) layers were thermally deposited at pressure of $\sim 10^{-6}$ mbar. The OLED devices were encapsulated by customized glass cavity and sealed with UV curable epoxy (NOA 61, Norland Products). Each substrate consists of 6 pixels, each having an area of 10 $mm^2$. Current-Voltage-Luminance (IVL) characteristics of devices were recorded using a source-meter (B2901A, Keysight Technologies) and luminance meter (CS-200, Konica Minolta). The electro-luminescence spectra of the OLEDs were recorded using a fiber-optic spectrometer (USB 4000, Ocean Optics).

### 2.7. Fabrication and characterization of PSCs

The perovskite precursors,1.2 M $MAPb(I_{0.5}Br_{0.5})_3$ (methylammonium lead iodide–bromide) and $FAPb(I_{0.5}Br_{0.5})_3$ (formamidinium lead iodide–bromide), were dissolved in a mixture of dimethylformamide (DMF)/dimethyl sulfoxide (DMSO) (4:1 vol ratio), while $CsPb(I_{0.5}Br_{0.5})_3$ (cesium lead iodide–bromide) was dissolved in pure DMSO. The solutions were then mixed to a favored ratio by adjusting the volume of each solution to achieve the desired molar ratio for $Cs_{0.1}FA_{0.75}MA_{0.15}PbI_{1.5}Br_{1.5}$ (Cesium formamidinium methylammonium lead iodide bromide) perovskite precursor. Further, poly(bis(4-phenyl) (2,4,6-trimethylphenyl)amine) (PTAA) film as reference hole-transport layer (HTL) was prepared by spin coating 2 mg/mL PTAA solution on cleaned ITO substrates at 4000 rpm for 30 s, followed by thermal annealing at 100 °C for 10 min. **L-H** and **L-F** solutions were prepared by dissolving the powders in dichlorobenzene (5 mg/mL). The **L-H** and **L-F** films as HTLs were deposited on cleaned ITO substrates by spin-coating the corresponding solutions at 4000 rpm for 30 s, followed by thermal annealing at 100 °C for 10 min. The wide-bandgap perovskite precursor solution ($Cs_{0.1}FA_{0.75}MA_{0.15}PbI_{1.5}Br_{1.5}$) was spin coated onto the substrate using a 2-step spin coating program (2000 rpm for 2 s, and then 4000 rpm for 20 s), and 200 μL anhydrous chlorobenzene antisolvent was dropped onto the spinning substrate. The as-prepared perovskite film was annealed at 100 °C for 1 h. The devices were finished by sequentially thermally evaporating $C_{60}$ (30 nm), BCP (7.5 nm), and Ag (80 nm). The device active area is 8 $mm^2$. The devices were illuminated with a solar simulator (Newport, Oriel class AAA, 94063A) at 100 mW/$cm^2$ illumination (AM 1.5 G), equipped with a calibrated silicon reference cell and source meter (Newport, 91150 V) certified by NREL. The J-V curves were recorded with a source monitor unit (Keithley 2420) as reverse (1.2 V to −0.1 V) scans at a sweep rate of 100 mV/s.

## 3. Results and discussion

### 3.1. Materials design and synthesis

The symmetric planar pyrene geometry was selected as the central core of **L-H** and **L-F** to provide high charge-carrier mobility, which is beneficial for the overall performance of OLEDs as well as PSCs [65–69]. The electron-rich triphenylamine (TPA) groups, which are the most efficient and well-known moieties providing high-performance HTLs in PSCs [38,44,66,70], were chosen as the end-capping units. For **L-F**, fluorination strategy was adopted to enhance film morphology and packing [66] and thus the overall device performance, as well as to achieve highly stable SMOS. In fact, fluorination plays a two-fold role when designing new materials for organic electronics, through (i) increasing the stability of the compounds used, and (ii) profoundly affecting their packing (and thereby charge-transport properties) in the solid state [71–73].

The synthesis of **L-H** and **L-F** is shown in Scheme 1. Further details are provided in the Experimental Section and in the Electronic Supporting Information (ESI†). **L-H** was prepared in good yield (73%) by Suzuki-coupling reaction between previously reported 4-methoxy-N-(4-methoxyphenyl)-N-(4-(4,4,5,5-tetramethyl-1,3,2-dioxaborolan-2-yl) phenyl)aniline(**L**) [74] and 1,3,6,8-tetrabromopyrene. For synthesis of **L-F**, first 4-bromo-2-fluoro-N,N-bis(4-methoxyphenyl)aniline (**1**) was prepared with 80% yield by Ullman coupling reaction from low cost precursors, namely 1-iodo-4-methoxybenzene and 4-bromo-2-fluoroaniline. Subsequently, Miyaura borylation of **1** gave the corresponding boronic ester derivative 2-fluoro-N,N-bis(4-methoxyphenyl)-4-(4,4,5,5-tetramethyl-1,3,2-dioxaborolan-2-yl)aniline (**2**) (yield = 78%). Finally, **L-F** was achieved by Suzuki-coupling reaction of **2** with 1,3,6,8-tetrabromopyrene in 71% yield. Both **L-H** and **L-F** required not only few synthetic steps (3), but also allowed for a cost-effective production (~30$/g, determined according to a previously reported method [50], details provided in ESI see Table S2). Furthermore, both the derivatives are easily soluble in common organic solvents such as chloroform, tetrahydrofuran, and dichloromethane. This allowed their further purification by column chromatography. $^1$H NMR, $^{13}$C NMR and mass spectroscopy confirmed the purity of the synthesized compounds (see all the data in the Experimental Section and ESI†).

## 4. Thermal, optical and electrochemical properties

The TGA and DSC measurements of **L-H** and **L-F** revealed their good thermal stability with decomposition temperatures ($T_d$, defined as 5% weight loss under $N_2$ atmosphere) of 395 °C for **L-H** and 415 °C for **L-F**. In addition, both showed high glass transition temperatures ($T_g$), 144° for **L-H** and 142 °C for **L-F**, whereas their melting points ($T_m$) were recorded at 260 °C and 266 °C, respectively. The enhancement in thermal stability of **L-F** can be attributed to the presence of C–F bonds, which in turn could result into improvement of device lifetime [75]. It is worth noting that both **L-H** and **L-F** exhibit higher thermal stability as compared to previously reported pyrene-based hole-transporting SMOS [51,66,76,77].

The optical properties of **L-H** and **L-F** in chloroform ($10^{-5}$ M) are presented in Fig. 1a and Table 1. Both SMOS showed almost identical absorption spectra, with the lowest-energy absorption band at 415–418 nm corresponding to π-π* transition of the central pyrene core. The 80 nm red shift in absorption compared to pristine pyrene (338 nm) [13] originates from the extended conjugation [78]. The band at 370–372 nm is attributed to n-π* transition and the band at 300 nm to the π-π* transition of the triphenylamine moieties [79,80]. The photoluminescence spectra of the molecules in chloroform (Fig. 1a and Table 1), measured by exciting the samples at 400 nm, exhibited an emission band at 500 and 539 nm for **L-H** and **L-F**, respectively, red-shifted by 107 and 146 nm as compared to pristine pyrene (393 nm) [13]. The larger red-shift for **L-F**, arising from meta-fluorination, can be

**Table 2**
Thermal, optical and electrochemical properties of **L-H** and **L-F**.

| SMOS | λabs (nm) Solution | Film | λemission (nm) Solution | Film | HOMO (eV) | LUMO (eV) | Eg (eV) | Tg (oC) | Td (oC) | Tm (oC) |
|---|---|---|---|---|---|---|---|---|---|---|
| **L-H** | 300, 370, 415 | 300, 374, 415 | 500 | 530 | −5.42[a], −4.74[b] | −2.71 | 2.71[c], 2.86[b] | 144 | 395 | 260 |
| **L-F** | 300, 372, 418 | 300, 378, 425 | 539 | 556 | −5.62[a], −4.96[b] | −2.96 | 2.66[c], 2.77[b] | 142 | 415 | 266 |

[a] HOMO level determined by PESA.
[b] Energy levels and $E_g$ determined by computational analysis.
[c] Optical bandgap. LUMO levels are determined from the experimentally measured HOMO values and optical bandgap.

ascribed to both inductive and mesomeric effects [81,82]. Meta-fluorination renders the pyrene core electron deficient because of the strong electron-withdrawing character of the fluorine atom [83]. As a result, when compared to **L-H**, **L-F** shows better electron delocalization from pyrene core to the peripheral triphenylamine moieties. As regards the emission spectra of **L-H** and **L-F** in solution and in solid state (Fig. 1 and Table 1), the emission maxima are red shifted by 30 and 17 nm, respectively. This is due to the more pronounced intermolecular interactions in the solid state [80]. The different dielectric constants in solution and in the solid may additionally contribute to the red shift in solid state [ 84,85]. The optical bandgap ($E_g$) is estimated from the intersection of the normalized absorption and emission spectra in solution. The intersection wavelengths for **L-H** and **L-F** are 456 nm and 466 nm, which lead to $E_g$ of approximately 2.71 and 2.66 eV, respectively. These results are in good agreement with earlier reports on pyrene derivatives [82].

In order to explore the potential of these materials for optoelectronic applications, we performed PLQY measurements using Rhodamine B dye as standard (literature quantum yield 31%) and the values are shown in Table 1. The **L-H** compound exhibits 75% PLQY value whereas **L-F** compound shows 80%. The electron withdrawing fluorine substitution enhances the PLQY. Though the PLQY value of **L-F** is higher than that of **L-H**, **L-F** exhibited higher FWHM of 93 nm compared to that of 67 nm of **L-H**. To determine the ionization potential (IP) or HOMO of **L-H** and **L-F**, the photoelectron spectroscopy in air (PESA) measurements were carried out, as shown in Fig. 2. Thin films of **L-H** and **L-F** were deposited on ITO-coated glass by spin coating and the photoelectron yield ratio was measured with respect to the applied UV-energy. The slope of the photoelectron yield curve (Fig. 2) provides an estimate of the highest occupied molecular orbital (HOMO) level of the corresponding materials [86]. Thus, HOMO values for **L-H** and **L-F** are −5.42 and −5.62 eV, respectively. The corresponding LUMO values, determined from the optical band gaps-HOMO value difference, are −2.71 eV for **L-H** and −2.96 eV for **L-F**. The deeper HOMO level of **L-F** (−5.62 eV) as compared to that of **L-H** (−5.42 eV) is attributed to inductive electron-withdrawing character of the meta-fluorines, which is in good agreement with the red-shifted absorption/emission spectra and the different optical bandgaps as discussed above. Further details are given in Table 2, Figs. S7 and S8 (ESI†).

### 4.1. Computational analysis and hole-mobility of L-H and L-F

The energy levels are shown in Fig. 3 (left for **L-H** and right for **L-F**). In both cases, HOMO is delocalized over the whole molecular system, which facilitates the hole-transport when used as HTMs. Meanwhile, LUMO is more localized on the central fused pyrene core and partially on triphenylamine units. This indicates that there is a degree of charge-transfer in the transition responsible for the lower-energy peak in absorption and PL spectrum. The computed HOMO/LUMO energy levels are −4.74/-1.88 eV for **L-H** and −4.96/-2.19 eV for **L-F** respectively (Fig. 3 and Table S1). The lower HOMO/LUMO levels of **L-F** as compared to **L-H** are due to inductive electron-withdrawing behavior of fluorinated core. The HOMO-LUMO gaps for **L-H** and **L-F** were calculated as 2.86 and 2.77 eV, respectively. The HOMO-LUMO gaps are somewhat higher than the optical gap, as expected, as the latter is determined from the onset of absorption. The computed HOMO/LUMO values are higher than the experimental levels, which can be related to the functional/basis set used as well as the fact that calculations were performed on isolated molecules in gaseous state while PESA measurements were carried out on solid state thin films. The computed LUMO is naturally higher than the one estimated from the *onset* of optical absorption as the latter includes broadening effects.

The computed absorption peak of **L-H** is at 495 nm and emission maximum at 593 nm, while the corresponding values for **L-F** are 513 nm/615 nm (see Fig. S9). DFT/TD-DFT calculations thus confirm the downward shift of HOMO, LUMO, and the gap due to fluorination, in agreement with the experiments. The absolute values of the computed peaks are somewhat redshifted, as is expected with the B3LYP functional for transitions involving charge transfer.

The hole mobilities, determined with Photo-CELIV [63], were $1.9 \times 10^{-4}$ cm [2]/Vs for **L-H**, $7.0 \times 10^{-6}$ $cm^2$/Vs for **L-F**, and $8.1 \times 10^{-6}$$cm^2$/Vs for the reference PTAA (see Fig. 4 and Table 3). The hole-mobility of **L-H** is thus two order of magnitude higher compared to that of **L-F**. We attribute this difference to the deepening of HOMO

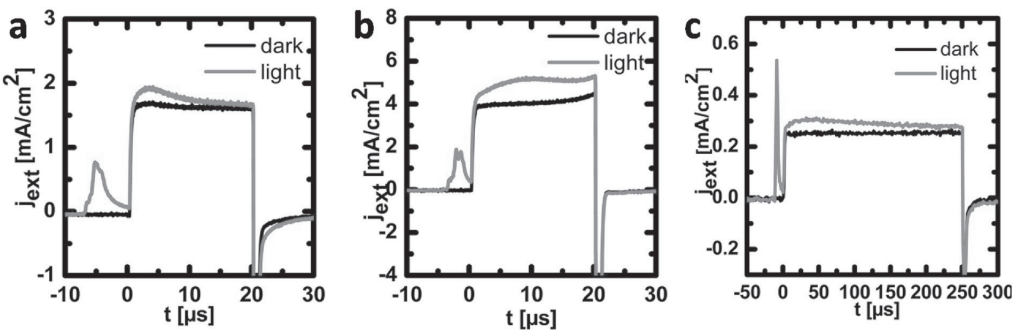


**Fig. 4.** Photo-CELIV curves for **L-H (a)**, **L-F (b)** and PTAA (c). The voltage slopes used were A = 100000 V/s, A = 200000 V/s and A = 20000 V/s, respectively.

**Table 3**
Summary of OLED device performance of pyrene-based SMOS.

| SMOS | TOV (V) | Current Efficiency (cd/A) | Max Brightness (cd/m$^2$) | CIE | EL peak (nm) | PL Solid State (nm) |
|---|---|---|---|---|---|---|
| L-H | 4.5 | 1.3 | 2255.2 | 0.31, 0.61 | 517 | 518 |
| L-F | 4.5 | 3.7 | 1759.8 | 0.25, 0.60 | 528 | 545 |

energy level of **L-F** due to the presence of fluorine atoms, which increases both the ionization potential and electron affinity, thereby resulting in a decrease in the hole-mobility of **L-F** as compared to **L-H**.[92]

### 4.2. Investigation of OLED devices

To apply **L-H**/**L-F** as the emitter layer of an OLED device, their morphology in thin films deposited on indium doped tin oxide (ITO) was investigated by atomic force microscopy (AFM), as shown in Fig. 5. The root mean square (RMS) roughness for both **L-H** and **L-F** films was below 0.2 nm (Fig. 5a and b). This indicates smooth films, which can be beneficial for OLED devices as it helps in uniform deposition of electron-transporting layer over the emitting layer. This in turn leads to uniform injection of charge carriers, resulting in homogeneous brightness throughout the emitting surface. The device efficiency has strong dependence on solution processability of the emitter material. The low surface roughness indicates that aggregation of the SMOS in the solid state is negligible during the solution processing stage and this is attributed to the propeller structure of TPA group attached at the 1, 3, 6 and 8 positions of pyrene core. A smooth thin film without aggregation is thus an essential prerequisite to fabricate a highly efficient device. Additionally, the adhesion force profile at nanoscale was studied in order to understand the effect of fluorination on film properties. The source of force in this case is the attractive force in air due to capillary meniscus formed by the small molecule, which extends to tens of nm beyond the surface (Fig. 5c and d). The probe end radius was fixed for both cases to measure the relative difference of adhesion forces between **L-H** and **L-F** samples. It was observed that the fluorinated **L-F** exhibited better adhesion compared to **L-H**, which indicates that the fluorine atoms in **L-F** affect the surface properties of the thin films. The difference in adhesion profile could be due to the different packing of small molecules in the case of **L-F,** leading to a negligible increase in surface roughness, too. This is expected due to the presence of hydrophobic fluorine atoms at the terminal end of each molecule. Ab initio calculations indicated comparable intermolecular interaction between **L-H** and between **L-F** molecules of around 1.9 eV (computed differences were on the order of room-temperature kT, see Fig. S14 in ESI). The observed

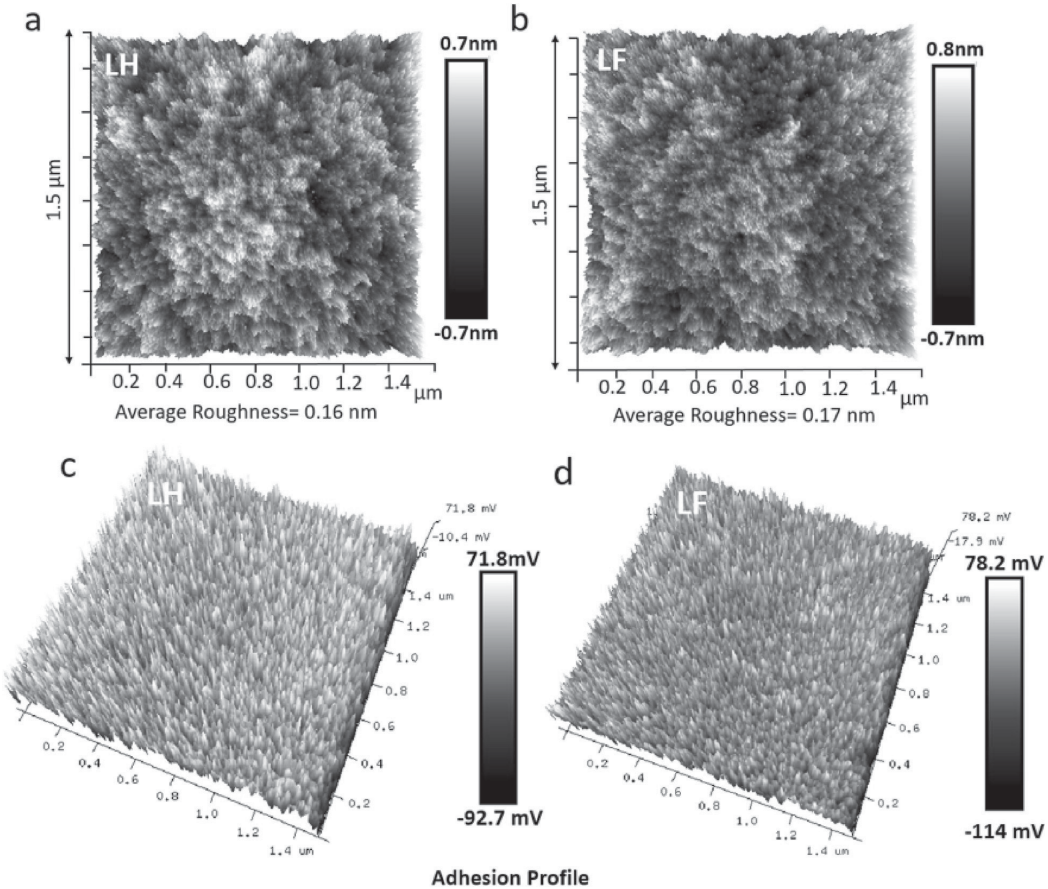


**Fig. 5.** AFM images (1.5 × 1.5 µm) of 50 nm thin film of (a) **L-H**, (b) **L-F** spin coated onto a glass/ITO substrate. Adhesion force profile of (c) **L-H** and (d) **L-F** molecule to investigate thin film surface behavior.

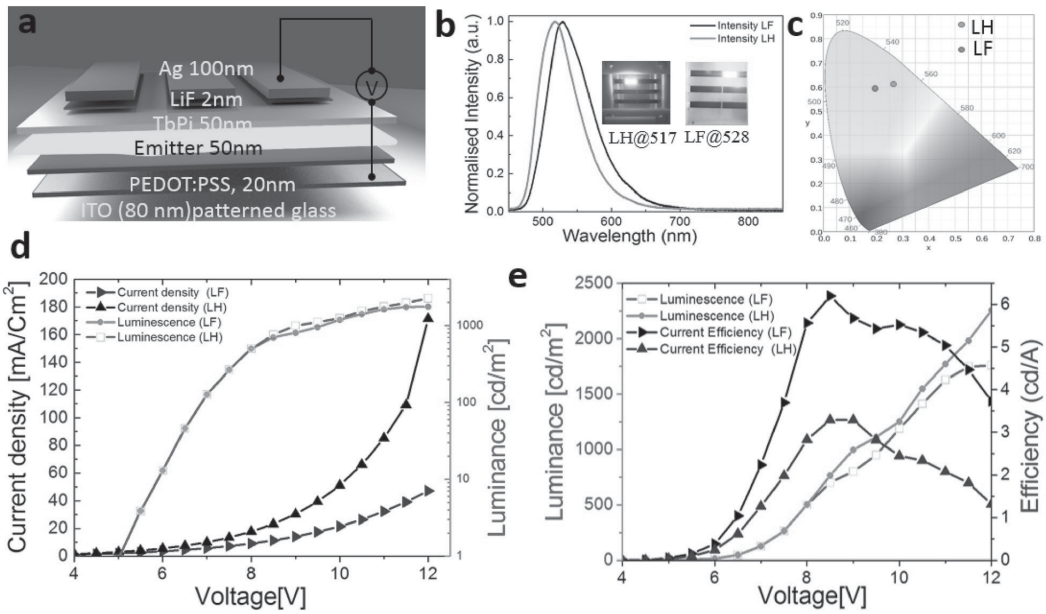


**Fig. 6.** (a) Device structure of OLEDs used in this study; (b) Electroluminescence (EL) for OLEDs. Inset: picture of an OLED pixel; (c) Chromaticity diagram showing the CIE coordinates of the OLEDs; (d) Current density and luminance with respect to voltage of device; (e) Brightness and efficiency characteristics.

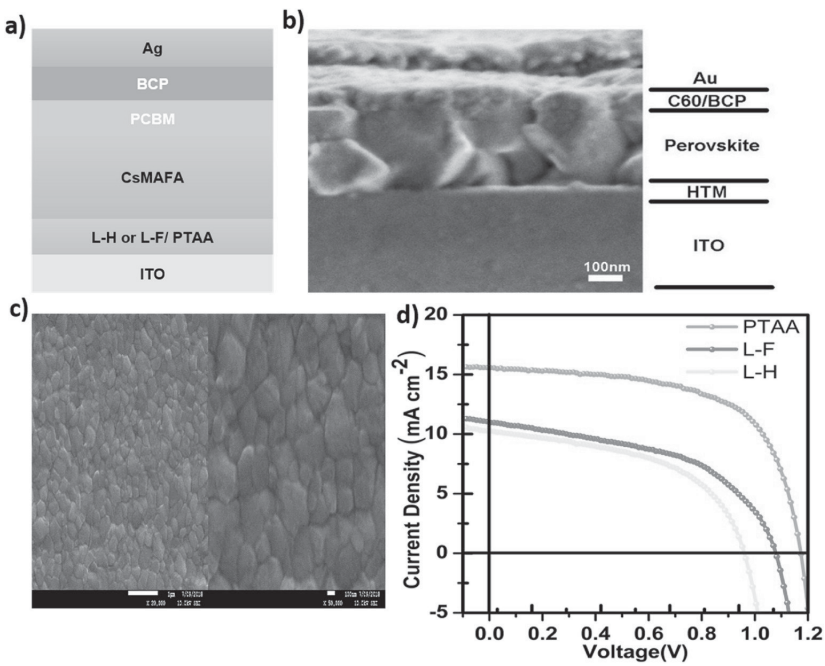


**Fig. 7.** (a) Perovskite solar cell device structure; (b) SEM cross-section image showing the different composition layers; (c) SEM images showing morphology of perovskite layers 1 μm and 100 nm scales, and (d) JV curves of mixed perovskite solar cell (CsMAFA) based on various hole transport materials including **L-H**, **L-F**, and **PTAA**.

improved film quality is therefore likely due to differences in interactions with the solvent out of which the films are deposited and to hydrophobicity induced by fluorination.

The OLED devices were based on the following architecture (Fig. 6a): ITO/PEDOT:PSS (20 nm)/**L-H** or **L-F** (50 nm)/TPBi(50 nm)/LiF(2 nm)/Ag (100 nm). The ITO-coated glass and LiF/Ag act as the anode/cathode, whereas TBPi/PEDOT:PSS act as electron/hole-transporting layers. When forward bias is applied to the device, the electrons injected from the cathode and holes injected from the anode recombine in the active layer, generating photons emitting in the green part of the spectrum. The observed electroluminescence (EL) of the devices is shown in Fig. 6b, with inset showing an actual pixel of the devices. The EL spectrum for **L-H** shows a maximum at 517 nm with full width at half maximum (FWHM) of 67 nm while the maximum for **L-F** is at 528 nm with FWHM of 73 nm. The CIE coordinates (Fig. 6c) for **L-H** and **L-F**-based OLEDs are (0.32, 0.61) and (0.25, 0.60), respectively. The turn-on voltage (Fig. 5d) for both OLEDs is rather low, ca. 4.5V, indicating low hole injection barrier between PEDOT:PSS and **L-H**/**L-F**. The **L-F**-based OLED shows a maximum brightness of 1759.8 cd/m$^2$ at 12 V with a current efficiency of 3.7 cd/A at a current density of 47.2 mA/cm$^2$. For **L-H**-based OLED, the brightness is around 2255.2 cd/m$^2$ at 12 V, while the current efficiency (1.3 cd/A) at current density of 171.49 mA/cm$^2$ is lower than **L-F**-based OLEDs (Fig. 6d and e and OLED device details are shown in Table 3).

The solid-state photoluminescence of **L-H** and **L-F** were recorded by keeping the photon density of excitation radiation and other conditions similar. The spectra (Fig. S10) shows a higher intensity ($\sim 28.1 \times 10^6$) in the case of **L-F** compared to **L-H**. However, the EL intensity of **L-F** is lower compared to **L-H**, at the same voltage (12 V). This can be attributed to two reasons. First, there is a built-in dipole moment in the case of **L-F** molecules due to the terminating fluorine entity. The injected carrier screening effect will lead to lowering of the HOMO levels during the device operation, which is evident from blue shift of the EL maxima (528 nm) with respect to the solid state emission maxima (545 nm). Secondly, the better hole-mobility of **L-H** ($2 \times 10^{-4}$ cm [2]/Vs) leads to efficient hole-injection and balances the electron injection rate, thereby increasing the recombination to generate higher brightness compared to **L-F**. 25 devices were fabricated with both **L-H** and **L-F** (Fig. S11) to demonstrate the reproducibility of the results. The performance of the OLEDs can be further enhanced by optimizing the layer thickness, and by perfecting the molecular design to tune HOMO-LUMO levels, tuning the device structure. Deep HOMO values of these low-cost materials are important for developing a cost-effective, stable, and efficient OLED device.

### 4.3. Investigation of PSC devices

In order to test the applicability of **L-H** and **L-F** as HTMs in dopant-free PSCs, we used them together with the CsMAFA perovskite active layer [$Cs_{0.1}FA_{0.75}MA_{0.15}Pb(Br_{0.5}I_{0.5})_3$, ($E_g = 1.82$ eV)] with a *p-i-n* device configuration ITO/HTM/perovskite/PCBM/BCP/Ag (Fig. 7a). In addition to **L-H** and **L-F** as HTMs, PTAA was used in reference devices. PCBM was used as an electron-transporting compact layer, and 2,9-dimethyl-4,7-diphenyl-1,10-phenanthroline (BCP) as an electron-extracting and hole-blocking layer [49]. The energy levels of each layer are illustrated in Fig. S12.

The complete PSC device structure schematic is shown in Fig. 7a, whereas Fig. 7b a Scanning Electron Microscopy (SEM) cross section image of the device. The SEM image clearly indicates a thin layer of HTM deposited between ITO coated glass and the perovskite layer. Other layers such as active mixed halide perovskite, electron transporting layers (C60/BCP), and the silver electrode can be seen clearly. Fig. 7c the morphology of the photoactive perovskite thin films on a substrate, whereas Fig. 7d shows the corresponding current-voltage (J-V) characteristics of perovskite photovoltaic devices measured under the AM 1.5G and 100 mW cm$^2$ standard experimental conditions. The corresponding photovoltaic parameters are presented in Table 3. The champion device with dopant-free **L-H** as HTL exhibited a short circuit current density ($J_{sc}$) of 10.25 mA/cm$^2$, an open circuit voltage ($V_{oc}$) of 0.87 V, a fill factor (FF) of 55.7%, and a PCE of 5.03%. The device-based dopant-free **L-F** HTL showed a $V_{oc}$ of 1.07 V, a $J_{sc}$ of 10.98 mA/cm$^2$, a FF of 50.3%, and a PCE of 5.93%. The PSC device details using **L-H** and **L-F** as hole transporting layers are shown in Table 4.

**Table 4**
Summary of PSC devices based on the different SMOS.

| HTMs | Voc (V) | Jsc (mA cm$^{-2}$) | FF (%) | PCE (%) |
|---|---|---|---|---|
| **PTAA** | 1.179 | 15.57 | 61.8 | 11.35 |
| **L-H** | 0.879 | 10.25 | 55.7 | 5.03 |
| **L-F** | 1.074 | 10.98 | 50.3 | 5.93 |

The higher open circuit voltage of **L-F**-based PSCs compared to **L-H**-based ones is a clear signature of deeper HOMO of the **L-F** compound [65], strongly attributed to the substitution of electron withdrawing fluorine atom on the TPA moiety, that ensures a better energy matching with perovskite valence band [85].

The reference devices based on PTAA showed a $V_{oc}$ of 1.17 V, a $J_{sc}$ of 15.57 mA/cm$^2$, a FF of 61.8%, and a PCE of 11.35% under identical conditions. We assume that the lower PSC device performance of L-H and L-F HTMs compared to the PTAA-based ones is due to their deeper HOMO energy levels compared to PTAA, which might not be suitable/well-align to the valence band of the corresponding perovskite structure. Further studies are needed to further clarify this issue. Even though the device performance is relatively low under dopant-free conditions, their low cost render them competitive to costly HTMs at least for applications such as indoor solar cells where higher PCE is not the main requirement. Apart from higher efficiency, stability is one of the main drawbacks of current perovskite solar cell technology and requirement of low cost dopant free HTM has a great important. In our current study, we reported dopant free HTMs via elegant molecular engineering including fluorination strategy to enhance thermal stability of the HTM.

## 5. Conclusions

In summary, we have synthesized and investigated two pyrene-based solution-processable functional organic semiconductors, **L-H** and the fluorinated **L-F**, using triphenylamine substituents at 1, 3, 6, and 8 positions by Suzuki coupling reactions. Both materials exhibited wide UV–Vis absorption from 290 nm to 500 nm, with an optical band gap of 2.71 eV for **L-H** and 2.66 eV for **L-F**. Their HOMO energy levels were −5.42 eV (**L-H**) and −5.62 eV (**L-F**). Fluorination of TPA end capping group deepens the HOMO level, improves the thermal stability, and enhances the film adhesion of the **L-F** compound as compared to **L-H** counterpart. These materials were used as light emitting active layers in OLEDs and hole transporting materials in PSCs. Both **L-H** and **L-F** display excellent electroluminescence properties with emission peaks at 517 nm and 528 nm, maximum brightness of 2255.2 cd/m$^2$ and 1759.8 cd/m$^2$, and current efficiency of 1.3 cd/A and 3.7 cd/A, respectively. Though the **L-H** based compound exhibits higher brightness, the current efficiency of **L-F** based OLED is two times higher than the OLED employing **L-H**. When both **L-H** and **L-F** are used as dopant-free hole transporting layers in mixed halide perovskite devices, **L-F**-based devices exhibits a power conversion efficiency (5.93%) with an open circuit voltage of 1.074 V. **L-H** based dopant free HTM shows a PCE of 5.03% and an open circuit voltage of 0.879 V. The performance enhancement of OLEDs and PSCs based on **L-F** clearly indicates the beneficial effect of fluorination on the optoelectronic properties of pyrene-based semiconductors, which we attribute to better energy level alignment and better film quality of **L-F** material.

Finally, we believe that fluorinated pyrene-based semiconductors hold great promise for the development of low-cost and high-performing green OLED devices, and potentially also for dopant-free PSC devices,

with further molecular and device engineering optimization.

## Declaration of competing interest

The authors declare that they have no known competing financial interests or personal relationships that could have appeared to influence the work reported in this paper.

## Acknowledgements

J.S. and A.S. share equal contribution for this work. J. S. is grateful to the Fortum Foundation (201800260) and Finnish Foundation for Technology Promotion. A.S. is thankful to QUT for offering him QUT-PRA scholarship to conduct his research work. Some of the data reported in this paper were obtained at the Central Analytical Research Facility (CARF) operated by the Institute for Future Environments (IFE), Queensland University of Technology (QUT). P.S. is thankful to QUT for the financial support from QUT core funding (QUT/322120-0301/07), and to the Australian Research Council (ARC) for the Future Fellowship (FT130101337). P.V., M.N., S.D., and R.Ö acknowledge financial support from Jane & Aatos Erkko foundation (project ASPIRE), and A.P. from the Academy of Finland (Decision number 311142). This work is part of the Academy of Finland Flagship Programme, Photonics Research and Innovation (PREIN, Decision number 320165).

## Appendix A. Supplementary data

Supplementary data to this article can be found online at https://doi.org/10.1016/j.orgel.2019.105524.

## References

[1] L. Duan, L. Hou, T. Lee, J. Qiao, D. Zhang, G. Dong, J. Mater. Chem. 20 (2010) 6392–6407.
[2] L.M. Leung, W.Y. Lo, S.K. So, K.M. Lee, J. Am. Chem. Soc. 122 (2000) 5640–5641.
[3] T.W. Kelley, P.F. Baude, C. Gerlach, D.E. Ender, D. Muyres, M.A. Haase, D.E. Vogel, S.D. Theiss, Chem. Mater. 16 (2004) 4413–4422.
[4] V. Coropceanu, J. Cornil, D.A. da Silva Filho, Y. Olivier, R. Silbey, J.L. Brédas, Chem. Rev. 107 (2007) 926–952.
[5] B.P. Rand, J. Genoe, P. Heremans, J. Poortmans, Prog. Photovolt. Res. Appl. Prog. 15 (2007) 659–676.
[6] A. Mishra, P. Bäuerle, Angew. Rev. 51 (2012) 2020–2067.
[7] A. Mishra, M.K.R. Fischer, P. Bäuerle, Angew. Chem. 48 (2009) 2474–2499.
[8] Y. Wu, M. Marszalek, S.M. Zakeeruddin, Q. Zhang, H. Tian, M. Gr, W. Z, Energy Environ. Sci. 5 (2012) 8261–8272.
[9] L. Calió, S. Kazim, M. Grätzel, S. Ahmad, Angew. Chem. Int. Ed. 55 (2016) 14522–14545.
[10] P. Vivo, J. Salunke, A. Priimagi, Materials 10 (2017) 1087.
[11] P.M. Sonar, H.D. Pham, X. Li, W. Li, S. Manzhos, A.K.K. Kyaw, Energy Environ. Sci. (2019) 0–82.
[12] M.Y. Lo, C. Zhen, M. Lauters, G.E. Jabbour, A. Sellinger, J. Am. Chem. Soc. 129 (2007) 5808–5809.
[13] P. Sonar, M.S. Soh, Y.H. Cheng, J.T. Henssler, A. Sellinger, Org. Lett. (2010) 2008–2011.
[14] B.Y. Yang, F. Wudl, Adv. Mater. 21 (2009) 1401–1403.
[15] M.E. Thompson, Stephen R. Forrest, Chem. Rev. 107 (2007) 923–925.
[16] S.R. Forrest, Nature 428 (2004) 911–918.
[17] M.O. Neill, S.M. Kelly, Adv. Mater. 23 (2011) 566–584.
[18] B. Yong, S. Zhao, H. Fu, A. Peng, Y. Ma, D. Xiao, J. Yao, Adv. Mater. 20 (2008) 2859–2876.
[19] H.D. Pham, H. Hu, F. Wong, C. Lee, W. Chen, K. Feron, S. Manzhos, H. Wang, N. Motta, Y.M. Lam, P. Sonar, J. Mater. Chem. C 6 (2018) 9017–9029.
[20] R. Mai, X. Wu, Y. Jiang, Y. Meng, B. Liu, X. Hu, J. Roncali, G. Zhou, J. Liu, K. Kempa, J. Gao, J. Mater. Chem. A 7 (2019) 1539–1547.
[21] M. Cai, T. Xiao, E. Hellerich, Y. Chen, R. Shinar, J. Shinar, Adv. Mater. 23 (2011) 3590–3596.
[22] J. Chen, C. Shi, Q. Fu, F. Zhao, Yue Hu, J. Mater. Chem. 22 (2012) 5164–5170.
[23] Xu. Zhu, J. Peng, Y. Caoa, J. Roncali, Chem. Soc. Rev. 40 (2011) 3509–3524.
[24] L.S. Hung, C.H. Chen, Mater. Sci. Eng. 39 (2002) 143–222.
[25] F. So, B. Krummacher, M.K. Mathai, D. Poplavskyy, S.A. Choulis, J. Appl. Phys. 102 (2007), 091101.
[26] Y. Im, S.Y. Byun, J.H. Kim, D.R. Lee, C.S. Oh, K.S. Yook, J.Y. Lee, Adv. Funct. Mater. 27 (2017) 1603007.
[27] M. Zhu, C. Yang, Chem. Soc. Rev. 42 (2013) 4963–4976.
[28] L. Duan, J. Qiao, Y. Sun, Y. Qiu, Adv. Mater. 23 (2011) 1137–1144.
[29] H. Sasabe, J. Kido, Chem. Mater. 23 (2011) 621–630.
[30] Y. Li, J. Liu, Y. Zhao, Y. Cao, Mater. Today 20 (2017) 258–266.
[31] W.S. Yang, B.-W. Park, E.H. Jung, N.J. Jeon, Science 356 (2017) 1376–1379 (80-.).
[32] J.A. Christians, P. Schulz, J.S. Tinkham, T.H. Schloemer, S.P. Harvey, B.J. Tremolet De Villers, A. Sellinger, J.J. Berry, J.M. Luther, Nat. Energy 3 (2018) 68–74.
[33] L. Chen, F. De Angelis, S. Jin, Y.-K. Sun, P.V. Kamat, ACS Energy Lett. 3 (2018) 261–263.
[34] Best research-cell efficiency chart | photovoltaic research | NREL. https://www.nrel.gov/pv/cell-efficiency.html. (Accessed 9 June 2019).
[35] M. Wang, Z. Zang, B. Yang, X. Hu, K. Sun, L. Sun, Sol. Energy Mater. Sol. Cells 185 (2018) 117–123.
[36] Q. Sun, X. Gong, H. Li, S. Liu, X. Zhao, Y. Shen, M. Wang, Sol. Energy Mater. Sol. Cells 185 (2018) 111–116.
[37] J. Liu, Y. Wu, C. Qin, X. Yang, T. Yasuda, A. Islam, K. Zhang, W. Peng, W. Chen, L. Han, Energy Environ. Sci. 7 (2014) 2963.
[38] R. Azmi, S.Y. Nam, S. Sinaga, Z.A. Akbar, C.L. Lee, S.C. Yoon, I.H. Jung, S.Y. Jang, Nano Energy 44 (2018) 191–198.
[39] T. Singh, T. Miyasaka, Adv. Energy Mater. 8 (2018) 1–9.
[40] Q. Wang, N. Phung, D. Di Girolamo, P. Vivo, A. Abate, Energy Environ. Sci. 12 (2019) 865–886.
[41] Y. Di, Q. Zeng, C. Huang, D. Tang, K. Sun, C. Yan, Y. Wang, S. Ke, L. Jiang, X. Hao, Y. Lai, F. Liu, Sol. Energy Mater. Sol. Cells 185 (2018) 130–135.
[42] M. Saliba, S. Orlandi, T. Matsui, et al., Nat. Energy 1 (2016), https://doi.org/10.1038/nenergy.2015.17, 15017.
[43] PTAA - Poly[bis(4-phenyl)(2,4,6-trimethylphenyl)amine], Sigma-Aldrich, 2018.
[44] H.D. Pham, H. Hu, K. Feron, S. Manzhos, H. Wang, Y.M. Lam, P. Sonar, Sol. RRL (2017) 1700105.
[45] T. Leijtens, T. Giovenzana, S.N. Habisreutinger, J.S. Tinkham, N.K. Noel, B. A. Kamino, G. Sadoughi, A. Sellinger, H.J. Snaith, ACS Appl. Mater. Interfaces 8 (2016) 5981–5989.
[46] H. Chen, D. Bryant, J. Troughton, M. Kirkus, M. Neophytou, X. Miao, J.R. Durrant, I. McCulloch, Chem. Mater. 28 (2016) 2515–2518.
[47] I.B. Berlman, Handbook of Fluorescence Spectra of Aromatic Molecules, Academic Press, New York, 1971.
[48] K.Z. Förster, T. Kasper, Report of Bunsen Society for Physical Chemistry, 1955, pp. 976–981.
[49] J.K. Salunke, P. Sonar, F.L. Wong, V.A.L. Roy, C.S. Lee, P.P. Wadgaonkar, Phys. Chem. Chem. Phys. 16 (2014) 23320–23328.
[50] Q.Q. Ge, J.Y. Shao, J. Ding, L.Y. Deng, W.K. Zhou, Y.X. Chen, J.Y. Ma, L.J. Wan, J. Yao, J.S. Hu, Y.W. Zhong, Angew. Chem. Int. Ed. 57 (2018) 10959–10965.
[51] D. Li, J.-Y. Shao, Y. Li, Y. Li, L.-Y. Deng, Y.-W. Zhong, Q. Meng, Chem. Commun. 54 (2018) 1651–1654.
[52] B. Bin Cui, C. Zhu, S. Yang, Y. Han, N. Yang, L. Zhang, Y. Wang, Y. Jia, L. Zhao, Q. Chen, ACS Omega 3 (2018) 10791–10797.
[53] N.J. Jeon, J. Lee, J.H. Noh, M.K. Nazeeruddin, M. Grätzel, S. Il Seok, J. Am. Chem. Soc. 135 (2013) 19087–19090.
[54] J. You, G. Li, R. Wang, Q. Nie, Z. Wang, J. Li, Phys. Chem. Chem. Phys. 13 (2011) 17825.
[55] H. Cho, S. Lee, N.S. Cho, G.E. Jabbour, J. Kwak, D.-H. Hwang, C. Lee, ACS Appl. Mater. Interfaces 5 (2013) 3855–3860.
[56] T.M. Figueira-Duarte, K. Mullen, Chem. Rev. 111 (2011) 7260–7314.
[57] W. Kohn and L. J. Sham, Phys. Rev. DOI:10.1103/PhysRev.140.A1133.
[58] Gaussian 09, Revision A.02 M.J. Frisch, G.W. Trucks, H.B. Schlegel, G.E. Scuseria, M.A. Robb, J.R. Cheeseman, G. Scalmani, V. Barone, G.A. Petersson, H. Nakatsuji, X. Li, M. Caricato, A. Marenich, J. Bloino, B.G. Janesko, R. Gomperts, B. Mennucci, H.P. Hratchian, J.V. Ortiz, A.F. Izmaylov, J.L. Sonnenberg, D. Williams-Young, F. Ding, F. Lipparini, F. Egidi, J. Goings, B. Peng, A. Petrone, T. Henderson, D. Ranasinghe, V.G. Zakrzewski, J. Gao, N. Rega, G. Zheng, W. Liang, M. Hada, M. Ehara, K. Toyota, R. Fukuda, J. Hasegawa, M. Ishida, T. Nakajima, Y. Honda, O. Kitao, H. Nakai, T. Vreven, K. Throssell, J.A. Montgomery Jr., J.E. Peralta, F. Ogliaro, M. Bearpark, J.J. Heyd, E. Brothers, K.N. Kudin, V.N. Staroverov, T. Keith, R. Kobayashi, J. Normand, K. Raghavachari, A. Rendell, J.C. Burant, S. S. Iyengar, J. Tomasi, M. Cossi, J.M. Millam, M. Klene, C. Adamo, R. Cammi, J. W. Ochterski, R.L. Martin, K. Morokuma, O. Farkas, J.B. Foresman, D.J. Fox, Gaussian, Inc., Wallingford CT, 2016.
[59] C. Adamo, D. Jacquemin, Chem. Soc. Rev. 42 (2013) 845–856.
[60] A.D. Becke, J. Chem. Phys. 98 (1993) 5648–5652.
[61] J. Tomasi, B. Mennucci, R. Cammi, Chem. Rev. 105 (2005) 2999–3093.
[62] S. Grimme, J. Antony, S. Ehrlich, H. Krieg, J. Chem. Phys. 132 (2010) 154104.
[63] Thin Solid Films 452 (2004) 290–293.
[64] J. Lorrmann, B.H. Badada, O. Inganäs, V. Dyakonov, C. Deibel, J. Appl. Phys. 108 (2010) 113705.
[65] R. Sandoval-Torrientes, I. Zimmermann, J. Calbo, J. Aragó, J. Santos, E. Ortí, N. Martín, M.K. Nazeeruddin, J. Mater. Chem. A 6 (2018) 5944–5951.
[66] D. Deng, Y. Zhang, J. Zhang, Z. Wang, L. Zhu, J. Fang, B. Xia, Z. Wang, K. Lu, W. Ma, Z. Wei, Nat. Commun. 7 (2016) 13740.
[67] C.R. Patrick, G.S. Prosser, Nature (1960) 1021.
[68] W.J. Feast, P. Wilfried, C. Taliani, Chem. Commun. (2001) 505–506.
[69] F. Cozzi, F. Ponzini, R. Annunziata, M. Cinquini, J.S. Siegel, Angew. Chem. Int. Ed. 9 (1995) 1019–1020.
[70] K. Rakstys, A. Abate, M.I. Dar, P. Gao, V. Jankauskas, E. Kamarauskas, S. Kazim, S. Ahmad, M.K. Nazeeruddin, J. Am. Chem. Soc. 137 (2015) 16172–16178.
[71] Materials (Basel). 6 (2013) 1205–1236.
[72] P. Gratia, A. Magomedov, T. Malinauskas, M. Daskeviciene, A. Abate, S. Ahmad, M. Grätzel, V. Getautis, M.K. Nazeeruddin, Angew. Chem. Int. Ed. 54 (2015) 11409–11413.

[73] X. Liu, F. Kong, Z. Tan, T. Cheng, W. Chen, T. Yun, F. Guo, J. Chen, RSC Adv. 6 (2016) 87454–87460.
[74] Z. Zhao, J.H. Li, X. Chen, X. Wang, P. Lu, Y. Yang, J. Org. Chem. 74 (2009) 383–395.
[75] J. Lu, P.F. Xia, P.K. Lo, Y. Tao, M.S. Wong, Chem. Mater. 18 (2006) 6194–6203.
[76] W. Schroeder, P. Wilcox, K. Trueblood, A. Dekker, Anal. Chem. 23 (1951) 1740–1747.
[77] L. Li, B. Jiao, Y. Yu, L. Ma, X. Hou, Z. Wu, RSC Adv. 5 (2015) 59027–59036.
[78] F. Babudri, G.M. Farinola, F. Naso, R. Ragni, Chem. Commun. (2007) 1003–1022.
[79] Z. Li, Z. Wu, W. Fu, P. Liu, B. Jiao, D. Wang, G. Zhou, X. Hou, J. Phys. Chem. C 116 (2012) 20504–20512.
[80] D. Chercka, S.-J. Yoo, M. Baumgarten, J.-J. Kim, K. Müllen, J. Mater. Chem. C 2 (2014) 9083–9086.
[81] J. Salbeck, N. Yu, J. Bauer, F. Weissörtel, H. Bestgen, Synth. Met. 91 (1997) 209–215.
[82] J.K. Salunke, F.L. Wong, K. Feron, S. Manzhos, M.F. Lo, C.S. Shinde, D. Lee, A. Patil, V.A.L. Roy, P.P. Sonar, P. Wadgaonkar, J. Mater. Chem. C 4 (2016) 1009–1018.
[83] J. Jasieniak, M. Califano, S.E. Watkins, ACS Nano 5 (2011) 5888–5902.
[84] A.R. Chaudhry, R. Ahmed, A. Irfan, A. Shaari, A.G. Al-sehemi, Sci. Adv. Mater. 6 (2014) 1–13.
[85] S. Ryu, H. Noh Jun, J. Jeon Nam, Y.C. Kim, W.S. Yang, J. Seo, S. Il Seok , Energy Environ. Sci. 7 (2014) 2614–2618.
[86] S.S. Kalanur, U. Katrahalli, J. Seetharamappa, Principles of Fluorescence Spectroscopy, Kluwer Academic/Plenum Publishers, New York 2nd Edition, 1999.